Impact of the local metabolic milieu on bone fracture healing

Inaugural–Dissertation

to obtain the academic degree

DOCTOR RERUM NATURALIUM (Dr. rer. nat.)

submitted to the Department of Biology, Chemistry and Pharmacy

of Freie Universität Berlin

by

JULIA LÖFFLER (M.Sc.)

2019

Diese Arbeit wurde vom 01.12.2014 zum 31.01.2019, unter der Leitung von Dr. Stefan Kempa, MDC, Berlin-Buch, Dr. Anke Dienelt und Prof. Dr. Georg Duda, beide JWI/BCRT, Charité Universitätsmedizin Berlin, erstellt.

1. Gutachter: Dr. Stefan Kempa
2. Gutachter: Prof. Dr. Georg Duda

Disputation am: 09.04.2019

Summary

Nowadays, an increasing demand for sophisticated regenerative therapies is experienced, due to the globally prolonged life expectancy. Bone is an interesting model to study regenerative processes as it can regenerate without scar formation even in adults. Therefore, successful bone regeneration and its well-composed interaction of cellular and molecular processes acts as a blueprint for tissue regeneration. Evidence from experimental and clinical studies showed that especially early inflammatory responses shape fracture healing outcome. It is now appreciated that cellular metabolism determines immune as well as stromal cell functionalities and phenotypes. As bone regeneration is a highly energy consuming process, sufficient nutritional supply and cellular energy demands are hypothesized to be key aspects to effective healing. Specifically, the local metabolic microenvironment may affect cell communication, thus influencing the inflammatory response during bone repair. However little, attention has so far been given to the metabolic supply following bone injury and to which extent metabolism and metabolic signaling impact bone healing.

This work gives novel insights into the crosstalk of metabolism, inflammation and cellular communication during the onset of bone regeneration. Application of mass spectrometric methods allowed untargeted metabolic and proteomic profiling of an *in vivo* rat femoral osteotomy healing model. Comparing successful versus impaired bone healing revealed differences in the quantity of metabolites and metabolic enzymes of the central carbon metabolism. Interestingly, successful healing showed a stronger increase in signaling molecules and biosynthetic precursor molecules originating from glycolysis (lactate) and the TCA cycle (α-ketoglutarate, succinate) during the first days of bone fracture repair. This was accompanied by resolution of inflammation, up-regulation of mitochondrial proteins for ATP synthesis (oxidative metabolism), tissue revascularization and tissue remodeling. Succinate, an intermediate of the TCA cycle, associated with auto- and paracrine signaling properties and increased at day 7 during successful healing, gained special interest during this work. Succinate effectively influenced human macrophage cytokine transcription and enhanced the osteogenic differentiation potential of primary mesenchymal stromal cells *in vitro*. While this work gives first insights into the metabolic regulation during early bone regeneration, it remains to be investigated whether succinate can also positively influence bone regeneration *in vivo* and which cells specifically mediate and participate in metabolic signaling during the healing process.

Zusammenfassung

Die weltweit ansteigende Lebenserwartung sorgt für einen kontinuierlich steigenden Bedarf an hoch entwickelten regenerativen Therapien. Ein interessantes Studienmodel stellen insbesondere Knochen dar, aufgrund ihrer besonderen Eigenschaft der fehlenden Narbenbildung selbst im Erwachsenenalter. Die Erforschung des perfekt abgestimmten Zusammenspiels aus zellulären und molekularen Prozessen während der erfolgreichen Knochengeneration ermöglicht unter Umständen die Erstellung eines allgemein gültigen Bauplanes für Gewebsregeneration. Bisherige Forschungsergebnisse zeigten, dass vor allem die frühe inflammatorische Phase den Prozess der Knochenheilung stark beeinflusst. Neueste Erkenntnisse legen nahe, dass der Energiestoffwechsel die Funktionalität und den Phänotyp von Immun- und Stromazellen bestimmt. Die Schritte der Knochenregeneration sind mit einem hohen Energieumsatz verbunden. Demzufolge ist es wahrscheinlich, dass die Versorgung mit Nährstoffen und der zelluläre Energiebedarf wichtige Aspekte darstellen. Insbesondere die lokale metabolische Mikroumgebung könnte Einfluss auf die Zell-zu-Zellkommunikation ausüben und somit die Knochenheilung beeinflussen. Bisher wurden der metabolischen Homöostase, deren Veränderung aufgrund einer Verletzung und Einfluss auf den Knochenheilungsprozess nur geringfügig Aufmerksamkeit gewidmet.

Die vorliegende Arbeit beschreibt neue Erkenntnisse über den Zusammenhang zwischen Knochengeneration, Stoffwechsel und zellulärer Kommunikation. Die Anwendung massenspektrometrische Methoden ermöglichte das Profiling des Metaboloms und Proteoms von Frakturgewegen eines in vivo Rattenfemurosteotomiemodeles. Der Vergleich von erfolgreich und beeinträchtigt heilender Frakturen ergab quantitative Unterschiede in den Stoffwechselprodukten und Enzymen des zentralen Kohlenstoffwechsels.

Untersuchungen zeigten einen stärkeren Anstieg von biosynthetischen Vorläufer- und Signalmolekülen aus der Glykolyse (Laktat) und dem Citratzyklus (α-Ketoglutarat, Succinat) in der frühen Phase der erfolgreichen Knochenheilung. Damit einhergehend wurden die Verminderung der Entzündung, der Anstieg von mitochondrialen Proteinen der ATP Synthese sowie die Revaskularisierung des Frakturkallus und Gewebsumbau festgestellt. Ein besonderes Augenmerk stellten die erhöhten Succinat-Werte dar, welche in der frühen Heilungsphase erfolgreich heilender Frakturen gemessen wurden. Aktuelle Literatur beschreibt auto-und parakrinen Eigenschaften dieses Stoffwechselintermediates. In anschließenden *in vitro* Experimente wurde gezeigt, dass die Zugabe von extrazellulärem Succinat sowohl die Transkiption von Zytokinen in humanen Makrophagen, als auch das osteogene Differenzierungspotenzial von humanen, primären mesenchymalen Stromazellen beeinflusst. Die Untersuchung der Wirkungsweise in der *in vivo* Knochenregeneration ist der nächstlogische

Schritt und sollte in folgenden Arbeiten untersucht werden. Des Weiteren verbleibt zu klären, welche Zelltypen insbesondere durch den Stoffwechsel und dessen Signale während der Frakturheilung beeinflusst werden.

Acknowledgement

I am struggling to find those first, perfectly phrased words that summarize your emotions when looking back the time of your PhD. Where to begin, who to thank first and how to say it right, because everyone who has accompanied me on this intense, challenging, exhilarating, sometimes frightening and frustrating but also memorable and valuable journey made an impact in their own, special way. THANK YOU!!!

During my PhD, I had the honor being part of two different labs and I would like to express my sincere gratitude to all my lab mates, present and former: thank you for making this time special! Thanks for all the support along the way, for all the laughs, the inspiration, for sharing some of the frustration and all the joy.
To the members of the ZET-Team: Ana, Andrea, Anke, Anne, Antje, Caro, Dorit, Janine, Janosch, Martin, Melanie, Simon, Sven, Taimoor and Wera. It was such a pleasure being part of your scientific crew. Thank you so much for taking me in, for caring and listening and the numerous scientific and social adventures.
To the lab members from Stefan's group: Alina, Birte, Christin, Chris, Ela, Fardad, Guido, Henning, Henning, Jenny, Matthias, Martin, Nadine, Olya, Şafak, Susi and Tobias. Thanks for sharing your knowledge and passion about coffee, a good drink and great science – and for making the sometimes never-ending journey to and from Buch always worth it.

Special acknowledgement goes to my supervisors Stefan Kempa and Georg Duda. I would like to thank Stefan Kempa for his guidance, the patience and the great amount of trust he puts in you and everyone in his group. I would like to particularly acknowledge Georg Duda for his advice and leadership throughout my PhD. For all the opportunities he has given, that let to my professional and personal development and progress.
Another very special thanks goes to Anke Dienelt, who was the one that sparked my interest for this project. Thank you for all your support, your tireless effort and the enthusiasm that you have put in every part of our work.

I had the great opportunity to take part in the BSRT graduate program, where I found other likeminded young scientists, which have shared this journey and one or another afterwork drink with me. They have become wonderful friends that I would not want to have missed for the world.

An dieser Stelle möchte ich meiner Familie danken, auf deren uneingeschränkte Unterstützung ich immer zählen kann. Ohne eure Hilfe in jeder Lebenslage, eure Ermutigungen all meine

Interessen und Ziele zu verfolgen, euer unermüdliches Bestreben jede Schwierigkeit doch noch zu meinen Gunsten zu steuern und euer Vertrauen in all meine Entscheidungen wäre ich nicht so weit gekommen. Danke für Alles.
Darüber hinaus möchte ich Nicolas Fritz danken, der mich über den gesamten Zeitraum hinweg in allen möglichen und unmöglichen Situationen unterstützt hat. Du hast jede Stimmungsschwankung und jedes zerknirschte Gegrummel meinerseits mit unendlicher Geduld bezwungen, hast mich beruhigt, wenn ich nicht weiterwusste und immer nach vorne geschaut.

Zu guter Letzt möchte ich allen Freunden danken, deren Unterstützung und Freundschaft mir sehr viel bedeuten und die mir in so vielen Lebenslagen geholfen haben.

Eigenständigkeitserklärung

Hierdurch versichere ich, Julia Löffler, dass ich meine vorliegende Dissertation selbstständig und ohne unerlaubte Hilfe angefertigt habe. Die aus fremden Quellen (direkt oder indirekt) übernommenen Gedanken und Informationen wurden als solche gekennzeichnet.
Die Dissertation wurde bisher nicht in dieser oder leicht abgewandelter Form in einem anderen Promotionsverfahren eingereicht.

Berlin, den 31.01.2019

Unterschrift……

Content

Abbreviations

3PG	3-Phosphoglycerate
3PHP	3-Phosphohydroxypyruvate
ALDH7A1	Aldehyde dehydrogenase 7 family member A1
ALP	Alkaline Phosphatase
AMPK	5‘adenosine monophosphate-activated protein kinase
ANOVA	Analysis of variance
ATP	Adenosine triphosphate
BCA	Bicinchoninic acid assay
BLVRB	Biliverdin reductase B
CATG	Cathepsin G
CATK	Cathepsin K
CCM	Central carbon metabolism
CCR7	C-C chemokine receptor 7
CD	Cluster of differentiation
cDNA	Complementary DNA
CoA	Coenzyme A
CPT1	Carnitine palmitoyltransferase 1
CS	Citrate synthase
DHAP	Dihyroxyacteonphosphate
DMSO	Dimethylsulfoxid
DNA	Deoxyribonucleic acid
DTT	Dithiothreitol
ECM	Extracellular matrix
ELISA	Enzyme-linked Immunosorbent Assay
EM	Expansion medium
F-1,6-BP	Fructose-1,6-bisphosphate
F-2,6-BP	Fructose-2,6-bisphosphate
$FADH_2$	Flavin adenine dinucleotide
FAO	Fatty acid oxidation
FAS	Fatty acid synthesis
FCS	Fetal calf serum
FOXO	Forkhead-Box-Protein O3
G6P	Glucose-6-phosphate
GAP3	Glyceraldehyde 3-phosphate

GAPDH	Glyceraldehyde 3-phosphate dehydrogenase
GC-MS	Gas-chromatography coupled mass spectrometry
GLUT1	Glucose transporter 1
GPR	G-protein coupled receptor
HIF-1α	Hypoxia inducible factor 1 alpha
HPLC	High-performance liquid chromatography
HSC	Hematopoietic stem cell
IAA	Idoacetamide
IFNγ	Interferon gamma
IL-1/4/6/10	Interleukin 1/4/6/10
IL-1Ra	Interleukin 1 receptor antagonist
IRG1	Immune responsive gene 1
KCL	Potassium chloride
LAMP2	Lysosome specific associated membrane protein 2
LC-MS	Liquid-chromatography coupled mass spectrometry
LDH	Lactate dehydrogenase
LFQ	Label-free quantification
LPS	Lipopolysaccharide
MCM6	Minichromosome maintenance complex component 6
MCP1	Monocyte chemoattractant protein 1
M-CSF	Macrophage colony-stimulating factor
MCW	Methanol:chloroform:water
MeOH	Methanol
MeOX	Methoxamine hydrochloride
MIP	Macrophage inflammatory protein
MMP	Matrix metalloproteinase
MRC1	Mannose receptor C-type 1
MS	Mass spectrometry
MSTFA	*N*-Methyl-*N*-(trimethylsilyl) trifluoroacetamide
MSC	Mesenchymal stromal cell
NADH	Nicotinamide adenine dinucleotide
NaOH	Sodium hydroxide
NET	Neutrophil extracellular trap
NF-κB	Nuclear factor 'kappa-light-chain-enhancer' of activated B-cells
NMR	Nuclear magnetic resonance
NO	Nitric oxide
O_2	Molecular oxygen

OCN	Osteocalcin
OD	Optical density
OM	Osteogenic medium
OPG	Osteoprotegerin
OxPhos	Oxidative phosphorylation
PBS	Phosphate-buffered saline
PDGF	Platelet derived growth factor
PDHC	Pyruvate dehydrogenase complex
PDK1	Pyruvate dehydrogenase kinase isoenzyme 1
PE	Phycoerythrin
PEP	Phosphenolpyruvate
PFA	Paraformaldehyde
PFK-1	Phosphofructokinase 1
PFK-2	Phosphofructokinase 2
PFKFB1	6-phosphofructo-2-kinase/fructose-2,6-biphosphate 1
PGE2	Prostaglandin E2
PHD	Prolyl hydroxylase
PHGDH	3-Phosphoglycerate dehydrogenase
PMA	Phorbol 12-myristate 13-actetate
PMM2	Phosphomannomutase
pNPP	4-nitrophenylphosphate
PPP	Pentose phosphate pathway
PTH	Parathyroid hormone
RAG-1	Recombinant activating gene 1
RANK	Receptor Activator of NF-κB
RANKL	RANK Ligand
RNA	Ribonucleic acid
ROI	Region of interest
ROS	Reactive oxygen species
RPL13A	Ribosomal Protein L13a
Runx2	Runt-related transcription factor 2
SDF-1	Stromal cell-derived factor 1
SDH	Succinate dehydrogenase
siRNA	Small interfering RNA
SPP1	Osteopontin
TBP	TATA Box-binding protein
TCA cycle	Tricarboxylic acid cycle

T_{EFF}	Effector T cell
T_{EMRA}	Cytotoxic $CD8^+$ terminally differentiated memory T cells
TFA	Trifluoroacetic acid
TGF-β	Transforming growth factor beta
T_{MEM}	Memory T cell
TMS	Trimethylsilyl
TNF-α	Tumor necrosis factor alpha
TOF	Time of flight
TRAP	Tartrate-resistant acid phosphatase
T_{REGS}	Regulatory T cells
UQCRFS1	Ubiquinol-cytochrome c reductase, rieske iron-sulfur polypeptide
VEGF	Vascular endothelial growth factor
α-KG	Alpha-ketoglutarate
α-SMA	Alpha-smooth muscle actin

Figures

Tables

1. Introduction

1.1. Relevance of bone healing in aging societies

The aging of European populations is accompanied by increasing numbers of bone injuries and fractures [1, 2]. This demographic change demands for sophisticated regenerative therapies restoring tissue health and integrity. Five to fifteen percent of all fractures show impaired healing and formation of pseudarthrotic structures, depending on fracture type and localization [3-5]. Incidents of non-unions are independent of age and determined by several patient-specific risk factors, like severity of fracture and comorbidities [6]. Fracture non-unions are not only a burden to the patient but put a substantial financial strain on our health systems [7]. There is a definite need for innovational therapeutic applications and even preventive measures. Research from the Julius-Wolff Institute showed that the early phases of fracture healing are prone to disturbances and that prolonged inflammatory signaling is one cause leading to an impaired healing outcome [8]. Further work established a link between non-unions in patients and elevated ratios of $CD8^+$-terminally differentiated cytotoxic memory T cells (T_{EMRA}), which enhances the local inflammatory response [9].

Although the significance of the early fracture healing responses has been recognized, detailed studies investigating the molecular cascades that determine the different phenotypes of fracture healing are missing so far. Until now, most research in this regard has focused on impaired revascularization of the fracture gap as a factor hindering healing [10, 11]. However, the molecular mechanisms preceding impaired revascularization or influencing prolonged inflammatory signaling remain to be unraveled.

Bone regeneration is an interesting subject to study, as it recapitulates central steps of embryogenic bone development. Besides the liver, bone is the only organ in the adult body that has – theoretically – unlimited and scarless healing potential, making bone healing a blueprint model for tissue regeneration.

1.2. The structure and function of bones

1.2.1. Bone as an organ

The adult skeletal system contains about 206-208 bones, which can be categorized into flat, long, short, irregular and sesamoid bone [12]. Each shape holds a different function – flat and irregular bones protect inner organs, long bones enable mobility and weight support, short bones usually offer stability, while sesamoid bones protect tendons.

Two main forms of bony tissue are found within bones: cortical (or compact) and trabecular (or spongy) bone [13]. Cortical bone surrounds the bone marrow cavity, forming a dense and compact structure. Trabecular bone on the other hand, often located at the end of long bones, has honeycombed features and is interspaced with hematopoietic bone marrow. The bone matrix is mainly composed of organic fibers like collagen I, non-collagenous proteins and inorganic minerals.

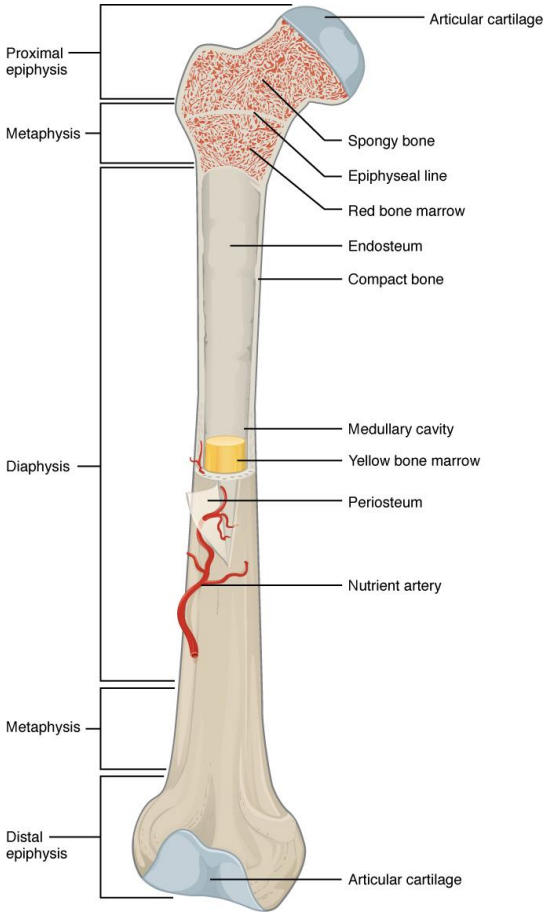

Figure 1. Important anatomical structures of long bones.

Figure taken from Rice University [14].

Besides functioning as the central part of human mobility, stability and hematopoiesis, bone exerts vital functions as an endocrine organ. As such, bone is highly involved in calcium and phosphate homeostasis and modulates glucose tolerance by secretion of osteocalcin [15]. Many of these processes rely on continuous bone remodeling by a fine-tuned orchestration of bone formation by osteoblasts and bone resorption through osteoclast activity. Bone remodeling not only ensures molecular functionality but also functional adaptation to mechanical loading according to Wolff's law; other environmental stresses and repair of microdamages [16, 17].
Hormonal secretion from bone bridges its physiological function and the regulation of systemic glucose metabolism. Bone health and successful bone regeneration after trauma, thus are key factors to human physiology.

1.2.2. Cellular composition of the bone

The living part of bone consists of four major cell types: osteoblasts, osteocytes, osteoclasts and bone lining cells (also called osteogenic cells),(**Figure 2**) [18].

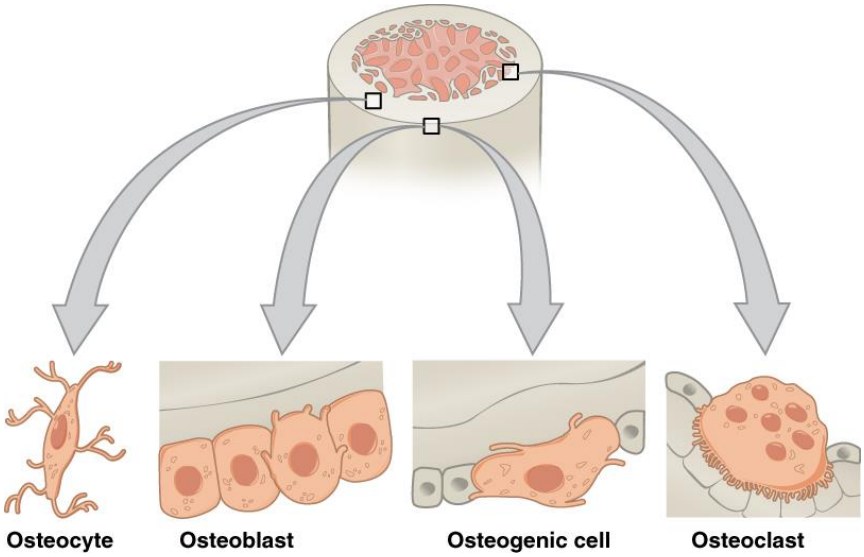

Figure 2. Major bone cell types found within bone tissue.

Osteoblasts start to secrete bone matrix, trapping some of them within the mineralized tissue. Trapped osteoblasts differentiate into osteocytes. Osteogenic or bone lining cells share properties with osteoblasts. Bone resorbing osteoclasts derive from the monocytic lineage. Figure taken from Rice University [14].

Osteoblasts, derived from bone marrow mesenchymal stromal cells (MSCs), synthesize the bone matrix and further regulate osteoclast activity [19]. Osteoblasts produce new bone matrix by *de novo* collagen I biosynthesis and subsequent mineralization through hydroxyapatite deposition [20, 21]. MSCs differentiate towards the osteoblastic phenotype by activation of the canonical Wnt pathway through β-catenin signaling, leading to transcription of osteogenic factors like RUNX2 and lineage commitment [22-25].

Bone matrix mineralization leads to enclosement of osteoblasts within the mineralized tissue. These entrapped osteoblasts transform into terminally differentiated osteocytes, making up the majority of cells existing in adult bone (approximately 90-95%). Osteocytes perform mechanosensing and -transducing tasks within bone, through their network of cytoplasmic extensions, the lacunocanalicular system [26]. Upon mechanical stimuli placed on bone, changes of the interstitial fluid flow within the canaliculi are sensed by osteocytes and transduced into chemical signals. By this mechanism, osteocytes can regulate bone formation by osteoblasts and bone resorption by osteoclasts [27].

The bone resorbing unit is formed by osteoclasts which derive, contrary to osteoblasts and osteocytes, from the monocytic lineage of bone marrow hematopoietic stem cells [28]. Osteoclasts

mediate bone degradation by enzymatic digestion of the matrix. Osteoclastogenesis and specific marker gene expression (e.g. tartrate-resistant acid phosphatase (TRAP) and cathepsin K (CATK)) is dependent on signals from receptor activator of nuclear factor κB-ligand (RANKL) and macrophage colony stimulating factor (M-CSF). Maturation of osteoclasts occurs as several premature osteoclasts fuse to form big multinucleated cells. Mature osteoclasts enclose a sealed compartment between the bone surface and their ruffled basal membranes, the active resorption zone. Within this resorption compartment, hydrogen ions are released resulting in acidification of the area and dissolution of the inorganic bone material. Organic bone material is degraded by subsequent enzymatic activity of cathepsin K, which mainly breaks down collagen I [29, 30].
Bone lining cells have long been neglected in bone research and are thought to arise from the osteoblastic lineage, as they share certain features with osteoblasts like alkaline phosphatase (ALP) and localization at the bone surface. Different to the general functions of osteoblasts, that synthesize collagen, bone lining cells have been found to resorb protruding collagen from the bone matrix, most likely by matrix metalloproteinase activity. Recent studies have started to highlight the importance of bone lining cells for orchestration of bone remodeling. Everts et al. suggest bone lining cells to clear left-over demineralized non-digested collagen by osteoclasts, before new collagen synthesis can take place [31]. By using lineage tracing models, another study identified bone lining cells as a potential source of osteoblasts besides MSCs in adults [32].

Bone remodeling, the coupling between resorption and formation, is finely tuned by a variety of factors in order to maintain a positive balance between these two processes. Key regulator pathways are: (1) the axis of osteoprotegrin (OPG) along with RANKL and RANK and (2) endocrine signaling. Osteoclasts become activated by ligation of their surface receptor RANK. Their activation is regulated by osteoblasts secreting the paracrine factors RANKL and OPG. Secretion of RANKL and its ligation of RANK stimulates bone resorption, while secretion of OPG, a RANK decoy receptor, mediates osteoclast inhibition by neutralizing RANKL activity.

As outlined earlier, bone metabolism is connected to the systemic energy metabolism. Osteocalcin (OCN) a peptide hormone, secreted from osteoblasts locally regulates osteocyte maturation [33]. Systemically, OCN can mediate glucose tolerance by stimulating insulin synthesis in pancreatic β-cells and increasing insulin sensitivity in adipose tissue and muscles (via active uncarboxylated form: unOCN). In mice and human studies, total serum OCN (tOCN) levels have been associated with diabetes and metabolic syndrome, demonstrating a close connection between energy metabolism, the nutrient status and bone physiology [34, 35].

1.2.3. Bone regeneration after trauma

Even though bone is a strong tissue that can carry large loads, application of too high forces on bones will eventually lead to tissue failure and fractures. Fracture healing can occur via two ways: primary or direct and secondary or indirect healing. However, direct healing occurs seldom as it requires correct anatomical reduction, biomechanically competent lamellar bone and no more than 1 mm space between the bone entities [36]. Secondary healing is the by far more common process that occurs during bone regeneration and will be referred to within this thesis. Secondary or indirect fracture healing is comprised of (1) intramembranous and (2) endochondral ossification [37].

(1) Intramembranous ossification: bone tissue is formed along structures build by mesenchymal stromal cells, which after forming a cluster of cells start to differentiate into osteoblasts and secret extracellular matrix (mainly collagen I), followed by mineralization.

(2) Endochondral ossification: bone formation requires development of cartilage (hypertrophic chondrocytes) prior to ossification, creating woven bone. Tissue remodeling will transform woven bone into lamellar bone and restore its biomechanical strength [3].

Endochondral ossification is the process induced after most fracture injuries and occurs during growth of tubular bones. It will be referred to as bone regeneration, during the course of this work. The following section gives a detailed overview of secondary endochondral fracture healing, which can be divided into five consecutive phases: (1) hematoma formation with pro-inflammatory signaling, (2) anti-inflammatory hematoma, (3) soft callus formation, (4) hard callus formation and (5) remodeling.

After trauma and tissue damage peripheral and intramedullary blood enters the site of injury, alongside with first immune cells, as a result of the disrupted local vascular network [38]. A pro-inflammatory response is initiated by the present cells and a hematoma is formed as the blood coagulates (**Figure 3, panel 1**). This first pro-inflammatory phase, which includes among others high levels of tumor necrosis factor alpha (TNF-α), interleukin 6 (IL-6) and interleukin 1 (IL-1), is essential for healing progression by promoting angiogenesis and attracting further immune cells [39-41]. During this early inflammatory response TNF-α, mainly expressed by macrophages is central for recruiting further immune cells. IL-1 is also highly secreted by macrophages and promotes primary cartilage production, angiogenesis and induces IL-6 secretion in osteoblasts

[42, 43]. IL-6 secretion stimulates angiogenesis by vascular endothelial growth factor (VEGF) and induces differentiation of osteoclasts and osteoblasts [37, 44].
Recruitment of MSCs, reduction of pro-inflammatory signaling and transition towards an anti-inflammatory response is mediated by a shift in cytokine secretion. Influx of cells, which are highly metabolically active in order to mediate their functions, and the absence of adequate nutrient supply through a damaged vascular network, leads to a nutrient deprived and anaerobic micromilieu. Especially, within this hypoxic surrounding, macrophages switch their cytokine secretion profile and start secreting pro-angiogenic and anti-inflammatory factors, like vascular endothelial growth factor, interleukin 10 (IL-10) and transforming growth factor beta (TGF-β). VEGF secretion is upregulated in macrophages in response to hypoxia inducible factor 1 (HIF-1) and local lactate accumulation [45, 46]. Limited supply of nutrients like hypoglycemia have also shown *in vitro* to decrease pro-inflammatory cytokine secretion (TNF-α) in macrophages within a hypoxic environment [47]. All named processes lead to the first wave of revascularization, providing oxygen and nutrients (**Figure 3, panel 2**). In parallel, stromal derived factor 1 (SDF-1) expression is increased within the fracture micromilieu recruiting MSCs into the site of injury [48]. The primary hematoma slowly transitions into a soft callus made up of fibrin-rich granulation tissue. Fresh supply of nutrients and oxygen enables cartilage formation by MSCs differentiating into chondrocytes, starting at the fracture ends. Collagen I and III primarily make up the soft callus matrix produced at this stage [49] (**Figure 3, panel 3**). These areas of new hypertrophic chondrocytes are poorly vascularized. In order to progress with mineralization new vessels need to be formed – the second wave of angiogenesis during fracture healing is initiated. Chondrocytes express high levels of VEGF, leading to blood vessel ingrowth, at the same time cartilage degradation and remodeling takes place, facilitating formation of new vasculature. Matrix degradation is conducted by matrix metalloproteinases (MMPs) [50, 51] (**Figure 3, panel 4**).

Osteogenic signaling initiates tissue mineralization and conversion from a soft to a hard callus. Osteoblasts start to secrete collagen fibers, which later on are mineralized by hydroxyapatite deposition and crystallization of calcium and phosphate [52]. The resulting woven bone provides biomechanical stability to a certain extent, however full biomechanical capacity is not reinstated. By a second resorption phase that can take up months to years, woven bone structure is remodeled into lamellar bone surrounding the bone marrow cavity and restoring its full biomechanical properties [37] (**Figure 3, panel 5**). Remodeling is achieved by a fine-tuned cycle of bone resorption by osteoclasts and bone formation by osteoblasts.
Bone regeneration is a highly orchestrated process involving the synergy of several cell types. There is intensified evidence on the importance of metabolic signaling as a crucial mediator for successful bone healing.

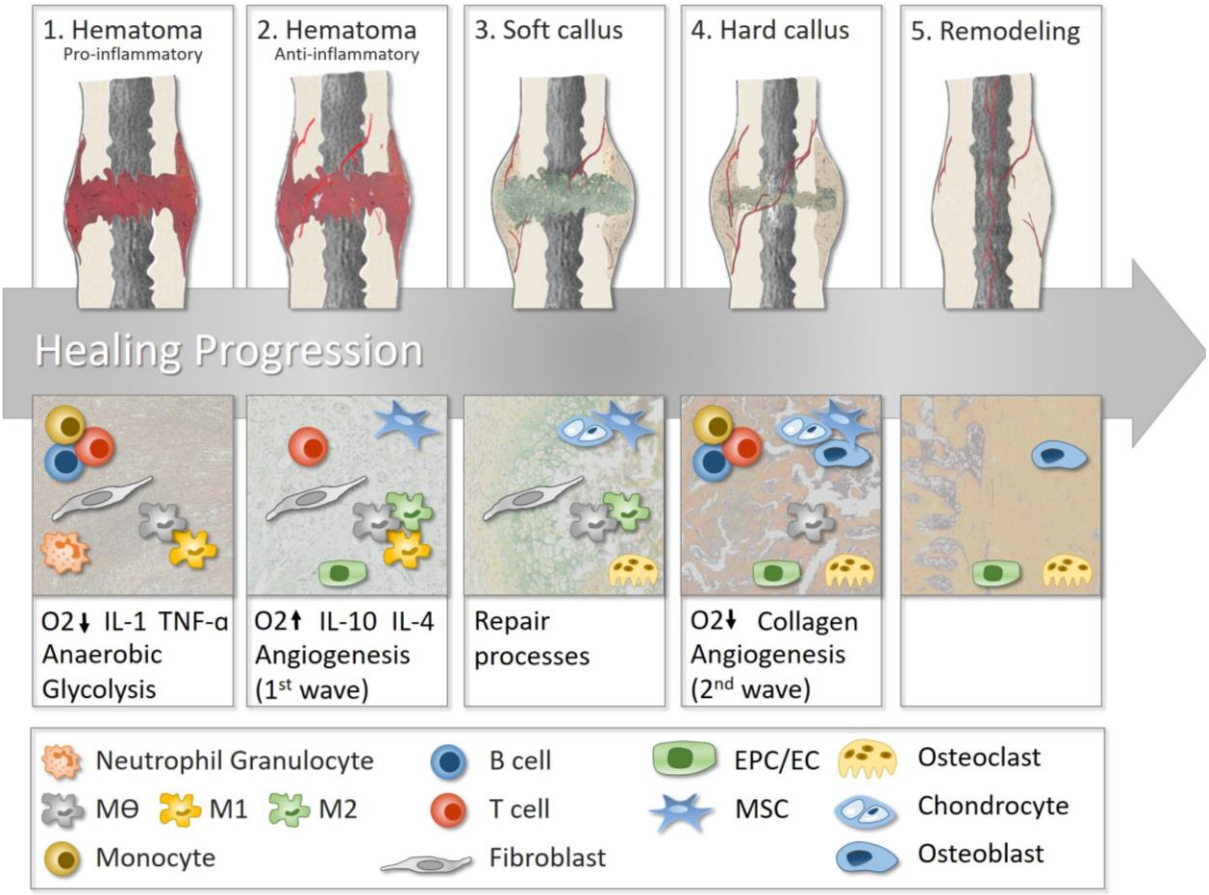

Figure 3. The five consecutive phases of bone healing and the involved cell types.

Major influx of innate immune cells during the pro-inflammatory phase (1), the anti-inflammatory phase is characterized by a switch in immune cell subsets and vessel development (2). Chondrogenic differentiation and proliferation is observed during soft callus formation (3). A second angiogenic wave and subsequent tissue mineralization defines central events of hard callus formation (4). Remodeling processes by osteoblasts and osteoclasts restore the original bone structure and tissue stability. Taken from: Loeffler et al. [53].

1.2.4. Immune cells in bone regeneration

The strong link between the immune system and initiation and progression of bone regeneration has been described partially throughout the previous section. Over the last years, research has extended the knowledge on osteoimmunology and proven a dependence of successful fracture healing on a variety of immune cells from the innate and adaptive immune response.

Bone regeneration is substantially delayed when macrophages are depleted [54, 55]. Fracture calli under such conditions show increased fibrotic tissue and less tissue mineralization. Macrophages are important for bone metabolism, can induce mineralization of the bone matrix and influence osteogenic differentiation, as shown *in vitro* and *in vivo* [56-58]. There is a high amount of evidence underlining the importance of classically activated (M1-like) and alternatively activated (M2-like) macrophages on different levels of successful bone repair. M1 macrophages, releasing pro-inflammatory cytokines, are needed to initiate the early inflammatory response, while M2 macrophages contribute to the resolution of inflammation and tissue regeneration [58]. Both subtypes have been reported to induce osteoblastic differentiation of MSCs. M2 macrophages further promote revascularization of the fracture callus [59-61].

Neutrophils are the most abundant cells in the early hematoma and important for its initial formation by secreting a fibronectin rich extracellular matrix before other cells can infiltrate the hematoma [62, 63]. Neutrophil depletion by lymphocyte antigen 6 complex (Ly-6C) antibody treatment resulted in decreased monocyte and macrophage recruitment, leading to impaired fracture healing [64]. However, excess neutrophil infiltration after serve trauma may lead to compromised bone regeneration [65].

Investigations using recombinant activating gene 1 knock out (Rag-$1^{-/-}$) mice, lacking adaptive immune responses, as their production of T and B cells is abrogated, show accelerated bone repair and callus maturation [66]. On the contrary, subsequent studies showed that bone quality was reduced in mice lacking mature T and B cells, their bones showed less elasticity and higher susceptibility to breakage [67]. Additionally, T cells influence osteoblast differentiation and induce anti-inflammatory signaling from MSCs by IL-17 secretion [68, 69]. Current research highlights that regulatory T cells (T_{REGS}) play a significant role in bone homeostasis, by regulating osteoclastogenesis and osteoclast apoptosis [70].

In patients that display fracture non-unions, an increased ratio of circulating T_{EMRA} has been positively correlated with failure or delay of successful bone healing [9].

We are just starting to understand the manifold ways in which immune cells influence bone regeneration and which mechanism have beneficial or adverse effects. Immune cell functionality however, is highly dependent on metabolic reprogramming and signaling. Metabolism and its possible implication on inflammation and tissue regeneration will be highlighted in the following chapter.

1.3. Cellular metabolism

Cellular metabolism defines the number of biochemical reactions a cell engages to provide energy and molecules for its overall needs (e.g. proliferation, maintenance) and function. The energetic state of a cell and the connected chemical reactions are closely monitored and arranged in a systematic manner by metabolic pathways. Generally, one can differentiate metabolic pathways into anabolic (build up) and catabolic (breakdown) reactions. Uptake of sugars, lipids or amino acids, their breakdown into smaller entities (catabolism) and sequential utilization of these building blocks for biosynthesis of new macromolecules (anabolism) is mainly regulated by the central carbon metabolism (CCM), which is highly conserved across different organisms. The CCM includes glycolysis, fermentation, tricarboxylic acid cycle (TCA cycle), pentose phosphate pathway, lipid and amino acid pathways [71]. The central carbon metabolism is coupled to mitochondrial respiration or oxidative phosphorylation, serving as the central producer of ATP.
As cellular needs or the conditions of its surroundings may change rapidly, cells can adapt their metabolism accordingly. When a cell undergoes differentiation, it usually specializes or modifies its function, thus changes its energetic/metabolic requirements. This rearrangement of nutrient utilization is termed metabolic reprogramming and was discovered in transformation of tumor cells. Recent research has highlighted metabolic reprogramming to be a feature that is also important in stem cell differentiation and immune cell activation and polarization [72-74].

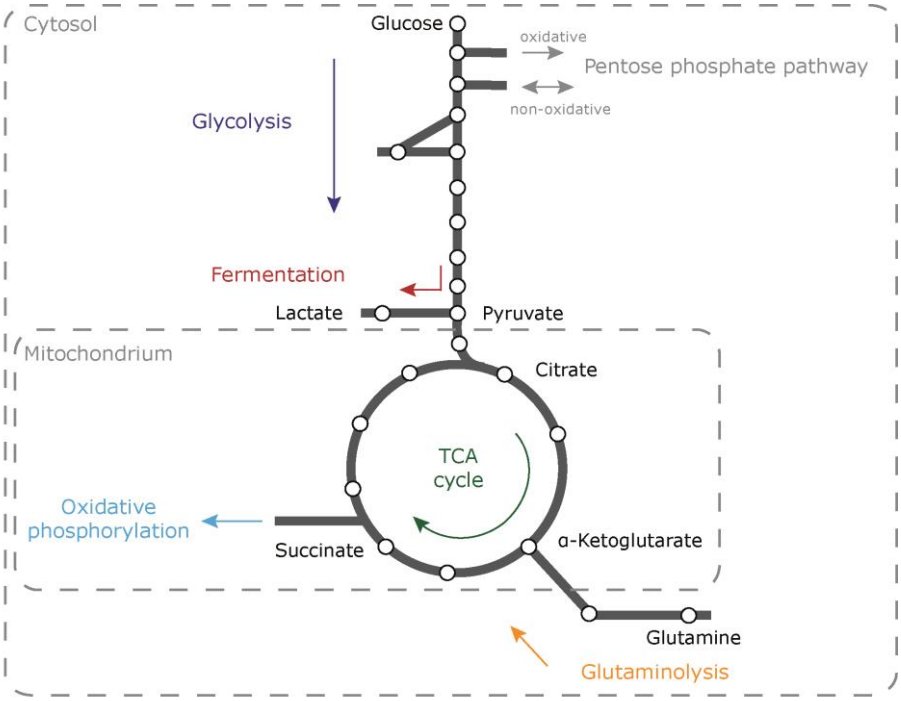

Figure 4. Metabolic pathways that make up the central carbon metabolism.
Glycolysis fuels most metabolic pathways. Under anaerobic conditions, glucose is transformed into lactate. When oxygen is present, the carbons derived from glucose are shuttled into the TCA cycle and fully oxidized during oxidative phosphorylation. Glutaminolysis replenishes the TCA cycle. Adapted from [75].

1.3.1. Introduction to selected central metabolic pathways

1.3.1.1. Glycolysis

Consumption of glucose is the most important energy supply of mammalian metabolism and regulated by ten consecutive enzymatic reactions termed glycolysis. The pathway can be divided into two phases, each containing five reactions; (1) the investment phase, where ATP is consumed and (2) the pay-off phase where ATP is produced, ending with generation of pyruvate and an energetic yield of net two molecules of ATP [75].
The investment phase begins with the phosphorylation of glucose to glucose-6-phosphate (G6P) under ATP consumption, this is an irreversible reaction and G6P is confined to the cell (**Figure 5**). Next steps include isomerization by hexophosphate-isomerase and ATP dependent phosphorylation by phosphofructokinase 1 (PFK-1), another rate-regulatory step within glycolysis [75]. The resulting fructose-1,6-bisphosphate (F-1,6-BP) is split into two three-carbon containing molecules: dihydroxyacetone phosphate (DHAP) and glyceraldehyde 3-phosphate (GA3P), where DHAP can be isomerized to GA3P [76].
GA3P enters the second phase of glycolysis, where the first two reactions by glyceraldehyde phosphate dehydrogenase and phosphoglycerate kinase produce one 3-phosphoglycerate (3PG) plus one molecule of NADH and ATP (two molecules of NADH and ATP per molecule of glucose). Two further reactions form phosphoenolpyruvate (PEP), which is transformed to pyruvate in a final step catalyzed by pyruvate kinase (PK). This step yields another two molecules of ATP per glucose molecule and is tightly regulated. Under presence of oxygen, glucose derived carbons enter the TCA cycle and are ultimately used in mitochondrial respiration for maximal ATP synthesis [75].

Under hypoxic conditions, lactic acid fermentation is engaged and pyruvate is converted to lacate by lactate dehydrogenase (LDH), thereby replenishing the NAD^+ needed for GA3P oxidation in the first step of the pay-off phase. During anaerobic glycolysis, glucose is oxidized only partially, which generates two molecules of ATP, approximately 5.5% of glucose's oxidative capacity.

Glycolytic intermediates fuel into several other metabolic pathways. One example is 3PG, which feeds into the *de novo* serine biosynthesis by 3-phosphoglycerate dehydrogenase activity and from there on into the one-carbon cycle, that mediates amino acid homeostasis, nucleotide biosynthesis and epigenetic maintenance [77, 78].

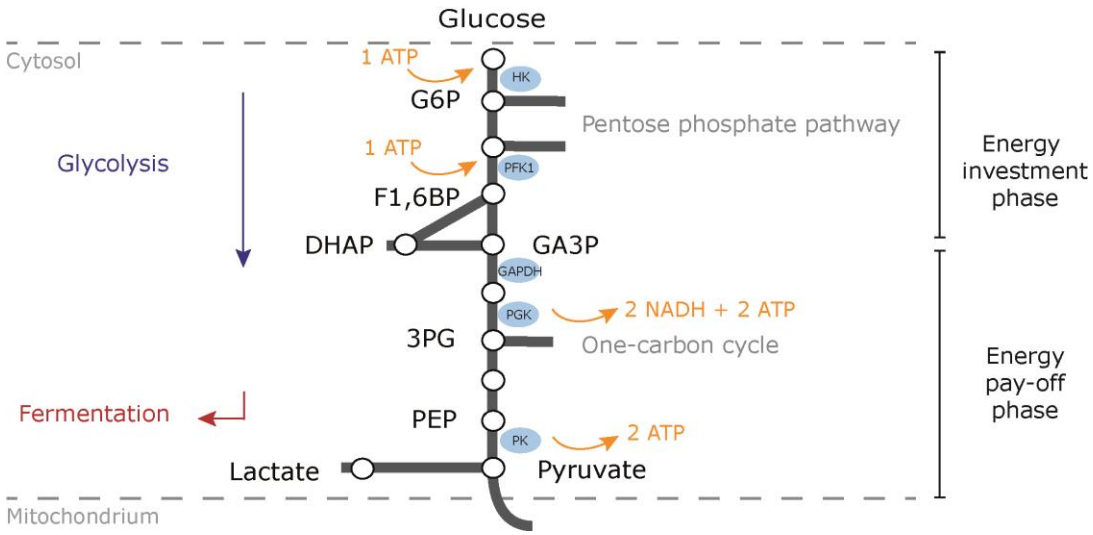

Figure 5. Schematic display of the glycolytic pathway with selected intermediates and enzymes. Glucose is converted to G6P by HK. Under sufficient oxygen levels, it is oxidized during subsequent steps of the glycolytic pathway and fed into the TCA cycle, which takes place in the mitochondria of a cell. When oxygen levels are low, lactate is formed from glucose as an end-product. Enzymes are depicted in blue ovals. Energy consuming and producing steps are marked with orange arrows. HK: Hexokinase, PFK-1: phosphofructokinase 1, GAPDH: glyceraldehyde 3-phosphate dehydrogenase, PGK: phosphoglycerate kinase, PK: pyruvate kinase. Figure adapted from [75, 79, 80].

1.3.1.2. TCA cycle

Under aerobic conditions pyruvate is translocated from the cytosol (place of glycolysis) into the mitochondrial matrix, where it is converted into acetyl-Coenzyme A (acetyl-CoA). Acetyl-CoA reacts with oxaloacetate forming citrate (catalyzed by citrate synthase), thus entering the TCA cycle. During a full run of the TCA cycle acetyl-CoA is oxidatively broken-down; its stored energy is released in a step-wise manner and transferred onto energetic intermediates like NADH and $FADH_2$ [75, 79] (**Figure 6**). The second reaction of the TCA cycle transforms citrate to isocitrate, which is consecutively transformed into α-ketoglutarate (α-KG) by isocitrate dehydrogenase. Alpha-ketoglutarate dehydrogenase decarboxylates α-KG and succinyl-CoA is formed. During the last two reactions the energetic intermediate NADH is generated. Succinate dehydrogenase (SDH) catalyzes the sixth reaction: the conversion from succinate to fumarate with generation of FADH. This step is highly oxygen dependent, as SDH is also a part of the electron transport chain, where it forms complex II. The last two steps of the TCA cycle comprise fumarate to malate conversion and malate to oxaloacetate regeneration (under NADH production), which react with acetyl-CoA thus completing the cycle [76, 79]. In summary, one molecule of GTP (easily convertible to ATP), three molecules of NADH and two molecules of $FADH_2$ are produced by the TCA cycle. NADH and $FADH_2$ release electrons to the electron transport chain, thus creating a high electron gradient

between inner and outer mitochondrial matrix. This electrochemical gradient ultimately fuels ATP biosynthesis during oxidative phosphorylation within the mitochondrial respiratory chain [75].

Just like glycolysis, the TCA cycle is regulated by fine-tuned mechanisms. Pyruvate dehydrogenase complex (PDHC) and citrate synthase (CS) regulate pyruvate oxidation to acetyl-CoA and its fueling of the TCA cycle respectively. Both enzymes are controlled by various mechanism. PDHC is inhibited by pyruvate dehydrogenase kinases, which is activated by high levels of ATP, NADH or acetyl-CoA. Citrate synthase is also inhibited by a high cellular energetic state [81]. Pyruvate dehydrogenase kinase isoenzyme 1 (PDK1) expression is additionally induced under low oxygen conditions via HIF-1, displaying one of the protective mechanisms against hypoxic reactive oxygen species (ROS) engaged by cells [82].

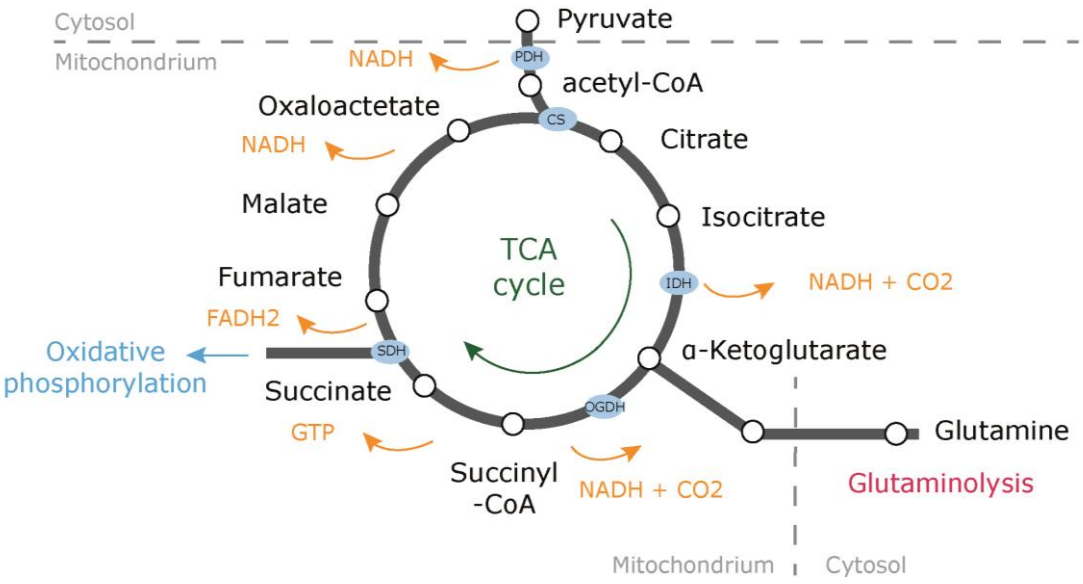

Figure 6. Schematic display of the TCA cycle, its metabolic intermediates and selected enzymes.
Pyruvate enters the TCA cycle and the mitochondria under oxygen tension by pyruvate dehydrogenase (PDH). Succinate dehydrogenase (SDH) is oxygen dependent and also a part of the mitochondrial respiratory chain. Under high energy demand the TCA cycle can be replenished by glutaminolysis. Enzymes are depicted in blue ovals. Energy generating reactions are marked by orange arrows. CS: citrate synthase, IDH: isocitrate dehydrogenase, ODGH: α-ketoglutarate dehydrogenase. Figure adapted from [75, 79, 80].

Fueling the TCA cycle is not only relevant in regard to generating energy; many intermediates provide building units for the biosynthesis of amino acids, nucleic acids, fatty acids or hormones. Therefore, there are more ways to fuel the TCA cycle than by glycolytic breakdown. Acetyl-CoA can further be generated by β-oxidation of fatty acids and during intense energetic demand (e.g. high muscular activity), lactate can be transformed into pyruvate and further to acetyl-CoA to promote the TCA cycle [83]. Another way of replenishing the TCA cycle is by glutaminolysis, which is explained further in a later sections of this chapter.

1.3.1.3. Oxidative phosphorylation

Under non-proliferative and normoxic conditions, cells normally utilize oxidative phosphorylation (OxPhos) as a final step for carbohydrate and fat breakdown to maximize the ATP yield. This efficient coupling of biochemical pathways generates in total 36 ATP per molecule of glucose (net yield), 2 through glycolysis and another 34 by oxidative phosphorylation [84, 85]. The process is driven by electrons derived from NADH and $FADH_2$, which are transferred onto the electron transport chain complex I and complex II respectively. From both complexes the electrons are passed onto Coenzyme Q (ubiquinone), transporting them to complex III. Cytochrome c further passes the electrons to complex IV, where they are transferred to O_2 forming H_20. The passing of electrons through each complex of the electron transport chain is coupled to a proton transfer from the mitochondrial matrix to the intermembrane space. This chemiosmotic coupling and the electric potential of protons create an electrochemical gradient across the inner membrane driving the protons back into to mitochondrial matrix. However, protons can only pass the membrane through a protein channel, e.g. the one of complex V (ATP synthase). Thus, the energy stored from the electrochemical gradient can be utilized to generate ATP, as each proton passing the channel drives ATP synthesis. A total of four protons are necessary to generate one molecule of ATP.

Cells and biological processes that require a great amount of ATP over a sustained period often engage OxPhos. For instance, T_{REGS} and alternatively activated M2 macrophages rely on oxidative metabolism to exert their functions [73, 84].

1.3.1.4. Pentose phosphate pathway

The pentose phosphate pathway (PPP) diverts at G6P from glycolysis and is the major producer of NADPH for anabolic reactions and provides precursor molecules for nucleotide biosynthesis. The production of high levels of NADPH, makes the PPP important for antioxidant production and ROS scavenging [86]. The PPP consists of two phases: (1) oxidative phase and (2) non-oxidative phase. By the end of the oxidative phase, two molecules of NADPH and one molecule of ribulose 5-phosphate are produced. During the non-oxidative phase of the PPP ribulose 5-phosphate can be converted into ribose 5-phosphate, which is important for nucleotide biosynthesis [75].

1.3.1.5. Amino acids in metabolism

Amino acids are important molecules in cellular physiology. Besides the role of some amino acids as protein residues (proteinogenic amino acids), amino acids can play an important role in energy metabolism. Glycolysis and the TCA cycle provide building blocks for biosynthesis (e.g. nucleotides, amino acids, fatty acids), which are taken out from the energetic pathways. To counteract cataplerosis of metabolic intermediates and ensure the continuation of energy metabolism, there are mechanisms necessary for replenishing e.g. the TCA cycle. This is particularly important under limited carbohydrate supply or when the energetic demand exceeds the levels of available carbohydrates.
One prominent example is glutamine break down by glutaminolysis, which is not only highly used by cancer cells but also by fast proliferating lymphocytes [73, 87-89]. Glutamine is broken down by glutaminase to form glutamate and further to form α-KG, via three possible ways: (1) by glutamate dehydrogenase, (2) glutamate pyruvate transaminase (also alanine transaminase) and (3) glutamate oxaloacetate transaminase. As a subsequent step, α-KG can enter and replenish the TCA cycle (anaplerosis) [90].

1.3.2. Conditions with high energetic demand – the Warburg effect

Cellular metabolism is highly dynamic and can be adapted within minutes or seconds according to the surrounding conditions and a cell's needs. Under challenging conditions with a high cellular demand for energy (e.g. inflammation, tumor microenvironment, high proliferation), cells are able to shift their metabolic profile towards aerobic glycolysis, also termed 'Warburg effect'. Glucose is rapidly converted to lactate, despite the presence of oxygen thereby bypassing the TCA cycle and mitochondrial respiration. This phenomenon was originally described as the "Warburg Hypothese" in 1930 by Otto Heinrich Warburg for cancer cells and has been regarded as a special tumor prerequisite for some time [91, 92]. However, since several years research has discovered the usage of aerobic glycolysis in immune cells, especially during proliferation and inflammatory responses [73, 93, 94].

Although the oxidation of glucose to lactate only renders 5.5% of ATP when compared to the full oxidative capacity of glucose (including TCA cycle and OxPhos), aerobic glycolysis is the choice of rapidly dividing or differentiating cells, for it generates ATP at a higher pace than mitochondrial respiration could [95]. Aerobic glycolysis further provides the cell with biosynthetic intermediates for the generation of nucleotides (e.g. G6P shuttled into the PPP) and amino acid synthesis (e.g. 3PG used for *de novo* serine biosynthesis) [96-99]. Another feature of the Warburg effect is the inhibition of enzymes of the citric acid cycle (e.g. aconitase by accumulation of ROS or

succinate dehydrogenase), leading to a truncated or fragmented TCA cycle [100, 101]. In order to generate sufficient energy and biosynthetic intermediates, conversion of glutamine to α-KG is increased during aerobic glycolysis [102].

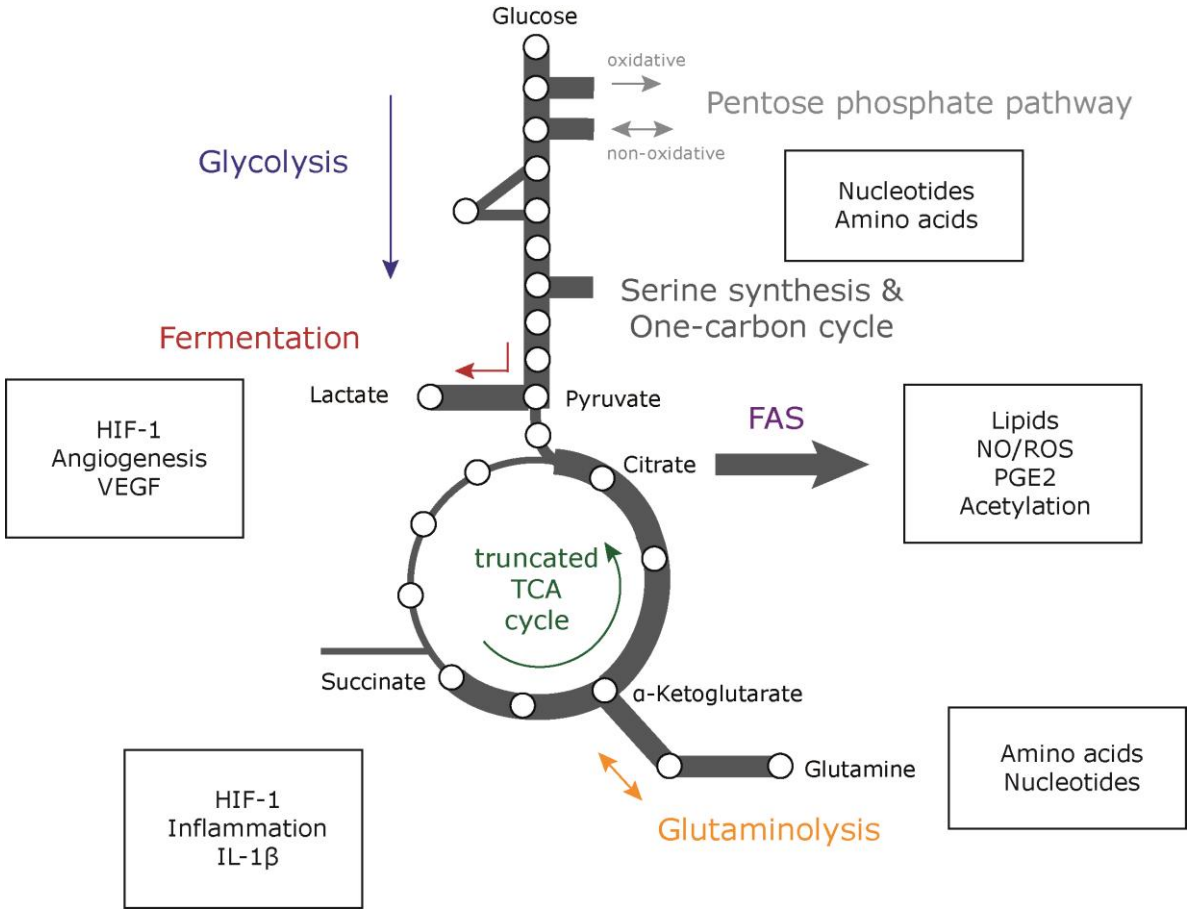

Figure 7. Metabolic pathways under high energy demand – aerobic glycolysis.

Under conditions with a high demand for rapid energy and biosynthetic precursor provision, cells make use of the "Warburg effect". Glucose is shuttled into lactate, besides oxygen presence. The TCA cycle is truncated twice and accumulation of citrate and succinate can be seen. Via glutaminolysis the TCA cycle is replenished. At the indicated branching points, biosynthetic building blocks are withdrawn from the system for production of amino acids, nucleotides, cytokines and other signaling molecules. FAS: fatty acid synthesis, NO: nitric oxide, PGE2: prostaglandin E2. Adapted from [73, 98].

Lactate accumulation is a prominent feature of aerobic glycolysis and acts as a signaling molecule inducing the expression of VEGF, TGF-β and HIF-1 [103-106]. Within the tumor microenvironment this leads to tumor growth and vessel development. As aerobic glycolysis also happens under inflammatory conditions, the induced transcription factors help resolving inflammation and restoring tissue integrity [107, 108].

Additionally, the TCA cycle intermediate succinate has gained attention over the last years, as also holds properties of a signaling molecule. Succinate accumulates, when the TCA cycle is truncated at SDH, e.g. under low oxygen levels or by mutations of the beta subunit (SDHB) frequently seen in cancer cells [109, 110]. Succinate has been reported to stabilize HIF-1α via inhibiting prolyl hydroxylase (PHD) and further induce IL-1β expression, thereby influencing inflammation [111]. Lactate and succinate have specific G-protein coupled receptor, GPR81 and GPR91 respectively, proposing a wide range of biological functions for these and certainly other metabolic intermediates [112, 113].

The current chapter shows that metabolism, provision of energy and its regulation plays a central role in all biological processes. In the following chapter, it will be highlighted how bone regeneration may be fueled by energetic circuits, specifically by focusing on energy expenditure of major cell types involved in bone healing.

1.4. Metabolic demands of cell types staging fracture healing

The healing of bone after a traumatic incident is organized by a highly synchronized cooperation of different cell types, as described earlier. Each major cell type engaging in fracture healing has specific metabolic requirements, which will be described individually.

1.4.1. Neutrophils

Neutrophils are the first-line defense mechanism and make up most of the fracture hematoma right after injury and up to 24 hours afterwards. Already in 1982 studies by Borregaard and Herlin identified glycolysis as major driver of neutrophil energy metabolism. This was determined for resting states and under phagocytosis [114]. Neutrophil extracellular trap (NET) formation, thus the fighting of pathogens, is highly dependent on glycolysis and glucose uptake. When cells were cultured in glucose free medium, no NETs were released [115]. Other studies have reported, that neutrophil activation is triggered by mitochondrial ATP production and a switch to glycolytic pathways occurs only after first activation of neutrophils [116].

1.4.2. Macrophages

Monocytes and macrophages are attracted to the fracture hematoma through chemokines released by neutrophils. Upon activation monocytes undergo metabolic reprogramming and switch from oxidative phosphorylation to a highly glycolytic phenotype. Monocytes further differentiate to either M1 – classically activated macrophages or M2 – alternatively macrophages, dependent on the stimuli they receive [117-120].

Like monocytes, classically activated macrophages (M1 macrophages) rely on glycolytic energy production. Lipopolysaccharide (LPS), a major pro-inflammatory stimulant, induces a strong glycolytic profile in M1 macrophages similar to the Warburg effect, by promoting HIF-1α stabilization, PFK-1 activation, nitric oxide production and a broken TCA cycle [121]. In fact, M1 macrophages demonstrate a broken or fragmented TCA cycle at two points of the pathway, (1): after isocitrate dehydrogenase, resulting in the accumulation of citrate and itaconate, (2): at SDH abrogating the conversion of succinate to fumarate and leading to a rise in succinate levels by anaplerosis through α-KG [111, 122, 123]. Citrate acts as a precursor for fatty acid synthesis and contributes to the production of ROS and NO, both potent inflammatory mediators [121]. Itaconate on the other hand, is important for anti-bacterial properties of M1 macrophages [124, 125].

Accumulation of succinate after LPS stimulation leads to stabilization of HIF-1α, promoting the glycolytic profile of M1 macrophages and inflammation by inducing *IL-1β* transcription [111]. Another way of increasing the glycolytic flux in M1 macrophages is the transcription of phosphofructokinase 2 (PFK-2) after LPS stimulation. PFK-2 regulates fructose-2,6-bisphosphate (F-2,6-BP), a glycolytic intermediate which allosterically activates PFK-1, thus increasing the turn-over of glycolysis [123, 126, 127].
M1 macrophages play an important role in the initial pro-inflammatory response of fracture healing. At that stage, the hematoma microenvironment becomes increasingly hypoxic; making the reliance on glycolysis, independent from oxygen levels a coherent choice. The glycolytic metabolism enables M1 macrophages to highly proliferate and induce pro-inflammatory signaling (e.g. IL-1β) coupled with HIF-1α stabilization, which in turn can induce angiogenesis. Additionally, lactate accumulates, further triggering vessel formation, that provides the fracture hematoma with oxygen and nutrients [53]. These pro-inflammatory feedback mechanisms gradually transform the hematoma into an anti-inflammatory milieu.

The promotion of oxygen supply within the fracture hematoma favors the appearance of M2 macrophages, which are associated with tissue regeneration and rely on oxidative phosphorylation and fatty acid oxidation (FAO) as their main source of energy [120, 122, 128]. Activation of both pathways is central for the anti-inflammatory properties of M2 macrophages. Low HIF-1α levels in M2 macrophages and their surroundings induce a reduced flux of glucose into lactate. Additionally, they express 6-phosphofructo-2-kinase/fructose-2,6-biphosphatase 1 (PFKFB1). In contrast to the PFK-2 isoform expressed in M1 macrophages, PFKFB1 catalyzes a fast breakdown of F-2,6-BP, thus decreasing glycolytic activity [123]. Glutamine metabolism is important for M2 functionality, especially the production of α-KG through glutaminolysis. A high α-KG/succinate ratio supports M2 phenotype by augmenting FAO, while high succinate levels produced by glutaminolysis favor M1 macrophages (see previous section). Presence of α-KG together with oxygen, is a requirement of proline hydroxylation in collagen production [129]. It has been shown, that M2 macrophages can undergo transformation and produce collagen, possibly by accumulation of high α-KG levels [130, 131]. This might be an important feature driving bone healing. Schlundt et al. have also shown, that increasing the number of M2 macrophages, enhanced endogenous bone formation [55]. Tissue regenerating M2 macrophages need high amounts of ATP for sustained periods. This is met by FAO, channeled through carnitine palmitoyltransferase 1 (CPT1), which is highly expressed in M2 macrophages [132].

1.4.3. T cells

T cells are involved in many major steps of bone healing and employ, just like macrophages, different metabolic pathways depending on their phenotype and function [133]. Naïve T cells switch from a metabolically quiescent state towards highly glycolytic phenotypes (aerobic glycolysis) when differentiating into effector T cells (T_{EFF}), while transformation of memory T cells (T_{MEM}) induces oxidation of glucose and fatty acids [94]. T_{EFF} comprise $CD8^+$ cytotoxic T cells and $CD4^+$ helper T cells, which again can be divided in Th1, Th2 and Th17 cells. As they are highly proliferative upon activation, they convert most of the enhanced glucose uptake into lactate, thus gaining high levels of ATP for increased biosynthesis within a short time frame. It has been postulated by the group of Erica Pearce, that GAPDH from T cells senses extracellular glucose availability to ensure that complete T cell activation is only possible when sufficient glucose substrate is present [99]. In the case of low glucose levels, GAPDH interferes with the translation of interferon gamma (IFNγ). Interestingly, though activated T_{EFF} cells are highly glycolytic, they also rely on glutaminolysis for proliferation and provision of TCA cycle intermediates, Additionally, OxPhos is still needed to maintain $NADH/NAD^+$ cycling for protein biosynthesis, whereas mitochondrial ROS production is supportive of T effector cell activation [99, 134].
T_{REGS} mark another important T cell subset. In contrast to the previously mentioned T_{EFF} cells, T_{REGS} use a mixed cellular metabolism including glucose, OxPhos and β-oxidation of fatty acids [133, 135]. While T_{EFF} cells use FAS and decrease FAO, T_{REGS} show a contrasting picture. In fact, inhibition of acetyl-CoA carboxylase 1, an enzyme of FAS, limited Th17 cell differentiation and promoted formation of T_{REGS} [135].

Two waves of T cell migration into the facture callus have been observed: the first within the initial hematoma during both, pro- and anti-inflammatory responses and after soft callus maturation, supporting the second angiogenic wave [136]. Glycolytic T_{EFF} cells are central during the inflammatory response of the fracture hematoma. The second wave of T cell infiltration is likely comprised of larger numbers of T_{REGS}, given the increasing oxygen levels of the metabolic surroundings. T_{REGS} are known to support tissue remodeling and promote angiogenesis. Recently, they have been reported to mediate bone remodeling, suggesting a positive role in later stages of fracture healing [137, 138].

1.4.4. B cells

A detailed picture on the contribution of B cells to fracture healing is still missing. Similar to what is seen for T cells, B cells migrate in a biphasic fashion into the fracture callus. Remarkably, research from Könnecke et al. reported that levels of B cells outnumbered those of T cells during

the second wave of migration into the fracture callus [136]. Activated B cells upregulate OxPhos and the TCA cycle for energy production, hence their numerous appearance is in accordance with the rising tissue oxygenation [139].

1.4.5. Mesenchymal stromal cells and derived bone cells

The natural surroundings of MSCs are characterized by hypoxic conditions ranging between 4-7% oxygen (O_2), thus glycolysis is their main energy provider [140, 141]. Osteogenic differentiation of MSCs during callus mineralization is accompanied by metabolic rewiring towards OxPhos, engagement of the TCA cycle and an increase of mitochondrial mass [142]. The importance of oxygen supply and oxidative metabolism becomes apparent, as high glucose culturing conditions and low oxygen levels inhibit osteogenesis [143, 144]. Moreover, acetylation of RUNX2 and Osterix, both central osteogenic transcription factors, increases their activity and the osteogenic differentiation potential [145, 146]. Acetylation is dependent on acetyl-CoA availability, thus directly connected to citrate production from the TCA cycle [147]. Revascularization and sufficient oxygen mark a prerequisite for differentiation of osteoblasts and progression towards a mineralized callus. Furthermore, collagen production is dependent on the presence of α-KG and oxygen, facilitating proline hydroxylation [129].

Hypoxic conditions on the other hand, favor chondrogenic differentiation of MSCs and chondrogenic culture is associated with a rapid decline of oxygen consumption, while glycolysis is upregulated and accounts for 89% of chondrogenic energy production [72, 148, 149]. Several studies have linked localization of glycolytic enzymes with areas of extracellular matrix production, suggesting a close relation between energy production through glycolysis and matrix assembly [150, 151]. Insulin growth factor-I (IGF-1) stimulates chondrogenesis as indicated by collagen X and proteoglycan expression, strengthening the notion of glucose dependence for matrix generation [152]. Studies comparing the energy state of resting and hypertrophic cartilage, observed a slightly increased usage of oxidative metabolism in hypertrophic chondrocytes [153, 154]. Indeed, early studies of cartilage mineralization in chicks revealed that during vessel ingrowth, hypertrophic chondrocytes in close proximity to the vessels exhibit higher levels of oxidative metabolism than the rest. This increased oxidative metabolism is connected to beginning of cartilage mineralization [153].
During fracture healing cartilage differentiation occurs in areas of low oxygen, subsequently vessels sprout into areas of hypertrophic cartilage, inducing mineralization and transition to the hard callus phase.

1.4.6. Osteoclasts

Osteoclast precursors, deriving from monocytic cells upregulate the expression of glucose transporter 1 (GLUT1) and glycolytic enzymes. HIF-1α and glucose are crucial elements to osteoclast differentiation and function, for their knock-down and deprivation inhibits the bone resorbing properties of osteoclasts [155, 156]. During later stages of differentiation uptake of glutamine and anaplerosis of the TCA cycle by glutaminolysis gain importance for osteoclast energy generation. Bone resorption is a high-energy consuming process and osteoclasts need to keep their level of ATP above a certain threshold to maintain functionality. Constant activation of AMPK, a sensor for low cellular ATP levels, markedly inhibited osteoclastogenesis [157]. Further studies have observed increased mitochondrial respiration and biogenesis, in line with osteoclast differentiation and fusion to multinucleated cells [158, 159]. However, when osteoclasts where forced to rely solely on OxPhos, collagen I degradation showed strong impairment. Together with the observation of glycolytic enzyme localization along the F-actin ring in osteoclasts, it stands reason that high levels of ATP needed for resorbing bone derive from glycolysis, while overall survival may be regulated by oxidative metabolism [158].

1.4.7. Fibroblasts

Fibroblasts make up the connective tissue throughout our body and are an important cell type in fracture healing. There is only a limited amount of studies investigating fibroblast metabolism. It is known so far that quiescent fibroblasts have high glycolytic needs, which are slightly upregulated under proliferative conditions [160]. Quiescent fibroblasts engage a full TCA cycle, while in proliferating fibroblasts the TCA cycle is truncated at citrate and glutaminolysis is used for cycle anaplerosis [160, 161]. Fibroblasts highly proliferate within the first phases of fracture healing, where high turnover of proteins and increased matrix secretion and rearrangement is needed.

1.4.8. Endothelial cells

Angiogenesis is central to fracture healing and occurs in a two-phased fashion as discussed in earlier sections. Endothelial cells are highly glycolytic, even at a quiescent state. Next to stimulation by growth factors (e.g. VEGF), metabolism can drive vessel sprouting, as recent studies highlighted [162, 163]. Main metabolic drivers are 6-phosphofructo-2-kinase/fructose-2,6-bisphosphatase-3 increasing glycolysis and CPT1a, the rate-limiting step for FAO. Rising lactate levels through the heightened glycolytic flux also serve as an angiogenic signal [163, 164].

During vessel sprouting, glycolytic enzymes are relocated in the endothelial lamellopodia and filopodia and inhibition of glycolysis induces proliferative and structural defects [162]. Although OxPhos plays a minor role in endothelial metabolism, impairment of mitochondrial respiration was found to diminish neoangiogenesis in wound healing [165]. Until today, most studies investigating endothelial metabolism have been conducted *in vitro* and more work needs to be done to fully understand its regulatory mechanism. From what is known, one may speculate that endothelial cells are fit to adapt to different micromilieu where they induce sprouting as seen in fracture healing during anti-inflammatory signaling in early fracture hematoma and during soft callus maturation towards hard callus.

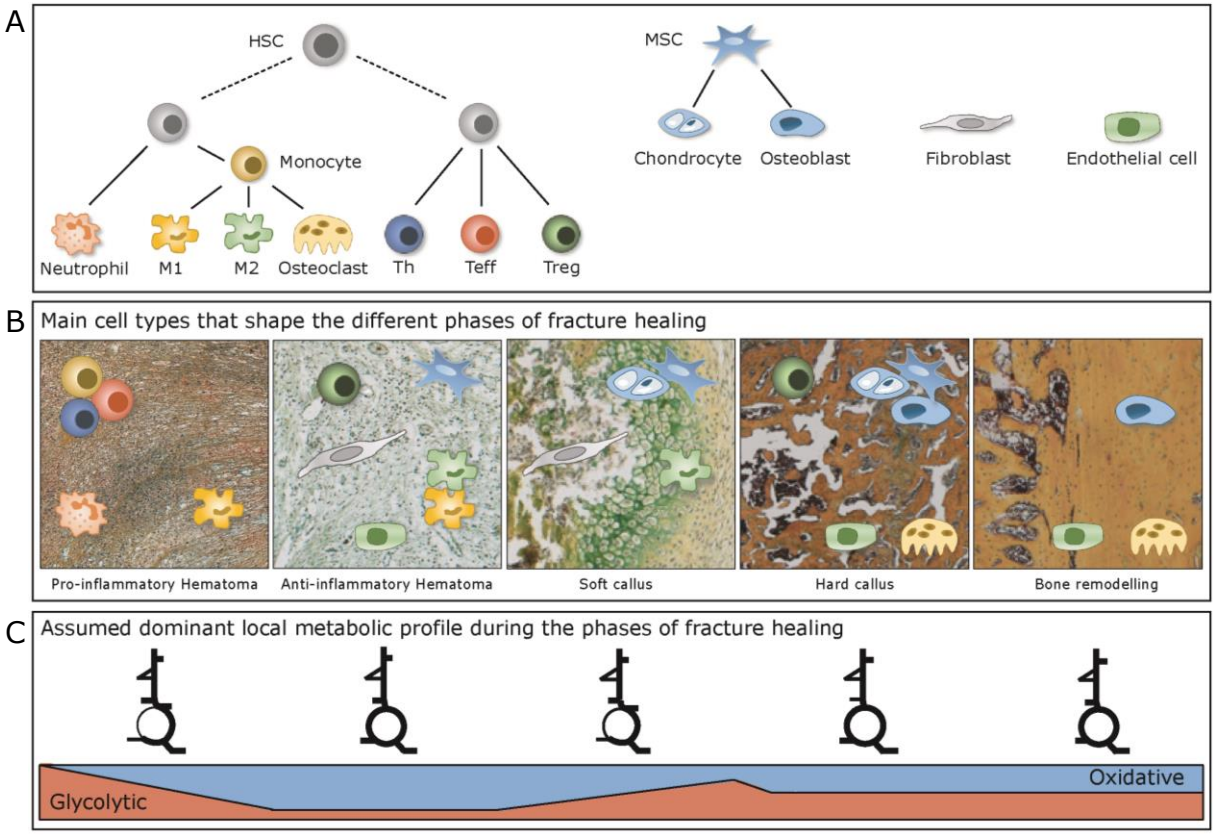

Figure 8. Summary of cells active during fracture healing and the theoretical metabolic profiles of the individual fracture healing phases.

(A) Major cell types present during the phases of fracture healing and their respective lineage connection. (B) The five consecutive phases of successful fracture healing and the main cell types active during each phase. (C) Theoretical metabolic profile of the local fracture mircomilieu during the respective phases of fracture healing. HSC: hematopoietic stem cell, MSC: mesenchymal stromal cell, M1: classically activated macrophage, M2: alternatively activated macrophage, Th: $CD4^+$ T helper cell, T_{EFF}: $CD8^+$ T effector cell, T_{REG}: regulatory T cell. Figure adapted after Loeffler et al. [53].

1.5. Technology-driven approaches to investigate tissue regeneration

The development of cutting-edge technologies, allows researchers to push the boundaries of so far known concepts in many fields. Especially “Omics” technologies have revolutionized biological and medical research due to their unbiased, non-targeted character and the opportunity to measure the molecular composition of a cell, tissue or organism in a holistic and high-throughput approach [166]. Omics technologies include: transcriptomics, genomics, epigenomics, proteomics and metabolomics, therefore viewing physiological processes from a complex systems perspective [167]. Single- or multi-omics are innovative approaches for clinical biomarker discovery, drug screenings and a more comprehensive understanding of normal physiological processes, as well as diseases and their aetiology [168, 169]. Integration of high-throughput technologies with molecular biology, biochemical pathways and bioinformatics define the novel field of systems biology [170].

Such integrated approaches are also highly interesting in regard to comprehend the remarkably complex mechanism of tissue regeneration and in particular bone fracture repair [171]. Over the last ten years, a continuous increase in publications, which combine “bone regeneration”, “bone”, “biomedical materials” and “computational biology” indicate the strong rise of this field [172]. Profiling of bone biopsies in healthy, osteoporotic and osteoarthritic conditions by proteomics, transcriptomics and epigenomics enabled the generation of a molecular disease map for postmenopausal osteoporotic conditions in women [173, 174]. Studies of the bone metabolic profile have so far concentrated on information derived from transcriptome studies and global metabolic analysis by metabolomics measurements in blood serum from osteoporotic and control rats [175, 176].

Metabolomics from bone tissue samples is rather unexplored [172], but represents a highly interesting topic, as bone metabolism is dynamic and bone itself employs functions as an endocrine organ, as discussed previously. Although extensively studied in regard to cellular processes and main physiological responses, bone regeneration under physiological and pathological conditions still lacks comprehensive understanding in regard to altered molecular processes and energy demands [172].
This thesis aims to address this gap by an integrated metabolic approach, which combines untargeted metabolomics and proteomics. The advantages of the two technologies will be discussed in more detail as follows.

1.5.1. Metabolomics

Metabolites are a diverse group of small molecules (e.g. sugars, amino acids, lipids), that are highly dynamic and can adapt to physiological changes within minutes or even seconds [177]. The metabolome is regarded to be the closest to the status quo of a biological system, as it marks the final downstream product of gene transcription and protein expression [166, 178]. Newest research has further highlighted that metabolites can loop back to influence chromatin organization and gene transcription, stressing the significance of the metabolic profile on physiological processes [179-182].

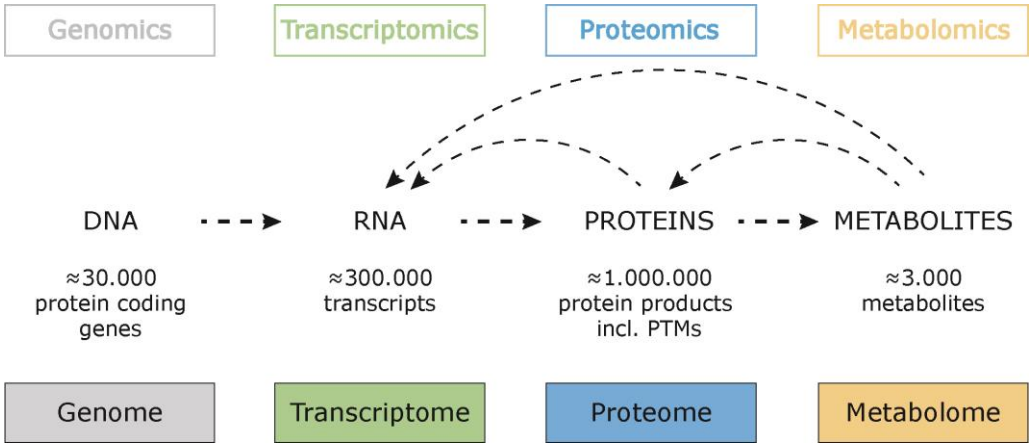

Figure 9. Most common omics technologies, their respective targets and network cross talk.
Information flows from DNA to RNA, proteins and metabolites. Metabolites can feedback to regulate protein and RNA levels, while proteins can influence RNA translation via feedback loops. Adapted and modified from Farid et al. and Horgan et al. [166, 183].

Analysis of the metabolome represents an analytical challenge, due to the great variety of its targets, being small molecules with chemical polarity properties ranging from highly water-soluble organic molecules to non-soluble lipids [184, 185]. Measurement of the whole metabolome therefore cannot be achieved by one technology only. For a broad analysis the metabolome is divided into subgroups, e.g. by polarity or functional groups. Each subgroup usually requires application of different protocols and technologies [186]. The most common methods applied are nuclear magnetic resonance (NMR) and mass spectrometry (MS), which can be further divided in liquid-chromatography coupled mass spectrometry (LC-MS) and gas-chromatography coupled mass spectrometry (GC-MS) applications. While NMR provides high accuracy of metabolite quantification and an advantage due to a less laborious sample preparation, it comes with drawbacks in regard to compound sensitivity [187]. The main advantages of mass-spectrometry based techniques are high sensitivity and a broad coverage of compound spectra. The preparation of samples however, requires chemical modification and stabilization prior to the analytical application.

1.5.2. Proteomics

The proteome comprises the set of all expressed proteins in a biological system at a given time [188]. Proteomics aims to understand distinct protein patterns, their isoform distribution and function within the complex biological system. Mass spectrometry has evolved as the primary tool for protein identification [189, 190]. Specifically, LC-MS approaches are the most widespread used application for high-throughput profiling of the proteome [191]. Investigation of the proteome can be distinguished into three main strategies as reviewed by Domon and Aebersold in 2010 – shotgun, directed and targeted proteomics [192]. Shotgun proteomics is the most widely used method and was applied during the work of this thesis. A targeted approach is applied when a specific hypothesis is tested, while shotgun or untargeted proteomics are used as a screening method for unknown protein composition in specimen [193].

The purpose of shotgun or discovery proteomics is to detect the maximal peptide component number in a given sample. It enables protein identification, their post translational modifications and – if combined with stable isotope-based labeling – absolute protein quantification [192]. Its main limitation lies in the bias of detecting the more abundant proteins, especially in complex samples, low-abundant proteins like cytokines or transcription factors will seldom be detected. Nevertheless, for discovery driven and hypothesis generating study designs, shotgun proteomics remains the method of choice [192].

1.6. Challenges in regeneration – How energy has a hand in it

Cells under challenging conditions are affected by the metabolic environment and employ metabolic crosstalk and cooperation. This concept has been long known for tumors and increasing evidence points towards similar mechanism being utilized during tissue regeneration, as outlined in the previous chapters. However, evidence for this metabolic crosstalk in tissue regeneration is missing so far. Cellular players participating in bone regeneration are likely to be influenced by accessible nutrient levels and metabolic signaling at each stage of the complex fracture healing process in regard to functionality and phenotype. It is hypothesized that the metabolic microenvironment governs tissue regeneration as another level of cellular communication and cooperation. However, under local energetic imbalances cellular composition, activity and crosstalk might be substantially altered by differentially induced metabolic reprogramming. Those imbalances may originate in underlying morbidities or conditions locally or systemically modifying nutrient or metabolite levels.

This project aims at assessing the metabolic microenvironment in fracture healing under (1) successful healing conditions and (2) impaired healing conditions. The rational is to determine, whether a modified activity of metabolism forms the basis of fracture healing failure and dissect possible cellular players involved.

2. Hypothesis

Immune and stromal cells participating in bone regenerative processes are sensitive to their surroundings and influenced, not only by growth factor signaling but also by metabolic signals present in the local fracture micromilieu. Fracture healing and repair is a complex mechanism of fine-tuned consecutive phases; disturbances may result in impaired healing or failure of healing, by e.g. excessive inflammation and fracture non-union. It is hypothesized that altered metabolic activation within the fracture callus, is connected to inadequate fracture repair leading to different metabolic reprogramming of cells and transformed cell-to-cell signaling. Fractures showing impaired healing may therefore show different levels of metabolic intermediates and proteins. Specific modification of metabolites or metabolic proteins may influence the fracture microenvironment and change fracture healing outcome. To test this hypothesis, different comprehensive strategies will be employed:

1) Metabolic and proteomic profiling of fracture tissue from an *in vivo* rat femoral 2 mm osteotomy healing model comparing successful healing and biologically impaired healing. Profiling will be performed by applying different mass-spectrometry techniques.

2) *Ex vivo* and *in vitro* characterization of the inflammatory response and immune cell composition of fractures showing successful healing versus impaired healing fractures, by histologic assessment, gene expression analysis and multiplex cytokine analysis. Detailed examination of the individual processes cooperating during healing progression is achieved in conjunction with metabolic and proteomic data.

3) Targeted modulation of the metabolic environment in immune and stromal cells *in vitro* (proof of concept). Functional and phenotypical assays will be used to investigate the impact of the metabolic modulation on selected cell types.

3. Material & Methods

A detailed list of the used materials and the respective manufacturers can be found in the supplement I.b.

3.1. *In vivo* experiments

3.1.1. Non-critical defect femoral osteotomy model

For the *in vivo* animal studies female three and twelve months old ex-breeder Sprague Dawley rats from Charles River WIGA Deutschland GmbH were used. This strategy was applied following previous studies from Preininger [194] and Strube [195], where it was shown that aged female rats, after a minimum of three litters, typically displayed a non-union over the time course of six weeks, when receiving a 2 mm osteotomy gap in the left femoral midshaft. This serves as a model for biologically impaired fracture healing and stands in contrast to the three months old rats, showing a complete fracture union after the same amount of time. The aged cohort (twelve months old animals that have had a litter of at least three) was kept at the "Tierexperimentelle Einrichtung der Charité Berlin, des Campus Virchow Klinikum" for aging, where they lived an artificial light-induced day-night rhythm of twelve hours at constant temperature (21°C) and humidity (60-70%). Diet contained dry pellets and water, which was consumed according to own needs. Animal experiments were conducted in compliance with the ARRIVE guidelines and according to the policies and principles of the Animal Welfare Act, the National Institutes of Health Guide for the Care and Use of Laboratory Animals, and the National Animal Welfare Guidelines. All animal experiments were approved by the local legal representative (Institutional Animal Care and Use Committees, LaGeSo, G0120/14, G0172/15).

3.1.2. External fixation

The external fixation system used for this work comprised a steel fixation bar and 4 titanium clampy, which are fixated by head screws and locknuts at each side. The external fixateur is placed unilaterally on the left femoral bone with 4 titanium kirschner wires, each 1.23 mm in diameter (**Figure 10A**). The distance between the outer and inner wire on each side is 4 mm, while there is a 10 mm distance between the inner wires, where a standardized 2 mm fracture gap was introduced. This was achieved by the help of a sawing template, placed on the wires and the fixateur (**Figure 10B**). The fixateur bar was always placed in the same distance from the left leg by using a plastic block of 7.5 mm height. A sketch of the assembled and fixated system stabilizing the osteotomized femur is found in **Figure 10C.**

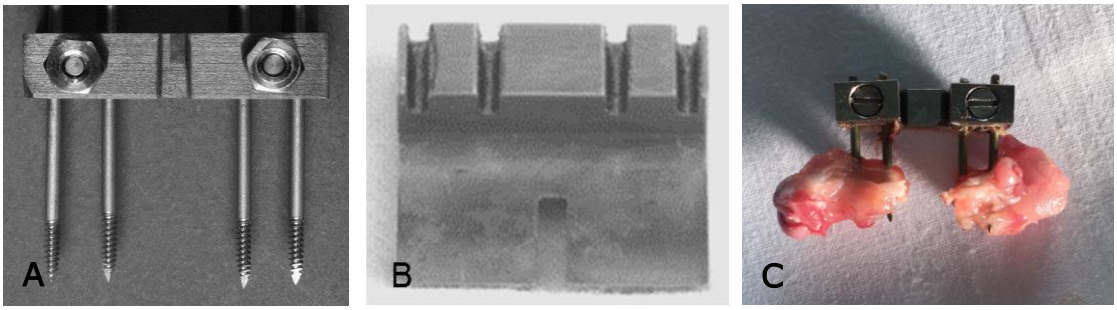

Figure 10. External fixation system for osteotomized rat femurs.

Custom made external rat femoral fixator after Strube et al. [195]was used for this work. (A) Assembled steel fixator with bar, screws, nuts and titanitum Kirschner wires. (B) Sawing template for 2 mm osteotomy (C) Image of external fixator holding the dissected osteotomized femoral bone with remaining muscle tissue. Pictures adapted from Strube et al. and Preininger et al. [194, 195].

3.1.3. Surgical procedure

All animals included in the study, were assessed for their overall health and body weight. In preparation for the surgical procedure animals received 20 mg Tramadol per kilogram body weight, as an anti-pain agent. Animals were anesthetized with 0.3 mg/kg Medetomidin Domitor and 60 mg/kg Ketamin by intraperitoneal injection prior to surgical procedure. To prevent infection, 45 mg/kg Clindamycin was administered by subcutaneous injection and eyes were prevented from drying out by application of Bepanthen® eye balm. A longitudinal skin incision was made over the left femur. The bone was exposed by blunt fascia dissections. Unilateral external fixators were used to stabilize the fracture, made of stainless steel and titanium. For an exact placement of the four wire holes (diameter: 1 mm), a drilling template was used for every procedure. The first wire hole was placed by optical assessment, vertical to the femur orientation, at the distal side of the femur midshaft (diaphysis). It was drilled monocortically and the titanium wire was carefully fitted. The drilling stencil for the remaining wire holes was placed onto the first titanium wire. All other holes were drilled bicortically and the wires placed respectively. After incision of the titanium wires, the drilling template was exchanged for an external fixator bar and slightly fastened by screws with a 7.5 mm distance from the femoral bone. Using a sawing stencil to accomplish maximal reproducibility and standardization, the femur was double osteotomized with a width of 2 mm within the inner titanium wires. Saline solution was used throughout the procedure preventing unwanted tissue damage by heat induction. Muscle fascia and skin were closed using absorbable and non-absorbable sutures, respectively. Animals received 1.5 mg/kg Antisedan, an anesthetic antagonist, and were placed under red light until awakening. Animals were kept in cages of two after the surgical procedure to minimize wound nibbling and scratching and thereby disturbing the progression of healing. They received Tramadol as an anti-pain agent

though the drinking water for three days post-surgery. Throughout the whole period, animals were monitored for health, behavioral contentment and wound healing. Fracture healing was assessed after 3, 7 and 14 days by euthanization and femur dissection.

3.1.4. Sacrifice and specimen harvest

Animals were sacrificed at day 3, 7 and 14 post-surgery. They were administered 0.3 mg/kg Medetomidin and 60 mg/kg Ketamin for anaesthesia by intraperitoneal injection. For serum isolation, 5-10 ml blood was drawn by intracardial punctuation and later centrifuged at 2.000 x g for 10 minutes to separate blood cells and clotting components from the serum. Aliquots were stored at -80°C until further usage. Animal sacrifice was performed by intracardiac injection of 7 ml potassium chloride (KCl) solution (1 M), inducing cardiac arrest. The operated left femur was dissected and dislodged from the joints, followed by gentle removal of the surrounding and remaining muscle tissue. Depending on the down-stream analysis, different protocols were carried out:

1) For Ribonucleic acid (RNA), metabolite and protein analysis, the hematoma was extracted from the osteotomy gap, together with 1 mm of the neighboring proximal and distal tissue (region of interest), placed in cryo vials and snap frozen in liquid nitrogen and stored in nitrogen tanks until further processing (see chapter 3.2.).

2) For *ex vivo* cytokine explant cultures, the hematoma was carefully extracted from the osteotomy gap, together with 1 mm of the neighboring tissue from distal and proximal. Each specimen was weighted and covered with a respective amount of prewarmed media before culturing (see chapter 3.3.).

3) For histological analysis, femurs were placed in 4% paraformaldehyde (PFA)/phosphate buffered saline (PBS) for tissue fixation. External fixateurs were not removed until embedding commenced. Condyles on the distal and proximal sides were incised to ensure full tissue penetration of the fixating solution (see chapter 3.4.).

3.2. *In vitro* analysis animal fracture model

3.2.1. Fracture hematoma tissue extraction for RNA isolation

For gene expression analysis, femurs were excised from animals euthanized 3, 7 and 14 days after osteotomy. Surrounding muscle tissue was dissected from the bone and the area containing the fracture callus plus 1 mm proximal and distal to the osteotomy gap was detached from the rest and immediately transferred into liquid nitrogen. Subsequently, tissue samples were grinded with a plastic pestle and steel motar, while kept frozen using liquid nitrogen and dry ice. The finely ground tissue was transferred to eppis, containing 3 big and 20 small ceramic beads in 1 ml TRIzol Reagent (LifeTechnologies). The tissue is further disrupted by using a Precellys® Homogenizer, twice for 30 seconds, with a cooling step in-between. 0.2 ml chloroform was added to each sample containing 1 ml TRIzol Reagent, shaken vigorously and incubated at room temperature for two to three minutes. Samples were centrifuged at 12.000 x g for 15 minutes at four degrees for phase separation. The upper aqueous phase was carefully removed and all further RNA isolation steps were carried out using the PureLink RNA Mini Kit from Thermo Fisher Scientific according to the manufacturer's protocol. In brief, 0.35 ml of lysis buffer and 0.35 ml of 100% ethanol was added to each aqueous phase and loaded on the spin column. Columns were centrifuged at 12.000 x g for 15 seconds at room temperature. Columns were washed with 700 µl Wash Buffer I and 15 seconds centrifugation at 12.000 x g, before DNase digest was performed. 80 µl of PureLink DNase mixture was added onto the membrane and incubated for 15 minutes at room temperature. In the subsequent washing steps first 350 µl of Wash Buffer I are added to the column followed by two times 500 µl of Wash Buffer II. RNA was eluted with 50 µl of RNase free water. RNA concentration was determined using a Nano-Drop spectrophotometer. Samples with inappropriate λ=260/280 ratios were excluded from further analysis.

3.2.2. cDNA synthesis and gene expression analysis

Complementary DNA (cDNA) synthesis was performed using with iScript™ cDNA Synthesis Kit from Bio-Rad Laboratories. For each cDNA reaction an input of 500 ng RNA was used in a 20 µl reaction of the following composition:

Table 1. cDNA 1x reaction mix.

Chemical	Amount
5x iScript reaction mix	4 µl
iScript reverse transcriptase	1 µl
RNA	500 ng
Nuclease free H_2O	x µl (up to 20 µl)

cDNA synthesis was done applying a standardized run protocol on a thermal cycler (**Table 2**). The resulting cDNA had a concentration of 25 ng/µl.

Table 2. cDNA synthesis run protocol.

Time	Temperature
5 min	25°C
30 min	42°C
5 min	85°C
∞	4°C

Gene expression was determined via quantitative real time polymerase chain reaction (qRT-PCR) (LightCycler® 480, Roche), with the DNA-intercalating agent SYBR®GREEN. Every time a specific PCR product was synthesized during the amplification run, a fluorescent light signal was emitted when binding to the dsDNA. Transcript analysis was performed in 384-well plates using a standard set up with 10 µl, comprising of 6 µl reaction mix and 4 µl cDNA- water solution (**Table 3**). cDNA input was 12.5 ng per each reaction and run in duplicates. Prime sequences (supplement **Table 24**) were generated using NCBI website and tested for specificity and primer dimers. Expression of each gene was calculated according to the ddCT method with adjustment for primer efficiency and normalization to TATA-Box binding protein (Tbp) expression by utilizing the REST software [196]. The housekeeping gene Tbp was tested against others and was found to be the most stable gene in all investigated samples.

Table 3. Composition of 1x reaction mix and 1x cDNA-H_2O solution for 10 µl qPCR reaction.

Reaction mix		cDNA-water solution	
5 µl	SYBR®GREEN	0.5 µl	cDNA (25 ng/µl)
0.5 µl	Primer forward	3.5 µl	H_2O
0.5 µl	Primer reverse		

3.2.3. Metabolomics of fracture hematoma tissue

To evaluate the metabolic profile of the different healing phenotypes, metabolomic analysis using Gas-chromatography coupled to mass spectrometry (GC-MS) was conducted. Hematoma tissue was ground as described under section 3.2.1. A certain amount of the finely ground tissue was transferred into new vials and the tissue weight was determined. For each 50 mg of tissue 1 ml of methanol-chloroform-water (MCW, 5:2:1 v/v/v) was added. The MCW solution was supplemented with cinnamic acid at a final concentration of 2 µg/ml, used as an internal standard for metabolite quantification. MCW-sample mixture was further homogenized by sonification. Samples were shaken for 30 minutes at 10°C, 200 rpm, to extract the metabolites from the tissue. The remaining water volume (half of the calculated MWC) was added and further shaken for 5 minutes. Phase separation samples were centrifuged for 10 minutes at 10.000 x g at 4°C. The mixture had separated into an upper aqueous phase containing the polar metabolites and a lower apolar phase containing lipids. 500 µl from the polar phase was transferred twice into new eppis and vacuum-dried in a Speed-Vac. Once all liquids had been removed the samples were stored at -20°C until further processing.

3.2.3.1. Derivatisation

Derivatisation protocol was conducted before GC-MS analysis, improving their volatility, stability and allowing a more global metabolic profiling on the GC-MS. A combined approach of methoxination and siylation was used as derivatisation standard for all samples analyzed [197-201]. Samples were retrieved from the freezer and any moisture that may have formed was dried in a Speed-Vac. Methoxyamine hydrochloride (MeOX) was solved in a pyridine solution at a concentration of 40 mg MeOX solved per 1 ml of pyridine. To the dried samples MeOX-pyridine was added and incubated for 1 hour at 30°C stabilizing ketoacids. As a second derivatisation step silylation with *N*-Methyl-*N*-(trimethylsilyl (TMS)) trifluoroacetamide (MSTFA) was applied, covering polar groups with a non-polar TMS-group. In order to calculate the retention indices for each metabolite during data analysis, nine alkanes were added to the MSTFA, serving as retention index standards at a final concentration of 2% (v/v). Samples were incubated for 1.5 hours with MSTFA at 37°C. Before samples were put on the GC-MS, they were centrifuged at maximum speed for 5 minutes. The liquid was split in technical replicates, transferred into glass vials and sealed by crimping a lid onto it, containing a rubber patch for syringe injection.

For metabolite quantification a mixture of 63 compounds, stock concentration of 1 mg/ml in 20% methanol (MeOH), is used (**Table 30**). A series of 8 dilutions (1:1, 1:2, 1:5, 1:10, 1:20, 1:50, 1:100,

and 1:200) was prepared, vaccum-dried and stored at -80°C. Upon sample measurement, one set of quantification standards was derivatized along with the samples and subsequently measured.

3.2.3.2. GC-MS measurement

All tissue samples were measured in a 1:5 split with 1 µl injection volume on a gas chromatography coupled to time of flight mass spectrometer (Pegasus III- time-of-flight (TOF)-MS-System., St. Joseph,MI, USA) from LECO®. Quality of injection and alkane peaks were regularly monitored and temperature regulated. The following temperature program was applied during sample injection: 30 seconds of 80°C, followed by a gradient with 12°C/minute up to 120°C. This is followed by a second gradient with 7°C/minute up to 300°C and a final hold for 2 minutes. Temperature program used once the sample was injected as follows: 2 minutes heating to 67.5°C, temperature gradient up to 120°C with 5°C steps per minute. Second gradient with 7°C rise per minute up to 200°C, followed by 12°C per minutes up to 320°C. The last temperature was held for 6 minutes. In case of miss-injections, the sample was re-measured with a new technical replicate. Sample order was randomized, artefacts due to a longer standing time in experimental groups was thus avoided. Mass spectra were recorded in a mass range of 60 to 600 mass units with 10 spectra/s at a detector voltage of 1650 V.

3.2.3.3. GC-MS data analysis

Raw data and peaklists from the GC-MS were extracted and base-line corrected using the suppliers software ChromaTOF®. For further data analysis, normalization and quantification Maui-VIA, an in-house GC-MS data analysis software by Kuich et al.[202], was used. It provided a metabolite identification and annotation by targeted library search for metabolite spectra and retention time index via visual inspection. Initiation of a new project included importing baseline corrected raw files, peaklists and a metabolite database. Retention indices for each metabolite and sample were calculated using alkane-specific masses, which were added during derivatisation [203]. To annotate measured metabolites a reverse search was performed, using the imported metabolite database and searching for similar spectra in the measurements. Afterwards identified and annotated peaks were checked manually and confirmed or altered by visual comparison and a similarity score. Annotated metabolites were exported and quantified by the software. Relative metabolite quantification values were used for further analysis in order to compare a greater variety of metabolites within all probes.

3.2.4. Proteomics of fracture hematoma tissue

For a deeper understanding of the molecular profile of fracture healing at different time points and phenotypes proteomic characterization by high performance liquid chromatography (HPLC) mass spectrometry was conducted. Ground, frozen tissue was topped up with urea buffer and sonificated in a Bioruptor®. Urea buffer was used to induce protein denaturation. The homogenate was centrifuged at maximum speed for 10 minutes, 4°C and the supernatant transferred to a new tube. Total protein content per sample was determined bicinchoninic acid assay (BCA) after Paul K. Smith using a colorimetric read-out at λ=562 nm absorbance [204, 205]. 100 µg protein per sample was digested in urea buffer and dithiothreitol (DTT), reducing disulfide bonds in cysteine residues. 11 mM idoacetamide (IAA) was used to modify the free sulfhydryl (SH) groups, preventing an anew disulfide bond formation. A double digest with Lysine-C and trypsin was conducted to cleave the carboxyl sites of arginine and lysine, in order to have a broad coverage of peptides in the LC-MS. Digestion was stopped by lowering the pH using trifluoroacetic acid (TFA). Samples were desalted and stored using StageTips (Stop-and-go-extraction tips) [206].

3.2.4.1. Stage Tips

18 µg of peptides were loaded onto the StageTips according to the published protocol. Samples were washed and desalted with an acetid acid-water solution. If needed, peptides were stored in this format at 4°C. Elution of peptides into a new vial was done with an acetonitrile-water-acetic acid mixture. The eluted peptides were dried in the SpeedVac and reconstituted in 15 µl Buffer A before they were placed on the LC-MS for analysis.

3.2.4.2. LC-MS measurement

Peptides eluted were separated by reverse-phase chromatography on an in- house made 25 cm columns C18-Reprosil-Saphir (Dr. Maisch, inner diameter: 75 µm, particle diameter: 1.8 µm) using nanoflow HPLC system (Agilent 1200), coupled directly via nano-electrospray ion source (Proxeon) to linear ion trap quadrupole (LTQ) Orbitrap Velos (Thermo Fisher Scientific). Peptides were loaded on the column with a flow rate 200 nl/min. Elution was performed with a 220 min gradient of buffer B (2 - 50%) at a flow rate of 250 nl/min. Column was washed with 90% buffer B for 10 min and re-equilibrated with buffer A between the runs. Mass spectra were acquired in a positive mode applying a data-dependent analysis switch between survey MS scan (m/z 300-1700, resolution R=60’000) and MS/MS spectra acquisition. The 20 most intense ions (Top20) of each survey MS scan were selected for fragmentation and MS/MS spectra acquisition. Mono-

charged ions, ”potential” contaminants, were excluded from analysis. Samples were measured in two technical and at least two biological replicates.

3.2.4.3. Raw data processing and data clean-up

Raw files from the LTQ Exactive was processed using the MaxQuant computational platform developed by Jürgen Cox and Mathias Mann [207] and afterwards controlled and analyzed for quality after Bielow et al. [208] Via the peptide search engine andromeda, integrated into MaxQuant software, species specific databases were loaded. As we performed an untargeted approach, label-free quantifications (LFQ) settings and unique peptides were selected. Other parameters were: Proteases - Trypsin (cleavage behind lysine (K) and arginine (R) with restriction after proline (P), ion masses search with a maximum of mass deviation of 7 ppm, variable modifications of methionine oxidation and N-terminal acetylation as well as unique peptide quantification to distinguish between protein isoforms was activated.

To perform data clean-up removing contamiants, normalization and visualization from the MaxQuant out-put, Perseus software was used, developed by the same group [209]. The general workflow is depicted in **Figure 11**.

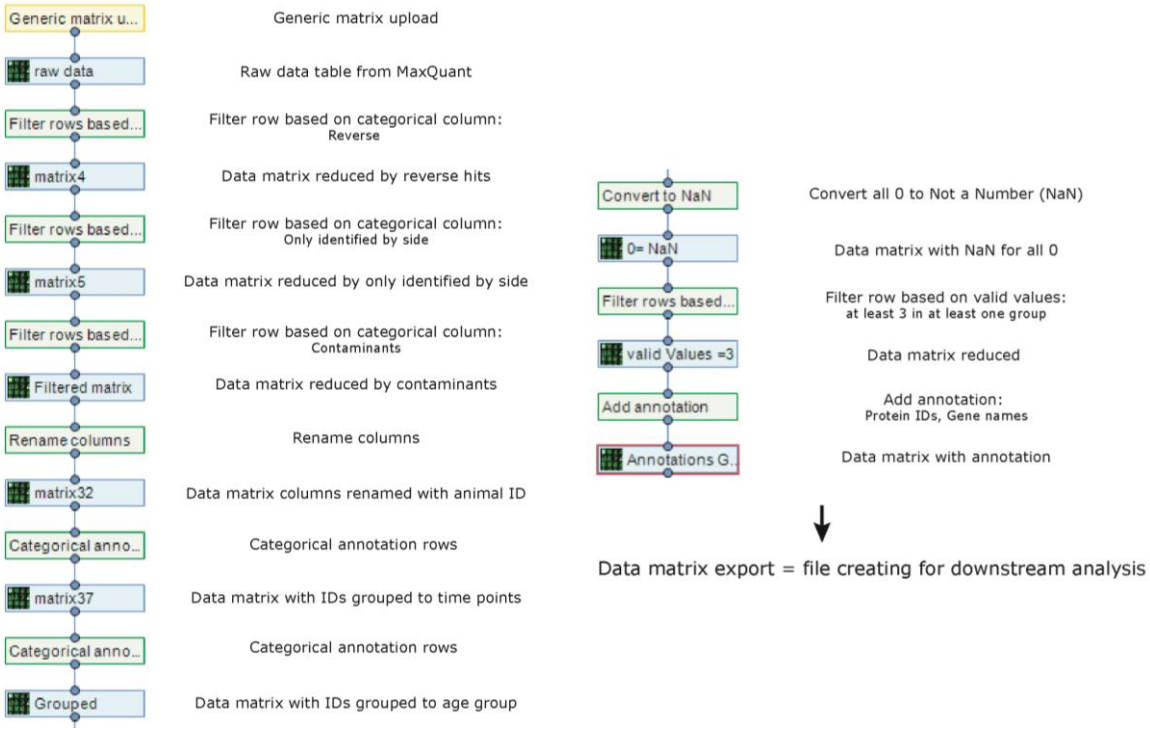

Figure 11. Workflow of data clean-up after MaxQuant raw file upload using the Perseus software tool.

3.3. *Ex vivo* hematoma explant culture model

To evaluate the inflammatory profile of the hematoma micromillieu, an *ex vivo* hematoma explant culture was performed. Upon femur dissection, the hematoma and 1 mm of distal and proximal femur tissue was removed from the rest of the bone. The specimen was weight, put in tissue culture well and 2 µl of prewarmed RMPI Medium, supplemented with 10% fetal calf serum (FCS) and 1% penicillin/strepavidin was added for each mg of the explant, this ensured the same cytokine concentration between smaller and bigger specimen. The hematoma explants were cultured for 24 hours at 37°C. After 24 hours culture supernatant was harvested and centrifuged for 15 minutes at 1.000 x g at 4°C. The liquid, without any fragments was transferred into an Eppendorf tube and stored at - 80°C until multiplex analysis.

3.3.1. Multiplex cytokine analysis – Bio-Plex®

Using a multiplex approach enables one to test several target cytokines within one sample. The Bio-Plex® Pro™ Rat cytokine 23-plex Assay (#12005641) from Bio-Rad, was applied in this setting, an immunoassay based on magnetic beads coupled to capture antibodies. The assay was performed according to manufacturer's instructions. In brief, a standard series was produced and 1x coupled beads were prepared. 50 µl of the 1x coupled beads were added to each well of the assay plate and washed twice using the magnetic washing station. Therefore, the plate was securely clipped onto the magnet, ensuring the remaining of the antibody-coupled beads within the wells. Next, 50 µl of standards and undiluted explant culture medium was added to the wells, sealed and incubated for 1 hour at 850 rpm, room temperature. 10 minutes before application, 1x detection antibodies were prepared from the 20x stock solution. The microplate was washed three times using the magnetic washing station and 25 µl of 1x biotinylated detection antibodies was added to each well. Detection antibodies were incubated to 30 minutes. The plate was washed three times, 1x streptavidin-phycoerythrin (PE) coupled was added to each well and incubated for 10 minutes. Streptavidin recognizes biotinylated structures of the detection antibodies. The coupled fluorescent PE-signal was detected using a luminometer, set at the proposed instrument settings. The bead-coupled target cytokines were detected by different bead regions, supplied by the manufacturer.

3.4. Histological tissue analyses resolving tissue distribution

3.4.1. Specimen preparation

For histological analysis, femurs were fixed in a 4% PBS/PFA solution for 24 h at 4°C. For tissue cryo-protection femurs are then transferred into ascending sucrose solutions for 24 h at 4°C each (sucrose solutions: 10%, 20% and 30%). Before progressing to the embedding procedure, all parts from the external fixator (screws, fixator bar and titanium wires) needed to be carefully removed without disrupting any of the hematoma tissue. All femurs were embedded in the same orientation (**Figure 12**) into a rectangle stain mold (in-house-made), where beforehand a layer of SCEM-Medium was placed on the bottom. Next, the specimens were fully covered by carefully filling up the mold with SCEM-Medium. Generation of air bubbles and changes in orientation needed to be avoided in order to obtain high quality sample cryo blocks. As a last step the specimen were frozen by immersing the molds in a beaker containing cold *n*-Hexan, surrounded by dry-ice to ensure constant low temperatures thus a rapid freezing process. The SCEM blocks, containing the femurs, were detached from the stain mold, labeled and stored at -80°C until further handling.

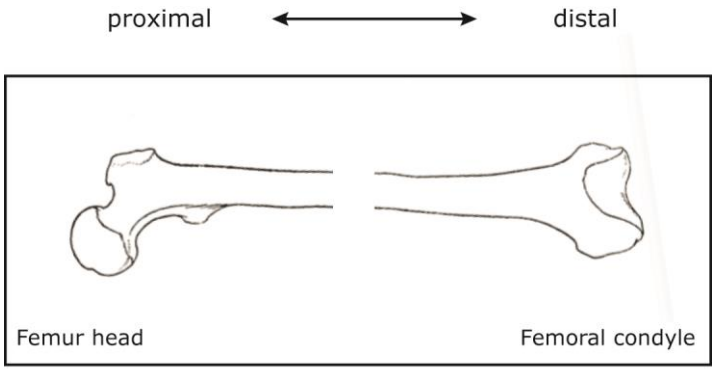

Figure 12. Orientation of specimen during embedding and freezing.
Femurs are placed in house-made mold and covered with SCEM-Medium before freezing in cold *n*-Hexan.

Table 4. Solutions used for specimen preparation, embedding and freezing.

Step	Solution
Fixation	4% PFA/PBS
Cryo protection	10% sucrose H_20 solution
	20% sucrose H_20 solution
	30% sucrose H_20 solution
Specimen freezing	Ice-cold *n*-Hexan

3.4.2. Slide preparation for histological staining

For all down stream investigations, the frozen cryo-embedded sample were sectioned into 5 µm thick slices using Kawamoto's film method [210]. In this process a transparent, adhesive cyro tape is used, allowing the sectioning of calcified tissues. The C9 tape was used for all following investigations, suitable for immune fluorescent and immune-histochemical stainings. The samples were sectioned using a Leica microtome cryostat at a constant chamber temperature of -30°C. The cryo block containing the femur was placed and fastened with SCEM-medium on a specimen chuck and afterwards into the specimen holder within the microtome chamber. Next, the sectioning blade (Feather® microtome blade, N35HR) was inserted carefully into the cutting device. Specimen orientation was adjusted parallel in relation to the cutting edge and sectioning blade. To start with the sectioning process, the hand-wheel was unlocked and turned, moving the specimen along the blade and thus cutting a defined slice. Slices of 30 µm were cut until reaching the plane of interest, the transversal section in the middle of the femur, indicated by appearance of the drill holes from the stabilizing titanium wires adjacent to both sides of the osteotomy gap. Thickness was reduced to 5 µm and prior to each cut, a size-fitted C9 cryo-tape was placed over the tissue cross-section. The tape was held with pincers, while slowly cutting the tissue underneath. At the end, the section was placed with the non-adhesive side on a microscopy glass slide, that the tissue is facing upwards and fixed with sticky tape on the sides. This procedure was repeated until enough slides were obtained, the slides were stored at -80°C in special cases until further handling.

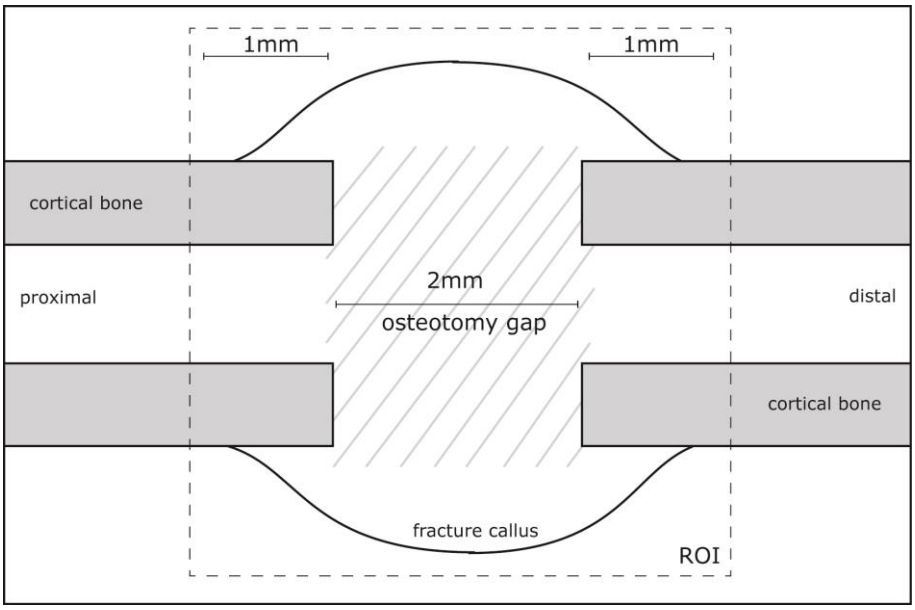

Figure 13. Schematic overview of the fracture hematoma region of interest (ROI) used for histological analysis, RNA extraction, protein and metabolite analysis.

3.4.3. Histological staining

3.4.3.1. Movat pentachrome staining

Movat's pentachrome staining was developed to distinguish between multiple connective tissues on one slide. The applied procedure of five subsequent stainings results in a yellow/orange color for mineralized bone, yellow color for collagen fibers, a greenish-blue staining for cartilage, dark red coloring for osteoids, bright red for elastic fibers and black staining for nuclei (**Table 5**). Prior to the staining procedure, slides were thawed for 45 minutes, then fixed for 15 min with 4% PFA/PBS. After fixation, samples were rehydrated for 5 minutes before beginning with the first staining of alcian blue for 30 minutes. Alcian blue targets acid proteoglycans structures like chondroitin sulfate by electrostatic binding at a pH of 2.5. This is followed by short immersion into 3% acetic acid and a 1 hour incubation in alkaline ethanol, stabilizing the blue-green pigment. After a 10 minutes washing step in cold tap water and immersion in aqua dest. for complete ethanol removal, slides were incubated in Weigert's Iron hematoxylin solution for 15 minutes used for staining nuclei. Next, another washing step is applied to remove surplus hematoxylin solution, here slides are rinsed in aqua dest. and then incubated for 15 minutes in cold tap water. Cell plasma staining is done by the application of brilliant crocein acid fuchsine for 15 minutes, followed by differentiation in 0.5% acetic acid. The slides were then incubated for 20 minutes in phophotungstic acid, which binds to the fibers of connective tissues, thereby replacing anions of already binding dyes and decolorizing the tissues for the final staining step. Saffron du gatinias solution, an alcoholic extract of dried saffron pigments is used for final connective tissue staining, resulting in a bright yellow color.

Table 5. Staining result of slides for Movat pentachrome staining.

Tissue	Staining result
Mineralized bone	Yellow/orange
Collagen fibers	Yellow
Cartilage	Greenish-blue
Osteoids	Dark red
Elastic fibers	Bright red
Nuclei	Black

3.4.4. Immunehistochemistry

To visualize specific proteins the process of immunohistochemistry is utilized, where the antigens of interest are targeted with selective antibodies on a tissue slide. The most common practice to visualize the antigen-antibody complex, is to have an enzyme coupled antibody, e.g. with a peroxidase or fluorochrome that is able to catalyze a visible color reaction.

3.4.4.1. α-smooth muscle actin staining

Vessel staining for vascularization analysis was done using an immunohistochemical approach. The target antigen used is alpha-smooth muscle actin (α-SMA) which is highly expressed in vessel smooth muscle cells. Positive staining results in a bright pink color, using an alkaline phosphatase reduction of the applied chromogen. Prior to staining procedure, slides were thawed for 45 minutes. The area to be stained, was encircled with a hydrophobic pen, fixed with 4% PFA/PBS for 15 minutes and rehydrated with 1x PBS twice for 5 min. All subsequent staining steps were carried out in a humid chamber, at room temperature, unless states otherwise. To block against unspecific background binding, samples were incubated for 30 minutes with 2% normal horse serum before applying the primary antibody solution, 1:400 (α-SMA, Dako M0851) over night at 4°C. The next day, slides were washed twice with 1xPBS for 5 minutes each, followed by incubation for 30 minutes with the secondary antibody, 2% in 2% PBS/BSA (anti-mouse biotinylated, rat-adsorbed). During the incubation time, the avidin-biotin complex (ABC-AP Vectastain Kit – SP 5000) should be prepared, according to manufactures instructions. After two washing steps, the AB- complex is applied to the tissue section for 50 min. Avidin has a high affinity for biotinylated sites, therefore form a complex with a biotinylated enzyme of choice (here: alkaline phosphatase) and further bind to the biotinylated secondary antibody. Afterwards slides were incubated twice (à 5 minutes) with chromogen buffer, before visualizing the α-SMA positive vessels by adding alkaline phosphatase substrate (Red AP Substrate Kit, Vector – SK 5100) to the chromogen buffer, which was catalyzed into a bright pink color at the sites of the target structures. Color development was observed under the microscope and ended by immersing the slides in 1xPBS. Nuclei were counter stained using Mayers Hämalaun for 1.5 minutes, followed by 5 minutes incubation in tap water and appeared blue/purple in color.

3.4.5. Image capturing and parameter quantifications

Pictures of the stained samples were taken with Zeiss Axioscope 40 Microscope, 10x objective (plus condenser) and the corresponding Imaging AxioVision LE Software (Carl Zeiss). White balance and focus were adjusted for each sample. A tile scan was used to image the fracture gap region of interest, which was set to be 4 mm in width and spanning the whole callus region in height. The 4 mm width included 2 mm osteotomy region and 1 mm on both, proximal and distal sides. A schematic overview of the determined region of interest can be seen in **Figure 13**.

Vessel quantification for α-SMA stainings was done with ImageJ (Version 1.44p; http://rsbweb.nih.gov/ij/) using a semi-automated method on blinded sections. Vessels were counted manually in a blinded approach. Inclusion criteria were a clear endothelial cell border, a visible lumen and non-muscle association. Our region of interest (ROI) included the osteotomy gap and 1 mm proximal and distal (**Figure 13**) from it and was analyzed for all time points and experimental groups.

Tissue quantification for Movat Pentachrome stainings was done using ImageJ. A semi-automated macro (IOCT.Sass.Dienelt.1.03), developed in-house by Mario Thiele, was applied to each picture, creating masks for the various tissue types by manual annotation of tissue areas and color thresholds. At the beginning, for each picture the ROI was defined and a length calibration done. The threshold color was defined for all white fields in the picture, making up the void area. Cortical bone was manually selected and mineralized tissue defined by a color threshold, here yellow. Areas of cartilaginous tissue, appearing blueish-green, were manually selected, as well as the hematoma area. At the end, the macro calculated the determined areas for each tissue type specified beforehand, in relation to the ROI and scale bar set at the beginning of the macro.

All values obtained from the different histological analysis mentioned above were sorted for each experimental group and condition and statistical testing by one-way-analysis of variance (ANOVA) was performed using GraphPad Prism Version 8.

3.5. *In vitro* experiments with human cell lines serving as artificial fracture hematoma model

In vitro analysis were pursued after characterizing the *in vivo* model and establishing target molecules. Therefore, a cell culture model of monocytes to macrophage differentiation and polarization was established and osteogenic differentiations from primary MSCs were carried out.

3.5.1. THP-1 cell culture

To study the implications of succinate on monocyte to macrophage differentiation and polarization of M1 and M2 macrophages, the human monocytic cell line THP-1 was selected for culture. THP-1 is a cell line derived from a young acute monocytic leukemia patient and often used to analyze immunological questions regarding monocyte/macrophage properties [211, 212]. They further hold the capacities to polarize into classically activated macrophages (M1) and alternatively activated macrophages (M2). The cells are cultured in RMPI 1640 containing 2 mM of glutamine and 11.1 mM glucose. Medium is supplemented with 10% FCS, 1% penicillin/streptomycin and 0.05 mM ß-mercaptoethanol. Cells have been reported to showing difficulties upon new culture establishment and it is recommended to order growing cultures, if possible. The cell line was purchased from the European Collection of Authenticated Cell Culture (ECACC) via the local distributor for Germany Sigma Aldrich. As it was not possible to obtain growing cultures, a cryo vial was bought and a new cell culture established. Upon thawing, it is vital to handle the cells with great care and use RPMI 1640 + 20% FCS until the culture reaches exponential growth. This can take up to 1 week or longer, and cell number needs to be checked every day. Cells were thawed and put in 4 ml prewarmed RPMI + 20% FCS with a subsequent centrifugation for 5 minutes at 100-150 x g, room temperature to remove the cryoprotectant. The supernatant was removed and cell were resuspended in new RPMI 1604 + 20% FCS in a calculated volume, resulting in a concentration of 3-5 $x10^5$ cells per milliliter. Resuspension of the cells in this concentration is vital for proper cell growth. Cell concentration was checked every day and adjusted with 20% FCS supplemented media accordingly. At times a huge number of cells underwent apoptosis before the viable cells could take over and proliferate. Dead cells were identified optically under the microscope and removed manually. Viable cells formed cluster before entering the exponential growth phase, and could then be transferred to RPMI supplemented with 10% FCS, which is used as maintenance medium and throughout experiments. They were kept in 75 cm^2 suspension cell culture flasks and splitted before the concentration would overgrow $1x10^6$ cells per milliliter.

3.5.1.1. Monocyte to macrophage polarization

For the *in vitro* differentiation von THP-1 monocytic cells to macrophages, cells were seeded at a concentration of $5x10^5$ – $1x10^6$ per well using a tissue-culture 6 well plate in 3 ml RPMI. Cells were stimulated for 72 hrs with 100 ng/ml Phorbol 12-myristate 13-acetate (PMA), transforming the suspension culture into an adherent one [211]. Before the attached and activated monocytes/macrophages were polarized into classically activated macrophages (M1) and alternatively activated macrophages (M2), they were incubated for 24 hours in RPMI + 10% FCS without PMA. Medium was changed afterwards, for M1 polarization 10 ng/ml LPS and 20 ng/ml IFNγ were added to the designated wells, while 20 ng/ml IL-4 and 20 ng/ml IL-13 were used for M2 polarization. Polarization was terminated after 72 hours. Conditioned Medium was collected, aliquoted and stored at -80°C until further usage. For target gene analysis cells were washed twice with PBS and lysed in 600 µl RLT Lysis buffer (Qiagen, RNeasy® Mini Kit) and stored at -80°C until RNA isolation.

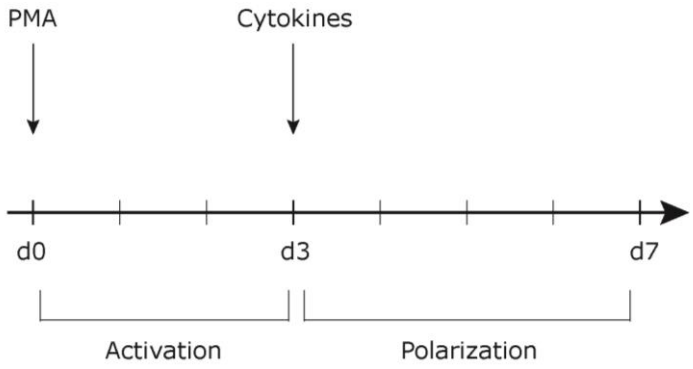

Figure 14. Schematic overview of THP-1 differentiation from monocytes to macrophages.

Cultures investigating the effect of succinate on macrophage polarization had added inclining concentrations of physiological succinate at the same time as cytokine administration – 50 mM and 500 mM succinate at final concentration. Conditioned media and RNA samples were collected as described above.

3.5.2. Primary human MSC culture

Primary human MSCs were isolated from patient bone marrow , which was obtained during surgical procedures of hip or joint replacement, according to the ethics approval EA099/10 and after written informed consent, once contagious maladies were excluded. Bone marrow was suspended in 50 ml PBS and passed through a 100 µm pore sized cell strainer, to exclude larger clumps. The bone marrow suspension was centrifuged for 10 minutes at 800 x g. PBS was removed and the cell pellet resuspended in 20 ml PBS. Bone marrow monoculear cells were isolated from there using a density gradient. 25 ml histopaque placed in a falcon, carefully overlaid with 10 ml of bone marrow cell suspension and centrifuged for 30 minutes at 1.160 x g without breaks. Interphase containing the bone marrow mononuclear cells, was extracted with a transfer pipette, washed twice and finally resuspended in DMEM low glucose, 10% FCS. All cells were seeded in a 300 cm^2 tissue culture flask, after 4 days MSCs have attached at the bottom of the flask and medium is exchanged the first time. Cells were expanded for 14 days, then splitted and reseeded as passage 1. This was repeated until passage 2 and cells, which not immediately underwent experimental procedures, were stored in liquid nitrogen. Cell isolation and cultivation was done according Pittenger [23] identification of the cultivated cells as human MSCs was done according to the International Society for Cellular Therapy [213, 214].
For thawing, vials containing MSCs were put in a 37°C waterbath. Once thawed, 4 ml prewarmed DMEM low glucose, supplemented with 10% FCS, 1% Glutamax and 1% penicillin/streptomycin, is added to the cells. Cells were centrifuged at 350 x g for 5 minutes; the supernatant was removed to eliminate remaining dimethylsulfoxid (DMSO), used as a cryoprotectant. The cell pellet was resupended and seeded on 300 cm^2 tissue culture flasks. Cells were grown until reaching 80% confluency and media was changed every three to four days.

3.5.2.1. Osteogenic differentiation

For all experiments cells were thawed in passage 2, expanded until 80% confluency was reached and reseeded for experimental conduct in passage 3. Osteogenic differentiation was conducted using a standardized operating procedure established in our laboratory after Krause et al. [215-217]. When cells reached 80% confluency (approximately $6.4x10^4/cm^2$), they where washed twice with 30 ml PBS and detached from the culture flask using 4 ml prewarmed trypsin. Upon trypsin application, flasks were put into the incubator for 2-3 minutes, shaken and put back for 1-2 minutes. Cell detachment was checked under the microscope, if all cells were in suspension, trypsination was stopped adding 16 ml of prewarmed DMEM wtith 10% FCS. If more than one culture flask was seeded per patient, cells were pooled and cell number was determined using

CasyTT cell counter. Depending on the down-stream analysis cells were seeded in different concentrations and well plates. All seeding concentrations and plate formats can be found in the following table:

Table 6. Well plate formats and cell seeding concentrations used for osteogenic differentiation of MSCs.

Plate format	Cell number
96 well plate	$2.05x10^3$
48 well plate	$4.8x10^3$
24 well plate	$12.8x10^3$
6 well plate	$6.14x10^4$

The next day, medium was changed and osteogenic differentiation induced. Further, wells surrounding the ones used for experimental analysis were filled with medium to minimize edge effects. For control wells, medium was simply exchanged with the same medium used for expansion For osteogenic wells medium was replaced with osteogenic medium, containing ascorbic acid, necessary for collagen synthesis, β-glycerolphosphate and dexamethasone. The complete formulation of osteogenic medium can be found in **Table 7**. To study the effect of succinate on mineralization, 50 mM and 500 mM of succinate was added to expansion medium (EM) and osteogenic medium (OM) and put in designated wells. Osteogenic differentiation lasted for 18 days in total. For alkaline phosphatase activity, measurements were performed at the day of induction (day 0), day 4 and day 7. For measurement of mineralization content via alizarin red staining, differentiation was stopped at day 11, 14 and 18. For gene expression analysis, cells were harvested at day 0, 4 and 7. Two to three wells were pooled and lysed in 600 µl RLT buffer.

Table 7. 1x solution (1 ml) of osteogenic medium.

Substance	Volume	Concentration (final)
Dexamethasone	10 µl	0.1 µM
L-ascorbic acid	1 µl	50 µM
β-glycerol phosphate	50 µl	10 mM
Penicillin/Streptomycin	10 µl	1x
Glutamax	10 µl	1x
FCS	100 µl	10%
DMEM- low glucose	819 µl	

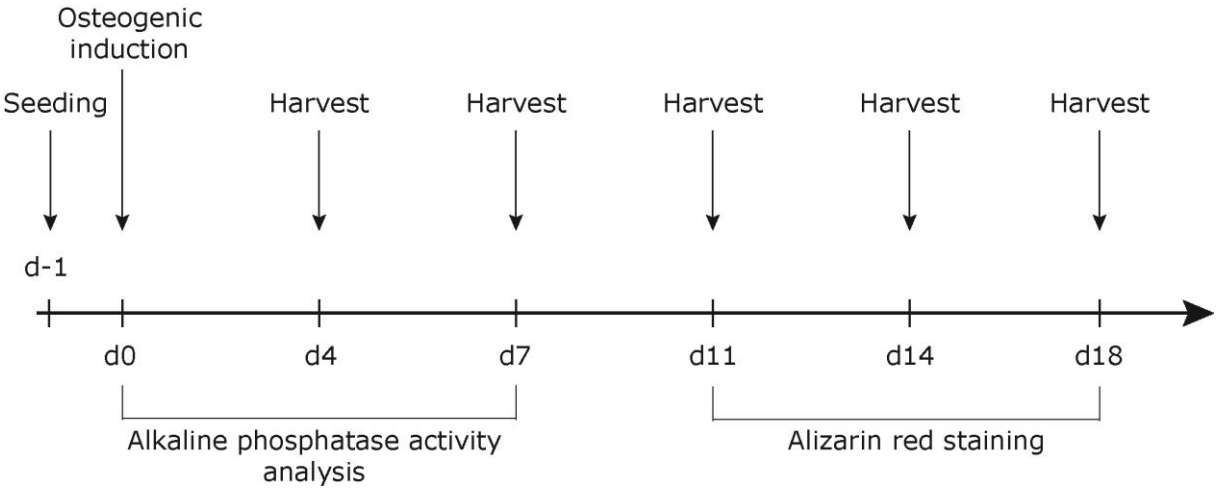

Figure 15. Schematic overview of osteogenic differentiation of human MSCs and read out time points.

Alkaline phosphatases (ALP) are highly expressed in skeletal bone tissue and its activity is involved bone metabolism and homeostasis [218, 219]. During early phases of osteogenic differentiation ALP activity increases, therefore acting as a good marker for it. To measure ALP activity, 4-nitrophenylphosphate (pNPP) was given to the cells and the production of 4-nitrophenolate determined by photometry at optical density (OD) λ=405 nm. Prior to ALP activity measurement, metabolic activity of the cells was determined after 1 hour incubation with PrestoBlue®. Wells were discarded of PrestoBlue®, washed with PBS and prewarmed ALP Buffer. 100 µl ALP Buffer was added to each well and 100 µl pNPP given on top. After 10 minutes incubation at 37°C, the reaction was stopped by application of 200 µl 1M sodium hydroxide (NaOH). 100 µl in duplicates was transferred to a 96-well plate and measured at OD=405 nm. Enzyme activity was determined using the absorbance coefficient (ε). With ε = 18450 L x mol-1 x cm-1 and d = 0.3294 cm.

$$\mathrm{C} = (E - E0)/\varepsilon \times d$$

E = adsorbance (OD)

E_0 = adsorbance blank (OD)

c = molar concentration [mol/L]

ε = molar absorbance coefficient [L x mol-1 x cm-1]

d = thickness of layer [cm] – e.g. 0.3294 cm for a 96-well, filled with 100 µL

Alizarin red (AR) staining was used for quantification of produced mineralized calcium matrix during osteogenic differentiation at its later time points, namely day 11, 14 and 18. The amount of calcium deposition was determined by colorimetry at an OD of 562 nm. Prior to alizarin red staining, PrestoBlue® for metabolic activity and Hoechst staining for cell quantification was

performed in all wells. Osteogenic differentiation was stopped at day 11, 14 and 18. Cells were fixed with 4% PFA/PBS for 10 minutes and washed with PBS. For Hoechst staining, the plate was first measured without Hoechst at λ=364 nm/460 nm to generate background values. Subsequently Hoechst staining (1:1000) was applied for 10 minutes in the dark and measured at λ=364 nm/460 nm to generate the values for cell quantification, as Hoechst stains the DNA. Wells were next washed with aqua dest. and overlayed with 150 µl 0.5% alizarin red solution. Incubation for 10 minutes at room temperature resulted in red staining where mineralized matrix was present. Wells were washed three times with aqua dest. to remove excessive staining. Plates were dried and pictures of the matrix were taken. 124 µl of cetylpyridniumchloride were added to each 48-well, resolving the calcium matrix and resulting in a purple colored solution. 100 µl were transferred to a 96-well plate and adsorption measured at λ=562 nm.
Statistical analysis were performed using GraphPad Prism Software. One- and two-way ANOVAs were applied to determine statistical testing.

3.5.3. RNA isolation *in vitro* set-up

RNA isolation from all *in vitro* experiments was performed with the RNeasy® Mini Kit from Qiagen according to manufacturer's instructions. In brief, cells lysed in RLT buffer were taken from -80°C and thawed on ice. 6 µl of β-mercaptoethanol (14.3 M) was added to each 600 µl RLT per eppi. RNA isolation was performed under the safety fume hood, all areas and materials cleaned with RNaseZap™ prior to the procedure. Samples were homogenized five times by passing it through a gauge with a 0.9 mm diameter attached to a RNase free 1 ml syringe. The homogenized lysates were loaded onto the genomic DNA (gDNA) spin column and spun for 30 seconds at >8.000 x g, room temperature. 600 µl of 70% ethanol was added to each flow-through, mixed well, next transferred to the RNeasy spin column and centrifuged at >8.000 x g for 15 seconds at room temperature. 700 µl were transferred once at a time, if there was more sample, the previous step was repeated. All flow-through was discarded and the column was washed with 700 µl RW1 buffer. Again, the flow-through is discarded and the column washed twice with 500 µl RPE buffer. The column was placed into a new and labeled Eppendorf tube. 30-50 µl of RNase free water was loaded directly onto the column membrane and incubated for one up to two minutes. RNA was eluted in a final centrifugation step and either stored at -80°C or immediately measured at the Nanodrop spectrometer for concentration and subsequent cDNA synthesis.

3.5.4. cDNA synthesis and gene expression analysis

cDNA synthesis was performed using with iScript™ cDNA Synthesis Kit from Bio-Rad Laboratories, as described before in chapter 3.2.2.

Gene expression was determined via quantitative real time PCR (Light Cycler® 480, Roche), with the DNA-intercalating agent SYBR®GREEN, as described in chapter 3.2.2.
Prime sequences were generated using NCBI website and tested for specificity and primer dimers **Table 24**. Expression of each gene was calculated according to the ddCT method with adjustment for primer efficiency and normalization to RPL13a expression [220]. Among many tested, ribosomal protein L13a (RPL13a) was found the most stable-expressed across all samples and therefore used as a reference gene.

3.5.5. Enzyme-linked Immunosorbent assay (ELISA)

Conditioned medium and cytokine secretion from cell culture were measured using Quantikine ELISA kits from R&D Systems. Kits used: human-TNF-α and human-Interleukin 1β ELISAs were performed according to the manufacturer's instructions. In brief, for each ELISA a standard series was produced. Media samples were slowly thawed on ice and if necessary, samples were diluted with the respective calibrator diluent. Needed chemicals and incubation times are depicted in **Table 8**. Standards and Samples were incubated for 2 hours in microplates coated with the respective antibody. If present, the fitting antigen attached to the antibody and was bound to the well surface. To remove all excess sample and prevent unspecific binding, all wells were washed 3-4 times with 1x wash buffer. The respective ELISA conjugate was given to the wells, containing a detection-antibody labeled with horseradish peroxidase (HRP) binding to the captured analyte and incubated for 1 hour. Microplates were washed 3-4 times, tetramethylbenzidine substrate was added to each well. A blue coloring appeared in relation to the amount of analyte present during an incubation time of 20 minutes. The reaction was stopped by adding stop solution and color change to yellow appeared. The absorbance was measured at λ=450 nm.

Table 8. Overview of solutions and incubation times used for different ELISA kits.

ELISA	Calibrator diluent	Assay diluent	Sample incubation	Conjugate incubation
TNFα	RD6-35 (1x)	RD1F	2 hours	1 hour
IL-1β	RD5-5	-	2 hours	1 hour

3.6. Statistical analyses

All statistical analyses were performed using GraphPad Prism Software, Version 8 unless stated otherwise.

For histological assessment, parameters were tested for statistical difference and significance by one-way ANOVA and Bonferroni post-hoc correction.

For gene expression analysis, calculated expression values extracted from REST software were tested for statistical difference and significance by one-way ANOVA and Bonferroni post-hoc correction.

Statistical significance for metabolite levels was tested between the experimental groups for each day with unpaired Welch's t-test for unequal variance.

Analysis for proteomic data was performed using Perseus Software [209], statistical testing for LFQ value difference and significance was done using one-way ANOVA and Bonferroni post-hoc correction.

For multiplex cytokine array data, values were tested for statistical difference and significance by one-way ANOVA and Bonferroni post-hoc correction.

Cytokine secretion levels measured by ELISA were tested for statistical difference and significance by one-way ANOVA and Bonferroni post-hoc correction.

Metabolic activity of osteogenic differentiation per MSC donor was tested for statistical difference and significance comparing treatment groups one-way ANOVA and Bonferroni post-hoc test.

ALP enzymatic activity of osteogenic differentiation per MSC donor was tested for statistical difference and significance comparing treatment groups by one-way ANOVA and Bonferroni post-hoc test.

Matrix mineralization of osteogenic differentiation per MSC donor was tested for statistical difference and significance comparing treatment groups along time by two-way ANOVA and Turkey post-hoc test.

4. Results

4.1. *In vivo* model of successful versus impaired fracture healing

4.1.1. Characterization of the 2 mm femoral osteotomy rat model – evaluation of tissue distribution by histological analysis

For this work, a 2 mm femoral osteotomy rat model of impaired fracture healing was used. The model was established by Kratzel, Preininger and Strube. They showed that young female rats show successful fracture healing, while aged female rats with a minimum of three litters display biologically impaired healing – resulting in non-union and formation of pseudathrosis at six weeks after osteotomy (healing end point) [194, 195, 221]. In order to validate successful versus impaired healing for early time points within this model, which has not been investigated in detail so far, specific parameters of fracture repair were determined and compared first by histological assessment.

Movat pentachrome overview staining was applied to analyze the tissue distribution and tissue quantity present during fracture healing within the osteotomy gap (**Figure 16**). Analysis of the Movat pentachrome staining revealed a tendency of prolonged hematoma persistence within the osteotomy gap for aged animals; additional less new bone formation by mineralizing tissue was detected. Moreover, aged animals frequently showed a structural obstruction of the distal bone marrow cavity by fibrous (blue-greenish) and mineralized tissue (yellowish in color). Another striking feature that was observed in tissue sections of aged animals was a perpendicular alignment of fibrous tissue (arrows, **Figure 16**). On the other hand, a horizontal orientation of fibrous tissue was seen in young animals at the same time point (day 14), bridging the osteotomy gap between the proximal and distal fracture entities.

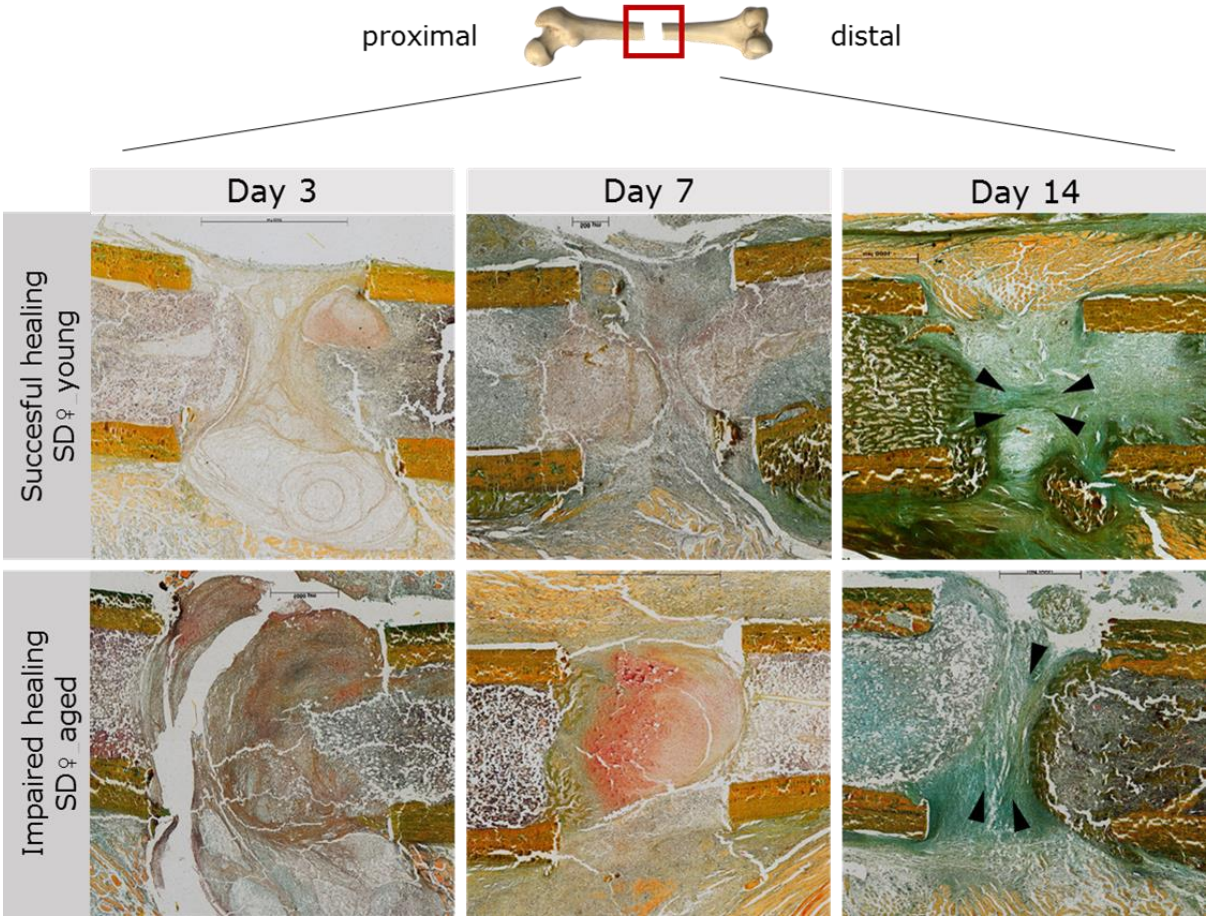

Figure 16. Movat pentachrome staining for fractures from young and aged rats at day 3, day 7 and day 14 after osteotomy.

Hematoma tissue (red- rose color) is more prominent in fractures of aged animals. Cartilage formation and mineralization is stained blue-green and yellow respectively. Black arrows indicate fiber orientation of fibrous tissue. Pictures were taken of the ROI, 2 mm fracture gap width and 1 mm to the distal and proximal side of the osteotomy gap.

Detailed histomorphometric quantification revealed a 2.5-fold significant increase of mineralized tissue in young animals (0.25 ± 0.19 % of total area) compared to aged animals (0.10 ± 0.04 % of total area) at day 14. Cartilage formation was not altered between the experimental groups at all time points. A tendency of more connective tissue formation was observed in young animals at day 3 (young: 43.46 ± 3.38 % of total area; aged: 36.79 ± 9.55% of total area) and day 7 (young: 59.31 ± 10.5 % of total area; aged: 50.11 ± 10.26% of total area). This was accompanied by a greater perseverance of hematoma tissue within the osteotomized area in aged animals at day 3 (young: 6.30 ± 8.15 % of total area; aged: 19.44 ± 16.91% of total area) and day 7 (young: 5.01 ± 5.13 % of total area; aged: 16.43 ± 13.88 % of total area) as displayed in **Figure 17**.

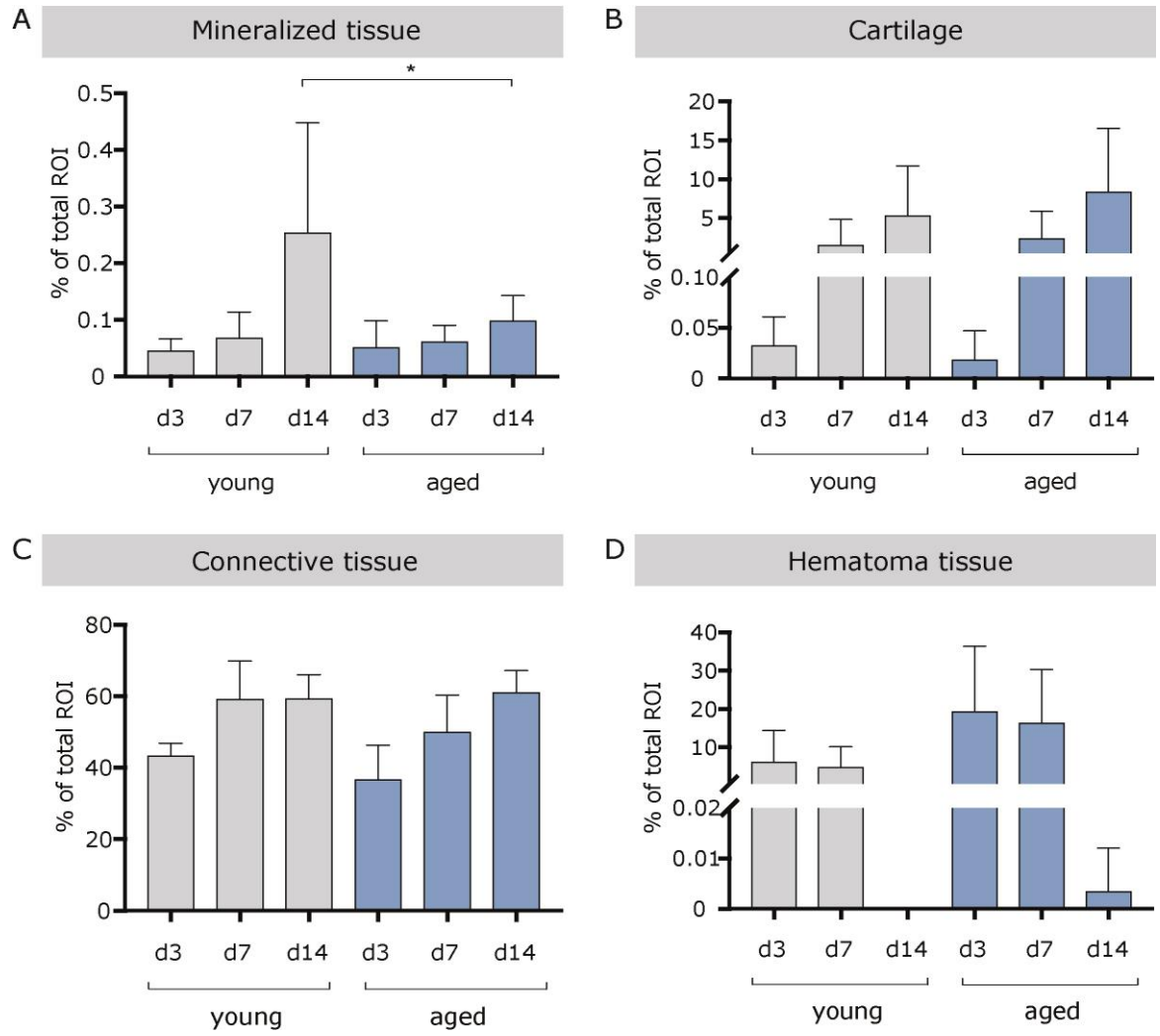

Figure 17. Quantification of Movat pentachrome staining for bone repair parameters.

Parameters were defined and quantified using an in-house analysis macro for Image J. Histomorphometric analyses of four fracture repair parameters: mineralized tissue, cartilage, connective tissue and hematoma tissue in young and aged animals at day 3, day 7 and day 14 after osteotomy. Calculated percentages refer to the total area investigated (ROI). (A) Young animals show a significant increase in bone formation by amount of mineralized tissue at day 14. (B) Cartilage formation is unchanged between young and aged animals. (C) At day 3 and 7 connective tissue shows a mild increase in young animals, while aged animals display a trend of more hematoma tissue present in the fracture gap at the same days (D). The same time points for the two animal groups were tested against each other. *≤0.05 p-value. One-way-ANOVA. n= 4-6.

Additional to bone formation parameters, new vessel formation was assessed by αSMA immunohistochemistry. α-SMA positive vessels were counted in a double-blinded approach. At day 3 no significant difference in vessel number could be measured between young and aged animals. At day 7 a significant increase in vessels was noted for young animals (young: 28.4 ± 11.47; aged 11.17 ± 5.63). The number of forming vessels continued to be higher in young rats also at day 14 (young: 36.6 ± 4.97; aged: 19.33 ± 7.92). Therefore, vessel numbers showed a 2.5 and 1.9-fold increase from day 7 onwards in young animals compared to aged ones (**Figure 18**).

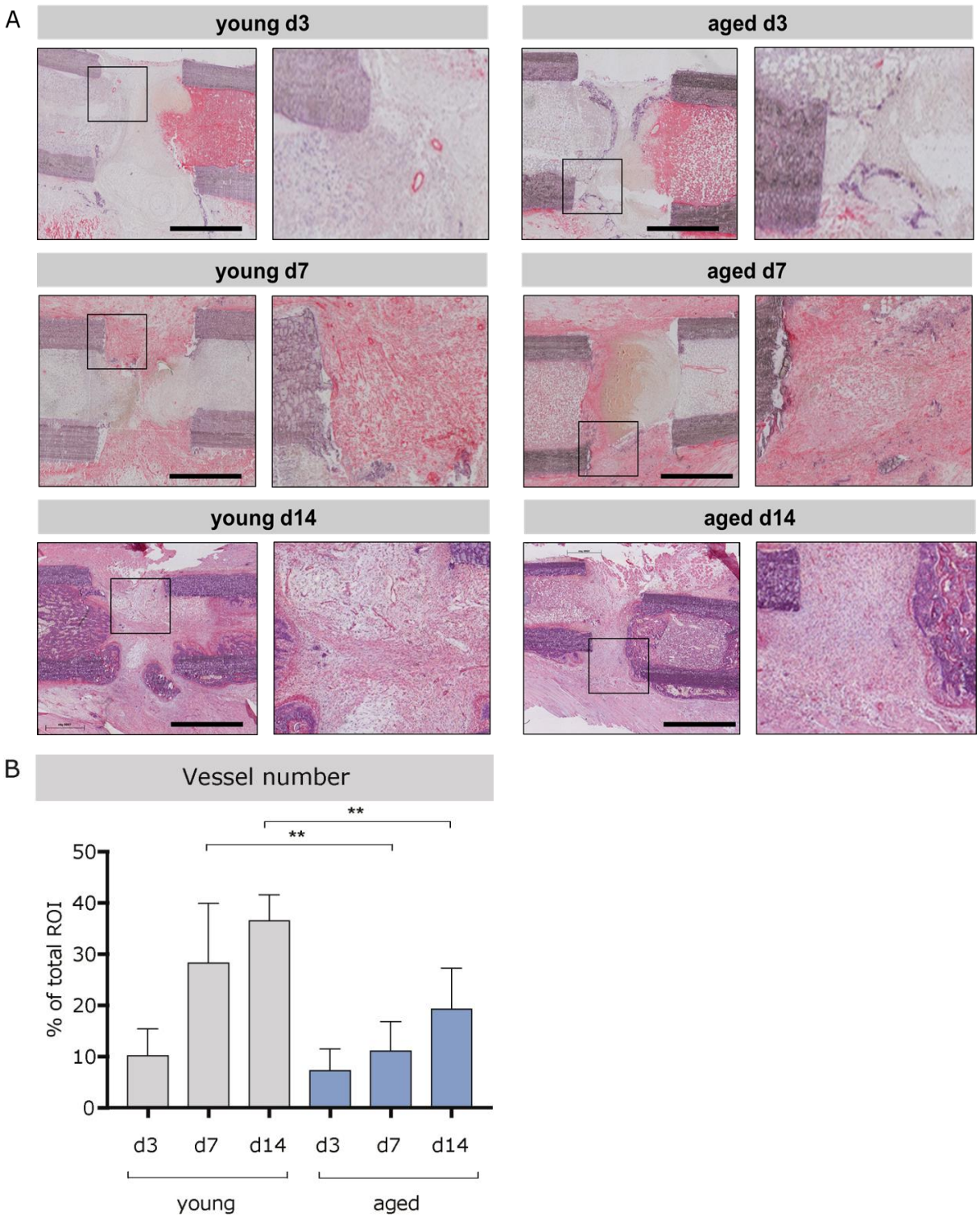

Figure 18. α-SMA staining for vessel quantification in bone regeneration.

(A) Each panel displays a different time point, starting with day 3, day 7 in the middle and day 14 in the lowest row. Young (left) and aged (right) animals are compared. (B) Vessel number was determined in a double blinded-approach. Day 3 shows no differences between the two groups (young: 10.30 ± 5.11; aged: 7.33 ± 4.16), while at day 7 and day 14 an increase in vessel number can be observed. Day 7: young: 28.40 ± 11.47; aged: 11.17 ± 5.63. Day 14 – young: 36.60 ± 4.97; aged: 19.33 ± 7.92. **≤0.01 p-value. One-Way-ANOVA, n=4-6.

4.1.2. Angiogenic and osteogenic marker expression in rat fractures

To further validate the suitability of the animal model regarding a comparative analysis of successful and impaired fracture healing, angiogenic and osteogenic gene marker expression was assesed by qRT-PCR. Disturbed angiogenesis, as seen in the decreased amout of vessels in aged animals was supported by a reduced expression of the angiogenic factors: *Platelet derived growth factor alpha* and *beta* (*Pdgf-α. Pdgf-β)* [222] and *Hif1α* for day 3 and 7. Interesstingly, *Pdgf-β* and *Hif1α* showed an upregulation in the aged group at day 14, suggesting initiation of a transcriptional profile in order to cope with the limited supply, determined by the vessel number. *Pdgf-α*, showed a 3.6 and a significant 4.4-fold expression in young animals for day 3 and day 7. Transcript number for *Pdgf-β* was increased in young by 1.6-fold and 3.2-fold (significant) for day3 and 7 respectively. At day 14, aged animals significantly upregulated *Pdgf-β* expression by 2-fold. A similar pattern was seen for *Hif1α*, where day 3 and 7 showed corresponding 2.8- and 2.7-fold increase in young animals and 0.6-fold decrease at day 14 (**Figure 19A**).

Expression of osteogenic markers (*Wnt5a, osteopontin (Spp1), collagen type 1 alpha 2(Col1a2)*) showed significant higher levels of transcription for young animals, in line with the data from the histological analysis displaying more bone formation at the latest timepoint. *Wnt5a*, a potent mediator of osteogenesis [223] showed a significant 3.4- and 4.4-fold rise at day 3 and 7. *Spp1* expression was significantly higher (2.3-fold) at day 7 and slightly increased at day 14 (1.4-fold) in the successful healing group. Formation of new collagen I fibers in young animals was suggested by the significantly augemented expression of *Col1a2* at day 3 (7.1-fold) and day 7 (3.2-fold) (**Figure 19B**).

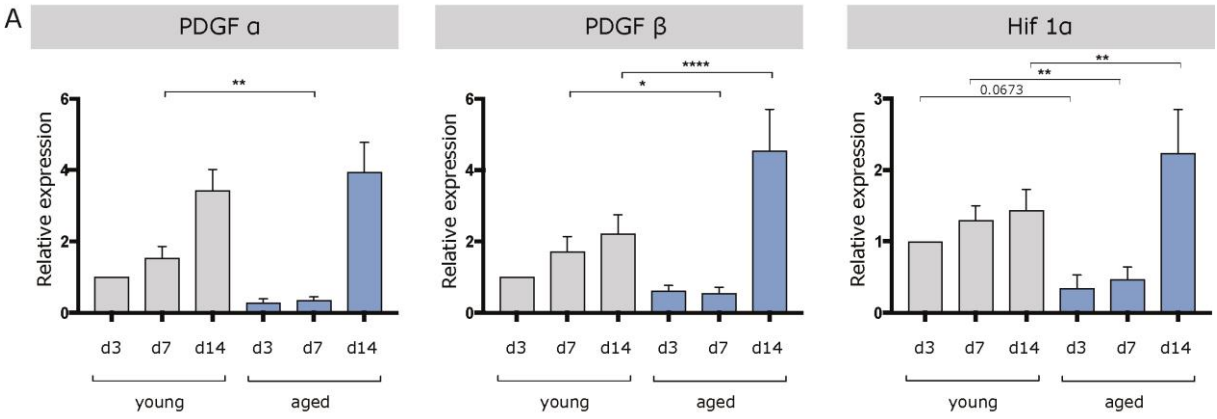

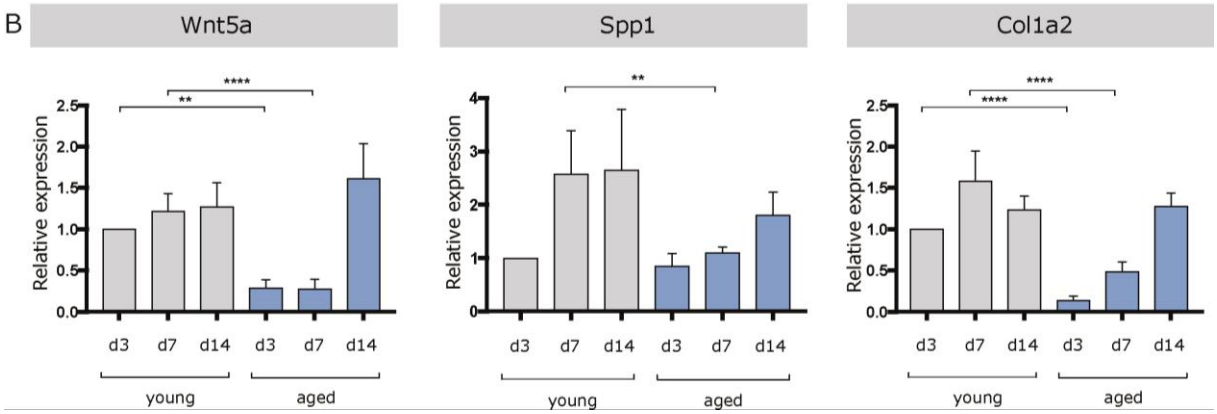

Figure 19. Expression of angiogenic and osteogenic markers in fracture hematoma of young and aged rats.

Angiogenic and osteogenic factor expression analysis in fracture hematoma tissue of young and aged animals. (A) Expression of angiogenic factors showed a decrease in aged animals for day 3 and 7 compared to young animals, while there was an upregulation for *Hif1α* and *Pdgf-β* at day 14 in aged animals compared to young animals. (B) Expression of osteogenic factors showed lower levels in aged animals compared to young animal. This was particularly seen at day 3 and 7, while no difference in expression levels can be seen at day 14 between the two age groups. *≤0.05; **≤0.01; ****≤0.0001 p-value. Relative expression, calculated to d3 young and the housekeeping gene *Tbp* using the REST software, n=3-6 One-way-ANOVA.

Taken together the obtained data from the histological assessment and gene expression analysis, confirmed that the 2 mm femoral osteotomy model of young versus aged ex-breeder Sprague Dawley rats was suitable as a fracture healing model also at early time points, where young rats displayed successful bone healing and aged rats displayed impaired fracture healing. This was especially seen in the expression data from angiogenic and osteogenic factors at day 3 and day 7, higher vessel number at day 7 and day 14 and increased tissue mineralization at day 14 in young animals compared to aged animals.

4.2. Molecular and metabolic profiling of successful versus impaired fracture healing in rats

4.2.1. Local metabolic tissue profiles of fractures from young and aged rats

One central rationale of this work was investigation of the metabolic profile of successful versus impaired healing fractures, which represents a new approach in the field of tissue regeneration. A different local metabolic activation was assumed depending on the healing phenotype. For that purpose, whole fracture hematoma extracts and un-fractured contralateral bone tissue (control) were measured for their metabolite composition by gas chromatography coupled mass-spectrometry. Almost 100 metabolite products were detectable throughout the tested samples. Best coverage was achieved for central carbon metabolism and amino acid metabolism intermediates, which will be focused on in the following and is displayed in the figure below (**Figure 20**).

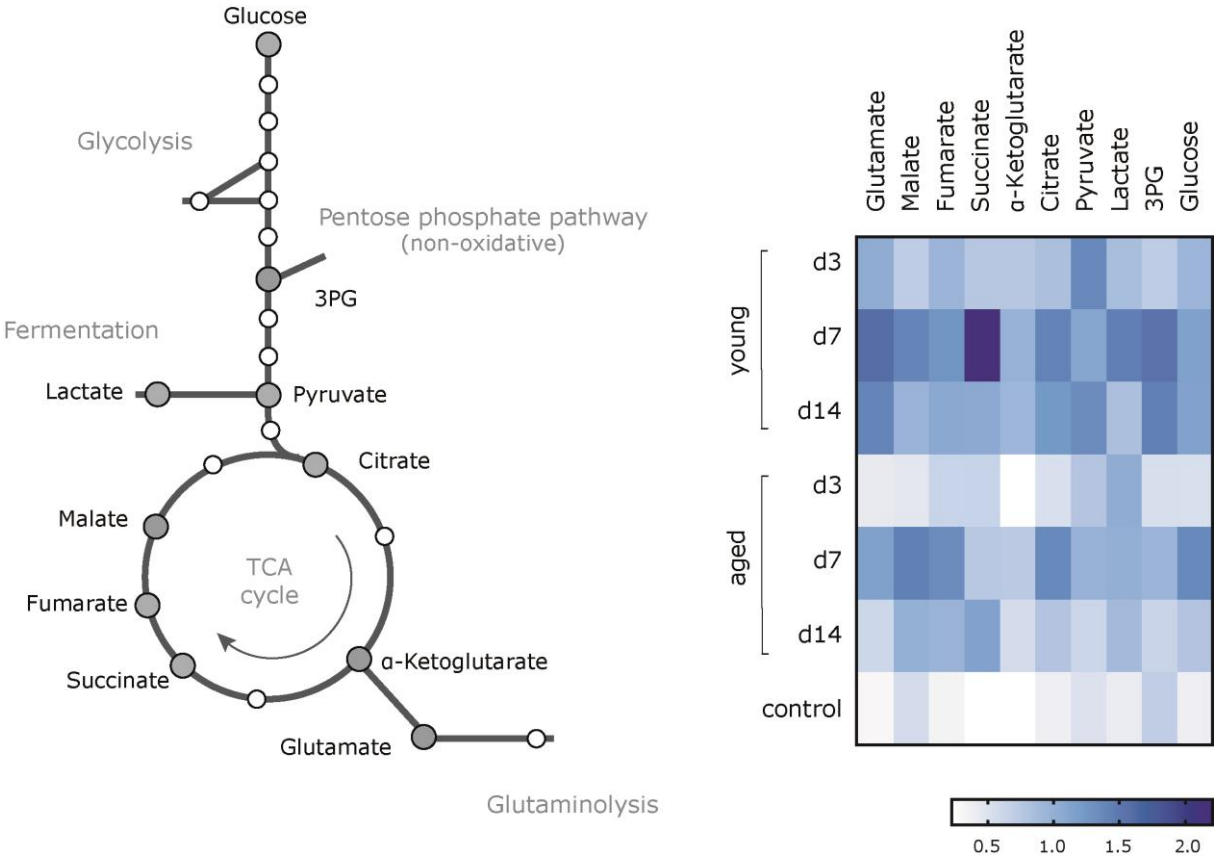

Figure 20. Schematic overview of the central carbon metabolism, its respective pathways and heat map of important intermediates.

Metabolites described in the following are highlighted by larger and grey-colored circles. Heat map displays relative metabolite abundances measured in whole tissue extracts and contralateral/unfractured bone (control), by color-coding for young and aged animals at the respective days analyzed.

No significant differences in the metabolic abundancies were detected at day 3 of fracture healing, for metabolites of the central carbon metabolism and amino acid metabolism (**Figure 21**).

At day 7 however, a trend of metabolite level increase was observed compared to the control data, while lactate and succinate significantly increased in young animal hematoma tissue. Further, alterations at central metabolic checkpoints between the two healing groups became evident. Glucose levels showed no difference between young and aged animals, suggesting no substrate limitations at the initiation of glycolysis. 3PG, six steps down-stream of glucose showed a significant 1.6-fold rise in young animals. Lactate, an important metabolic marker for oxygen levels [224] was 1.4-fold upregulated in young animals compared to aged, while pyruvate, a metabolite connecting glycolysis and the TCA cycle showed no such trend. Citrate, one of the first intermediates of the TCA cycle further displayed no differences in young and aged animals, similar to α-ketoglutarate. A significant 3-fold accumulation of succinate levels, was detected in hematoma tissue of young animals. At the same time, fumarate and malate levels were not altered between the two groups, suggesting a broken TCA cycle at succinate dehydrogenase. The metabolite data from day 7 suggested hypoxic signaling within the fracture hematoma of young animals, as indicated by the trend of lactate accumulation, and the significant rise in succinate levels. Succinate dehydrogenase, being a bi-functional enzyme of the TCA cycle and the mitochondrial electron-transport-chain, is oxygen dependent [109] and succinate to fumarate conversion is stalled upon low oxygen levels, a similar pattern is also seen under aerobic glycolytic conditions.

The metabolic profile at day 14 showed a different pattern compared to the earlier time points. Like at day 3 and 7, glucose levels did not differ between the two experimental groups, all changes within the pathway therefore account for different pathway activation. Contrasting to day 7 data, no differences in lactate levels between the groups were detected. Pyruvate on the other side, showed a marked increase in young animals (2.2-fold) and citrate was found to show the same tendency (1.6-fold), proposing a greater feeding of carbons into the TCA cycle. Succinate, fumarate and malate displayed similar levels in young and aged animals, indicative of a complete TCA cycle. Glutaminolysis appeared to be amplified in young animals as implied by high levels of glutamate and α-KG (2.3-fold and 1.7-fold, respectively). Furthermore, 3PG showed a 2.1-fold rise in young animal hematoma tissue. Under aerobic glycolysis 3PG is often used to generate building blocks for biosynthesis over serine biosynthesis or the phosphate pentose pathway [77, 78].

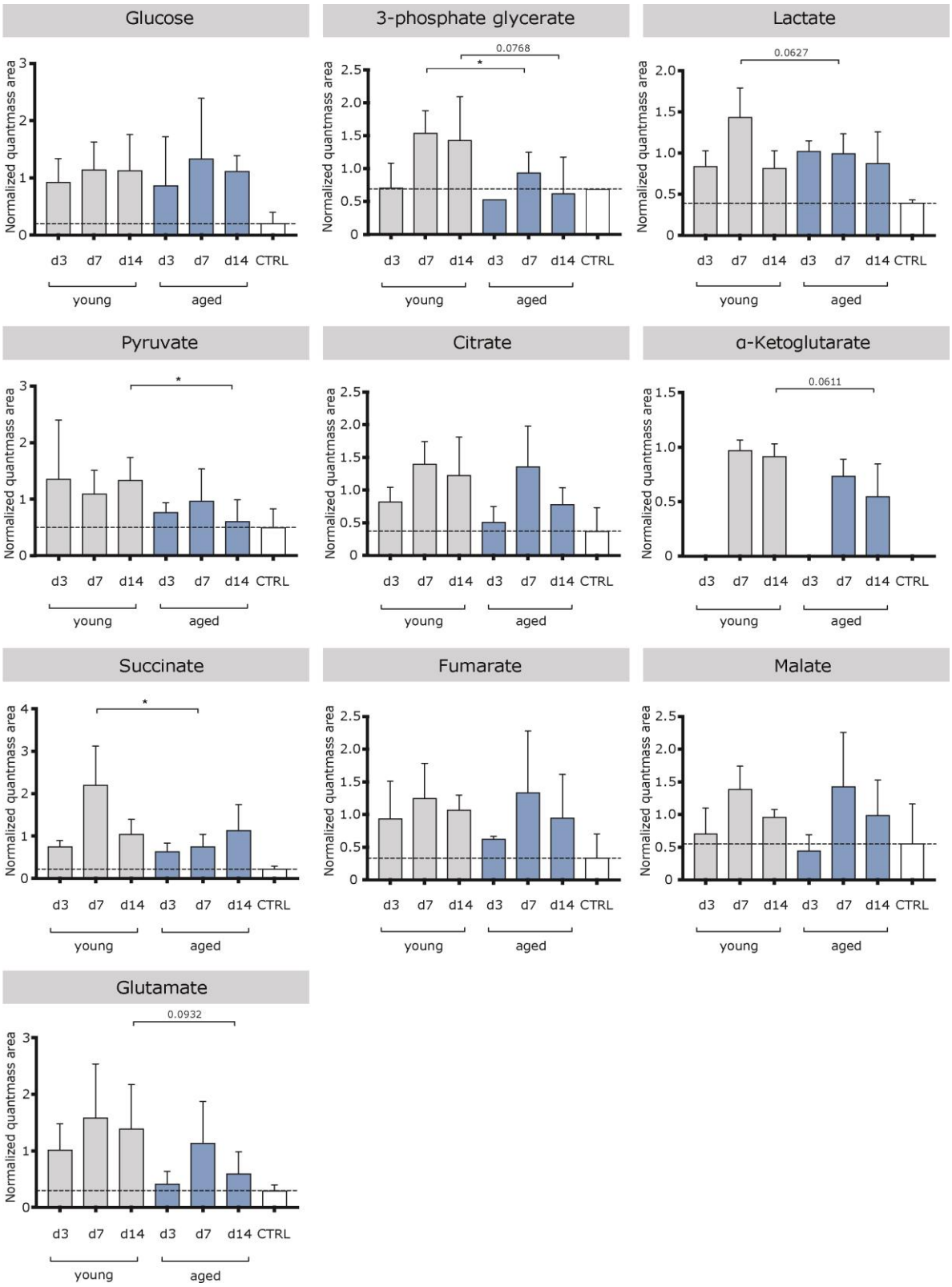

Figure 21. Metabolites of the central carbon metabolism in young and aged animal fracture hematoma tissue for day 3, day 7 and day 14.

Fracture tissue showed differences in relative metabolite abundance for young versus aged animals. Unfractured/contralateral bone served as control (CTRL) value and was additionally marked with a dashed line. *≤0.05 p-value. Data points indicating trends and close to significant difference were marked with the respective p-value. n=3-5, for experimental groups, n= 2 for control. Welch's t-test.

Taken together, day 14 metabolite profiles point toward a higher engagement of metabolic pathways in young animals, particularly seen in the high levels of pyruvate (but not lactate), an important checkpoint connecting glycolysis and TCA cycle/mitochondrial respiration [83, 225]. Presumed replenishment of the TCA cycle via glutaminolysis and formation of α-ketoglutarate, was further seen to a higher extend under successful healing conditions. Additional, 3PG accumulation, used to feed into serine biosynthesis pathway and pentose phosphate pathway under metabolically challenging conditions [77], indicated a high anabolic demand in young fracture hematoma. This is coherent with the data obtained from histological and gene expression analysis, were young animals exhibited a progressed healing state.

4.2.2. Metabolic pathway activity

As metabolism is very dynamic and can adapt to alterations within minutes or even seconds, metabolite ratios are even more meaningful in respect to pathway activity than the metabolite abundance. Succinate to fumarate ratio is an indicator for succinate dehydrogenase activity [226-228], thus for local oxygen levels or rather activation of hypoxic-signaling cascades. The succinate/fumarate ratio showed a 2-fold incline from day 3 to day 7 in young animals, and dropped by almost the same factor towards day 14 (**Figure 22A**). In aged animals, no increase in the succinate/fumarate ratio from day 3 to 7 was evident, while a slight increase in the ratio was seen at day 14. The succinate to fumarate ratio was greatest in younger animals (2.6-fold) compared to aged animals at day 7 of the healing process.

Lactate to pyruvate ratio can be used as a mean for tissue hypoxygenation and conversely for engagement of oxidative metabolism [229, 230]. Lactate/pyruvate peaked at day 7 (1.8-fold ascend from day 3 to day 7) and dropped by a factor of three towards day 14 in the young rat cohort. In the aged cohort no shift in the lactate/pyruvate ratio could be detected (**Figure 22B**). Additional, the lactate to glucose ratio gives a measure about lactate production in relation to glucose consumption [231]. The detected lactate production in unfractured bone was higher than in any of the measured fracture callus tissues (**Figure 22C**). Bone marrow is generally considered a site of low oxygen tension. MSCs and HSCs, residing in the bone marrow, need this hypoxic niche, to maintain their stemness [232, 233]. Young animals showed a peak of lactate production at day 7, similar to the lactate/pyruvate and succinate/fumarate ratios. Aged animals displayed a different lactate production pattern, where the highest peak was noticed at day 3 and values declined over the time. At day 3 lactate/glucose ratio was 2-fold higher in aged animals compared to young animals. This effect was reversed towards day 7, where young animals displayed higher lactate/glucose ratio, by 1.6 fold. At day 14 no difference was seen in lactate/glucose ratios.

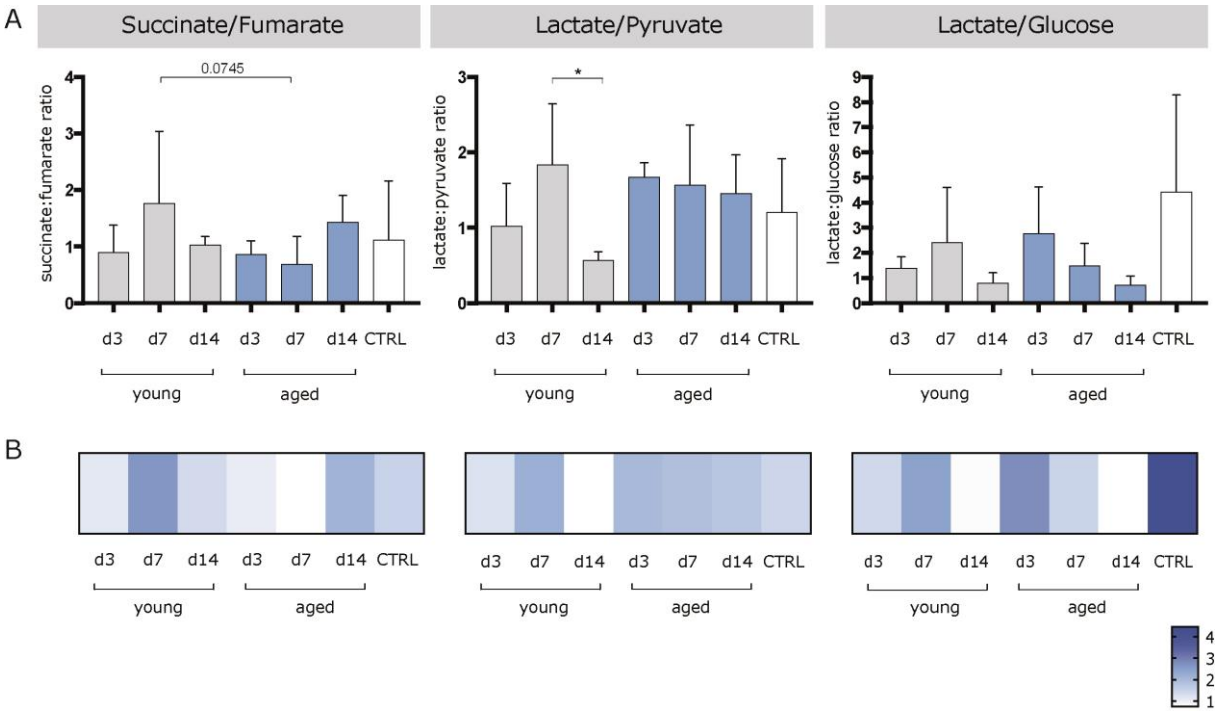

Figure 22. Metabolite ratios for aged and young fractures at the selected time points.

(A) Values of unfractured, contralateral bone serve as control values (CTRL). Succinate accumulation peaked at day 7 young animals, similar to lactate/pyruvate ratio and lactate/glucose ratio. Ratios for aged animals showed declining levels for lactate/pyruvate and lactate/glucose. A minor rise was seen for succinate accumulation at day 14 in aged animals. (B) Heatmap of the ratios from panel A, color-coding refers to relative ratios. To evaluate the dynamics within the experimental groups, statistical testing was performed for relative ratios between the time points for young and aged. * ≤0.05 p-value, data displaying trends close to significance are marked with the respective p-value.

The inspected metabolite ratios conclusively underline the described metabolic levels. No distinct pathway activation was visible at day 3 of healing in both young and aged animals, except for the higher lactate/glucose ratio in aged animals, as described above. At day 7 young animals showed an increased lactate and succinate accumulation compared to aged animals, a profile consistent with aerobic glycolysis and a fragmented TCA cycle. Lactate production and succinate accumulation in young animals were diminished at day 14 and higher levels of pyruvate suggested feeding of the TCA cycle. α-KG and glutamate levels indicated a replenishment of the TCA cycle through glutaminolysis, often seen in conditions with high demand for energy and building blocks for biosynthesis, for example cancer or tissue regeneration [74]. For aged animals, such distinct profiles could not be established; however, lactate/glucose and lactate/pyruvate ratios propose accumulation of lactate especially at day 3.

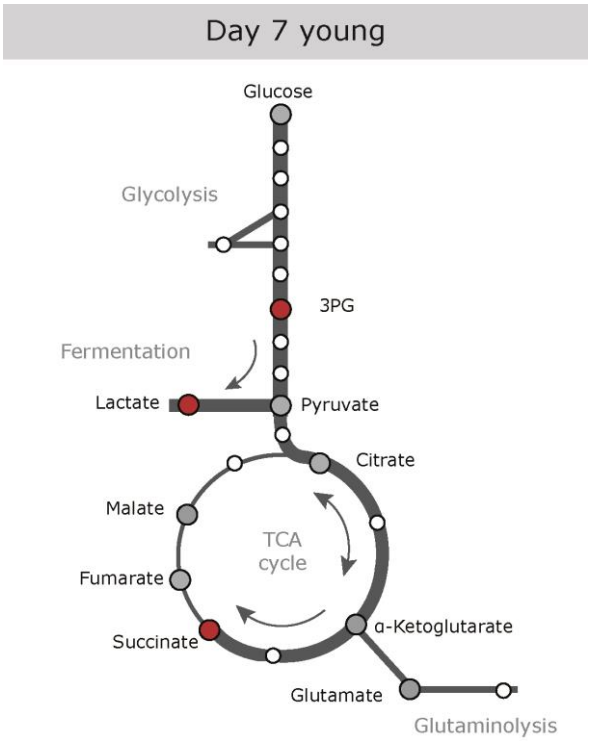

Figure 23. Schematic overview of assumed metabolic profile in fractures of young animals at day 7. Analyzed metabolite levels and metabolite ratios indicate increased glycolytic feed into lactate fermentation, thus lactate accumulation and a fragmented TCA cycle at succinate dehydrogenase, leading to succinate accumulation in fracture tissue of young animals at one week after osteotomy. Additionally, relative abundance of 3PG is increased.

4.2.3. Proteome analysis of the fracture hematoma

To further dissect the molecular characteristics of successful versus impaired healing conditions in the applied animal model and to test whether the patterns from previous metabolic analyses matched with respective metabolic enzymes, untargeted shotgun proteomics was performed from whole hematoma tissue. In order to achieve a deeper comprehension of the complex regulations of proteins during healing progression, first data analysis investigated hematoma tissue protein levels from young and aged animals separately. Label-free quantification (LFQ) intensities were normalized by z-score transformation. Clustering analysis and data visualization by heatmaps identified similar protein expression patterns for samples from same time points.

4.2.3.1. Molecular processes of successful fracture healing

Clustering of samples from young animals showed a strong grouping within the time points. All biological and technical replicates clustered together according to their state of healing (**Figure 24**). Only one biological sample from day 14 was grouped closer to day 7 than to its corresponding samples. Looking at its expression signature it can be derived to be a mixture of day 7 and day 14 protein profiles, indicating a transition phase between the two healing states. It may be concluded, that this particular animal showed a slightly slower bone regeneration. This may not be surprising, when considering biological variations and individuality.

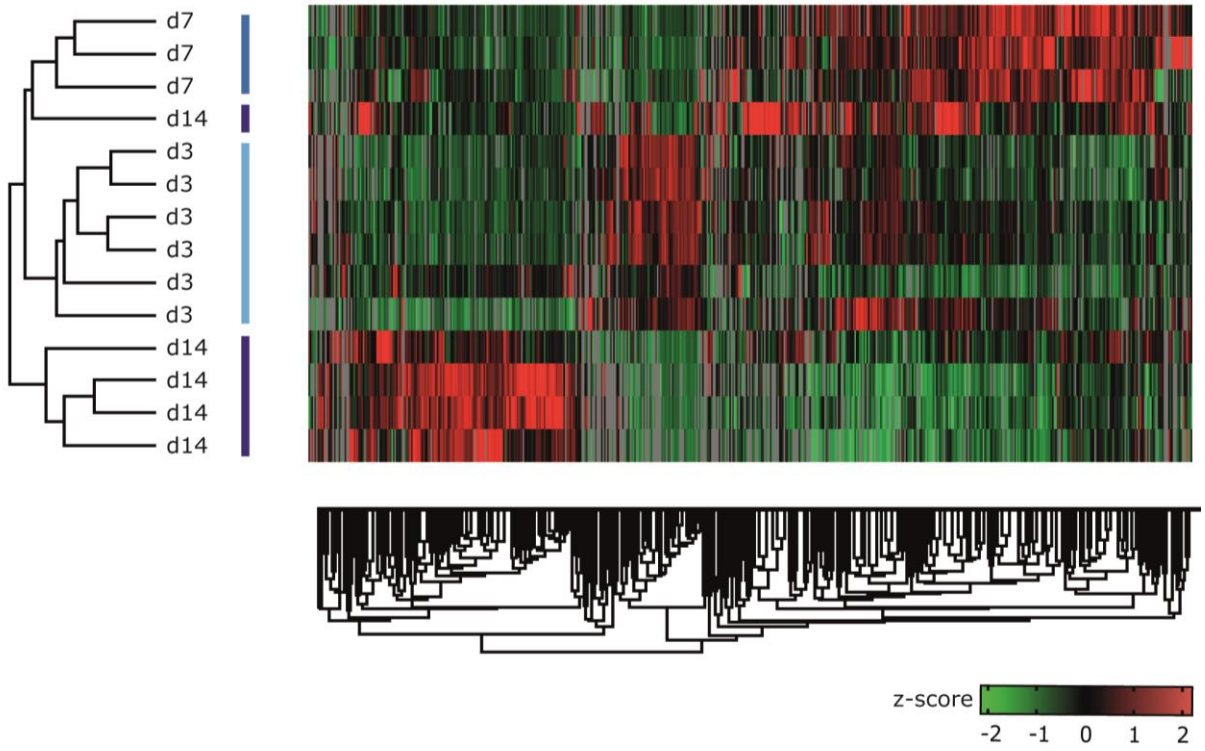

Figure 24. Clustering analysis of tissue hematoma from young rats shows grouping of samples according to the time point of dissection and healing stage.

Shown are z-score normalizations of label-free quantification (LFQ) intensities, low expression is displayed by a negative z-score in green, high protein expression (positive values) is displayed in red. No changes are depicted in black. Analysis was performed with Perseus software.

Clustering analysis highlighted that each time point has a unique protein expression pattern. Representative processes engaged at the different time points were identified using gene ontology overrepresentation enrichment analysis (gene ontology (GO) analysis using the web based analyzing tool: WebGestalt 2017, [234]). For each time point a separate gene ontology clustering was performed against background protein expression. Enrichment analysis showed that each time point during successful fracture healing had a specific protein expression pattern. Protein clusters, that were regulated the most included immune cell and complement activation, extracellular matrix (ECM) and cytoskeletal regulation and various metabolic pathways (**Figure 25**).

At day 3 a high engagement of immune processes and complement cascades could be detected, while metabolic processes and ECM regulation were underrepresented. As confirmed by histological assessment, tissue from the initial blood clot was still present at day 3 and overrepresentation of inflammatory proteins was coherent with previous results. Protein cluster from day 7 differ substantially from day 3. Protein turn-over processes displayed high activation, while metabolic protein cluster showed a decrease in expression compared to the other days. This pattern was reversed at day 14, especially for metabolic processes. Proteins from the central carbon metabolism were found to be highly enriched, parallel to activation of mitochondrial respiration (oxidative phosphorylation).

Immune processes showed a distinct downregulation, suggesting progression towards reparative responses of fracture healing, consistent with the results from histology and angiogenic marker gene expression. Furthermore, the protein data from fracture healing in young rat was in line with the observations from metabolic analysis, where a full engagement of the TCA cycle was detected for day 14. The data points towards a strong engagement of oxidative phosphorylation, an indicator for regenerative and biosynthetic processes.

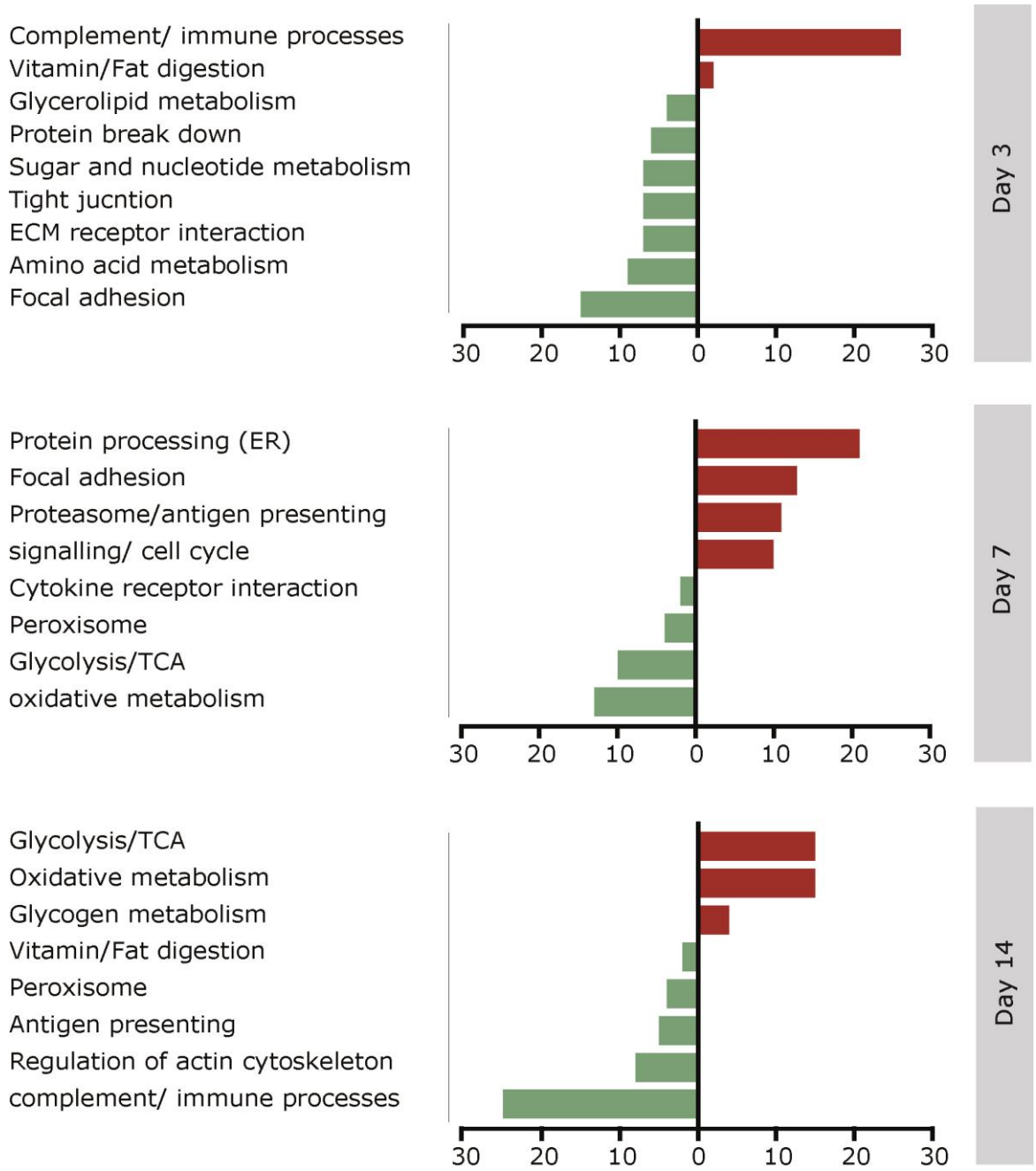

Figure 25. Up- and downregulation of biological processes for the selected time points of successful fracture healing.

For gene ontology analysis, protein expression was tested for each day against all other days. Significantly different protein expression from respective days were included in the overrepresentation enrichment analysis (ORA). Processes overrepresented are depicted in red, underrepresented processes are shown in green. X-axis shows number of protein within the clusters.

By summarizing the main regulated processes found in fracture hematoma tissue from young rats by gene ontology enrichment, a simplified time line of processes during early fracture healing was constructed (**Figure 26**). Based on the data that was obtained from the analyzed time points, a theoretical course of the protein cluster was interpolated for the time in between the respective time points.

At the earliest time point (day 3) a strong up-regulation of proteins from immune and complement processes was observed, while other protein groups were negatively regulated. Fracture healing at day 7 was marked by appearance of protein biosynthesis and breakdown clusters, parallel to a rise in extracellular matrix and focal adhesion molecules. Metabolic clusters of CCM proteins and oxidative metabolism proteins emerged at day 7; displayed a negative regulation for the respective time point. As healing progressed, tissue regenerative processes take over, that are in need of a vast amount of energy supplied by the engagement of oxidative phosphorylation [235]. This precept was reflected by a strong upregulation of glycolytic, TCA cycle and OxPhos proteins at day 14. With the presented work, it was possible to construct a time resolved sequence of important protein cluster present at the early days of successful fracture healing.
Representative protein data for central protein clusters displayed in the simplified timeline is depicted in **Figure 27**.

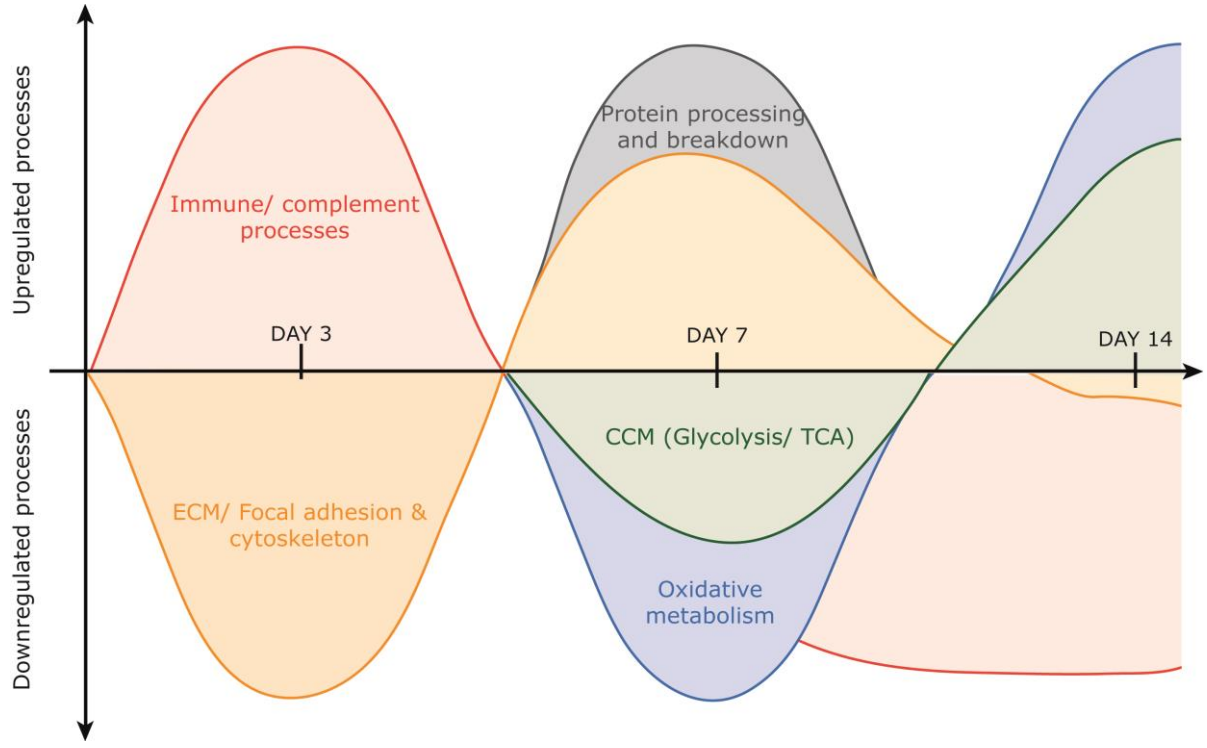

Figure 26. Simplified timeline of central mechanisms of sucessful fracture healing in young rats.
Regulated processes identified by GO term enrichment analysis, are depicted here in a simplified and summarized manner. Course of mechanism processes interpolated between the days analyzed. ECM: extracellular matrix, CCM: central carbon metabolism, TCA: tricarboxylic acid.

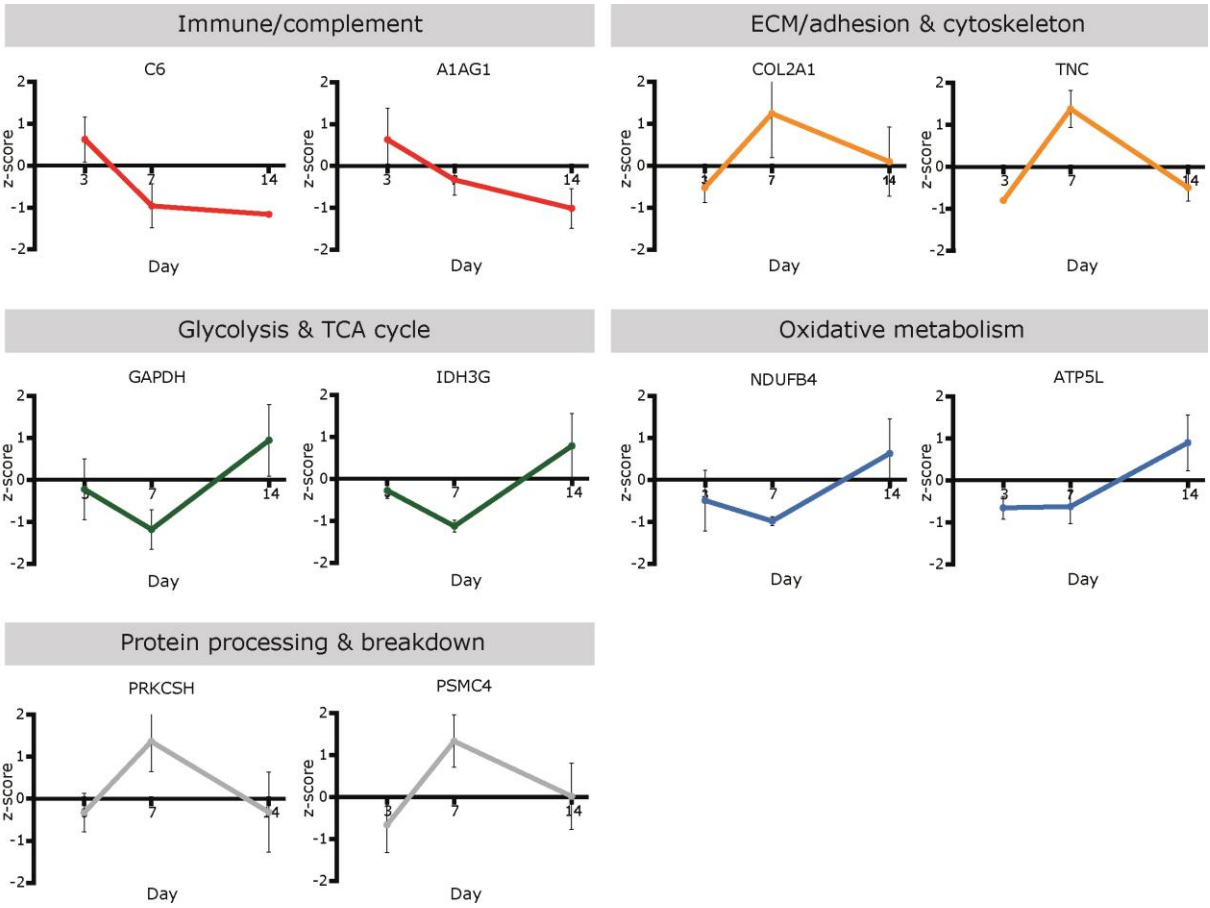

Figure 27. Descriptive protein data for all central processes regulated during sucessful fracture healing.

For the first cluster, complement component 6 (C6) and the actue phase protein alpha 1-acid glycoprotein 1 (A1AG1) are shown. Collagen 2 alpha 1 (COL2A1) and tenacin C (TNC) display the extra cellular matrix component. Glyceraldehyde 3-phosphate dehydrogenase (GAPDH) and Isocitrate dehydrogenase 3 gamma (IDH3G) represent the protein cluster for glycolysis and TCA cycle, while NADH dehydrogenase (ubiquinone) 1 beta subcomplex 4 (NDUFB4) and ATP synthase subunit g (ATP5L) represent oxdative metabolic cluster. Protein biosynthesis including endoplasmic reticulum processing and proteasome breakdown is exemplified by glucosidase II complex (PRKCSH) and 26s proteasome regulatory subunit, ATPase 4 (PSMC4). Z-score transformed LFQ quantities shown with SD.

4.2.3.2. Molecular processes of impaired fracture healing

Data clustering of samples from aged animals showed a time point specific distribution, similar to what was observed in young rats. However, only samples from day 3 showed a coherent clustering, while samples from day 7 and d14 were mixed. Thus, aged animals showed a higher heterogeneity at the two later time points (**Figure 28**).

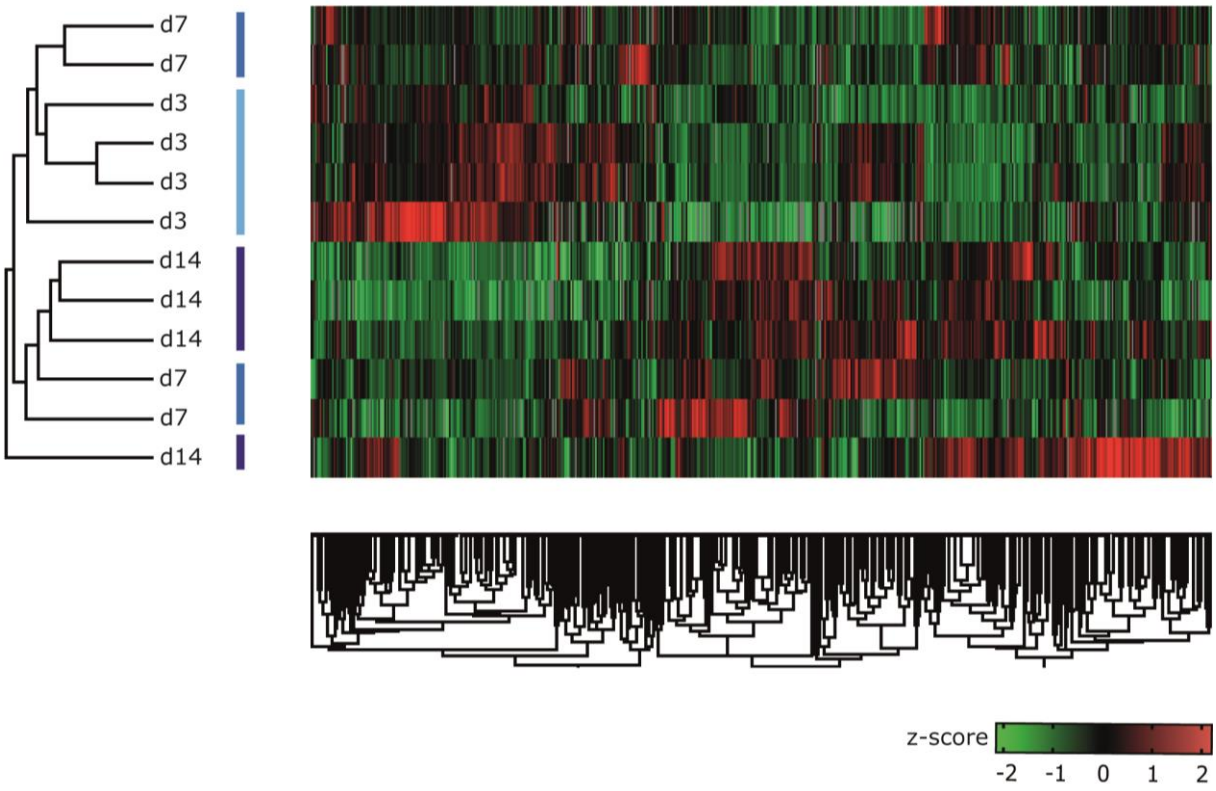

Figure 28. Heatmap clustering of samples from aged animals shows diversity in expression pattern at day 7 and 14.

Shown are z-score normalizations of label-free quantification (LFQ) intensities, low expression is displayed by a negative z-score in green, high protein expression (positive values) is displayed in red. No changes are depicted in black. Analysis was performed with Perseus software.

Similar to the workflow used on data of successful fracture healing, gene ontology enrichment analysis was performed for each time point (day 3, 7, 14) for impaired healing fracture hematoma tissue [234].

Different to successful healing, which mainly showed an upregulation of immune processes, a vast number of processes were upregulated at day 3 of impaired healing, including immune cell activation and migration, regulation of the actin cytoskeleton, folate and heme metabolism and cell cycle events (**Figure 29**). Amino acid metabolism and many processes involved in extracellular matrix organization were underrepresented at day 3, similar to what was observed in young animals. At day 7 protein processing and protein break down clusters were upregulated, as healing progressed and blood clot material is cleared. At the same time immune processes decrease. Interestingly, one could observe a differential regulation of extracellular matrix proteins. The ECM-receptor interaction cluster showed an overrepresentation compared to background protein data, while focal adhesions molecules were underrepresented. Day 14 showed an upregulation of TCA cycle proteins. The prominent cluster of oxidative phosphorylation proteins detected at day 14 in successful healing was absent in fracture tissue

showing impaired healing. Amino acid degradation and metabolism remarkably displayed a differential regulation; amino acid degradation was upregulated, while amino acid metabolism cluster showed a decreased protein abundance. Ribosomal proteins, that showed an overrepresentation at day 7, decreased towards day 14, indicative of diminished protein biosynthesis. Processes of the immune and complement system further decreased at day 14.

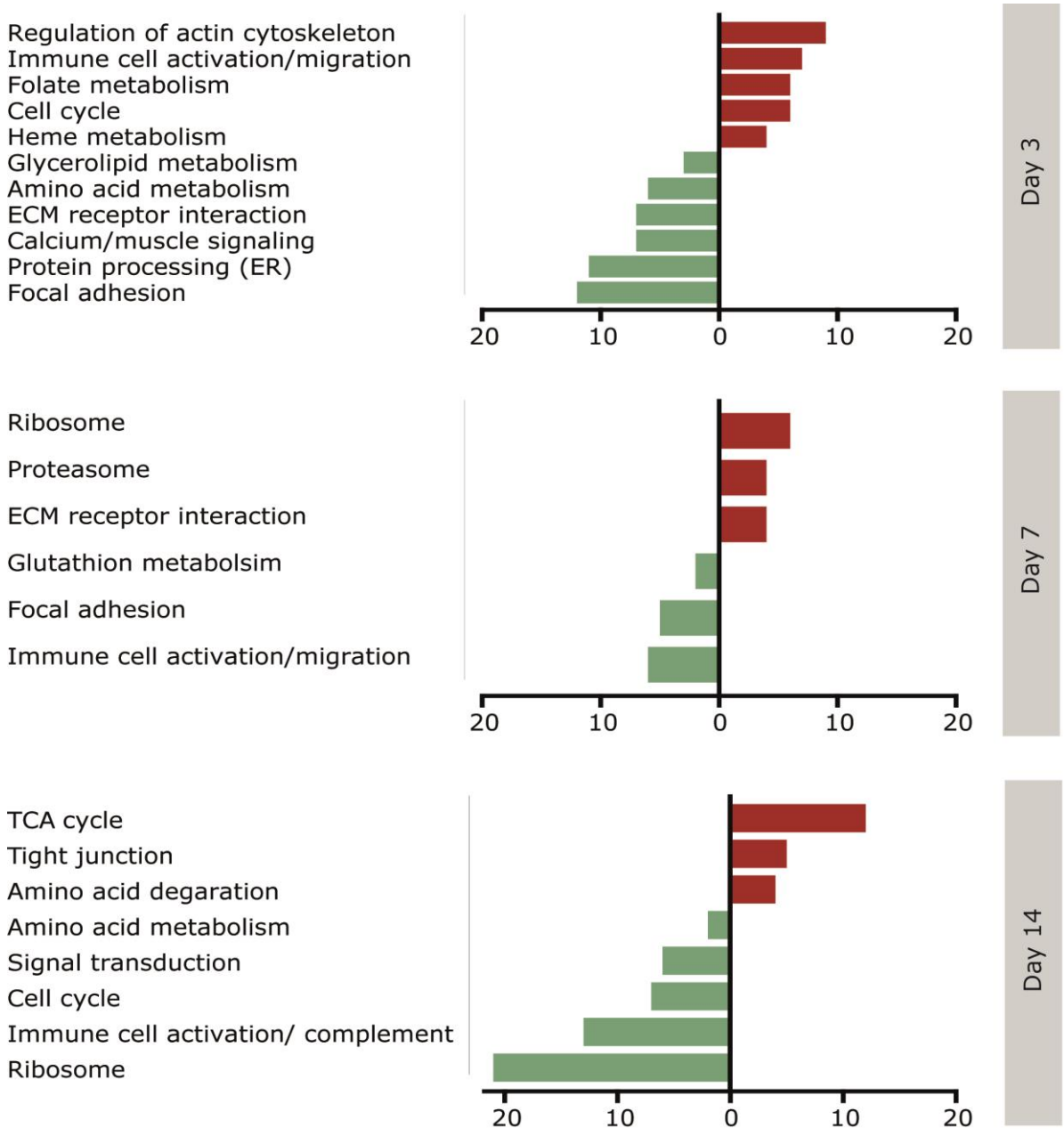

Figure 29. Up- and downregulation of biological processes for the selected time points of impaired fracture healing.

For gene ontology analysis, protein expression was tested for each day against all other days. Significantly different protein expression from respective days were included in the overrepresentation enrichment analysis (ORA). Processes overrepresented are depicted in red, underrepresented processes are shown in green. X-axis shows number of protein within the clusters.

Gene ontology term enrichment analysis revealed distinct differences between successful healing and impaired healing. One central difference was the lack of oxidative metabolism in impaired healing. Another difference could be seen in the variations of ECM, cytoskeletal- and adhesion protein regulation. While the respective cluster showed similar regulation at the time points analyzed for successful healing, diverse regulations were observed for impaired healing e.g. ECM-receptor interactions upregulated and focal adhesion downregulated at day 7.

As for successful healing, a timeline summarizing the main events was created for impaired healing conditions (**Figure 30**). Inflammatory and immune cell regulation peaked at day 3 and decreased over day 7 and day 14, as healing progressed. Similar patterns were noticed for folate, heme and glutathione metabolism (summarized under secondary metabolism). Proteins of the extracellular matrix showed a negative regulation at day 3, transforming to a positive regulation towards day 7. Focal adhesion proteins were underrepresented at day 3 and day 7. Protein biosynthesis and degradation peaked at day 7, similar to the events seen in successful healing. Main metabolic pathways engaged were amino acid and TCA cycle metabolism (CCM). Notably, no cluster of oxidative phosphorylation proteins could be identified, as seen in successful healing. This observation is in line with data from the metabolite analysis. It is reasonable to assume altered tissue regenerative processes in aged animals at day 14, compared to young animals.

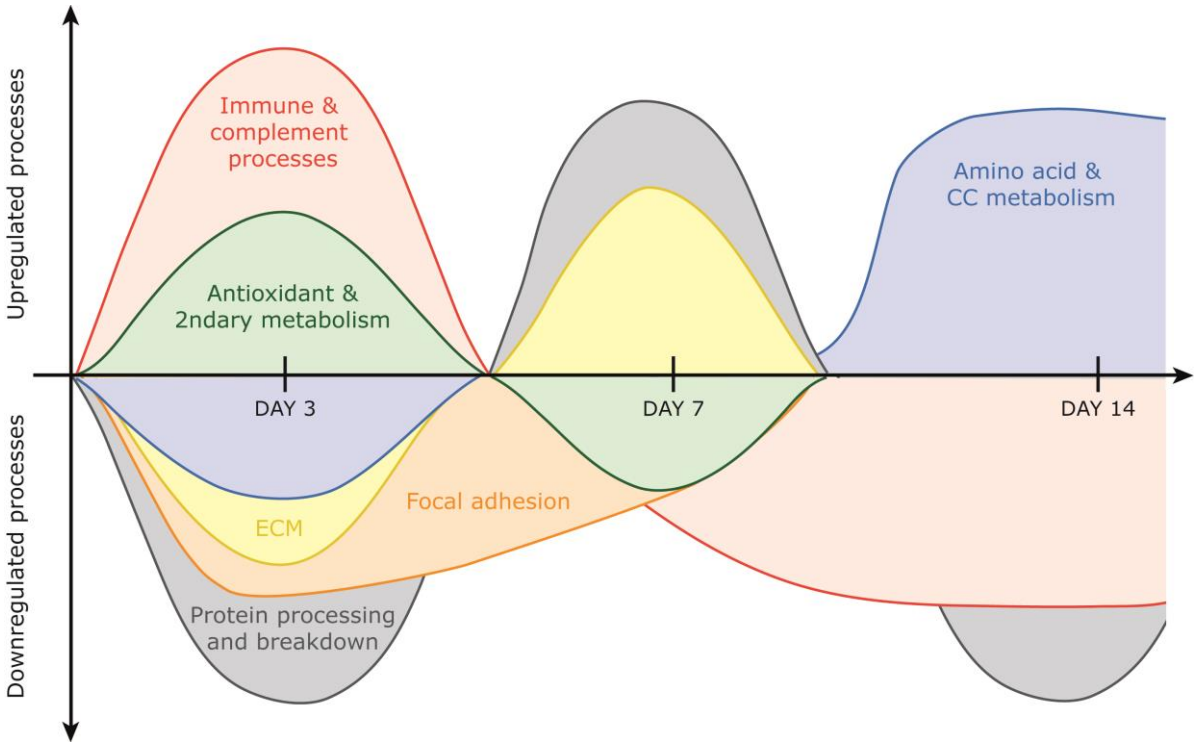

Figure 30. Simplified timeline of central mechanisms of impaired fracture healing in aged rats.
Processes were identified by GO term enrichment analysis and are depicted here in a simplifing and summarizing manner. Processes interpolated between the analyzed days. ECM: extracellular matrix, CC: central carbon (metabolism).

Characteristic protein data for the central regulated processes depicted in the previous figure can be found in **Figure 31**.

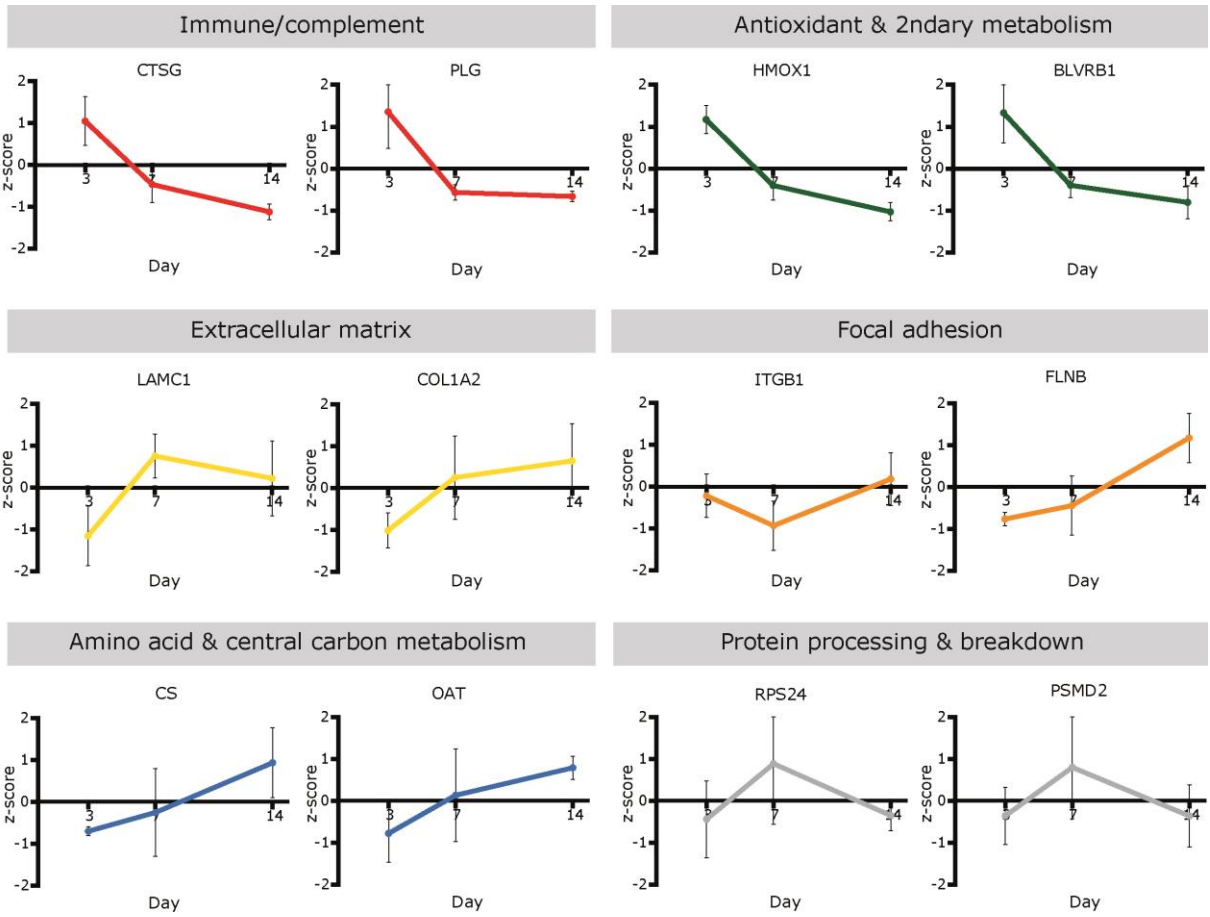

Figure 31. Descriptive protein data for central regulated processes identified in impaired healing conditions from aged rats.

Cathepsin G (CTSG) and plasminogen (PLG) represent protein cluster of immune and complement events. Proteins descriptive of antioxidant and secondary metabolism are heme oxygenase 1 (HOMX1) and biliverdin reductase 1 (BLVRB1). Laminin 1(LAMC1) and collagen 1α 2 chains embody extracellular matrix protein cluster, while focal adhesion regulation is exemplified by integrin β1 (ITGB1) and filament B (FLNB). Citrate synthase (CS) and ornithine aminotransferase (OAT) represent amino acid and TCA cycle processes. Ribosomal protein S24 (RPS24) and 26S proteasome non-ATPase regulatory subunit 2 (PSMD2) are shown for protein processing and breakdown. Z-score transformed LFQ quantities shown with SD.

4.2.4. Comparative analysis of protein data from successful versus impaired healing

After dissecting the regulation of processes during fracture healing for (1) successful healing in young rats and (2) impaired healing in aged rats, a direct comparative analysis between the two healing conditions was performed. Fold changes based on the (sum over mean) normalized LFQ intensities of each experimental group were calculated and cut off values for down- and up-regulated proteins were set. Ratios above the threshold ≥1.6 represent proteins that are upregulated by a factor of 1.6 in aged animals compared to young animals, while ratios ≤0.7 represent proteins with a lower expression in aged compared to young rats.

Gene ontology (GO) term enrichment analysis [234] was performed for the protein data identified through cut off application. The main protein cluster that were found to be differentially regulated in impaired versus successful healing enclose metabolic and extracellular matrix associated processes (**Figure 32A**).

At day 3 and day 7, the groups strongly underrepresented in impaired healing comprise contractile molecules and proteins of the ECM as well as ECM adhesion molecules. At day 14, metabolic proteins, especially those involved in oxidative phosphorylation, showed a strong downregulation in fractures of aged animals in relation to young ones (UQCRFS1: ubiquniol-cytochrome c reductase. Rieske iron-sulfur polypeptide 1, **Figure 32B)**. Parallel to oxidative phosphorylation, proteins of sugar metabolism (glycolysis/gluconeogenesis) and amino acid metabolism displayed lower levels in aged rats, as depicted for phosphomannomutase (PMM2) and aldehyde dehydrogenase 7 family member A1 (ALDH7A1) in **Figure 32B**.

Overrepresented protein cluster observed in impaired fracture healing of aged rats include immune and complement processes, lysosomal activity, ECM/ECM-receptor interaction and secondary metabolic pathways like heme and folate metabolism (e.g. BLVRB: biliverdin reductase B, **Figure 32A**). Interestingly, immune and complement proteins showed the strongest enrichment in all time points of impaired healing as seen exemplarily in cathepsin G (CTSG) levels (**Figure 32C**). Additional to immune cell processes, lysosome specific proteins displayed higher levels at day 3 and day 14 of impaired fracture healing (lysosome specific associated membrane protein 2 - LAMP2, **Figure 32C**). Further, increased levels of DNA replicational molecules (cell cycle processes) were identified, e.g minichromosome maintenance complex component 6 (MCM6), **Figure 32C**.

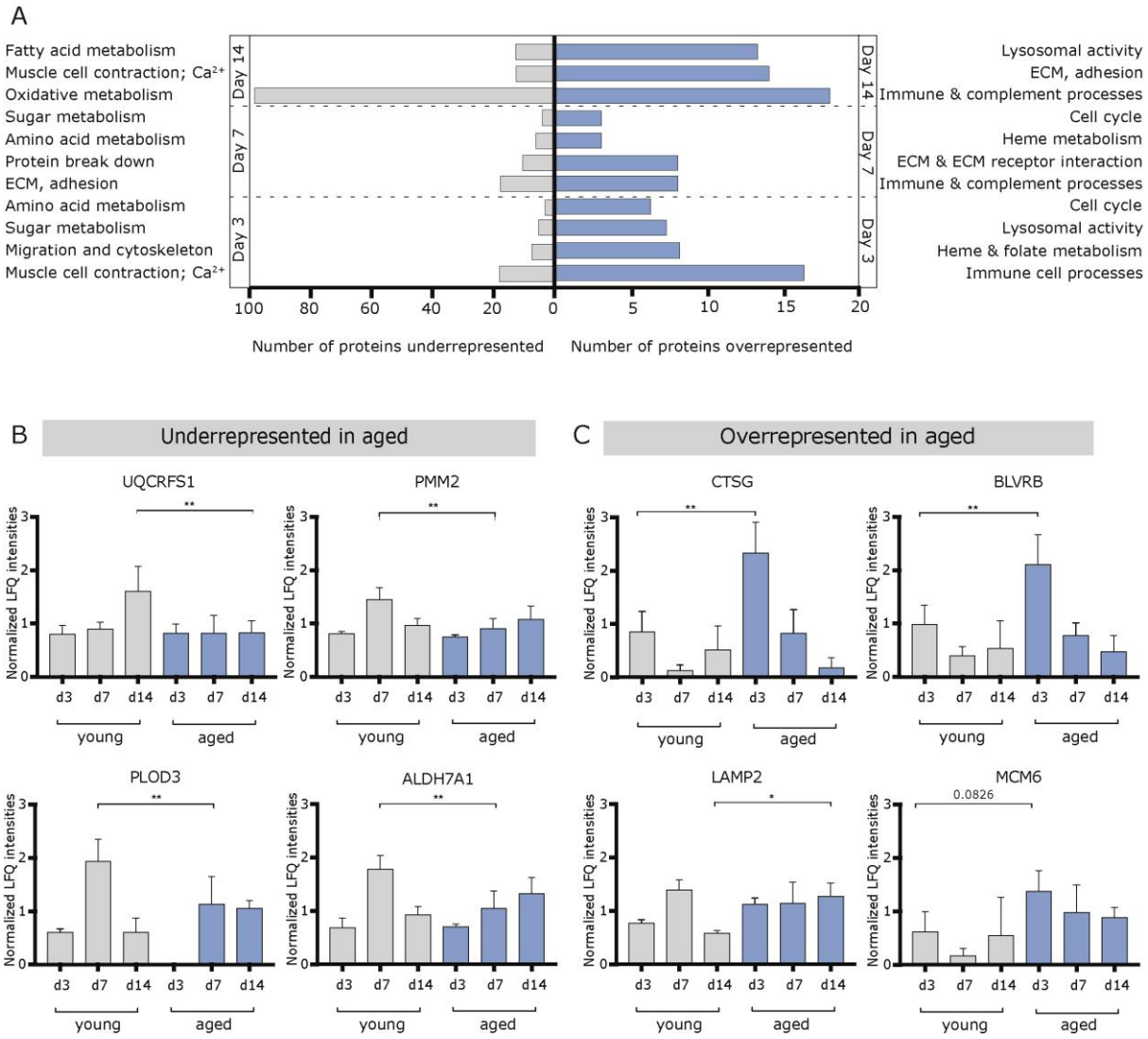

Figure 32. Identification of over- and underrepresented processes in aged animals showing impaired fracture healing in comparison to successful fracture healing (young rats).

(A) Gene ontology enrichment was performed for proteins showing higher levels (ratio aged/young cut off >1.6, grey) and lower levels in aged animals (ratio aged/young cut off <0.7, blue). Number of enriched proteins for each process is shown on the x-axis, time points are separated by vertical lines and displayed in ascending order from x-axis. (B) Representative protein data for central processes underrepresented in aged animals, as identified in enrichment analysis (A). UQCRFS1: ubiquinol-cytochrome c reductase, rieske iron-sulfur polypeptide 1, PMM2: phosphomannomutase 2, PLOD3: procollagen-lysine,2-oxoglutartate 5 dioxygenase 3 and ALDH7A1: aldehyde dehydrogenase 7 family member A1. (C) Representative protein data for main upregulated processes in fracture tissue from aged animals. CTSG: Cathepsin G, BLVRB: biliverdin reductase B, LAMP2: lysosome-associated membrane protein 2 and MCM6: minichromosome maintenance complex component 6. Shown are normalized label-free quantification (LFQ) intensities, n=4-5, *≤0.05; **≤0.01 p-value, ANOVA.

By comparison of up- and down regulated protein cluster in fracture healing between aged and young animals, it was possible to identify central dysregulated pathways in impaired healing fractures of aged rats. Histological assessment of fractures implied a prolonged inflammatory response, as the initial blood clot showed longer persistency within the osteotomy gap. The here presented data confirmed that inflammatory signaling showed an extended response in aged animals. Moreover, inflammatory and immune cell proteins displayed higher abundancies in impaired healing.

Investigation of the metabolome revealed a broken TCA cycle in young animals at day 7, with a resulting accumulation of succinate. This distinct signature was not seen in aged animals at the same or later time point, pointing at succinate as a molecule of further interest. The metabolic profile of day 14 showed engagement of the full TCA cycle and suggested increased biosynthesis and mitochondrial respiration, in young animals. Analysis of the proteomic data could confirm the metabolic-data driven hypothesis of energy biosynthesis by oxidative phosphorylation (mitochondrial respiration) in young animals at day 14 of fracture healing. This further reinforces the conclusion of increased tissue regeneration and remodeling in young animals, compared to fracture healing in aged animals at the same time point.

Extracellular matrix and adhesive molecules constitute another class of modulated proteins. They showed diverse distribution patterns between the two healing phenotypes but also within specific protein groups e.g. collagens, where no general mode of regulation can be derived. This complex topic provides interesting aspects for further investigations.

Within this thesis, further investigations focused on metabolic indications in fracture healing.

4.3. Inflammatory and immune profile of rat hematoma tissue

4.3.1. Marker expression of immune cell populations

Proteomic analysis identified large differences in inflammation/immune system processes, at the same time indicated the observed metabolic profiles different immune cell activation. Therefore, analysis of immune cell populations in rat fracture callus tissue was conducted by marker gene expression. Proteomic analysis demonstrated a modulation of inflammatory and complement proteins that occurred between young and aged animals as early as day 3. Thus, further analysis focused on innate immune populations like monocytes and macrophages.

mRNA expression analysis revealed a higher amount of cells from the monocyte/macrophage lineage at day 3 and 7 in young compared to aged animals, while at day 14 higher levels of expression were detected in aged animals. In accordance with protein data, expression of pro-inflammatory markers (e.g. *Cd80*, *TNFα*) was higher in aged animals, especially at day 3. Young animals on the contrary, exhibited a rather anti-inflammatory/remodeling expression profile (**Figure 33**).

Expression of the monocyte/macrophage marker *Cd14* [118, 236, 237], was significantly higher in young animals at day 3 and day 7 (2.7-fold and 5.4-fold respectively). Towards day 14, *Cd14* expression decreased in young animals, while it significantly increased in aged animals, leading to a 1.5-fold higher transcription in aged compared to young (**Figure 33A**).

Expression of the pan-macrophage marker *Cd68* [118, 236, 237] was slightly upregulated (young/aged: 2-fold) in the facture hematoma tissue of young animals at day 3 and showed a pronounced upregulation by 11.1-fold at day 7. At day 14, *Cd68* expression decreased by a factor of 2 in young compared to aged animals. Transcript numbers of the M1 macrophage marker *Cd80* showed higher expression in aged animals for all time points, with significant 1.5-fold upregulation at day 3 and 14. *Chemokine receptor 7* (*Ccr7*), another M1 macrophage marker [118, 236, 237], was strongly increased in aged animals at day 3 (16.4-fold), slightly decreased at day 7 and slightly increased at day 14 (4.2-fold; **Figure 33B**). The pro-inflammatory cytokine *Tnf-α* exhibited a similar profile, as *Ccr7*. Expression in aged animals was significantly elevated at day 3 by a fold change of 30.4 compared to young animals, while showing a continuous decrease at day 7 and 14. At day 7 a small rise in expression levels was seen in young animals (1.7-fold compared to aged), which significantly reduced until day 14.

Cd163, a surface marker highly expressed on M2 macrophages [118, 236, 237], displayed significantly elevated levels at day 3 in young versus aged animals (3.2-fold). Expression dropped sharply at day 7, resulting in comparable levels between the two age groups and increased at day 14 in both age groups, suggesting two waves of $Cd163^{+}$ cells migrating in the fracture hematoma.

Expression data from aged animals indicated a diminished population during the early *Cd163*+ response, while no difference was seen for the second wave of *Cd163* infiltration.

Interleukin-1 receptor antagonist (Il-1ra), another anti-inflammatory cytokine [236] was marginally downregulated in aged animals at day 3. At day 7 however, young animals showed a 4-fold upregulation of *IL-1ra* expression compared to aged animals. Expression levels at day 14 showed no differences between the two age groups. Expression of *Dectin-1,* a marker for angiogenic macrophages, increased over time in both age groups and displayed faintly higher levels in young animals at day 7 and day14.

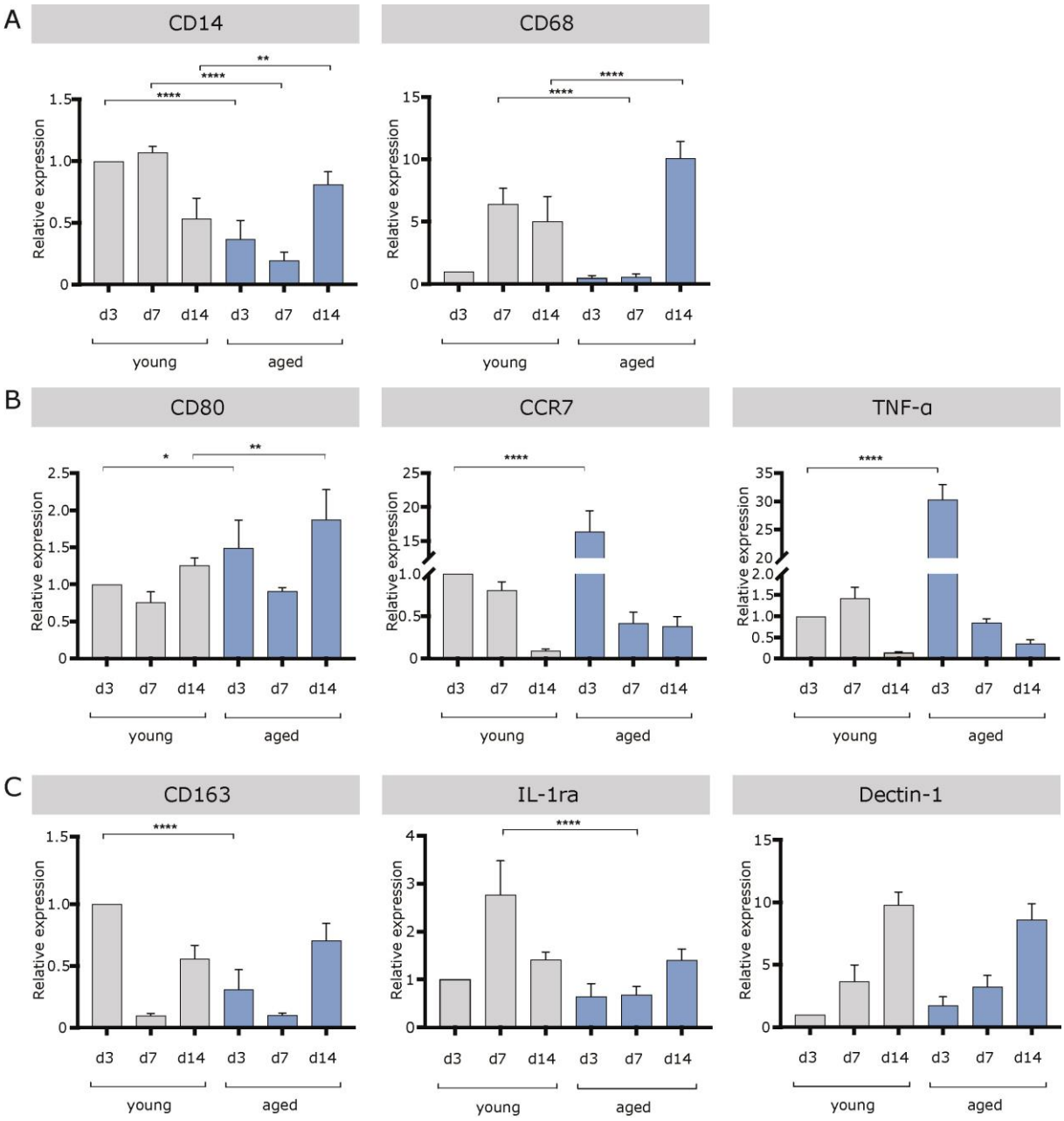

Figure 33. Expression of immune cell marker in fracture hematoma of young and aged rats.

Marker expression shows higher pro-inflammatory levels in aged animals and a profile of higher anti-inflammatory signaling in young animals. (A) *Cd14; Cd68* markers for monocytes/macrophages show

higher levels at day3 and7 in young rats, while levels reversed at day 14. (B) Pro-inflammatory, M1 marker expression displayed elevated levels in aged rats, most prominently at day 3. (C) Anti-inflammatory and M2 gene expression reveal greater transcript numbers in young rat.Expression analysis was performed with RNA isolated from whole fracture hematoma tissue, to ensure analysis of the complete microenvironment. Epression values are displayed as relative expression, to the housekeeping gene *Tbp*. All time points are normalized to day 3 young. *≤0.05; **≤0.01; ***≤0.001; ****≤0.0001 p-value. n=3-6; ANOVA.

Another important feature of macrophages is the expression and secretion of remodeling enzymes like matrix metalloproteinases [238-242]. *Mmp-2* levels were already detectable at day 3, with a 4-fold higher expression in young, while *Mmp-9* expression was not yet present. Expression of the two gelatinases *Mmp-2* and *Mmp-9* was significantly upregulated at day 7 in young animals (5.4- and 4.1-fold change respectively compared to aged animals; **Figure 34**).
Mmp-9 further showed a significant increase at day 14 (1.5-fold), while *Mmp-2* was downregulated by 1.6-fold in young versus aged rats.
Expression of the collagenase, *Mmp-13* was upregulated in young animals at the earlier time points (8-fold increase at day 7 in young animals compared to aged). However, a sharp increase at day 14 was detectable for both age groups; **Figure 34**.

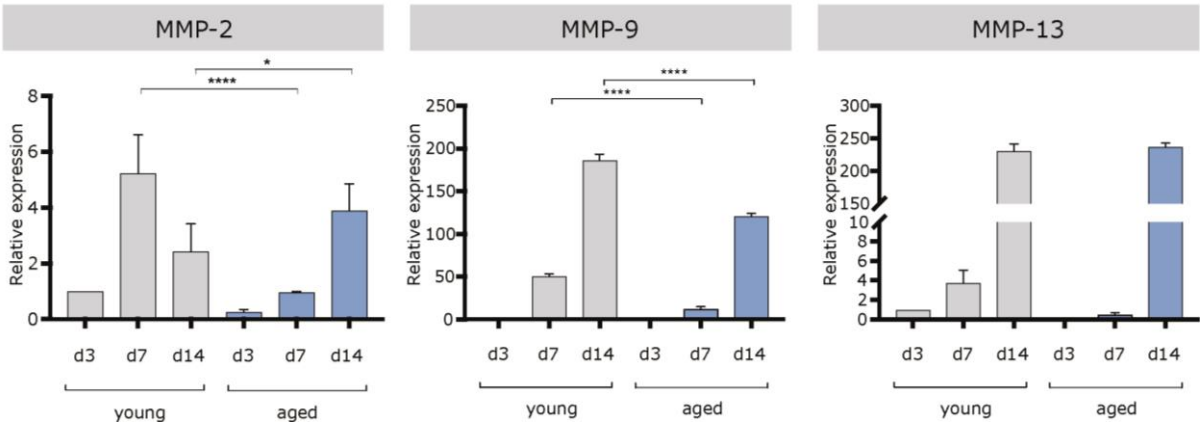

Figure 34. Expression of matrix metalloproteinases in fracture hematoma tissue of young and aged rats.

Expression of MMPs is higher in young animals compared to aged animals for the early time points (day 3 and day 7). Expression levels vary at day 14; *MMP-2* expression is lower in young animals than in aged ones, while *MMP-9* expression is increased in young animals. Expression of *MMP-13* shows equal levels in both age groups. Expression analysis was performed with RNA isolated from whole fracture hematoma tissue, to ensure analysis of the complete microenvironment. Epression values are displayed as relative expression, to the housekeeping gene *Tbp*. All time points are normalized to day 3 young. *≤0.05; **≤0.01; ***≤0.001; ****≤0.0001 p-value. n=3-6; ANOVA.

4.3.2. *Ex vivo* multiplex analysis of the fracture hematoma inflammatory milieu

Further assessment of the fracture hematoma inflammatory milieu, was performed by multiplex cytokine analysis from supernatant of hematoma explant culture. The following cytokines were detectable with the panel used: monocyte chemoattractant protein 1 (MCP-1), macrophage inflammatory protein 1 and 3 alpha (MIP-1α, MIP-3α), M-CSF, IL-6, IL-10 and VEGF. Three of the detected cytokines allowed a sophisticated statistical analysis and quantification, based on the respective standard curves. Interestingly, those cytokines were MCP-1, M-CSF and IL-1α, all highly involved in monocyte/macrophage activation and secretion [243-245]. MCP-1 and M-CSF cytokines showed elevated levels in young animals for most time points, while IL-1α displayed a prominent elevation in aged animals at the latest time-point investigated (day 14).

MCP-1 was significantly stronger secreted from fracture hematoma of young rats at day 3 (young: 4.77 ± 0.69 pg/ml; aged 2.85 ± 0.82pg/ml; **Figure 35**), secretion further increased at day 7 (young: 5.24 ± 4.05 pg/ml; aged: 1.6 ± 0.61 pg/ml) and day 14 (young: 8.51 ± 7.99 pg/ml; aged: 5.4 ± 3.63 pg/ml). For M-CSF, a similar trend of higher secretion was seen in the hematoma supernatant of young animals at day 3 (young: 0.064 ± 0.017 pg/ml; aged: 0.042 ± 0.008 pg/ml; **Figure 35**) while no difference was detectable at day 7 and 14 between the two groups. IL-1α showed increased secretion in young animals at day 3 compared to aged animals (young: 0.133 ± 0.025 pg/ml; aged: 0.01 ± 0 pg/ml; **Figure 35**), while at day 14 a substantial rise in IL-1α secretion in aged rats was noted (young: 0.042 ± 0.023 pg/ml; aged: 0.271 ± 0.191 pg/ml).

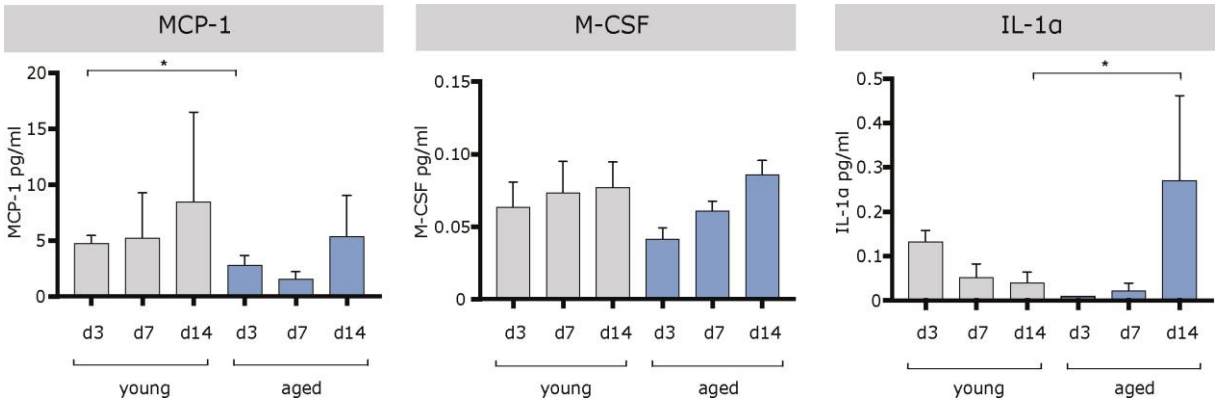

Figure 35. Secreted cytokines of 24 hours fracture hematoma explant cultures.

Higher levels of the monocyte/macrophage activating factors MCP-1 and M-CSF are detected at day 3 and day 7 in young animals. IL-1α shows a significant increase in aged animals at day 14. Cytokines present in the supernatant of ex vivo fracture hematoma cultures were analyzed using a multiplex panel * ≤0.05 p value; n=3-4, ANOVA.

Increased levels of MCP-1 suggested a higher recruitment of immune cells into the fracture site, as early as day 3 in fractures with successful healing. MCP-1 has further been shown to be highly expressed by M2 macrophages, parallel to M-CSF [243, 244]. IL-1α is, next to IL-1β, a potent pro-inflammatory cytokine highly secreted by monocytes and macrophages [245]. Higher levels in young animals, that declined over time indicated effective healing and transformation into anti-inflammatory and repair processes. An opposing picture was seen for aged animals, where IL-1α showed a steep incline towards day 14 suggesting ongoing pro-inflammatory signaling. The secretory cytokine data therefore indicated a modulation of the monocyte-macrophage axis, between successful and impaired healing and greater activation of M2 macrophages in young animals, consistent with the gene marker expression analysis (chapter 4.3.1.).

4.3.3 Summarizing the *in vivo* characterization of successful versus impaired fracture healing

Gene expression analysis of immune cell marker and the inflammatory profile showed higher levels of pro-inflammatory mediators in fracture hematoma tissue of aged animals. This was consistent with the results from the proteomic profiling approach. Young animals on the other hand, exhibited molecular markers for anti-inflammatory signaling and tissue remodeling, as well as different metabolic patterns, including a prominent accumulation of succinate early in healing progression.

A close connection between immune cells - specifically macrophages and dendritic cells - and metabolic pathway engagement leading to succinate accumulation is suggested by current research [121, 246, 247]. Papers from Kelly et al. [121] and Mills et al. [246], report succinate to act as a signaling molecule, that can induce transcriptional changes in the cells themselves and neighboring cells. Extending this mechanism toward the setting of this thesis, succinate accumulation, seen in fracture tissue of young animals at day 7 after trauma, may be a metabolically induced signal to transcriptionally change or induce certain processes within the fracture microenvironment needed for progression of regeneration. Knowing that innate immune cells, like pro-inflammatory macrophages are sensitive to succinate signaling [111], it was hypothesized that the other macrophage subtypes may be also affected by succinate signaling. Thus, further experiments were designed to asses a metabolic modulation of macrophages by succinate and possible implications on the fracture healing process.

4.4. Metabolic modulations of immune cells and MSCs – *In vitro* proof of concept

4.4.1. THP-1 as a model for macrophage polarization

To study the effects of succinate on macrophage function and its possible impact on M0/M1/M2 macrophage polarization, THP-1 cells were selected as a suitable model. This monocytic cell line has been widely used *for in vitro* investigations on macrophage characteristics upon treatment [211, 212]. THP-1 cells are able to differentiate into macrophages and can be further polarized into M1 macropahes by LPS and IFNγ stimulation and into M2 macrophages by IL-10 and IL-4 stimulation [211, 248]. The differentiation workflow is depicted in **Figure 36A.** The different macrophage subsets displayed morphological variations. Activated and non-polarized M0 macrophages displayed little lamellopodia, while M1 cells showed slightly more lamellopodia and filopodia (**Figure 36B**) In contrast, M2 macrophages displayed a big network of stretched out lamellopodia and filopodia, seemingly connecting several cells.

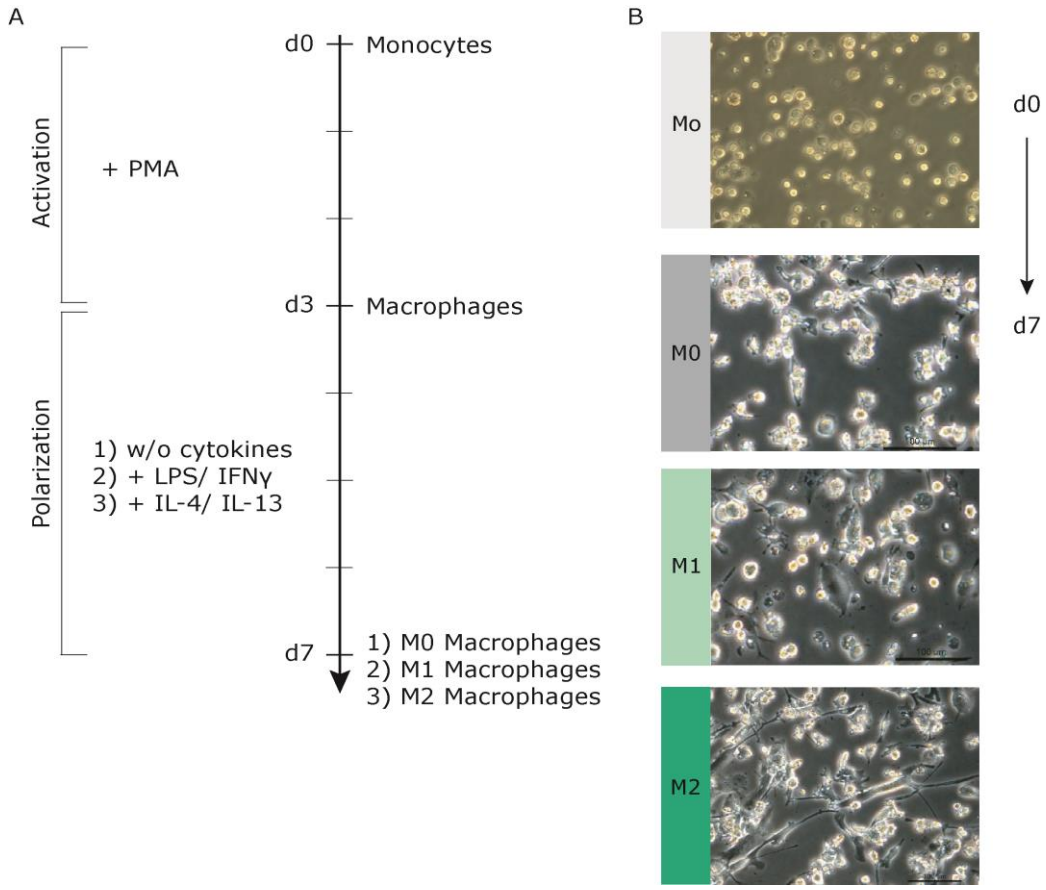

Figure 36. Differentiation and polarization of THP-1 monocytes into macrophages.

(A) Schematic workflow of monocyte to macrophage differentiation. (B) Suspension THP-1 monoctes before treatment (d0) and adherent macrophages after differentiation and polarization (d7). Mo: monocytes, M0: M0 macrophages, activated and not further polarized, M1: M1 activated macrophages by LPS and IFNγ stimulation, M2: M2 activated macrophages by IL-13 and IL-4 stimulation.

Activated and polarized cells were used for qRT-PCR analysis of M1 and M2 macrophage maker gene expression. Expression of marker genes was normalized to the housekeeping gene *RPL13A*, and related to d0 as a control value. Analysis by flow-cytometry proved troublesome due to high auto-fluorescence of the cell line and a change of granularity (side-scatter properties) during the differentiation process.

CD68 or macrosialin, often used as a pan-macrophage marker [249], was distinctly increased upon monocyte to macrophage activation, while it's expression was not affected by further polarization (d0 versus d7: M0 – 19.8-fold; M1 – 21.4-fold; M2 – 23.2-fold; **Figure 37A**). Likewise, *CD40* a marker of antigen presenting cells and as such highly expressed on macrophages, was upregulated. upon activation and polarization of THP-1 monocytes after 7 days (**Figure 37B**). However, expression levels varied significantly between M0, M1 and M2 macrophages, with M1 macrophages showing a 6-fold increase compared to M0 macrophages and a 2.7-fold increase compared to M2 macrophages. It is known that pro-inflammatory stimulation e.g. by IFNγ, upregulates *CD40* expression, making it a reliable marker for classically activated M1 macrophages [117]. The pro-inflammatory character of M1 macrophages was further demonstrated by an increase of *TNF-α* expression in M1 macrophages (3.3-fold increase compared to day 0, 3.6-fold increase compared M0 and 10.3-fold change related to M2 *TNF-α* expression). Interestingly, *IL-1β* expression, another pro-inflammatory cytokine, was highest in M0 macrophages, and even significantly different to M1 and M2 groups (100-fold). A time-course analysis (data not shown) of the differentiation process, further established that *IL-1β* expression is highest right after THP-1 monocyte activation with PMA.

Analysis of M2 marker expression revealed a distinct upregulation of *CD163* and *mannose receptor C-type1* (*MRC1)* in M2 and M0 macrophages respectively, when compared to M1 macrophages. *CD163* expression was only slightly increased by 1.2-fold comparing M0 to M2 macrophages but highly increased by 5.7-fold comparing M1 to M2 macrophages. *MRC1* expression in contrast was significantly elevated in M2 macrophages by 4.2-fold compared to M0 macrophages, while no expression of *MRC1* was detectable in M1 macrophages. Increased expression of the anti-inflammatory cytokine *TGF-β* emphasized the M2 macrophages characteristics (M2 versus M1 macrophages 6.5-fold). Interestingly, *TGF-β* expression was even higher in M0 macrophages (M0 versus M1: 11.5-fold; M0 versus M2: 1.7-fold). This upregulation of *TGF-β* in PMA treated THP-1 cells with no further polarization is consistent with accounts from literature [250].

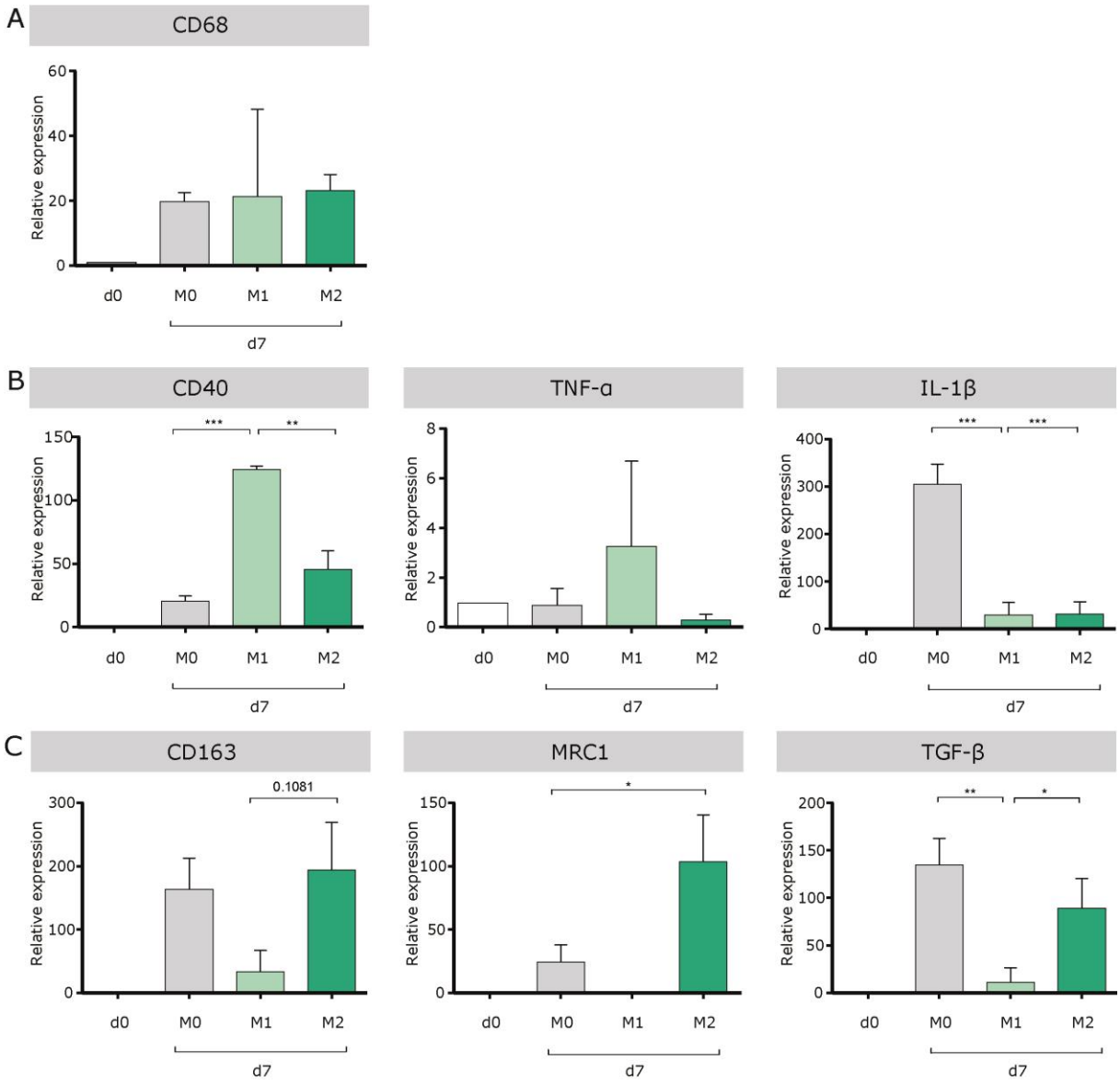

Figure 37. Expression and validation of genetic markers for M1/M2 polarization of differentiated and control THP-1 cells.

Activation and polarization of THP-1 monocytes toward macrophages was assessed by expression of the pan-macrophage marker *CD68* (A), further by expression of M1 and pro-inflammatory marker genes (B) and by expression of M2 and anti-inflammatory marker (C). THP-1 monocytes before treatment (d0 control), PMA activated THP-1 cells without further polarization at day 7 (M0), PMA activated THP-1 cells, polarized by LPS/IFNγ at day 7 (M1) and PMA activated and IL-13/IL-4 polarized THP-1 cells (M2). All genes were normalized to the housekeeping gene *RPL13A,* and analyzed in relation to d0. *≤ 0.05; **≤ 0.01; ***≤0.001 p-value. n=3, ANOVA.

Besides gene marker expression, cytokine secretion was evaluated for successful M1/M2 polarization by ELISA. Both pro-inflammatory cytokines (TNF-α; IL-1β) were secreted from LPS/IFNγ stimulated macrophages compared to the other conditions (**Figure 38**).

M1 macrophages displayed a significant TNF-α secretion compared to all other conditions (M0: 0.68 ± 0.76 ng/ml; M1: 6.02 ± 2.64 ng/ml; M2: 0.59 ± 0.38 ng/ml), and a 2000-fold upregulation compared to untreated THP-1 cells at day 0. Similar response was seen for IL-1β secretion. M1 classically activated THP-1 macrophages exhibited a significant upregulation in relation to all other conditions (M0: 3.22 ± 3.3 ng/ml; M1: 12.32± 7.53 ng/ml, M2: 4.2 ± 2.78 ng/ml). Compared to untreated THp-1 cells; M1 macrophages displayed a 112-fold upregulation of IL-1β secretion. The secretion pattern of IL-1β differs from the gene expression pattern in THP-1 macrophages, with unpolarized M0 macrophages showing the highest expression, whereas secretion was highest in M1 macrophages, as expected. This can be explained by the synthesis of IL-1β as a pro-cytokine, which exerts its biological function only after catalytic cleavage into mature IL-1β. Upregulation of expression and increased biological activity may thus not always occur at the same time. *In vitro* stimulation with LPS, is necessary to trigger NF-κB dependent expression of the NLRP3 inflammasome, in turn needed to activate capase-1, which cleaves the previously transcribed pro-IL1β into mature IL-1β [251].

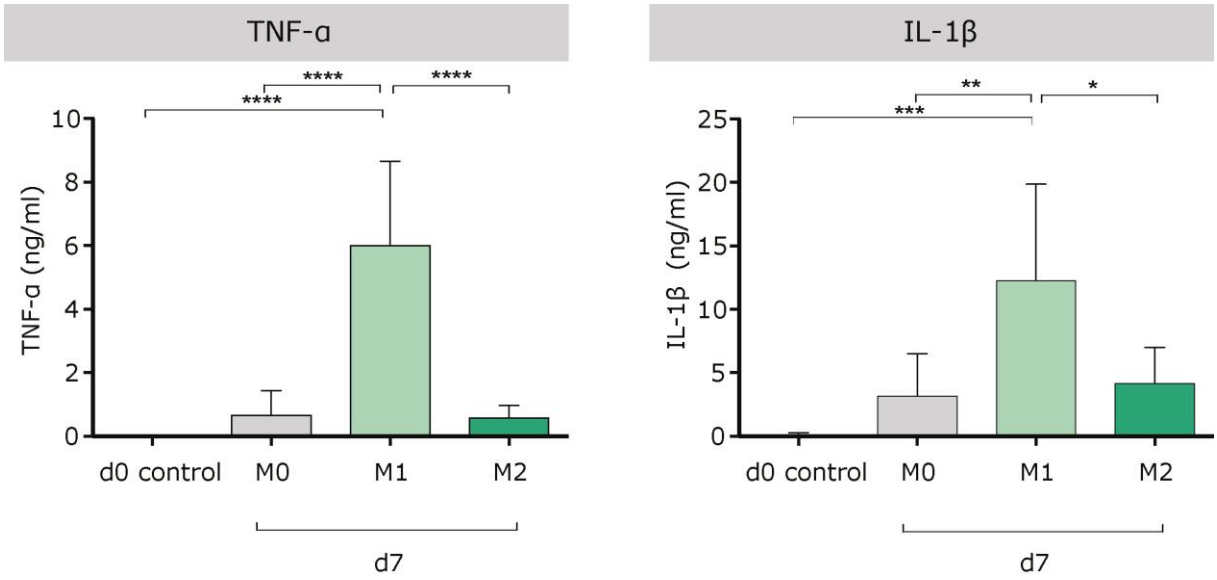

Figure 38. Cytokine secretion of THP-1 activated and polarized macrophages.

TNF-α and IL-1β secretion is highest for LPS/IFNγ polarized M1 macrophages after 7 days of differentiation Untreated THP-1 monocytes serve as a control (d0) M0: PMA activated macrophages without further polarization, M2: IL-13/IL-4 polarized M2 macrophages. *≤ 0.05; **≤ 0.01; ***≤0.001; **** ≤0.0001 p-value. n=3, One-Way-ANOVA.

Taken together the results from the gene marker analysis and the cytokine secretion profile, it is concluded that the applied differentiation protocol of THP-1 monocytes into macrophages and the subsequent polarization was a suitable model to investigate treatment effects on different macrophage subsets.

4.4.2. Metabolic modulation of THP-1 macrophages by succinate application

Succinate has been reported to highly accumulate in LPS stimulated macrophages. Over regulation of PHD it can stabilize and further activate HIF-1α [252, 253]. To dissect the cellular responses of other macrophage subsets (M0, M2) or a change in macrophage polarization (e.g. M1/M2 switch) in response to succinate accumulation, respective *in vitro* experiments were performed. Application of different succinate concentrations *in vitro* was found in the literature; those however, were often used at high concentrations and outside the physiological range [201, 254-256]. Plasma concentrations of succinate in humans and rodents are reported between 2-20 µM; the half-maximal response of succinate to its receptor SUCNR1 being 56 ± 8 and 28 ± 5 µM in humans and mice, respectively [257]. Inhibition of the succinate dehydrogenase with different small-interfering RNA (siRNA), induced to intracellular accumulation of succinate, ranging from 120.6 ± 32.0 to 446.8 ± 86.1 µM [253]. Based on the reported values, two concentrations, within the physiological range, were chosen for further downstream experiments: 50 and 500 µM.
Therefore, THP-1 cells were stimulated with PMA and polarized into M1 and M2 macrophages as described previously. 50 and 500 µM were added to the culture medium at the same time polarizing cytokines were applied, a schematic overview can be found below:

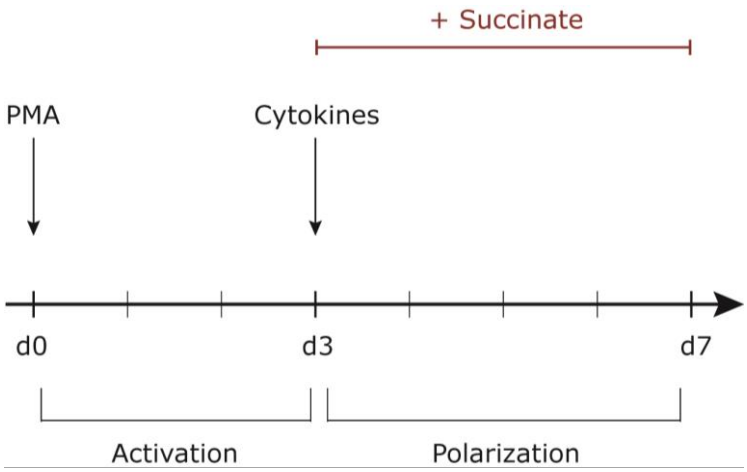

Figure 39. Schematic workflow of succinate administration during *in vitro* differentiation of THP-1 monocytes to M1 and M2 macrophages.

Interestingly, succinate administration induced strong *IL-1β* expression in M1 macrophages (**Figure 40**), while patterns of marker expression from the other genes did not show major changes after succinate administration. This confirms earlier findings from Tannahil et al. [111], who report an induction of IL-1β transcription by activation of HIF-1α after succinate accumulation in M1 macrophages. This transcriptional change towards pro-inflammatory signaling after succinate administration in M1 macrophages confirms that metabolites, here succinate, can have a direct impact on immune cell functionality by modifying their cytokine expression.

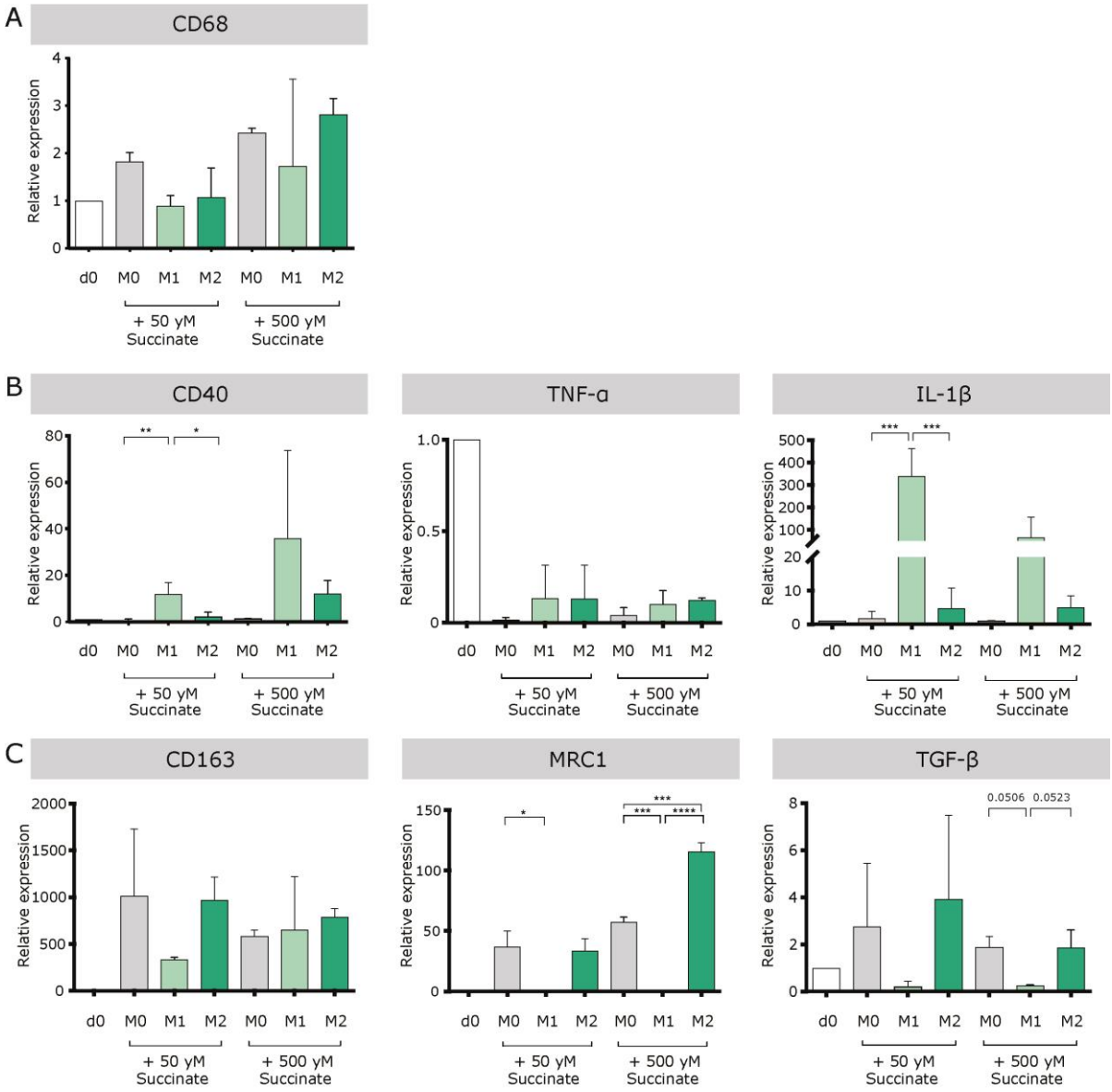

Figure 40. Expression of genetic marker genes of macrophage polarization in response to succinate treatment.

Macrophage marker expression after succinate administration A) CD68 shows no consistent pattern. B) *IL-1β* expression is highly upregulated in M1 macrophages upon succinate administration. C) M2 and anti-inflammatory marker expression are unaffected by succinate administration. All genes were normalized to *RPL13A,* as a housekeeping gene and analyzed in relation to d0. *≤ 0.05; **≤ 0.01; ***≤0.001; **** ≤0.0001 p-value. n=2-4, ANOVA.

4.4.3. Expression of SUCNR1 in macrophages

Signal transduction by succinate from cell to cell, has been proposed via the succinate specific G-protein coupled receptor (GPR91/SUCNR1) [112]. To evaluate the potential transcriptional changes of *SUCNR1* in macrophage differentiation and upon succinate administration, gene expression was analyzed. Expression increased upon monocyte to macrophage differentiation (16-fold M0 versus d0, 3-fold M1 versus d0 and 36-fold M2 versus d0, **Figure 41**) and was highest in M2 polarized macrophages with a 2.2-fold increase compared to M0 and a 11.3-fold increase compared to M1 macrophages. Upon succinate treatment, this pattern did not change significantly (**Figure 41B**). All differentiated macrophages displayed a slightly higher expression of *SUCNR1* when compared to undifferentiated but activated THP-1 monocytes (d0). M2 macrophages showed the highest levels of expression for both 50 µM succinate and 500 µM succinate administration (50 µM: 14.68 ± 20.04, 500µM: 19.51 ± 5.55). Hereby, 500 µM succinate administration induced a significant increase in SUCNR1 expression (M2 versus M0: 11.6-fold increase, M2 versus .M1: 13.07-fold increase). The same trend was visible with 50 µM succinate administration (M2 versus M0: 7.13-fold increase, M2 versus M1: 10.56-fold increase.

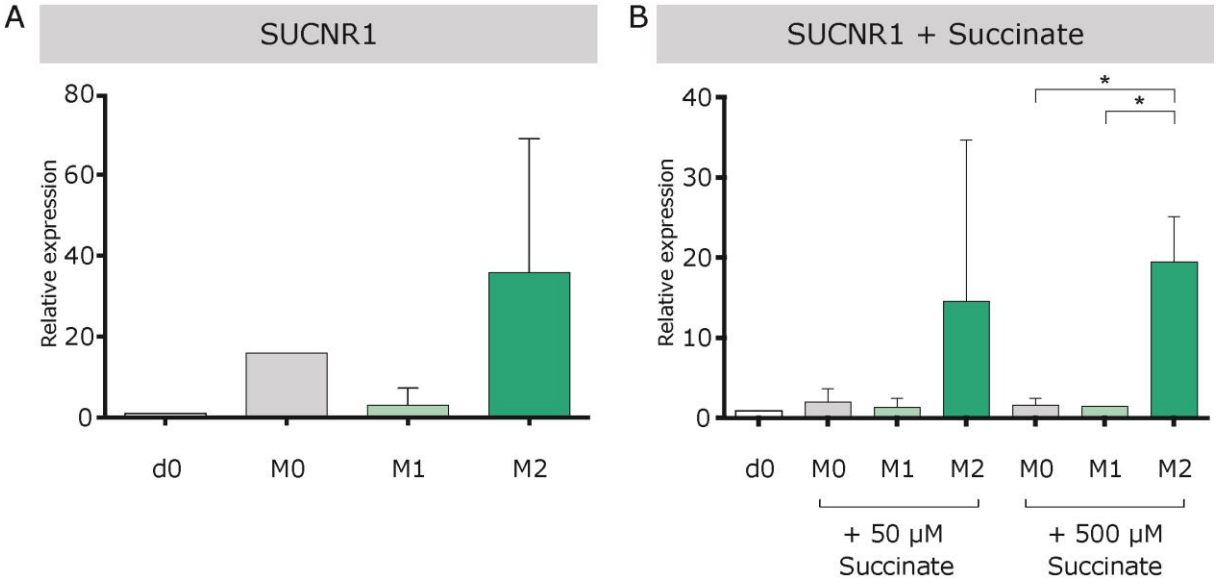

Figure 41. Expression profile of SUCNR1 in macrophages with and without succinate stimulation.

A) Differentiation of macrophages without succinate. B) Differentiation of macrophages stimulated with 50 µM and 500 µM succinate. Shown are THP-1 cells before treatment (d0), PMA activated THP-1 macrophages without further polarization at day 7: M0; PMA activated and polarized by LPS/IFNγ THP-1 macrophages at day 7: M and PMA activated and polarized by IL-13/IL-4 THP-1 macrophages: M2. SUCNR1 expression was normalized to the housekeeping gene *RPL13A* and analyzed in relation to d0.

*≤ 0.05 p-value. n=1-3, ANOVA.

4.4.4. Modulation of osteogenic differentiation by succinate application *in vitro*

Establishing a link between the metabolic signal succinate and cytokine expression in macrophages, evoked the question which other cell types, with central roles in fracture healing, might be susceptible to succinate modulation. One very recent paper by Peruzzotti-Jametti et al. shows that succinate accumulation in the cerebrospinal fluid derived from inflammatory macrophages can have a protective function in neuroinflammation, suggesting that succinate application or accumulation may also be beneficial in certain pathological conditions [258]. Current research further shows that succinate promotes *in vitro* angiogenesis in endothelial cells and that succinate pre-treated MSCs display increased cell migration and wound healing in a skin regeneration animal model [259, 260]. However, little is known so far about the role of succinate in fracture healing.

To investigate potential effects of succinate on fracture healing, osteogenic differentiation with human primary MSCs under the influence of succinate was conducted. MSCs from three different human donors were included in the investigations. Succinate was added to the culture medium in the same concentrations, as used for macrophage modulations: 50 and 500 µM. A schematic overview of the differentiation time-line is depicted below:

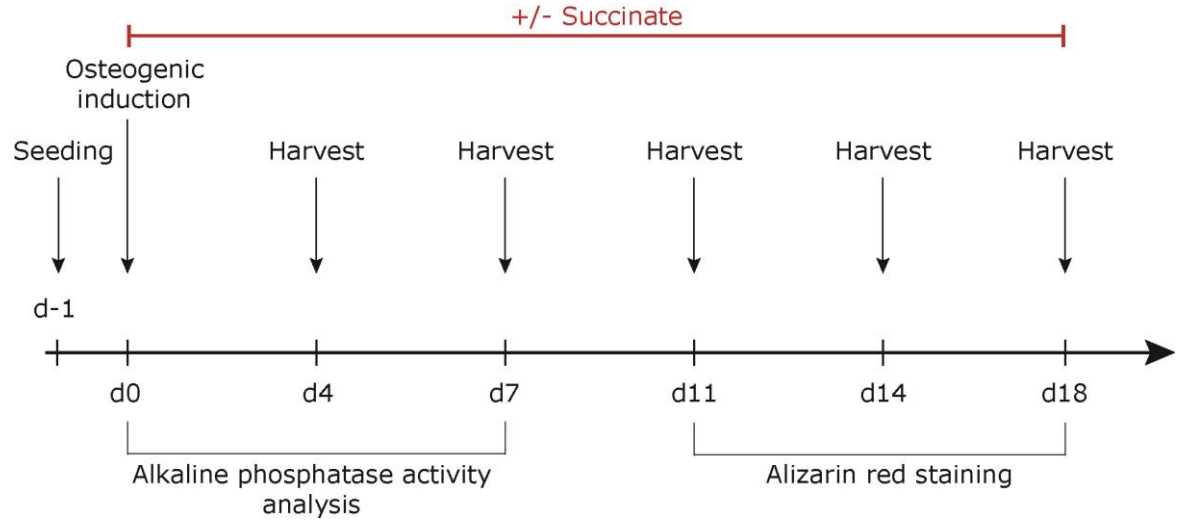

Figure 42. Schematic workflow of the osteogenic differentiation of MSCs with and without succinate treatment.

MSCs undergoing osteogenic differentiation showed a higher metabolic activity when succinate was added (**Figure 43**). Patient dependent differences in the time kinetics of cellular metabolic activity were noted; however, activity was increased upon succinate application for all patients, especially at later time points of differentiation. The unstimulated control displayed reduced metabolic activity compared to the treatment groups throughout the entire differentiation process. No major differences were noted for the treatment with 50 µM and 500 µM succinate.

Patient 1 showed a significantly higher activation for all time points tested, except day 11 in cells were 50 µM succinate was administrated (d4 - control: 1945.33 ± 51.45; 50 µM: 2134.33 ± 106.25; d7 – control: 2500.33 ± 166.87; 50 µM: 3864.67 ± 88.05). At say 14 and day 18 metabolic activity was significantly higher for both succinate concentrations (day 14 – control: 962.67 ± 55.34; 50 µM: 1580.33 ± 42.16; 500 µM: 1460 ± 30.67; day 18 – control: 608 ± 56.54; 50 µM: 1298.33 ± 13.05; 500 µM: 1243 ± 95.44).

Patient 2 showed a similar kinetic as patient 827, with both succinate concentrations showing significantly higher metabolic activity from day 4 onwards. The only difference between both treatment groups was at noticeable day 11, where application of 500 µM but not 50 µM succinate resulted in a significant difference to the control.

Osteogenic differentiation of patient 3 however, showed a different time kinetic in metabolic activity, with a continuous incline over the total differentiation process. Nevertheless and as observed for MSCs from the first two patients, metabolic activity was higher in the conditions with succinate treatment than in the control group from day 11 onwards (day 11 – control: 6632.33 ± 533.03; 50 µM: 9113.67 ± 279.79; 500 µM: 9278.67 ± 54; day 14 – control: 8006 ± 558.56; 50 µM: 10323 ± 166.58; 500 µM: 11197 ±171.75; day 18 – control: 12652.67 ± 1713.31; 50 µM: 15820.66 ± 1599.37; 500 µM: 18032.66 ± 702.67).

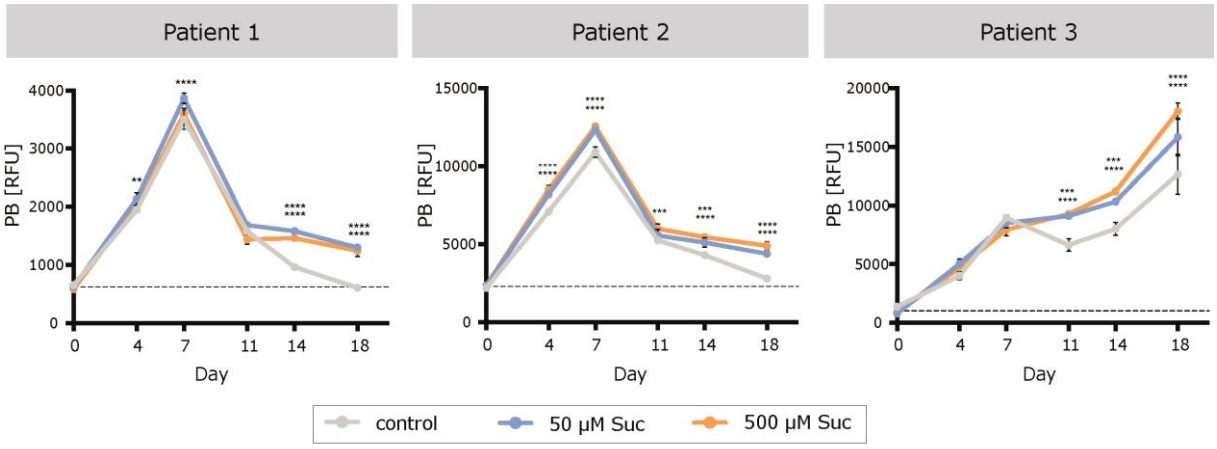

Figure 43. Metabolic activity of osteogenically differentiated MSCs with or without succinate administration.

Metabolic activity of osteogenically stimulated MSCs under succinate administration was assessed with a PrestoBlue® assay for three technical replicates per condition and time point. Controls were osteogenically differentiated without succinate treatment. Treatment groups include 50 µM and 500 µM succinate (Suc) administration to the osteogenic medium. RFU – relative fluorescent units. Statistical significance is indicated above the different days compared to control. Upper asterisk displays p-value for 50 µM, lower asterisk for 500 µM succinate groups. **≤ 0.01; ***≤ 0.001; ****≤0.0001 p-value. Two-way-ANOVA.

Next, ALP enzyme activity was assessed. ALP is involved in calcium and phosphorous matrix mineralization in bone and used as a frequent marker for bone formation [218]. MSCs showed higher ALP activity upon succinate treatment under osteogenic culturing conditions at day 7 compared to untreated controls. Increased activity was significant in two patients, while the third patient only showed a slight increase (**Figure 44**). Changes in control groups, matched by days and treatment, showed no significant alterations between the experimental groups.

In more detail, Patient 1 displayed minor changes in pNPP consumption or ALP activity between control and succinate treated groups at day 7 (control: 16.09 ± 0.57; 50 µM: 16.62 ± 0.47; 500 µM: 16.31 ±1.09). In contrast, ALP activity in MSCs in osteogenic medium from patient 2 significantly varied between control and succinate treatment at day 7 (control: 18.92 ± 0.86; 50 µM: 21.67 ± 0.81; 500 µM: 21.09 ± 1.54). This was also observed in MSCs from the third patient. Again, ALP substrate consumption, thus enzyme activity was significantly elevated in osteogenic culturing conditions with succinate treatment at day 7 (control: 11.57 ± 0.98; 50 µM: 13.21 ± 0.32; 500 µM: 13.72 ± 1.4).

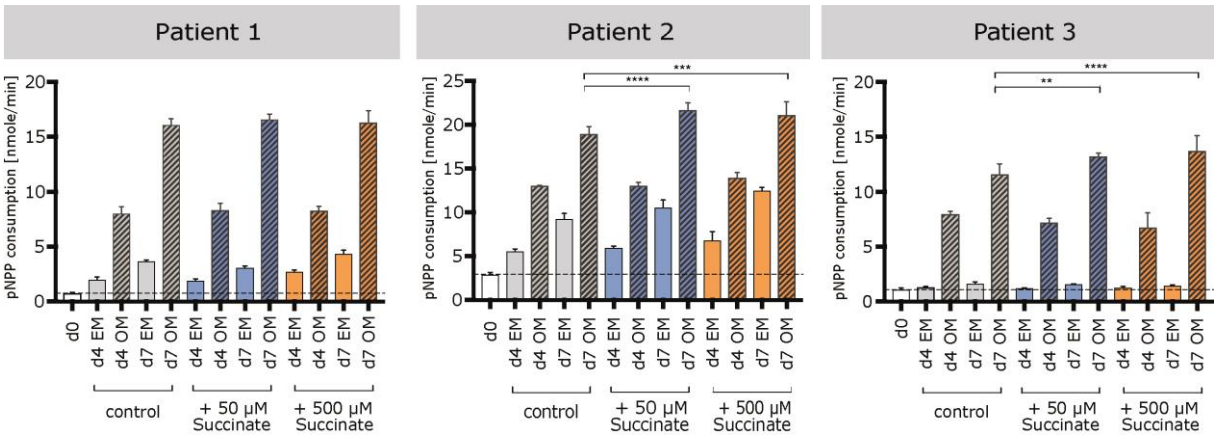

Figure 44. ALP activity in osteogenically stimulated primary MSCs treated with succinate.

MSCs of three human donors were cultured in osteogenic medium (OM) or expansion medium (EM) with or without succinate for 1 week. Succinate administration to the media enhanced ALP enzyme activity at day 7 in osteogenic conditions. Controls were cultured without succinate. Treatment groups include 50 µM and 500 µM succinate administration to EM and OM at all time points compared to controls without succinate treatment. Succinate administration to the media enhanced ALP enzyme activity at day 7 under osteogenic conditions. Three technical replicates were measured for each condition. **≤0.01; ***≤0.001; ****≤0.0001 p-value. ANOVA.

Successful osteogenic differentiation is further assessed by the extent of matrix mineralization at later time points. Visualization of the deposited mineralized matrices was achieved by alizarin red staining. MSCs from the three tested patients displayed different kinetics in mineralization speed and quantity, with MSCs from patient 1 and 2 showing a visible matrix mineralization already at

day 11 of differentiation, while MSCs from the third patient showed first calcium deposition within the matrix at day 14 (**Figure 45**). Nevertheless, all three patients presented increased alizarin red staining at day 18 when succinate was added. The most prominent effect of succinate treatment on matrix deposition was visible for patient 3 with 500 µM succinate administration, while patient 1 and patient 2, showed a more homogenous and thicker matrix upon succinate administration at day 18, irrespective of the succinate concentration added.

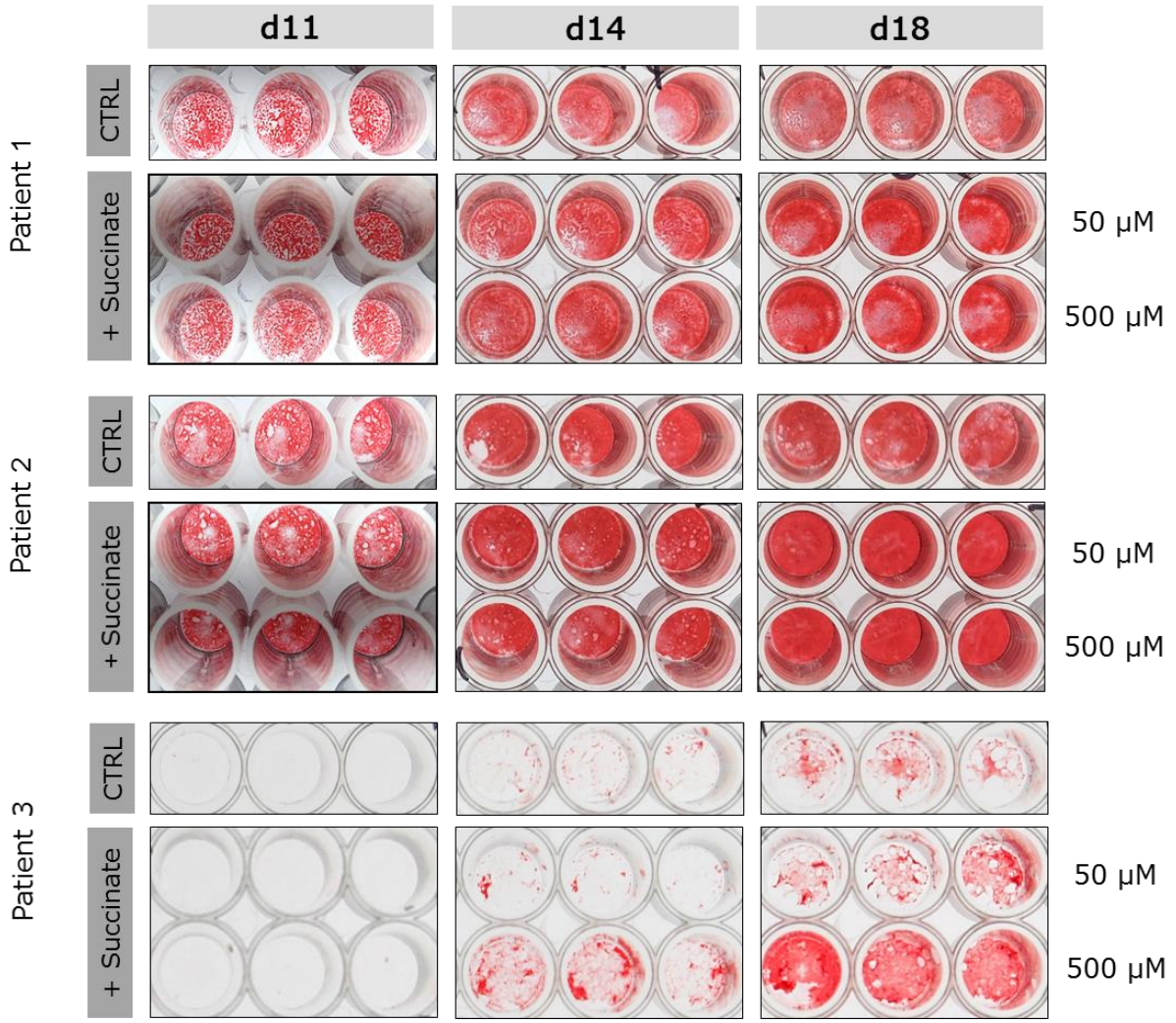

Figure 45. Alizarin red staining for matrix mineralization with and without succinate treatment.
MSCs from three human donors were stained after 11, 14 and 18 days of osteogenic differentiation. Each condition was run in triplicates in a 48-well plate. Control wells (CTRL) were treated with standard osteogenic medium; succinate treatment included 50 µM and 500 µM administration to the media. MSCs that were osteogenically stimulated with succinate showed an increase in calcium deposition within the matrix at day 18.

Alizarin red quantification analysis further revealed an increase of mineralized matrix from day 14 on for all patients upon succinate treatment. The effect at day 14 was strongest in the first and third patient while for patient 2 only 50 µM succinate administration resulted in a significant difference to the control (**Figure 46**). At day 18 both succinate concentrations showed significant higher calcium content in the matrix compared to the osteogenic differentiation without succinate administration. This effect was observed for all three patients. Succinate administration did not cause any effect in the non-osteogenic differentiation groups, treated with expansion medium.
Patient 3 showed the strongest response to succinate administration with an increase of 5.1-fold in mineralization for 500 µM succinate administration versus control at day 14. At day 18, the 500 µM group exhibited a 4.1-fold increase in matrix mineralization compared to control, while application of 50 µM succinate resulted in a 1.8-fold increase. Patient 1 demonstrated significant changes for both concentration at day 14 and 18. 50 µM and 500 µM succinate treatment showed a 1.5-fold increase at day 14, when compared to the control. At day 18 the fold change was significantly up by 1.2 and 1.3, respectively. Patient 2 only showed a significant response to 50 µM succinate administration at day 14. At day 18, both treatment groups exhibited similar, significant upregulations in matrix mineralization respective to the control (50 µM: 1.2-fold; 500 µM: 1.3-fold).

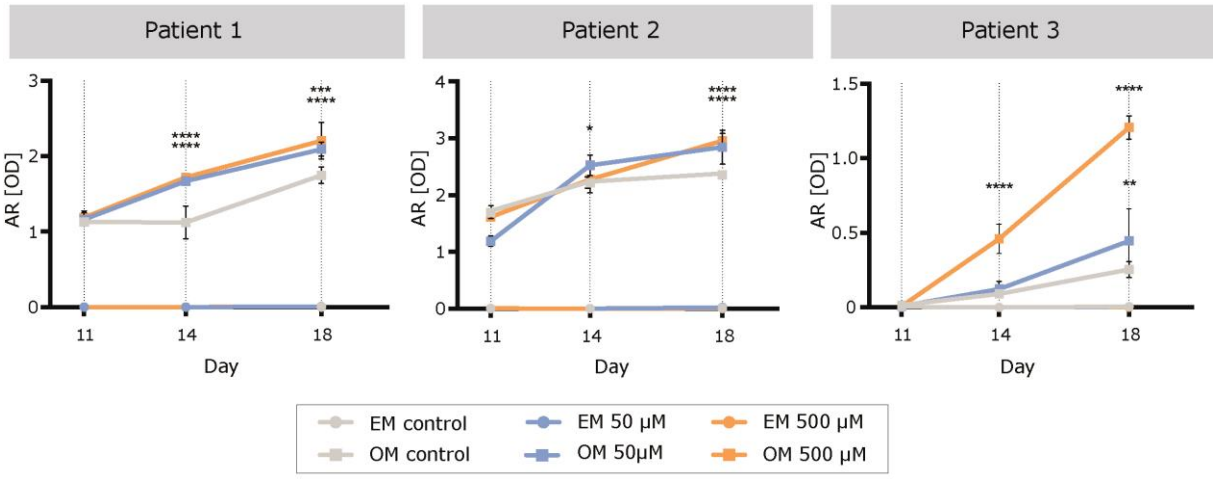

Figure 46. Matrix mineralization for osteogenic differentiation of human primary MSCs upon succinate treatment.

Calcium matrix was dissolved after alizarin red staining and quantified by absorbance measurement. Cells receiving expansion medium (EM) did not show increased matrix formation, while succinate administration increased matrix mineralization in all three patients. Cells undergoing osteogenic differentiation were cultured in osteogenic medium (OM), controls were cultured without succinate. Treatment groups were given 50 µM and 500 µM succinate to EM and OM for all time points. AR[OD]: alizarin red, optical density. Three technical replicates were measured for each condition and time. Asterisk lines represent statistical significance for the respective days, upper lines give the p-value for 50 µM succinate at a specific time, lower lines represent 500 µM. *≤0.05; **≤0.01; ***≤0.001; ****≤0.0001 p-value. Two-way-ANOVA.

Succinate treatment of primary human MSCs has proven to stimulate metabolic activity and subsequent ALP activity as well as matrix mineralization during osteogenic differentiation. Different responses and time kinetics could be observed between the three patients tested. However, succinate treatment resulted in an increased osteogenic response in almost all cases. This was especially true for the later time points day 14 and 18.

4.5. Summary

Using a rat 2 mm femoral osteotomy model to investigating the connection of metabolism and fracture healing in successful versus impaired healing conditions, it could be established that different metabolic pathways are engaged in a time-resolved manner as healing progresses. In addition, a differential metabolic regulation was observed between successful and impaired healing conditions, where impaired healing lacked increasing engagement of oxidative phosphorylation at day 14 of healing. Furthermore, accumulation of succinate, an intermediate of the TCA cycle, was found in fracture hematoma tissue of young rats showing successful fracture healing but not in aged rats, displaying impaired healing at day 7. Current research highlights diverse functions of succinate, besides that of a metabolic intermediate, making it an interesting target to study in regard to its cellular function and signaling properties during fracture healing. To study the effects of succinate in more detail further investigations were performed using two different *in vitro* models based on macrophages and MSCs, both relevant to processes of bone repair. It was possible to display effects of physiological succinate concentrations on processes like osteogenic differentiation and macrophage activity, which are important during fracture healing. On the one hand, it was shown that succinate was able to induce pro-inflammatory cytokine expression, like *IL-1β* in macrophages, thus influencing immune cell functionality. On the other hand, osteogenic culture of primary MSCs revealed that succinate administration enhanced alkaline phosphatase activity and matrix mineralization during osteogenic differentiation. The presented results suggest that paracrine signaling of succinate is an important regulator supporting successful bone regeneration.

5. Discussion

Bone regeneration is a well-orchestrated process, with a high demand for energy, nutrients and biosynthetic intermediates. Failure of fracture healing has been associated with impaired revascularization, prolonged inflammation and adverse biomechanical conditions [3, 8, 10, 44, 261-268]. The role of energy supply and metabolism during fracture healing has so far mostly been overlooked.

This thesis provides novel insights into the complex metabolic regulation of effective and successful fracture healing and in comparison reveals altered metabolic pathway activation in fractures of biologically impaired healing in rats. Changes in metabolism during the course of early fracture repair coincide with different healing responses, implying a strong connection between engagement of different metabolic profiles by cells and the progression of healing.

It could be validated that the TCA cycle intermediate succinate, can influence and shape the *in vitro* functionality of cells which take part in fracture repair. Specifically, succinate induced the transcription of *IL-1β* in pro-inflammatory macrophages and enhanced the osteogenic potential of human MSCs. This shows that metabolism plays a vital role during tissue regeneration and that metabolic intermediates hold the potential to act as signals supporting fracture healing progression by influencing the cytokine response and differentiation process in e.g. macrophages and MSCs.

5.1. Is the 2mm femoral osteotomy rat model an adequate system to study successful versus impaired fracture healing *in vivo*?

The model of impaired fracture healing in aged female rats as established by Kratzel, Preininger and Strube [194, 195, 221] was investigated in this thesis. Through application of histomorphometric analysis, increased tissue mineralization in young rats compared to aged rats was confirmed. Furthermore, higher levels of the angiogenic markers *PDGFα, PDGFβ* and *HIF 1α* in fracture tissue of young animals at day 3 and 7 were detected, likely leading to the increased development of vessels also detected in young animals. In parallel, upregulation of osteogenic genes was observed, whereas aged animals showed low expression of the osteogenic inducer gene *Wnt5α* and the bone matrix genes *Spp1* and *Col1α2.* Altogether, the results imply successful bone healing in young female rats already at two weeks after 2 mm femoral gap osteotomy. On the contrary, aged rats showed impaired bone healing, which was accompanied by prolonged blood clot persistence in the fracture gap, decreased bone mineralization and reduced revascularization of the fracture gap area. In particular, defective angiogenesis has been linked to poor fracture healing outcomes in clinical settings [264, 269], further validating our animal model as an appropriate system to study the *in vivo* mechanisms of defective bone regeneration.

5.2. Metabolic pathway engagement coincides with phases of fracture healing and shapes the fracture microenvironment

One central objective of this study was to determine the local metabolic profile of fracture healing under successful and impaired conditions. It was argued that altering levels of nutrients and metabolites within the local environment may lead to dysregulations in cellular responses, thus consequent impaired bone healing. The concept of metabolic reprogramming to adapt to limited nutrient availability or altered cellular energy demand is well established for tumor cells and has gained importance across the field of cellular biology, especially for cell differentiation and activation as seen in immune cells [96, 98, 148]. However, little research on this topic has been done in the field of tissue regeneration.

Differential regulation of several metabolites between fractures of young versus aged animals was identified beginning at day 7. Most prominent was the regulation of metabolites from the central carbon metabolism. At day 7, increasing levels of succinate were detected in the fracture hematoma of young animals. As metabolism is very dynamic, metabolite ratios give a good estimate about metabolic pathway activity. Not only increased levels of succinate were observed but also augmented succinate to fumarate ratios, implying succinate accumulation within the fracture microenvironment of successful healing at day 7. Accumulation of succinate within a cell or tissue may occur (1) during hypoxia, as the conversion of succinate to fumarate by succinate dehydrogenase is oxygen dependent, or (2) during increased TCA cycle replenishment by shuttling of α-KG into the TCA cycle towards succinate production [111, 122]. Succinate stabilizes HIF-1α by inhibition of HIF-α prolyl hydroxylase (PHD) leading to the transcription of angiogenic genes [253]. Concurrent with rising levels of succinate, an increase in angiogenic marker expression was observed in young animals between day 3 and 7, which also included *HIF-1α* transcripts. Additionally, greater numbers of newly formed vessels were detected. Lactate, another potent inducer of angiogenesis, also acts by stabilizing HIF-1α via PHD inhibition. This effect is particularly seen under conditions of aerobic glycolysis [103, 105, 270]. Although lactate accumulation in fracture hematoma of young animals did not reach statistical significance, when compared to aged animals at day 7, a trend of higher lactate levels was noticed in fracture tissue of young animals. Further evidence of a regulated lactate production in young animals was found in the lactate/pyruvate ratio. Increased lactate levels in regard to pyruvate corresponds to an increased amount of carbons shuttled into fermentation rather than the TCA cycle [229, 230], as seen for fracture tissue of young animals at day 7. In contrast, fractures from day 3 and 14 showed lower lactate/pyruvate ratios. Interestingly, this specific regulation was absent in fractures of aged animals, where the lactate/pyruvate ratio showed only minor differences between the investigated time points. Whether low local oxygen levels or aerobic glycolysis (Warburg effect),

are responsible for the lactate levels at day 7 of successful healing cannot be distinguished solely by metabolite levels. However, as young animals already show a distinct revascularization at this time point, enough oxygen provision can be assumed, thus aerobic glycolysis is a likely reasoning. The presented results suggest an effective coupling of angiogenesis and metabolic signals like lactate which initiate a cascade leading to the transcription of pro-angiogenic genes, a concept strongly highlighted and discussed in current research [235, 253, 271, 272]. Another interesting aspect is that vessel sprouting or branching by endothelial cells highly relies on glycolysis, even though the cells are exposed to high blood oxygen levels [162], indicative of the close connection of metabolism and angiogenesis. The data presented here proposes that successful fracture repair is connected to a metabolic shift, where succinate and possibly lactate accumulate and further act as signaling molecules to induce angiogenesis.

While there is strong indication of aerobic glycolysis as a main driver for fracture healing at one week after trauma, different metabolic pathways seem to underlie the healing cascade at the two week time point. Accumulation of pyruvate, citrate, α-KG, glutamate and diminished succinate/fumarate and lactate/pyruvate ratios, in tissue from fractures of young animals, imply the engagement of the full TCA cycle and a high demand for biosynthetic building blocks [273, 274]. Pyruvate connects glycolysis with the TCA cycle by conversion to acetyl CoA, which can enter the TCA cycle by forming citrate [275]. Citrate is an important intermediate, as it provides biosynthetic precursors for fatty acid synthesis and sterols [79]. Besides replenishing the TCA cycle, α-KG and glutamate are used to form glutamine and purine nucleotides [276]. Glutamate further serves as a precursor for proline and other amino acids [277]. Increased levels of the glycolytic intermediate 3PG give further evidence of amplified amino acid biosynthesis, as 3PG can be transformed into 3-phosphohydroxypyruvate (3PHP) by PHGDH, thus entering the serine synthesis pathway and fueling the one-carbon metabolism [77] (supporting data in supplement, I.a, **Supplement figure 1**). The one-carbon metabolism not only supports amino acid biosynthesis, but also the production of nucleotides [78]. Cell proliferation is particularly dependent on nucleotide synthesis and certainly important during regenerative processes.

A particularly interesting finding was detected when investigating the lactate to glucose ratio. The highest ratio was not found in the sampled fracture tissue but in contralateral, unfractured femoral bone from rats. Despite the high standard deviation, the data suggests strong activation of the lactic fermentation pathway as part of the metabolic homeostasis in unfractured and healthy bone tissue. Stem cell populations of HSCs and MSCs reside within the bone marrow. Work from several groups has emphasized on the importance of a hypoxic microenvironment within the stem cell niche for the cells to maintain their stemness [148, 233]. The increased lactate-derived-from-glucose production in unfractured bone may reflect this hypoxic microenvironment

of healthy bone marrow. Even though transient oxygen deprivation occurs during fracture healing, oxygen tension in the bone marrow is usually low. Several studies and mathematical modeling work have determined that the oxygen level of the bone marrow lies between 1 – 8%, depending on the site (1 – 6% for hematopoietic stem cell niche and 2 – 8% for mesenchymal stromal cell niche [278]). During fracture healing oxygen levels range between 5% immediately after fracture and 2% after 1 week [265, 279], quite similar to what is generally seen in the bone marrow. This provides further evidence that low oxygen levels may not be the sole factor inducing transcriptional profiles for e.g. angiogenesis during facture healing but that a second signal – possibly metabolically induced – may be needed.

5.3. Time-resolved protein profiling reveals molecular processes for successful and impaired healing fractures

The protein data obtained from untargeted proteomic analysis were in line with the determined metabolite profiles and gave additional evidence to some speculations about metabolic pathway engagements. While the metabolic profile seen in young animals at day 14 strongly suggested a full TCA cycle activation and the increased vascularization of the facture gap suggested oxidative metabolism engagement, protein data analysis confirmed an upregulation of proteins involved in oxidative phosphorylation under successful healing conditions. Mitochondrial respiration and oxidative metabolism are central characteristics of anti-inflammatory or regulatory cells and cells involved in tissue regeneration [53, 73, 98, 280].

A condition frequently leading to non-unions is an altered inflammatory phase. Research during the last years has elaborated the importance of inflammation on successful bone regeneration [40]. Depleting inflammatory immune cells during the initial phase of fracture healing leads to diminished regenerative capacities [54, 55].On the other hand, increased inflammatory signaling also hinders fracture healing, as seen in patients with an increased ratio of $CD8^+$ T_{EMRA} cells, who have a higher susceptibility for developing fracture non-unions [9]. Consistent with what is experienced in the clinic, analysis of the proteome showed elevated levels of pro-inflammatory molecules in the fracture tissue of impaired healing conditions in aged rats in our animal model.

Although fracture healing and non-unions have been studied quite intensely in various animal models and settings [3, 9, 10, 37, 39, 55, 63, 136, 194, 195, 279, 281-283], the proteomic analysis performed during this work dissected the molecular processes of fracture healing in a time-resolved manner. This was achieved for successful fracture healing as well as for impaired fracture healing. Processes and pathways activated during successful fracture healing displayed a

standard response to injury, with a high activation of immune processes during the earliest time point investigated and increased protein processing and ECM production at day 7. A striking finding was the high abundance of metabolic proteins measured in fracture tissue, as well as the distinct metabolic profile one could derive for the individual days and stages of the healing process. Those corresponded well with the analyzed metabolites levels, e.g. indicating high engagement of oxidative phosphorylation, which implies rising oxygen levels and increased regenerative processes at day 14 in successful healing.

Impaired fracture healing showed a more diverse regulation, especially in proteins involved in ECM and cytoskeletal assembly, indicating a dysregulation on this level compared to successful healing. Interestingly, different fiber orientation was observable in most of the histology slides from aged fracture tissue. Instead of creating a parallel bridge between the bone entities as observed in successful healing, the tissue fibers showed perpendicular alignment. Assembly and linkage of newly synthesized ECM proteins are important factors during wound healing. Fibronectin, an important glycoprotein of the ECM, is globular when secreted, its fibril end-confirmation is induced by contraction processes [284-286]. Matrix contraction, mediated by cells (e.g. fibroblasts) and matricellular proteins (vitronectin, tenascin etc.), is a crucial step in wound closing and progression of tissue regeneration [287-290]. The significance of proper ECM assembly and contraction becomes even more apparent as impairment of these results in fibrotic scar tissue formation [237, 291].

Another difference that marked impaired fracture healing was the absence of enrichments of oxidative metabolism in later stages of healing (day 14). In contrast to successful healing, this lack of oxidative metabolism together with lower vessel numbers (from histological data) may partially account for the observed impairment in healing progression. Instead, upregulation of amino acid, folate and heme metabolism was detected.

Together, these results highlight the interplay of immune responses, metabolic pathways, and ECM synthesis as well as contraction for bone regeneration. Metabolism can influence inflammation and immune cell activation, this further effects ECM synthesis and healing progression; it is vital to understand this connection, in order to fully understand regeneration. As this was a descriptive analysis, the results do not explain those underlying causalities. This limitation was addressed partially by performing *in vitro* experiments. However, further comprehensive studies need to be done to mechanistically understand this complex network.

5.4. Altered inflammatory/immune-axis between successful and impaired healing

The immune response is a crucial factor for every healing process and the amount of immune cells and subsets can influence healing progression and outcome. Investigation of immune marker gene expression showed higher levels of monocytes and macrophages in successful healing at the early days, which at day 14 shifted towards higher numbers in impaired healing. Although higher presence of monocyte/macrophage markers was seen in young animals during the early time points, they were accompanied by expression of anti-inflammatory markers (*CD163, IL-1Ra,* [118, 237]). At the same time, pro-inflammatory markers, like *CD80, CCR7* and *TNF-α* [236] were upregulated in aged animals, which matched the higher pro-inflammatory signals obtained for impaired healing from the proteome analysis.

The expression pattern of *CD80* and *CD163,* representative for M1-like and M2-like macrophages, showed a decreasing expression from day 3 to day 7 and increasing expression towards day 14. This two-waved pattern has already been observed for T cell and B cell migration into the fracture callus during healing [136]. Macrophages play an important part throughout healing processes [292]. The first recruitment is immediately after injury, inducing pro-inflammation. A phenotype switch from pro-inflammatory to anti-inflammatory macrophages is significant for resolving the local inflammation and promoting tissue repair [55]. Pro- and anti-inflammatory macrophages are present in wound tissue during vessel development and tissue ossification, their deletion during these later phases of healing results in a significant decrease in callus formation, impaired vascularization and reduced ossification, marking their pivotal role during all steps of healing [54, 293, 294].

It is noteworthy that the expression of monocyte and macrophage markers showed a remarkable upregulation in fracture tissue of impaired healing at day 14. *CD14*, *CD80* and *CD163* expression matched the biphasic pattern, as just discussed. However, significantly higher expression of *CD14*, *CD80* and *CD163* was detected compared to successful healing. The expression of *CD68* particularly increased in impaired healing at day 14, all together suggesting a massive activation and migration of macrophages into the callus. While macrophages are present during most phases of fracture repair and strongly participate in physiological wound resolution, prolonged or excessive macrophage activity may hinder healing and promote chronic wounds [119, 295]. Artificial local amplification of pro-inflammatory macrophages during the first days of fracture results in impaired fracture healing [296-298], as does systemic inflammation [299, 300]. A fine-tuned sequence of different macrophage subtypes from pro-inflammatory (M1-like) to various anti-inflammatory and tissue resolving (M2-like) types is needed for effective tissue and fracture

healing [301]. Any disturbances may lead to retardation of the healing process and in worst cases development of chronic wounds or excessive scar formation [119, 302].

The difference in expression of MMPs between successful and impaired healing is also remarkable. MMPs not only play an important role in ECM degradation and assembly but also substantially take part in other important processes during tissue development and regeneration, as has been established for MMP-2 and initiation of angiogenesis [303]. Young animals show higher *MMP-2* expression at day 3 and day 7 and a subsequent increase in vessel number at day 7 and 14 (**Figure 18**). MMP-9 recruits endothelial progenitor cells to sites of vessel development and may further promote vessel maturation as shown in studies investigating neuroblastoma [304-306]. In a zebrafish model of tissue regeneration after acute wounding, depletion of MMP-9 leads to diminished leukocyte infiltration into the wound area and reduced collagen fiber thickening [307], showing that MMP-9 is a significant modulator of tissue repair. Its expression is highly induced at day 7 and day 14 during both successful and impaired healing conditions. However, *MMP-9* expression levels in successful fracture healing surpass those measured in impaired healing by a large proportion.
Macrophages are a major source of MMPs and especially MMP-2 and MMP-9 derived from M2 macrophages promote angiogenesis and display higher proteolytic activity than MMPs derived from M1 macrophages, as investigated in cancer models [239, 308]. Together MMP-2 and MMP-9 dampen inflammation by a regulatory loop and induce the activation of TGF-β and VEGF [309]. MMP-9 is further involved in the shredding of the LPS receptor CD14, thus reducing the ability to transduce a pro-inflammatory signal [310]. Distinct regulation of both MMP-2 and MMP-9 seems important for fracture healing. On the contrary, expression of *MMP-13*, a collagenase that degrades helical collagen fibers instead of fragmented collagen, like MMP-2 and -9, is not altered extensively between successful and impaired healing, suggesting a deregulation of gelatinase (MMP2/9) levels and their activation, potentially induced by altered macrophage populations in impaired bone healing compared to successful healing.

Further assessment of the inflammatory milieu of successful versus impaired healing fracture hematoma was performed using a multiplex approach. Regrettably, only a small fraction of the cytokine analytes included in the array could be detected and statistically evaluated. Nonetheless, the detectable cytokines (MCP-1, M-CSF, IL-1α) originated from innate immune signaling, specifically monocyte/ macrophage signals. MCP-1, needed to induce MMP-9 in macrophages showed higher levels in successful healing for all time points [311]. At the same time, MCP-1 is a central signal in initiating macrophage responses in wound healing and reduced MCP-1 levels observed in non-healing diabetic wounds are associated with impaired macrophage activation. Adding MCP-1 to diabetic wounds restores macrophage responses and enhances healing [312].

M-CSF and IL-1α also displayed higher concentrations in the early days of successful bone repair. Similar to MCP-1, M-CSF is necessary to induce macrophage responses in healing and its deletion substantially impairs the healing capacity [313]. Furthermore, M-CSF polarizes macrophages towards an anti-inflammatory state [244, 314]. IL-1α, although low in acute wounds is upregulated upon sterile inflammation (after injury or trauma) [315, 316]. It is of interest that IL-1α levels are very low in aged fractures after injury but increase at day 14. As IL-α is high in chronic wounds, this may be a further indicator for the transition towards chronic inflammation and impaired healing in fractures of aged rats [317].

Recapitulating the major findings from the inflammatory characterization of successful versus impaired fracture healing: imbalance of the early inflammatory and immune response was observed in impaired fracture healing. Particularly, an imbalance of the monocyte/macrophage axis. This is further supported by the detected accumulation of succinate in fracture tissue of young animals at day 7, a prominent feature of pro-inflammatory macrophage's activation [252]. Succinate has increasingly attracted attention during the last years, as it holds properties of a signaling molecule and even a succinate-specific GPCR – GPR91 or SUCNR1 - has been discovered [318, 319].

5.5. *In vitro* application of succinate shapes macrophage cytokine transcription and osteogenic differentiation potential of MSCs

Upon stimulation, monocytes/macrophages undergo considerable metabolic reprogramming, in parallel to their phenotype adaptation [122]. If LPS is the central stimuli, macrophages will develop towards a pro-inflammatory phenotype and accelerate glycolysis accompanied by rising levels of succinate [111, 252]. This is achieved because LPS stimulation induces itaconate production by the immune responsive gene 1 (IRG1), which is necessary to mount anti-microbial defense mechanisms. Itaconate also inhibits SDH; therefore succinate accumulates [320]. On the other hand, increased TCA cycle replenishment over αKG may further lead to rising levels of intracellular succinate [123]. Intracellular succinate acts as a signaling molecule, and stabilizes HIF-1α thus inducing angiogenic signaling; moreover, it induces the transcription of *IL-1β*. Succinate can further promote signals in a paracrine manner, as the discovery of its specific receptor SUCNR1 uncovered and is involved in posttranslational protein modifications via succinylation [321]. Intensive research has established succinate as a marker for inflammation and associated it with several disease pathologies such as ventricular hypertrophy, cardiac ischemia reperfusion injury and rheumatoid arthritis [247, 322-325]. In several tumors, SDH is mutated leading to an abrogation of the TCA cycle and accumulation of succinate. Within the

tumor microenvironment succinate is regarded as an oncometabolite and a driver of tumorigenesis [326].

Despite the impressive evidence of succinate inducing pro-inflammation and aggravating disease conditions, an additional physiological mechanism may exit, putatively influencing fracture healing, as succinate is accumulated in fracture tissue of successful bone regeneration at day 7. Therefore, THP-1 monocytes were activated towards macrophages and consecutively polarized into M1-like or M2-like macrophages. Gene expression and cytokine secretion showed the expected patterns for M1 or M2 polarization. Therefore, macrophage differentiation with succinate administration to culturing media was conducted. Succinate administration was hypothesized to influence macrophage phenotypes and polarization. Results confirmed that succinate administration or accumulation induced high transcription of *IL-1β* in LPS/IFNγ polarized macrophages, in line with data by Tannahill [111]. However, no additional major changes in the macrophage marker expression were observed, indicating that succinate here acts primarily as an amplifier of *IL-1β* expression in *in vitro* polarized pro-inflammatory macrophages.

Succinate also stimulates migratory behavior, pro-inflammatory gene expression and T cell activation by dendritic cells [247]. This effect is mediated over the GPR91, also termed SUCNR1. Rubic and colleagues reported that SUCNR1 expression dramatically increases upon differentiation from monocytes to immature dendritic cells [247]. A similar pattern was noticeable for monocyte-macrophage differentiation presented in this thesis. Upon activation and differentiation towards macrophage subtypes, expression of *SUCNR1* increased. Interestingly, this effect was strongest in IL-10/IL-4 polarized macrophages with and without extracellular succinate treatment. The data suggest that although no changes in macrophage polarization marker expression were observed, M2-like macrophages may still be susceptible to succinate signaling. Moreover, macrophages cultured in media with extracellular succinate administration appeared to detach increasingly from the culture flask when compared to culturing and differentiation without succinate (no data shown).This may be an indicator for succinate-induced migration, which is reported for dendritic cells [247]. Whether there is an altered migratory behavior in macrophages, M2-like macrophages are sensitive to succinate signaling, and whether this is a mechanism important under physiological or pathological conditions, needs to be addressed by more detailed and in-depth investigations.

As a next question it was addressed if succinate could mediate paracrine signals e.g. from macrophages to other cells within the fracture hematoma. MSCs incorporate vital properties during fracture healing, as they can differentiate into osteogenic, chondrogenic and adipogenic lineages [327]. One study recently published, showed that succinate treatment induced human MSC migration by enhancing F-actin reorganization, which improved skin wound healing *in vivo* [328]. This effect of extracellular succinate application was mediated over SUCNR1.

The concentrations of succinate that induced MSC migration were within the physiological range, similar to the ones used in this thesis. The experiments investigating the effect of succinate treatment on osteogenic differentiation of MSCs showed that succinate has a positive effect on their osteogenic differentiation potential. Increased alkaline phosphatase activity of succinate treated and osteogenically stimulated cells was observed; further elevated matrix mineralization upon extracellular succinate administration was noted. Additionally, increased metabolic activity of osteogenically stimulated MSCs was noted that were additionally treated with succinate. This was true for most days during culturing, although differences in donors were seen. A possible explanation for the higher osteogenic differentiation upon succinate treatment might be the observed elevation in metabolic activity, where succinate fuels metabolism and respective biosyntheses.

As discussed earlier, many signaling properties of succinate are mediated by ligation of its receptor – SUCNR1. To test whether extracellular succinate treatment influenced *SUCNR1* expression in osteogenic differentiation, a respective gene expression analysis was performed. The data obtained showed diverse responses between the different donors and no consistent conclusion could be drawn. The receptor was expressed in most conditions although quite low transcript numbers were observed. At this point, it can neither be confirmed nor excluded, if the positive effect of succinate on osteogenic differentiation is mediated over SUCNR1. Further work, e.g. protein determination or receptor inhibition needs to be done to further elucidate the mechanism by which succinate acts on osteogenic differentiation and tissue regeneration.

5.6. Succinate: a link to the second peak of *IL-1β* expression in fractures and induced tissue mineralization?

There are additional conceivable mechanisms, which may link succinate to bone regeneration. As shown during this thesis and substantially by the work from others, succinate administration or accumulation leads to high transcriptional induction of *IL-1β* in pro-inflammatory macrophages [111, 252]. IL-1β is an important modulator during fracture healing and shows a bimodal expression pattern. The first peak promotes migration of immune cells into the hematoma, while the second peak occurs during the soft callus phase and regulates callus remodeling [282, 283]. Mumme et al. investigated the effect of low dose IL-1β on osteogenic differentiation of bone marrow MSCs [329]. They showed that IL-1β in concentrations from 50-1000 pg/ml induced higher matrix mineralization and enhanced cartilage remodeling.

Remarkably, gene expression analysis of *IL-1β* in fracture tissue of young animals showed a significant increase of transcripts at day 14 compared to aged fractures (**Figure 47**). This increase in *IL-1β* expression is seen in a time-series manner after succinate accumulation at day 7.

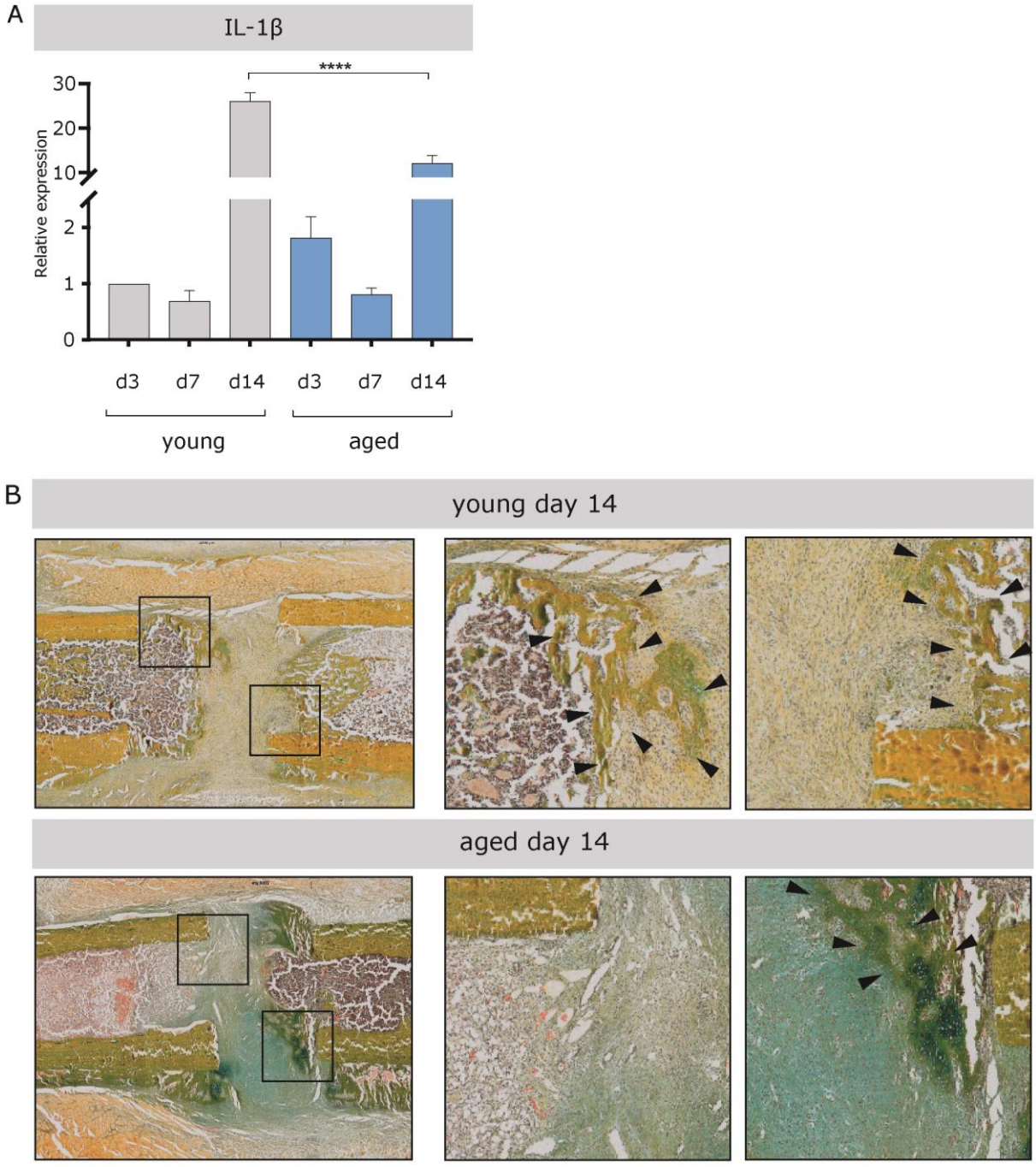

Figure 47. IL-1β expression levels in fracture healing coincides with tissue mineralization content.
A) IL-1β expression in fracture tissue of young and aged rats showed a significant increase at day 14 and between young and aged. Gene expression was analyzed in relation to the housekeeping gene *Tbp* and d3 young. B) Histological assessment of mineralized tissue at day 14 in the fracture gap of young and aged rats. Young rats show more tissue mineralization (yellow color), while fractures of aged rats show areas of unmineralized cartilage (blue-greenish color). Movat pentachrome staining. Mineralized tissue is marked by arrows *≤0.05 p-value, n=3-6, ANOVA.

Low dose IL-1β administration (0.1 ng/ml and 10 ng/ml) during osteogenic differentiation of human MSCs however, showed no increase in ALP activity and matrix mineralization in preliminary studies (**Figure 48**). Microscopically, higher cell contraction was observed under

IL-1β treatment and micrographs showed enhanced mineral nodule formation at day 4, which was not accompanied by higher ALP activity or matrix mineralization. Further investigations are needed to disentangle the underlying mechanisms, and determine if succinate induced *IL-1β* expression indeed positively influences the progression of bone regeneration as hypothesized.

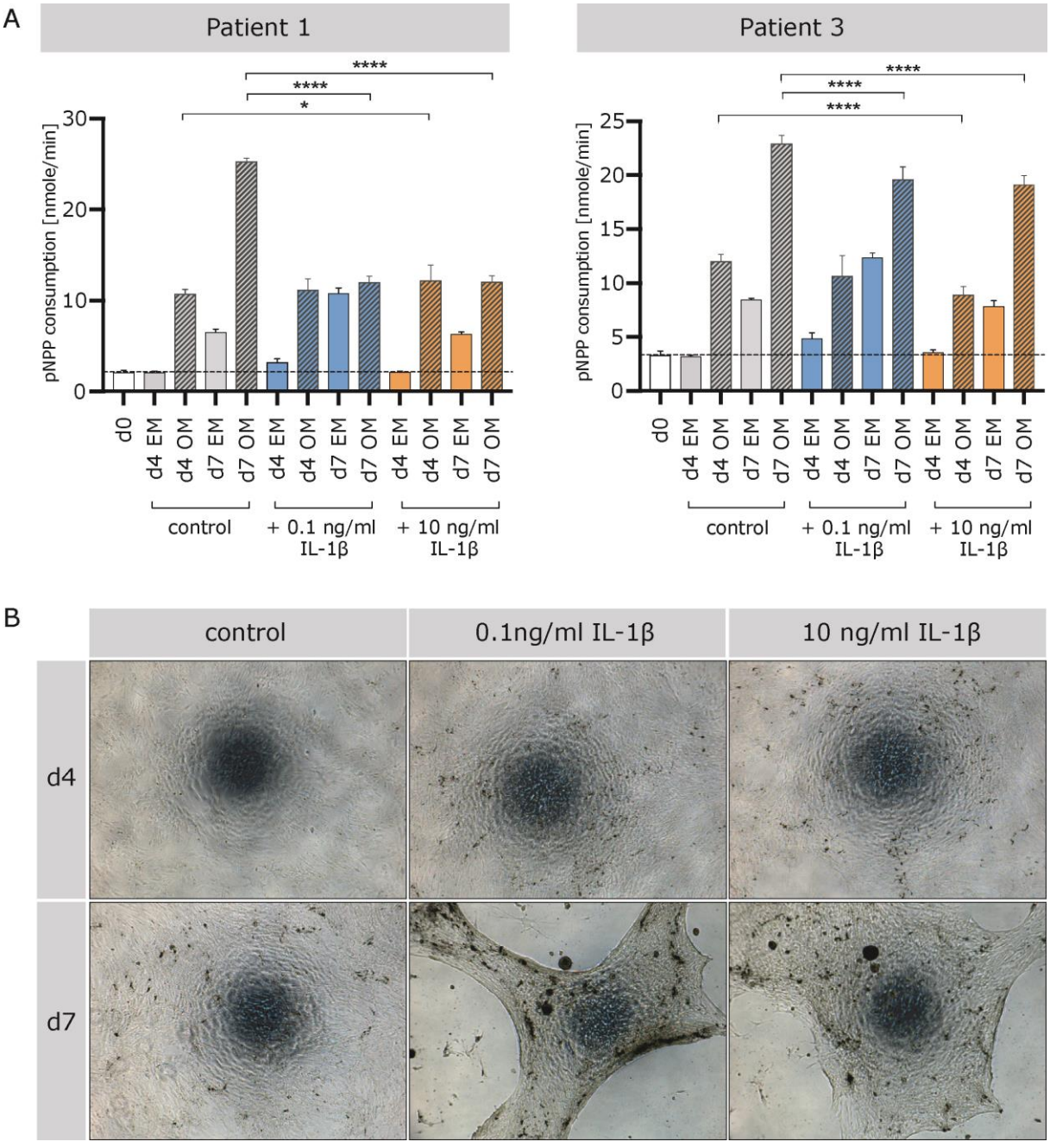

Figure 48. Osteogenic differentiation of primary human MSCs under the influence of low dose IL-1β. Human MSCs treated with low doses of IL-1β (0.1 ng/ml and 10ng/ml) show an increased number of mineral nodules during osteogenic differentiation compared to untreated osteogenic MSCs but show a clear reduction of ALP activity. A) ALP activity measured by nmole/min pNPP consumption at day 0, day 4 and day 7 with and without IL-1β administration. B) Light microscopic images of MSCs during osteogenesis. * ≤0.05; ****≤0.0001 p-value. n=3 technical replicates, One-way ANOVA.

5.7. Linking *in vitro* evidence with *in vivo* observations

The presented results underline potential connections of metabolic pathway engagement and their implications on tissue repair in the 2 mm femoral osteotomy model of successful versus impaired bone healing. Succinate, often seen as a booster of pro-inflammation, was identified as a promising mediator of metabolic signals promoting endogenous tissue repair. This notion is supported by recent reports of succinate aiding regeneration progression [328, 330]. One key study by Peruzzoti-Jametti and colleagues showed that succinate derived from inflammatory macrophages suppressed chronic inflammation in neurons [258].

A hypothetical mechanism of succinate signaling in the context of fracture healing may be as follows. Succinate accumulation, possibly induced by/in macrophages, (1) enhanced osteogenic differentiation from immigrating MSCs and (2) locally boosted a second peak of *IL-1β* transcription, thus regulating callus maturation, as indicated by the increased tissue mineralization detected in successful healing fractures at day 14. Furthermore, succinate (possibly together with lactate) accumulation metabolically induced a pseudohypoxia, independent of the actual oxygen levels present in the fracture tissue, stabilizing HIF-1α and promoting angiogenesis. The increased number of vessels from day 7 to day 14 in successful healing fractures, after succinate accumulation at day 7 may serve as additional evidence for this theory.

Primary human umbilical vascular endothelial cells upregulate motility, proliferation and tube formation *in vitro,* after exposure to succinate [259]. In the same publication, Mu and colleagues further demonstrated that succinate treatment was able to induce blood vessel formation *in vivo* in a model of transgenic zebrafish, by upregulation of VEGF expression [259]. Although this mechanistic regulation was not fully demonstrated during the work of this thesis, increasing levels of tissue succinate followed by higher vessel numbers and tissue mineralization is an encouraging indication.

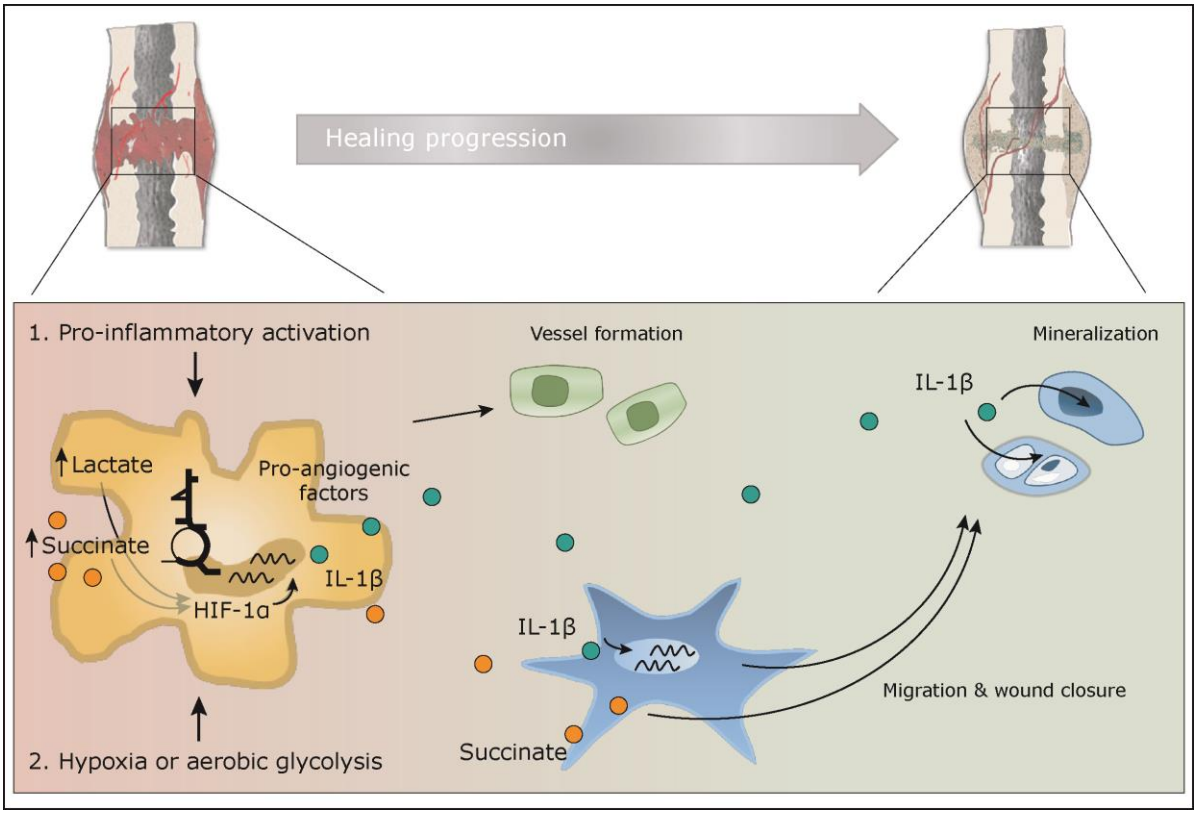

Figure 49. Hypothetical auto-and paracrine signaling mechanisms of succinate within the fracture microenvironment contributing to bone healing progression.

Succinate accumulates e.g. in macrophages following activation, hypoxia or aerobic glycolysis and leads to HIF-1α stabilization. This activates the transcription of angiogenic factors (e.g. VEGF) and induces vessel formation. HIF-1α further induces the transcription of IL-1β, which induces migration of MSCs to the injury site. IL-1β additionally induces callus maturation and mineralization. MSCs are also stimulated by succinate to migrate towards injury sites.

5.8. Limitations and outlook

This work is, to the best of my knowledge, the first to measure metabolic profiles of fracture healing stages and different healing conditions and to suggest that different regulation of metabolism is most likely connected to fracture healing outcome. Cellular metabolism has gained increasing attention over the last years – especially in cancer research and immune cell functionality [74, 84, 94, 96, 98, 161, 326, 331] – knowledge about its implications on healing processes however, is still at its very beginning. Here, the presented work showed that metabolic intermediates – e.g. succinate – may shape the microenvironment of fractures and contribute to the endogenous healing cascade by inducing the transcription of e.g. cytokines or growth factors.

Although this work started in an *in vivo* rodent animal model of fracture healing, the following *in vitro* studies were performed with human primary derived cells and a human cell line under the influence of extracellular succinate administration, bridging the concept of metabolic signaling in tissue regeneration from rats to the human system.

We are just starting to understand the profound connections between metabolism, matrix maturation and cellular function. More work needs to be done to unravel the exact mechanisms by which metabolites support healing processes and communication between the cells involved in repair cascades. In the here presented case, succinate may act as a positive signal supporting fracture healing. It is crucial to further dissect by which mechanism succinate transmits signals to e.g. macrophages and MSCs present in the fracture callus. Protein analysis of the receptor SUCNR1 and its subsequent knock down or specific inhibition e.g. by a small molecule [332, 333] will give more reliable insights on the therapeutic actions of succinate mediated over SUCNR1. Furthermore, extending the work to primary monocytes/macrophages and performing co-cultures of e.g. MSCs and macrophages pretreated with succinate will result in a better estimate of the *in vivo* regulation and mode of action of succinate during fracture healing.

As metabolism is highly dynamic and can adapt to environmental changes within minutes or even seconds, follow-up research questions, that investigate the metabolic profile of cells active during regeneration, should also contain carbon-tracing experiments which renders in-depth information about metabolic pathway activity and carbon/energy flow.

Though metabolism is now appreciated as an intersection to many cellular and physiological processes and research investigating metabolism and tissue responses to wounding, inflammation and regeneration has picked up in recent times, the specific crosstalk of immune and stromal cells in tissue repair is still unclear. Especially, knowledge on which level metabolic and molecular changes induce cell proliferation, inflammation, successful tissue regeneration or scar formation, is scarce as highlighted by a recent review from Eming and colleagues [235].

Metabolic crosstalk of cells and effects of metabolism on cellular function represents a new aspect to be considered when conducting research in the field of regenerative medicine and holds great potential for future therapeutic applications.

6. Bibliography

1. Kanis, J.A., et al., *A systematic review of hip fracture incidence and probability of fracture worldwide.* Osteoporosis International, 2012. **23**(9): p. 2239-2256.

2. Requena, G., et al., *Incidence Rates and Trends of Hip/Femur Fractures in Five European Countries: Comparison Using E-Healthcare Records Databases.* Calcified Tissue International, 2014. **94**(6): p. 580-589.

3. Einhorn, T.A. and L.C. Gerstenfeld, *Fracture healing: mechanisms and interventions.* Nat Rev Rheumatol, 2015. **11**(1): p. 45-54.

4. Tzioupis, C. and P.V. Giannoudis, *Prevalence of long-bone non-unions.* Injury-International Journal of the Care of the Injured, 2007. **38**: p. S3-S9.

5. Nandra, R., L. Grover, and K. Porter, *Fracture non-union epidemiology and treatment.* Trauma-England, 2016. **18**(1): p. 3-11.

6. Zura, R., et al., *Epidemiology of Fracture Nonunion in 18 Human Bones.* Jama Surgery, 2016. **151**(11).

7. Hernlund, E., et al., *Osteoporosis in the European Union: medical management, epidemiology and economic burden.* Archives of Osteoporosis, 2013. **8**(1-2).

8. Schmidt-Bleek, K., et al., *Boon and Bane of Inflammation in Bone Tissue Regeneration and Its Link with Angiogenesis.* Tissue Eng Part B Rev, 2015. **21**(4): p. 354-64.

9. Reinke, S., et al., *Terminally Differentiated CD8 T Cells Negatively Affect Bone Regeneration in Humans.* Science Translational Medicine, 2013. **5**(177): p. 177ra36-177ra36.

10. Sass, F.A., et al., *CD31+ Cells From Peripheral Blood Facilitate Bone Regeneration in Biologically Impaired Conditions Through Combined Effects on Immunomodulation and Angiogenesis.* J Bone Miner Res, 2017. **32**(5): p. 902-912.

11. Fassbender, M., et al., *Local Inhibition of Angiogenesis Results in an Atrophic Non-Union in a Rat Osteotomy Model.* European Cells & Materials, 2011. **22**: p. 1-11.

12. Andrew, W., *Human skeletal system.* Encyclopædia Britannica, 2018.

13. Gong, J.K., J.S. Arnold, and S.H. Cohn, *Composition of Trabecular + Cortical Bone.* Anatomical Record, 1964. **149**(3): p. 325-&.

14. University, R. https://opentextbc.ca/anatomyandphysiology/chapter/6-3-bone-structure/.

15. Fukumoto, S. and T.J. Martin, *Bone as an endocrine organ.* Trends in Endocrinology and Metabolism, 2009. **20**(5): p. 230-236.

16. Turner, C.H. and F.M. Pavalko, *Mechanotransduction and functional response of the skeleton to physical stress: The mechanisms and mechanics of bone adaptation*.* Journal of Orthopaedic Science, 1998. **3**(6): p. 346-355.

17. Wolff, J., *Das Gesetz der Transformation der Knochen.* Verlag von August Hirschwald, 1892(Berlin, Germany).

18. Buckwalter, J.A., et al., *Bone Biology .1. Structure, Blood-Supply, Cells, Matrix, and Mineralization.* Journal of Bone and Joint Surgery-American Volume, 1995. **77A**(8): p. 1256-1275.

19. Mackie, E.J., *Osteoblasts: novel roles in orchestration of skeletal architecture.* International Journal of Biochemistry & Cell Biology, 2003. **35**(9): p. 1301-1305.

20. Fernandez-Tresguerres-Hernandez-Gil, I., et al., *Physiological bases of bone regeneration II. The remodeling process.* Med Oral Patol Oral Cir Bucal, 2006. **11**(2): p. E151-7.

21. Fernandez-Tresguerres-Hernandez-Gil, I., et al., *Physiological bases of bone regeneration I. Histology and physiology of bone tissue.* Med Oral Patol Oral Cir Bucal, 2006. **11**(1): p. E47-51.

22. Logan, C.Y. and R. Nusse, *The Wnt signaling pathway in development and disease.* Annual Review of Cell and Developmental Biology, 2004. **20**: p. 781-810.

23. Pittenger, M.F., et al., *Multilineage Potential of Adult Human Mesenchymal Stem Cells.* Science, 1999. **284**(5411): p. 143-147.

24. Bodine, P.V. and B.S. Komm, *Wnt signaling and osteoblastogenesis.* Rev Endocr Metab Disord, 2006. **7**(1-2): p. 33-9.

25. Gaur, T., et al., *Canonical WNT signaling promotes osteogenesis by directly stimulating Runx2 gene expression.* J Biol Chem, 2005. **280**(39): p. 33132-40.

26. Knothe Tate, M.L., et al., *The osteocyte.* The International Journal of Biochemistry & Cell Biology, 2004. **36**(1): p. 1-8.

27. Manolagas, S.C., *Birth and death of bone cells: Basic regulatory mechanisms and implications for the pathogenesis and treatment of osteoporosis.* Endocrine Reviews, 2000. **21**(2): p. 115-137.

28. Boyle, W.J., W.S. Simonet, and D.L. Lacey, *Osteoclast differentiation and activation.* Nature, 2003. **423**(6937): p. 337-342.

29. Gowen, M., et al., *Cathepsin K knockout mice develop osteopetrosis due to a deficit in matrix degradation but not demineralization.* Journal of Bone and Mineral Research, 1999. **14**(10): p. 1654-1663.

30. Saftig, P., et al., *Functions of cathepsin K in bone resorption - Lessons from cathepsin K deficient mice.* Cellular Peptidases in Immune Functions and Diseases 2, 2000. **477**: p. 293-303.

31. Everts, V., et al., *The bone lining cell: Its role in cleaning Howship's lacunae and initiating bone formation.* Journal of Bone and Mineral Research, 2002. **17**(1): p. 77-90.

32. Matic, I., et al., *Quiescent Bone Lining Cells Are a Major Source of Osteoblasts During Adulthood.* Stem Cells, 2016. **34**(12): p. 2930-2942.

33. Shao, J., et al., *Bone Regulates Glucose Metabolism as an Endocrine Organ through Osteocalcin.* International Journal of Endocrinology, 2015.

34. Yeap, B.B., et al., *Reduced serum total osteocalcin is associated with metabolic syndrome in older men via waist circumference, hyperglycemia, and triglyceride levels.* European Journal of Endocrinology, 2010. **163**(2): p. 265-272.

35. Kanazawa, I., et al., *Serum Osteocalcin Level Is Associated with Glucose Metabolism and Atherosclerosis Parameters in Type 2 Diabetes Mellitus.* Journal of Clinical Endocrinology & Metabolism, 2009. **94**(1): p. 45-49.

36. Kaderly, R.E., *Primary bone healing.* Semin Vet Med Surg (Small Anim), 1991. **6**(1): p. 21-5.

37. Marsell, R. and T.A. Einhorn, *The biology of fracture healing.* Injury-International Journal of the Care of the Injured, 2011. **42**(6): p. 551-555.

38. Carano, R.A.D. and E.H. Filvaroff, *Angiogenesis and bone repair.* Drug Discovery Today, 2003. **8**(21): p. 980-989.

39. Einhorn, T.A., et al., *The Expression of Cytokine Activity by Fracture Callus.* Journal of Bone and Mineral Research, 1995. **10**(8): p. 1272-1281.

40. Schmidt-Bleek, K., et al., *Initial immune reaction and angiogenesis in bone healing.* Journal of Tissue Engineering and Regenerative Medicine, 2014. **8**(2): p. 120-130.

41. Kolar, P., et al., *The Early Fracture Hematoma and Its Potential Role in Fracture Healing.* Tissue Engineering Part B-Reviews, 2010. **16**(4): p. 427-434.

42. Kon, T., et al., *Expression of osteoprotegerin, receptor activator of NF-kappa B ligand (osteoprotegerin ligand) and related proinflammatory cytokines during fracture healing.* Journal of Bone and Mineral Research, 2001. **16**(6): p. 1004-1014.

43. Lee, S.K. and J. Lorenzo, *Cytokines regulating osteoclast formation and function.* Current Opinion in Rheumatology, 2006. **18**(4): p. 411-418.

44. Yang, X., et al., *Callus mineralization and maturation are delayed during fracture healing in interleukin-6 knockout mice.* Bone, 2007. **41**(6): p. 928-936.

45. Crowther, M., et al., *Microenvironmental influence on macrophage regulation of angiogenesis in wounds and malignant tumors.* Journal of Leukocyte Biology, 2001. **70**(4): p. 478-490.

46. Escribese, M.M., M. Casas, and A.L. Corbi, *Influence of low oxygen tensions on macrophage polarization.* Immunobiology, 2012. **217**(12): p. 1233-1240.

47. Guida, E. and A. Stewart, *Influence of hypoxia and glucose deprivation on tumour necrosis factor-alpha and granulocyte-macrophage colony-stimulating factor expression in human cultured monocytes.* Cellular Physiology and Biochemistry, 1998. **8**(1-2): p. 75-88.

48. Kitaori, T., et al., *Stromal Cell-Derived Factor 1/CXCR4 Signaling Is Critical for the Recruitment of Mesenchymal Stem Cells to the Fracture Site During Skeletal Repair in a Mouse Model.* Arthritis and Rheumatism, 2009. **60**(3): p. 813-823.

49. Ford, J.L., D.E. Robinson, and B.E. Scammell, *The fate of soft callus chondrocytes during long bone fracture repair.* Journal of Orthopaedic Research, 2003. **21**(1): p. 54-61.

50. Keramaris, N.C., et al., *Fracture vascularity and bone heating: A systematic review of the rote of VEGF.* Injury-International Journal of the Care of the Injured, 2008. **39**: p. S45-S57.

51. Moses, M.A., *The regulation of neovascularization by matrix metalloproteinases and their inhibitors.* Stem Cells, 1997. **15**(3): p. 180-189.

52. Ketenjian, A.Y. and C. Arsenis, *Morphological and Biochemical Studies during Differentiation and Calcification of Fracture Callus Cartilage.* Clinical Orthopaedics and Related Research, 1975(107): p. 266-273.

53. Loeffler, J., et al., *The Metabolic Microenvironment Steers Bone Tissue Regeneration.* Trends in Endocrinology and Metabolism, 2018. **29**(2): p. 99-110.

54. Raggatt, L.J., et al., *Fracture Healing via Periosteal Callus Formation Requires Macrophages for Both Initiation and Progression of Early Endochondral Ossification.* American Journal of Pathology, 2014. **184**(12): p. 3192-3204.

55. Schlundt, C., et al., *Macrophages in bone fracture healing: Their essential role in endochondral ossification.* Bone, 2018. **106**: p. 78-89.

56. Chang, M.K., et al., *Osteal tissue macrophages are intercalated throughout human and mouse bone lining tissues and regulate osteoblast function in vitro and in vivo.* Journal of Immunology, 2008. **181**(2): p. 1232-1244.

57. Vi, L., et al., *Macrophages promote osteoblastic differentiation in-vivo: implications in fracture repair and bone homeostasis.* Journal of Bone and Mineral Research, 2015. **30**(6): p. 1090-1102.

58. Gu, Q.L., H.L. Yang, and Q. Shi, *Macrophages and bone inflammation.* Journal of Orthopaedic Translation, 2017. **10**: p. 86-93.

59. Fernandes, T.J., et al., *Cord Blood-Derived Macrophage-Lineage Cells Rapidly Stimulate Osteoblastic Maturation in Mesenchymal Stem Cells in a Glycoprotein-130 Dependent Manner.* Plos One, 2013. **8**(9).

60. Guihard, P., et al., *Induction of osteogenesis in mesenchymal stem cells by activated monocytes/macrophages depends on Oncostatin M signaling.* Bone, 2012. **50**: p. S83-S83.

61. Gong, L., et al., *The Macrophage Polarization Regulates MSC Osteoblast Differentiation in vitro.* Annals of Clinical and Laboratory Science, 2016. **46**(1): p. 65-71.

62. Bastian, O.W., et al., *Neutrophils contribute to fracture healing by synthesizing fibronectin(+) extracellular matrix rapidly after injury.* Clinical Immunology, 2016. **164**: p. 78-84.

63. Hoff, P., et al., *Immunological characterization of the early human fracture hematoma.* Immunologic Research, 2016. **64**(5-6): p. 1195-1206.

64. Kovtun, A., et al., *The Crucial Role of Neutrophil Granulocytes in Bone Fracture Healing.* European Cells & Materials, 2016. **32**: p. 152-162.

65. Recknagel, S., et al., *Systemic inflammation induced by a thoracic trauma alters the cellular composition of the early fracture callus.* Journal of Trauma and Acute Care Surgery, 2013. **74**(2): p. 531-537.

66. Toben, D., et al., *Fracture Healing Is Accelerated in the Absence of the Adaptive Immune System.* Journal of Bone and Mineral Research, 2011. **26**(1): p. 113-124.

67. El Khassawna, T., et al., *T lymphocytes influence the Mineralization Process of Bone.* Frontiers in Immunology, 2017. **8**.

68. Han, X., et al., *Interleukin-17 enhances immunosuppression by mesenchymal stem cells.* Cell Death and Differentiation, 2014. **21**(11): p. 1758-1768.

69. Nam, D., et al., *T-Lymphocytes Enable Osteoblast Maturation via IL-17F during the Early Phase of Fracture Repair.* Plos One, 2012. **7**(6).

70. Bozec, A. and M.M. Zaiss, *T Regulatory Cells in Bone Remodelling.* Current Osteoporosis Reports, 2017. **15**(3): p. 121-125.

71. Noor, E., et al., *Central Carbon Metabolism as a Minimal Biochemical Walk between Precursors for Biomass and Energy.* Molecular Cell, 2010. **39**(5): p. 809-820.

72. Liu, Y.J. and T. Ma, *Metabolic Regulation of Mesenchymal Stem Cell in Expansion and Therapeutic Application.* Biotechnology Progress, 2015. **31**(2): p. 468-481.

73. Pearce, E.L. and E.J. Pearce, *Metabolic Pathways in Immune Cell Activation and Quiescence.* Immunity, 2013. **38**(4): p. 633-643.

74. DeBerardinis, R.J., et al., *The biology of cancer: Metabolic reprogramming fuels cell growth and proliferation.* Cell Metabolism, 2008. **7**(1): p. 11-20.

75. Löffler, G., *Basiswissen Biochemie mit Pathobiochemie ; mit 139 Tabellen ; [jetzt mit Farbtabellen]*. 7., komplett überarb. Aufl. ed. Springer-Lehrbuch / Springer-Lehrbuch. 2008, Heidelberg: Springer. XIII, 507 S.

76. Nelson, D.L., *Lehninger Biochemie mit 40 Tabellen*. 1., korr. Nachdr. 2005 der 3. Aufl. 2001 ed. Springer-Lehrbuch / Springer-Lehrbuch. 2005, Berlin u.a.: Springer. XXXVII, 1342 S.

77. Locasale, J.W., *Serine, glycine and one-carbon units: cancer metabolism in full circle.* Nature Reviews Cancer, 2013. **13**(8): p. 572-583.

78. Ducker, G.S. and J.D. Rabinowitz, *One-Carbon Metabolism in Health and Disease.* Cell Metabolism, 2017. **25**(1): p. 27-42.

79. Stryer, L., *Biochemie Biochemistry, dt.* 4. Aufl. ed. 1996, Heidelberg u.a.: Spektrum Akad. Verl. 1125 S.

80. Werner, C., T. Doenst, and M. Schwarzer, *Chapter 4 - Metabolic Pathways and Cycles*, in *The Scientist's Guide to Cardiac Metabolism*, M. Schwarzer and T. Doenst, Editors. 2016, Academic Press: Boston. p. 39-55.

81. Martius, C., *Citric Acid Cycle. Control and Compartmentation. Herausgeg. von J. M. Lowenstein. Marcel Dekker, Inc., New York-London 1969. 1. Aufl., XXI, 366 S., zahlr. Abb., $ 17.75.* Angewandte Chemie, 1970. **82**(12): p. 488-488.

82. Kim, J.-w., et al., *HIF-1-mediated expression of pyruvate dehydrogenase kinase: A metabolic switch required for cellular adaptation to hypoxia.* Cell Metabolism, 2006. **3**(3): p. 177-185.

83. Gray, L.R., S.C. Tompkins, and E.B. Taylor, *Regulation of pyruvate metabolism and human disease.* Cellular and Molecular Life Sciences, 2014. **71**(14): p. 2577-2604.

84. O'Neill, L.A.J., R.J. Kishton, and J. Rathmell, *A guide to immunometabolism for immunologists.* Nature Reviews Immunology, 2016. **16**(9): p. 553-565.

85. Cooper, G., *The Cell: A Molecular Approach. 2nd edition.* Sunderland (MA) 2000. Sinauer Associates.

86. Panieri, E. and M.M. Santoro, *ROS homeostasis and metabolism: a dangerous liason in cancer cells.* Cell Death & Disease, 2016. **7**.

87. Yang, L.F., S. Venneti, and D. Nagrath, *Glutaminolysis: A Hallmark of Cancer Metabolism.* Annual Review of Biomedical Engineering, Vol 19, 2017. **19**: p. 163-194.

88. Ganeshan, K. and A. Chawla, *Metabolic Regulation of Immune Responses.* Annual Review of Immunology, Vol 32, 2014. **32**: p. 609-634.

89. Mckeehan, W.L., *Glycolysis, Glutaminolysis and Cell-Proliferation.* Cell Biology International Reports, 1982. **6**(7): p. 635-650.

90. Altman, B.J., Z.E. Stine, and C.V. Dang, *From Krebs to clinic: glutamine metabolism to cancer therapy.* Nat Rev Cancer, 2016. **16**(10): p. 619-634.

91. Warburg, O., Wind, F. and Negelein, E., *The metaboliusm of tumors in the body.* J Gene Physiol., 1927. **8(6)**: p. 519-530.

92. Warburg, O., Posener, K. and Negelein, E., *Über den Stoffwechsel der Carcinomzelle.* Biochemische Zeitschrift, 1924. **152**: p. 319–344,.

93. Warburg, O., *Origin of Cancer Cells.* Science, 1956. **123**(3191): p. 309-314.

94. Fox, C.J., P.S. Hammerman, and C.B. Thompson, *Fuel feeds function: Energy metabolism and the T-cell response.* Nature Reviews Immunology, 2005. **5**(11): p. 844-852.

95. Locasale, J.W. and L.C. Cantley, *Metabolic Flux and the Regulation of Mammalian Cell Growth.* Cell Metabolism, 2011. **14**(4): p. 443-451.

96. Cairns, R.A., I.S. Harris, and T.W. Mak, *Regulation of cancer cell metabolism.* Nat Rev Cancer, 2011. **11**(2): p. 85-95.

97. Andrejeva, G., et al., *Metabolomics analysis reveals differential T cell serine metabolism as a target in autoimmunity.* The Journal of Immunology, 2018. **200**(1 Supplement): p. 167.7-167.7.

98. Pearce, E.L., et al., *Fueling immunity: insights into metabolism and lymphocyte function.* Science, 2013. **342**(6155): p. 1242454.

99. Chang, C.H., et al., *Posttranscriptional Control of T Cell Effector Function by Aerobic Glycolysis.* Cell, 2013. **153**(6): p. 1239-1251.

100. Gardner, P.R., et al., *Superoxide Radical and Iron Modulate Aconitase Activity in Mammalian-Cells.* Journal of Biological Chemistry, 1995. **270**(22): p. 13399-13405.

101. Waris, G. and H. Ahsan, *Reactive oxygen species: role in the development of cancer and various chronic conditions.* Journal of Carcinogenesis, 2006. **5**: p. 14-14.

102. Nain, V.B., R. Puria,B. Sahi, S., *Role of TCA cycle Truncation in Cancer Cell Energetics.* Current Trends in Biotechnology and Pharmacy, 2014. **8**(4): p. 428-438.

103. Kumar, V.B.S., et al., *Endothelial cell response to lactate: Implication of PAR modification of VEGF.* Journal of Cellular Physiology, 2007. **211**(2): p. 477-485.

104. Yalamanchi, N., et al., *Flexor tendon wound healing in vitro: Lactate up-regulation of TGF-beta expression and functional activity.* Plastic and Reconstructive Surgery, 2004. **113**(2): p. 625-632.

105. Lu, H.S., R.A. Forbes, and A. Verma, *Hypoxia-inducible factor 1 activation by aerobic glycolysis implicates the Warburg effect in carcinogenesis.* Journal of Biological Chemistry, 2002. **277**(26): p. 23111-23115.

106. Constant, J.S., et al., *Lactate elicits vascular endothelial growth factor from macrophages: a possible alternative to hypoxia.* Wound Repair and Regeneration, 2000. **8**(5): p. 353-360.

107. Porporato, P.E., et al., *Lactate stimulates angiogenesis and accelerates the healing of superficial and ischemic wounds in mice.* Angiogenesis, 2012. **15**(4): p. 581-592.

108. Trabold, O., et al., *Lactate and oxygen constitute a fundamental regulatory mechanism in wound healing.* Wound Repair and Regeneration, 2003. **11**(6): p. 504-509.

109. Bardella, C., P.J. Pollard, and I. Tomlinson, *SDH mutations in cancer.* Biochimica Et Biophysica Acta-Bioenergetics, 2011. **1807**(11): p. 1432-1443.

110. Aspuria, P.-J.P., et al., *Succinate dehydrogenase inhibition leads to epithelial-mesenchymal transition and reprogrammed carbon metabolism.* Cancer & Metabolism, 2014. **2**(1): p. 21.

111. Tannahill, G.M., et al., *Succinate is an inflammatory signal that induces IL-1 beta through HIF-1 alpha.* Nature, 2013. **496**(7444): p. 238-+.

112. Fonseca, M.D., et al., *GPR91: expanding the frontiers of Krebs cycle intermediates.* Cell Communication and Signaling, 2016. **14**.

113. Sun, S.R., et al., *Lactic Acid: No Longer an Inert and End-Product of Glycolysis.* Physiology, 2017. **32**(6): p. 453-463.

114. Borregaard, N. and T. Herlin, *Energy-Metabolism of Human-Neutrophils during Phagocytosis.* Journal of Clinical Investigation, 1982. **70**(3): p. 550-557.

115. Rodriguez-Espinosa, O., et al., *Metabolic requirements for neutrophil extracellular traps formation.* Immunology, 2015. **145**(2): p. 213-224.

116. Bao, Y., et al., *Mitochondria regulate neutrophil activation by generating ATP for autocrine purinergic signaling.* J Biol Chem, 2014. **289**(39): p. 26794-803.

117. Vogel, D.Y.S., et al., *Human macrophage polarization in vitro: Maturation and activation methods compared.* Immunobiology, 2014. **219**(9): p. 695-703.

118. Antonios, J.K., et al., *Macrophage polarization in response to wear particles in vitro.* Cellular and Molecular Immunology, 2013. **10**(6): p. 471-482.

119. Wynn, T.A. and K.M. Vannella, *Macrophages in Tissue Repair, Regeneration, and Fibrosis.* Immunity, 2016. **44**(3): p. 450-462.

120. Galvan-Pena, S. and L.A.J. O'Neill, *Metabolic reprograming in macropage polarization.* Frontiers in Immunology, 2014. **5**.

121. Kelly, B. and L.A. O'Neill, *Metabolic reprogramming in macrophages and dendritic cells in innate immunity.* Cell Res, 2015. **25**(7): p. 771-84.

122. Jha, A.K., et al., *Network integration of parallel metabolic and transcriptional data reveals metabolic modules that regulate macrophage polarization.* Immunity, 2015. **42**(3): p. 419-30.

123. Rodriguez-Prados, J.C., et al., *Substrate fate in activated macrophages: a comparison between innate, classic, and alternative activation.* J Immunol, 2010. **185**(1): p. 605-14.

124. Strelko, C.L., et al., *Itaconic Acid Is a Mammalian Metabolite Induced during Macrophage Activation.* Journal of the American Chemical Society, 2011. **133**(41): p. 16386-16389.

125. Michelucci, A., et al., *Immune-responsive gene 1 protein links metabolism to immunity by catalyzing itaconic acid production.* Proceedings of the National Academy of Sciences of the United States of America, 2013. **110**(19): p. 7820-7825.

126. Pilkis, S.J., et al., *The Role of Fructose 2,6-Bisphosphate in Regulation of Fructose-1,6-Bisphosphatase.* Journal of Biological Chemistry, 1981. **256**(22): p. 1489-1495.

127. Chesney, J., et al., *An inducible gene product for 6-phosphofructo-2-kinase with an AU-rich instability element: Role in tumor cell glycolysis and the Warburg effect.* Proceedings of the National Academy of Sciences of the United States of America, 1999. **96**(6): p. 3047-3052.

128. Tan, Z., et al., *Pyruvate Dehydrogenase Kinase 1 Participates in Macrophage Polarization via Regulating Glucose Metabolism.* Journal of Immunology, 2015. **194**(12): p. 6082-6089.

129. Tocaj, A., et al., *Alpha-ketoglutarate (AKG) inhibit osteoporosis development in postmenopausal women.* Journal of Bone and Mineral Research, 2003. **18**: p. S267-S267.

130. Medbury, H.J., et al., *Differing association of macrophage subsets with atherosclerotic plaque stability.* International Angiology, 2013. **32**(1): p. 74-84.

131. Roszer, T., *Understanding the Mysterious M2 Macrophage through Activation Markers and Effector Mechanisms.* Mediators of Inflammation, 2015.

132. Huang, S.C.C., et al., *Cell-intrinsic lysosomal lipolysis is essential for alternative activation of macrophages.* Nature Immunology, 2014. **15**(9): p. 846-855.

133. Buck, M.D., D. O'Sullivan, and E.L. Pearce, *T cell metabolism drives immunity.* Journal of Experimental Medicine, 2015. **212**(9): p. 1345-1360.

134. Weinberg, J.M., et al., *Mitochondrial dysfunction during hypoxia/reoxygenation and its correction by anaerobic metabolism of citric acid cycle intermediates.* Proc Natl Acad Sci U S A, 2000. **97**(6): p. 2826-31.

135. Berod, L., et al., *De novo fatty acid synthesis controls the fate between regulatory T and T helper 17 cells.* Nature Medicine, 2014. **20**(11): p. 1327-1333.

136. Konnecke, I., et al., *T and B cells participate in bone repair by infiltrating the fracture callus in a two-wave fashion.* Bone, 2014. **64**: p. 155-165.

137. Bruno, A., et al., *Orchestration of Angiogenesis by Immune Cells.* Frontiers in Oncology, 2014. **4**(131).

138. Pucino, V., et al., *Regulatory T Cells, Leptin and Angiogenesis.* Angiogenesis, Lymphangiogenesis and Clinical Implications, 2014. **99**: p. 155-169.

139. Waters, L.R., et al., *Initial B Cell Activation Induces Metabolic Reprogramming and Mitochondrial Remodeling.* iScience, 2018. **5**: p. 99-109.

140. Kofoed, H., et al., *Bone-Marrow Circulation after Osteotomy - Blood-Flow, Po2, Pco2, and Pressure Studied in Dogs.* Acta Orthopaedica Scandinavica, 1985. **56**(5): p. 400-403.

141. Grant, J.L. and B. Smith, *Bone Marrow Gas Tensions, Bone Marrow Blood Flow, and Erythropoiesis in Man.* Annals of Internal Medicine, 1963. **58**(5): p. 801-+.

142. Chen, C.T., et al., *Coordinated changes of mitochondrial biogenesis and antioxidant enzymes during osteogenic differentiation of human mesenchymal stem cells.* Stem Cells, 2008. **26**(4): p. 960-968.

143. Salim, A., et al., *Transient changes in oxygen tension inhibit osteogenic differentiation and Runx2 expression in osteoblasts.* Journal of Biological Chemistry, 2004. **279**(38): p. 40007-40016.

144. Dienelt, A. and N.I. zur Nieden, *Hyperglycemia Impairs Skeletogenesis from Embryonic Stem Cells by Affecting Osteoblast and Osteoclast Differentiation.* Stem Cells and Development, 2011. **20**(3): p. 465-474.

145. Lu, J., et al., *Osterix acetylation at K307 and K312 enhances its transcriptional activity and is required for osteoblast differentiation.* Oncotarget, 2016. **7**(25): p. 37471-37486.

146. Jeon, E.J., et al., *Bone morphogenetic protein-2 stimulates Runx2 acetylation.* Journal of Biological Chemistry, 2006. **281**(24): p. 16502-16511.

147. Guarente, L., *The Logic Linking Protein Acetylation and Metabolism.* Cell Metabolism, 2011. **14**(2): p. 151-153.

148. Pattappa, G., et al., *The Metabolism of Human Mesenchymal Stem Cells During Proliferation and Differentiation.* Journal of Cellular Physiology, 2011. **226**(10): p. 2562-2570.

149. Rajpurohit, R., et al., *Adaptation of chondrocytes to low oxygen tension: Relationship between hypoxia and cellular metabolism.* Journal of Cellular Physiology, 1996. **168**(2): p. 424-432.

150. Knull, H.R. and J.L. Walsh, *Association of Glycolytic Enzymes with the Cytoskeleton*, in *Current Topics in Cellular Regulation*, E.R. Stadtman and P.B. Chock, Editors. 1992, Academic Press. p. 15-30.

151. Masters, C., *Interactions between glycolytic enzymes and components of the cytomatrix.* The Journal of Cell Biology, 1984. **99**(1): p. 222s-225s.

152. Phornphutkul, C., K.Y. Wu, and P.A. Gruppuso, *The role of insulin in chondrogenesis.* Molecular and Cellular Endocrinology, 2006. **249**(1-2): p. 107-115.

153. Shapiro, I.M., et al., *Linkage between Energy Status of Perivascular Cells and Mineralization of the Chick Growth Cartilage.* Developmental Biology, 1988. **129**(2): p. 372-379.

154. Pollesello, P., et al., *Energy-State of Chondrocytes Assessed by 31p-Nmr Studies of Preosseous Cartilage.* Biochemical and Biophysical Research Communications, 1991. **180**(1): p. 216-222.

155. Indo, Y., et al., *Metabolic Regulation of Osteoclast Differentiation and Function.* Journal of Bone and Mineral Research, 2013. **28**(11): p. 2392-2399.

156. Ahn, H., et al., *Accelerated Lactate Dehydrogenase Activity Potentiates Osteoclastogenesis via NFATc1 Signaling.* Plos One, 2016. **11**(4).

157. Lee, Y.S., et al., *AMP kinase acts as a negative regulator of RANKL in the differentiation of osteoclasts.* Bone, 2010. **47**(5): p. 926-937.

158. Lemma, S., et al., *Energy metabolism in osteoclast formation and activity.* International Journal of Biochemistry & Cell Biology, 2016. **79**: p. 168-180.

159. Lee, W.C., et al., *Energy Metabolism of the Osteoblast: Implications for Osteoporosis.* Endocrine Reviews, 2017. **38**(3): p. 255-266.

160. Lemons, J.M.S., et al., *Quiescent Fibroblasts Exhibit High Metabolic Activity.* Plos Biology, 2010. **8**(10).

161. Ghesquiere, B., et al., *Metabolism of stromal and immune cells in health and disease.* Nature, 2014. **511**(7508): p. 167-176.

162. De Bock, K., et al., *Role of PFKFB3-Driven Glycolysis in Vessel Sprouting.* Cell, 2013. **154**(3): p. 651-663.

163. Schoors, S., et al., *Fatty acid carbon is essential for dNTP synthesis in endothelial cells (vol 520, pg 192, 2015).* Nature, 2015. **526**(7571): p. 144-144.

164. Eelen, G., et al., *Endothelial Cell Metabolism.* Physiological Reviews, 2018. **98**(1): p. 3-58.

165. Coutelle, O., et al., *Embelin inhibits endothelial mitochondrial respiration and impairs neoangiogenesis during tumor growth and wound healing.* Embo Molecular Medicine, 2014. **6**(5): p. 624-639.

166. Horgan, R.P. and L.C. Kenny, *'Omic' technologies: genomics, transcriptomics, proteomics and metabolomics.* The Obstetrician & Gynaecologist, 2011. **13**(3): p. 189-195.

167. Kitano, H., *Systems biology: A brief overview.* Science, 2002. **295**(5560): p. 1662-1664.

168. Kell, D.B., *Systems biology, metabolic modelling and metabolomics in drug discovery and development.* Drug Discovery Today, 2006. **11**(23-24): p. 1085-1092.

169. Gerhold, D.L., R.V. Jensen, and S.R. Gullans, *Better therapeutics through microarrays.* Nature Genetics, 2002. **32**: p. 547-552.

170. Alon, U., *An introduction to systems biology: Design principles of biological circuits.* Boca Raton: Chapman&Hall/CRC, 2007. https://doi.org/10.1016/B978-0-12-385075-1.00013-5 pmid:21601092.

171. McNamara, L.E., L.-A. Turner, and K.V. Burgess, *Systems Biology Approaches Applied to Regenerative Medicine.* Current pathobiology reports, 2015. **3**(1): p. 37-45.

172. Calciolari, E. and N. Donos, *The use of omics profiling to improve outcomes of bone regeneration and osseointegration. How far are we from personalized medicine in dentistry?* Journal of Proteomics, 2018. **188**: p. 85-96.

173. Reppe, S., et al., *Identification of transcriptional macromolecular associations in human bone using browser based in silico analysis in a giant correlation matrix.* Bone, 2013. **53**(1): p. 69-78.

174. Jemtland, R., et al., *Molecular Disease Map of Bone Characterizing the Postmenopausal Osteoporosis Phenotype.* Journal of Bone and Mineral Research, 2011. **26**(8): p. 1793-1801.

175. Ma, B., et al., *Metabolomic Profiles Delineate Signature Metabolic Shifts during Estrogen Deficiency-Induced Bone Loss in Rat by GC-TOF/MS.* Plos One, 2013. **8**(2).

176. Lv, H.H., et al., *Metabolomics and Its Application in the Development of Discovering Biomarkers for Osteoporosis Research.* International Journal of Molecular Sciences, 2016. **17**(12).

177. Metallo, Christian M. and Matthew G. Vander Heiden, *Understanding Metabolic Regulation and Its Influence on Cell Physiology.* Molecular Cell, 2013. **49**(3): p. 388-398.

178. Urbanczyk-Wochniak, E., et al., *Parallel analysis of transcript and metabolic profiles: a new approach in systems biology.* EMBO Rep, 2003. **4**(10): p. 989-93.

179. Lee, J.V., et al., *Akt-Dependent Metabolic Reprogramming Regulates Tumor Cell Histone Acetylation.* Cell Metabolism, 2014. **20**(2): p. 306-319.

180. Everts, A.G., et al., *Quantitative Dynamics of the Link between Cellular Metabolism and Histone Acetylation.* Journal of Biological Chemistry, 2013. **288**(17): p. 12142-12151.

181. Dai, Z.W., et al., *Methionine metabolism influences genomic architecture and gene expression through H3K4me3 peak width.* Nature Communications, 2018. **9**.

182. Schvartzman, J.M., C.B. Thompson, and L.W.S. Finley, *Metabolic regulation of chromatin modifications and gene expression.* Journal of Cell Biology, 2018. **217**(7): p. 2247-2259.

183. Farid, S.G. and G. Morris-Stiff, *"OMICS" technologies and their role in foregut primary malignancies.* Current Problems in Surgery, 2015. **52**(10): p. 409-441.

184. Kuehnbaum, N.L. and P. Britz-McKibbin, *New Advances in Separation Science for Metabolomics: Resolving Chemical Diversity in a Post-Genomic Era.* Chemical Reviews, 2013. **113**(4): p. 2437-2468.

185. Clish, C.B., *Metabolomics: an emerging but powerful tool for precision medicine.* Cold Spring Harbor molecular case studies, 2015. **1**(1): p. a000588-a000588.

186. van der Greef, J., et al., *Looking back into the future: 30 years of metabolomics at TNO.* Mass Spectrometry Reviews, 2013. **32**(5): p. 399-415.

187. Emwas, A.-H.M., *The Strengths and Weaknesses of NMR Spectroscopy and Mass Spectrometry with Particular Focus on Metabolomics Research*, in *Metabonomics: Methods and Protocols*, J.T. Bjerrum, Editor. 2015, Springer New York: New York, NY. p. 161-193.

188. Wilkins, M.R., et al., *Progress with proteome projects: Why all proteins expressed by a genome should be identified and how to do it.* Biotechnology and Genetic Engineering Reviews, Vol 13, 1996. **13**: p. 19-50.

189. Nesvizhskii, A.I., O. Vitek, and R. Aebersold, *Analysis and validation of proteomic data generated by tandem mass spectrometry.* Nature Methods, 2007. **4**(10): p. 787-797.

190. Chandramouli, K. and P.-Y. Qian, *Proteomics: challenges, techniques and possibilities to overcome biological sample complexity.* Human genomics and proteomics : HGP, 2009. **2009**: p. 239204.

191. Karpievitch, Y.V., et al., *Liquid Chromatography Mass Spectrometry-Based Proteomics: Biological and Technological Aspects.* Annals of Applied Statistics, 2010. **4**(4): p. 1797-1823.

192. Domon, B. and R. Aebersold, *Options and considerations when selecting a quantitative proteomics strategy.* Nature Biotechnology, 2010. **28**: p. 710.

193. Borràs, E. and E. Sabidó, *What is targeted proteomics? A concise revision of targeted acquisition and targeted data analysis in mass spectrometry.* PROTEOMICS, 2017. **17**(17-18): p. 1700180.

194. Preininger, B., et al., *An Experimental Setup to Evaluate Innovative Therapy Options for the Enhancement of Bone Healing Using Bmp as a Benchmark - a Pilot Study.* European Cells & Materials, 2012. **23**: p. 262-272.

195. Strube, P., et al., *A new device to control mechanical environment in bone defect healing in rats.* Journal of biomechanics, 2008. **41**(12): p. 2696-2702.

196. Pfaffl, M.W., G.W. Horgan, and L. Dempfle, *Relative expression software tool (REST) for group-wise comparison and statistical analysis of relative expression results in real-time PCR.* Nucleic Acids Res, 2002. **30**(9): p. e36.

197. Roessner, U., et al., *Simultaneous analysis of metabolites in potato tuber by gas chromatography-mass spectrometry.* Plant Journal, 2000. **23**(1): p. 131-142.

198. Colebatch, G., et al., *Global changes in transcription orchestrate metabolic differentiation during symbiotic nitrogen fixation in Lotus japonicus.* Plant Journal, 2004. **39**(4): p. 487-512.

199. Jonsson, P., et al., *A strategy for identifying differences in large series of metabolomic samples analyzed by GC/MS.* Analytical Chemistry, 2004. **76**(6): p. 1738-1745.

200. Dettmer, K., P.A. Aronov, and B.D. Hammock, *Mass spectrometry-based metabolomics.* Mass spectrometry reviews, 2007. **26**(1): p. 51-78.

201. Kushnir, M.M., et al., *Analysis of dicarboxylic acids by tandem mass spectrometry. High-throughput quantitative measurement of methylmalonic acid in serum, plasma, and urine.* Clin Chem, 2001. **47**(11): p. 1993-2002.

202. Kuich, P.H.J.L., N. Hoffmann, and S. Kempa, *Maui-VIA: A User-Friendly Software for Visual Identification, Alignment, Correction, and Quantification of Gas Chromatography–Mass Spectrometry Data.* Frontiers in Bioengineering and Biotechnology, 2014. **2**: p. 84.

203. Kováts, E., *Gas-chromatographische Charakterisierung organischer Verbindungen. Teil 1: Retentionsindices aliphatischer Halogenide, Alkohole, Aldehyde und Ketone.* Helvetica Chimica Acta, 1958. **41**(7): p. 1915-1932.

204. Smith, P.K., et al., *Measurement of protein using bicinchoninic acid.* Analytical Biochemistry, 1985. **150**(1): p. 76-85.

205. Olson, B.J.S.C. and J. Markwell, *Assays for Determination of Protein Concentration.* Current Protocols in Protein Science, 2007. **48**(1): p. 3.4.1-3.4.29.

206. Yu, Y., M. Smith, and R. Pieper, *A spinnable and automatable StageTip for high throughput peptide desalting and proteomics.* 2014.

207. Cox, J. and M. Mann, *MaxQuant enables high peptide identification rates, individualized p.p.b.-range mass accuracies and proteome-wide protein quantification.* Nature Biotechnology, 2008. **26**: p. 1367.

208. Bielow, C., G. Mastrobuoni, and S. Kempa, *Proteomics Quality Control: Quality Control Software for MaxQuant Results.* Journal of Proteome Research, 2016. **15**(3): p. 777-787.

209. Tyanova, S., et al., *The Perseus computational platform for comprehensive analysis of (prote)omics data.* Nature Methods, 2016. **13**: p. 731.

210. Kawamoto, T., *Use of a new adhesive film for the preparation of multi-purpose fresh-frozen sections from hard tissues, whole-animals, insects and plants.* Archives of Histology and Cytology, 2003. **66**(2): p. 123-143.

211. Park, E.K., et al., *Optimized THP-1 differentiation is required for the detection of responses to weak stimuli.* Inflammation Research, 2007. **56**(1): p. 45-50.

212. Auwerx, J., *The Human Leukemia-Cell Line, Thp-1 - a Multifaceted Model for the Study of Monocyte-Macrophage Differentiation.* Experientia, 1991. **47**(1): p. 22-31.

213. Krampera, M., et al., *Immunological characterization of multipotent mesenchymal stromal cells—The International Society for Cellular Therapy (ISCT) working proposal.* Cytotherapy, 2013. **15**(9): p. 1054-1061.

214. Dominici, M., et al., *Minimal criteria for defining multipotent mesenchymal stromal cells. The International Society for Cellular Therapy position statement.* Cytotherapy, 2006. **8**(4): p. 315-317.

215. Krause, U., A. Seckinger, and C.A. Gregory, *Assays of Osteogenic Differentiation by Cultured Human Mesenchymal Stem Cells*, in *Mesenchymal Stem Cell Assays and Applications*, M. Vemuri, L.G. Chase, and M.S. Rao, Editors. 2011, Humana Press: Totowa, NJ. p. 215-230.

216. Grässel, S., S. Stöckl, and Z. Jenei-Lanzl, *Isolation, Culture, and Osteogenic/Chondrogenic Differentiation of Bone Marrow-Derived Mesenchymal Stem Cells*, in *Somatic Stem Cells: Methods and Protocols*, S.R. Singh, Editor. 2012, Humana Press: Totowa, NJ. p. 203-267.

217. Jaiswal, N., et al., *Osteogenic differentiation of purified, culture-expanded human mesenchymal stem cells in vitro.* J Cell Biochem, 1997. **64**(2): p. 295-312.

218. Collin, P., et al., *Expression of collagen, osteocalcin, and bone alkaline phosphatase in a mineralizing rat osteoblastic cell culture.* Calcif Tissue Int, 1992. **50**(2): p. 175-83.

219. Sakano, S., et al., *Collagen and alkaline phosphatase gene expression during bone morphogenetic protein (BMP)-induced cartilage and bone differentiation.* Clin Orthop Relat Res, 1993(292): p. 337-44.

220. Kalagara, R., et al., *Identification of stable reference genes for lipopolysaccharide-stimulated macrophage gene expression studies.* Biology Methods and Protocols, 2016. **1**(1): p. bpw005-bpw005.

221. Kratzel, C., et al., *Characterization of a rat osteotomy model with impaired healing.* BMC Musculoskeletal Disorders, 2008. **9**: p. 135-135.

222. Laschke, M.W., et al., *Combined inhibition of vascular endothelial growth factor (VEGF), fibroblast growth factor and platelet-derived growth factor, but not inhibition of VEGF alone,*

effectively suppresses angiogenesis and vessel maturation in endometriotic lesions. Human Reproduction, 2006. **21**(1): p. 262-268.

223. Okamoto, M., et al., *Noncanonical Wnt5a enhances Wnt/beta-catenin signaling during osteoblastogenesis.* Sci Rep, 2014. **4**: p. 4493.

224. Hirschhaeuser, F., U.G.A. Sattler, and W. Mueller-Klieser, *Lactate: A Metabolic Key Player in Cancer.* Cancer Research, 2011. **71**(22): p. 6921-6925.

225. Lu, J., M. Tan, and Q. Cai, *The Warburg effect in tumor progression: Mitochondrial oxidative metabolism as an anti-metastasis mechanism.* Cancer Letters, 2015. **356**(2, Part A): p. 156-164.

226. Denko, N.C., *Hypoxia, HIF1 and glucose metabolism in the solid tumour.* Nature Reviews Cancer, 2008. **8**: p. 705.

227. Tretter, L., A. Patocs, and C. Chinopoulos, *Succinate, an intermediate in metabolism, signal transduction, ROS, hypoxia, and tumorigenesis.* Biochimica et Biophysica Acta (BBA) - Bioenergetics, 2016. **1857**(8): p. 1086-1101.

228. Lendvai, N., et al., *Succinate-to-Fumarate Ratio as a New Metabolic Marker to Detect the Presence of SDHB/D-related Paraganglioma: Initial Experimental and Ex Vivo Findings.* Endocrinology, 2014. **155**(1): p. 27-32.

229. Hodson, L., et al., *Metabolic Signatures of Human Adipose Tissue Hypoxia in Obesity.* Diabetes, 2013. **62**(5): p. 1417-1425.

230. Neill, W.A., et al., *Effect of decreased O2 supply to tissue on the lactate:pyruvate ratio in blood.* The Journal of Clinical Investigation, 1969. **48**(10): p. 1862-1869.

231. Cornford, E.M., et al., *Regional Analyses of CNS Microdialysate Glucose and Lactate in Seizure Patients.* Epilepsia, 2002. **43**(11): p. 1360-1371.

232. Tsai, C.-C., et al., *Benefits of hypoxic culture on bone marrow multipotent stromal cells.* American Journal of Blood Research, 2012. **2**(3): p. 148-159.

233. Zhang, C.C. and H.A. Sadek, *Hypoxia and Metabolic Properties of Hematopoietic Stem Cells.* Antioxidants & Redox Signaling, 2014. **20**(12): p. 1891-1901.

234. *WebGestalt.* 2017. http://www.webgestalt.org/option.php.

235. Eming, S.A., T.A. Wynn, and P. Martin, *Inflammation and metabolism in tissue repair and regeneration.* Science, 2017. **356**(6342): p. 1026-1030.

236. Awad, F., et al., *Impact of human monocyte and macrophage polarization on NLR expression and NLRP3 inflammasome activation.* PLOS ONE, 2017. **12**(4): p. e0175336.

237. Braga, T.T., J.S.H. Agudelo, and N.O.S. Camara, *Macrophages During the Fibrotic Process: M2 as Friend and Foe.* Frontiers in Immunology, 2015. **6**: p. 602.

238. Jager, N.A., et al., *Distribution of Matrix Metalloproteinases in Human Atherosclerotic Carotid Plaques and Their Production by Smooth Muscle Cells and Macrophage Subsets.* Molecular Imaging and Biology, 2016. **18**: p. 283-291.

239. Cardoso, A.P., et al., *Matrix metalloproteases as maestros for the dual role of LPS- and IL-10-stimulated macrophages in cancer cell behaviour.* BMC Cancer, 2015. **15**(1): p. 456.

240. Li, H., et al., *Modulation the crosstalk between tumor-associated macrophages and non-small cell lung cancer to inhibit tumor migration and invasion by ginsenoside Rh2.* BMC Cancer, 2018. **18**(1): p. 579.

241. Weiss, J.M., et al., *Macrophage-dependent nitric oxide expression regulates tumor cell detachment and metastasis after IL-2/anti-CD40 immunotherapy.* J Exp Med, 2010. **207**(11): p. 2455-67.

242. Firestein, G.S., et al., in *Kelley and Firestein's Textbook of Rheumatology (Tenth Edition)*, G.S. Firestein, et al., Editors. 2017, Elsevier. p. vii.

243. Sierra-Filardi, E., et al., *CCL2 Shapes Macrophage Polarization by GM-CSF and M-CSF: Identification of CCL2/CCR2-Dependent Gene Expression Profile.* Journal of Immunology, 2014. **192**(8): p. 3858-3867.

244. Martinez, F.O., et al., *Transcriptional Profiling of the Human Monocyte-to-Macrophage Differentiation and Polarization: New Molecules and Patterns of Gene Expression.* The Journal of Immunology, 2006. **177**(10): p. 7303-7311.

245. Gabay, C., C. Lamacchia, and G. Palmer, *IL-1 pathways in inflammation and human diseases.* Nature Reviews Rheumatology, 2010. **6**: p. 232.

246. Mills, E.L., et al., *Succinate Dehydrogenase Supports Metabolic Repurposing of Mitochondria to Drive Inflammatory Macrophages.* Cell, 2016. **167**(2): p. 457-+.

247. Rubic, T., et al., *Triggering the succinate receptor GPR91 on dendritic cells enhances immunity.* Nat Immunol, 2008. **9**(11): p. 1261-9.

248. Chimal-Ramírez, G.K., et al., *Monocyte Differentiation towards Protumor Activity Does Not Correlate with M1 or M2 Phenotypes.* Journal of immunology research, 2016. **2016**: p. 6031486-6031486.

249. Chistiakov, D.A., et al., *CD68/macrosialin: not just a histochemical marker.* Laboratory Investigation, 2016. **97**: p. 4.

250. Taipale, J., et al., *Induction of Transforming Growth-Factor-Beta-1 and Its Receptor Expression during Myeloid-Leukemia Cell-Differentiation.* Cell Growth & Differentiation, 1994. **5**(12): p. 1309-1319.

251. Afonina, I.S., et al., *Proteolytic Processing of Interleukin-1 Family Cytokines: Variations on a Common Theme.* Immunity, 2015. **42**(6): p. 991-1004.

252. Mills, E.L., et al., *Succinate Dehydrogenase Supports Metabolic Repurposing of Mitochondria to Drive Inflammatory Macrophages.* Cell, 2016. **167**(2): p. 457-470.e13.

253. Selak, M.A., et al., *Succinate links TCA cycle dysfunction to oncogenesis by inhibiting HIF-alpha prolyl hydroxylase.* Cancer Cell, 2005. **7**(1): p. 77-85.

254. He, W.H., et al., *Citric acid cycle intermediates as ligands for orphan G-protein-coupled receptors.* Nature, 2004. **429**(6988): p. 188-193.

255. Ariza, A.C., P.M. Deen, and J.H. Robben, *The succinate receptor as a novel therapeutic target for oxidative and metabolic stress-related conditions.* Front Endocrinol (Lausanne), 2012. **3**: p. 22.

256. Aguiar, C.J., et al., *Succinate modulates Ca2+ transient and cardiomyocyte viability through PKA-dependent pathway.* Cell Calcium, 2010. **47**(1): p. 37-46.

257. He, W., et al., *Citric acid cycle intermediates as ligands for orphan G-protein-coupled receptors.* Nature, 2004. **429**(6988): p. 188-93.

258. Peruzzotti-Jametti, L., et al., *Macrophage-Derived Extracellular Succinate Licenses Neural Stem Cells to Suppress Chronic Neuroinflammation.* Cell Stem Cell, 2018. **22**(3): p. 355-+.

259. Mu, X., et al., *Oncometabolite succinate promotes angiogenesis by upregulating VEGF expression through GPR91-mediated STAT3 and ERK activation.* Oncotarget, 2017. **8**(8): p. 13174-13185.

260. Ko, S.H., et al., *Succinate promotes stem cell migration through the GPR91-dependent regulation of DRP1-mediated mitochondrial fission.* Sci Rep, 2017. **7**(1): p. 12582.

261. Zdero, R., et al., *Biomechanical evaluation of periprosthetic femoral fracture fixation.* J Bone Joint Surg Am, 2008. **90**(5): p. 1068-77.

262. Claes, L., *Biomechanical principles and mechanobiologic aspects of flexible and locked plating.* J Orthop Trauma, 2011. **25 Suppl 1**: p. S4-7.

263. Claes, L.E., et al., *Effects of mechanical factors on the fracture healing process.* Clin Orthop Relat Res, 1998(355 Suppl): p. S132-47.

264. Hankenson, K.D., et al., *Angiogenesis in bone regeneration.* Injury-International Journal of the Care of the Injured, 2011. **42**(6): p. 556-561.

265. Carlier, A., et al., *Oxygen as a critical determinant of bone fracture healing-A multiscale model.* Journal of Theoretical Biology, 2015. **365**: p. 247-264.

266. Lim, J.C., et al., *TNF-alpha; contributes to diabetes impaired angiogenesis in fracture healing.* Bone, 2017. **99**: p. 26-38.

267. Kemmler, J., et al., *Exposure to 100% Oxygen Abolishes the Impairment of Fracture Healing after Thoracic Trauma.* PLOS ONE, 2015. **10**(7): p. e0131194.

268. Hausman, M.R. and B.D. Rinker, *Intractable wounds and infections: the role of impaired vascularity and advanced surgical methods for treatment.* Am J Surg, 2004. **187**(5a): p. 44s-55s.

269. Dickson, K., et al., *Delayed Unions and Nonunions of Open Tibial Fractures - Correlation with Arteriography Results.* Clinical Orthopaedics and Related Research, 1994(302): p. 189-193.

270. Hunt, T.K., et al., *Lactate, with oxygen, incites angiogenesis.* Oxygen Transport to Tissue Xxix, 2008. **614**: p. 73-80.

271. Majmundar, A.J., W.H.J. Wong, and M.C. Simon, *Hypoxia-Inducible Factors and the Response to Hypoxic Stress.* Molecular Cell, 2010. **40**(2): p. 294-309.

272. Fraisl, P., et al., *Regulation of Angiogenesis by Oxygen and Metabolism.* Developmental Cell, 2009. **16**(2): p. 167-179.

273. Gibala, M.J., et al., *Tricarboxylic acid cycle intermediate pool size and estimated cycle flux in human muscle during exercise.* Am J Physiol, 1998. **275**(2 Pt 1): p. E235-42.

274. Williams, N.C. and L.A.J. O'Neill, *A Role for the Krebs Cycle Intermediate Citrate in Metabolic Reprogramming in Innate Immunity and Inflammation.* Frontiers in immunology, 2018. **9**: p. 141-141.

275. Chinopoulos, C., *Which way does the citric acid cycle turn during hypoxia? The critical role of α-ketoglutarate dehydrogenase complex.* Journal of Neuroscience Research, 2013. **91**(8): p. 1030-1043.

276. Moffatt, B.A. and H. Ashihara, *Purine and pyrimidine nucleotide synthesis and metabolism.* The arabidopsis book, 2002. **1**: p. e0018-e0018.

277. Watford, M., *Glutamine Metabolism and Function in Relation to Proline Synthesis and the Safety of Glutamine and Proline Supplementation.* The Journal of Nutrition, 2008. **138**(10): p. 2003S-2007S.

278. Mohyeldin, A., T. Garzon-Muvdi, and A. Quinones-Hinojosa, *Oxygen in Stem Cell Biology: A Critical Component of the Stem Cell Niche.* Cell Stem Cell, 2010. **7**(2): p. 150-161.

279. Epari, D.R., et al., *Pressure, oxygen tension and temperature in the periosteal callus during bone healing - An in vivo study in sheep.* Bone, 2008. **43**(4): p. 734-739.

280. Vats, D., et al., *Oxidative metabolism and PGC-1 beta attenuate macrophage-mediated inflammation.* Cell Metabolism, 2006. **4**(3): p. 255-255.

281. Mehta, M., et al., *Influence of gender and fixation stability on bone defect healing in middle-aged rats: a pilot study.* Clin Orthop Relat Res, 2011. **469**(11): p. 3102-10.

282. Cho, T.J., L.C. Gerstenfeld, and T.A. Einhorn, *Differential temporal expression of members of the transforming growth factor beta superfamily during murine fracture healing.* Journal of Bone and Mineral Research, 2002. **17**(3): p. 513-520.

283. Gerstenfeld, L.C., et al., *Fracture healing as a post-natal developmental process: Molecular, spatial, and temporal aspects of its regulation.* Journal of Cellular Biochemistry, 2003. **88**(5): p. 873-884.

284. Erickson, H.P. and N.A. Carrell, *Fibronectin in Extended and Compact Conformations - Electron-Microscopy and Sedimentation Analysis.* Journal of Biological Chemistry, 1983. **258**(23): p. 4539-4544.

285. Johnson, K.J., et al., *The compact conformation of fibronectin is determined by intramolecular ionic interactions.* Journal of Biological Chemistry, 1999. **274**(22): p. 15473-15479.

286. Zhong, C.L., et al., *Rho-mediated contractility exposes a cryptic site in fibronectin and induces fibronectin matrix assembly.* Journal of Cell Biology, 1998. **141**(2): p. 539-551.

287. Bornstein, P. and E.H. Sage, *Matricellular proteins: extracellular modulators of cell function.* Current Opinion in Cell Biology, 2002. **14**(5): p. 608-616.

288. Bradshaw, A.D. and E.H. Sage, *SPARC, a matricellular protein that functions in cellular differentiation and tissue response to injury.* Journal of Clinical Investigation, 2001. **107**(9): p. 1049-1054.

289. Denhardt, D.T., C.M. Giachelli, and S.R. Rittling, *Role of osteopontin in cellular signaling and toxicant injury.* Annual Review of Pharmacology and Toxicology, 2001. **41**: p. 723-749.

290. Chiquet-Ehrismann, R. and M. Chiquet, *Tenascins: regulation and putative functions during pathological stress.* Journal of Pathology, 2003. **200**(4): p. 488-499.

291. Xue, M. and C.J. Jackson, *Extracellular Matrix Reorganization During Wound Healing and Its Impact on Abnormal Scarring.* Advances in wound care, 2015. **4**(3): p. 119-136.

292. Sinder, B.P., A.R. Pettit, and L.K. McCauley, *Macrophages: Their Emerging Roles in Bone.* Journal of Bone and Mineral Research, 2015. **30**(12): p. 2140-2149.

293. Xing, Z.Q., et al., *Multiple roles for CCR2 during fracture healing.* Disease Models & Mechanisms, 2010. **3**(7-8): p. 451-458.

294. El-Jawhari, J.J., E. Jones, and P.V. Giannoudis, *The roles of immune cells in bone healing; what we know, do not know and future perspectives.* Injury-International Journal of the Care of the Injured, 2016. **47**(11): p. 2399-2406.

295. Hesketh, M., et al., *Macrophage Phenotypes Regulate Scar Formation and Chronic Wound Healing.* International Journal of Molecular Sciences, 2017. **18**(7).

296. Reikeras, O., et al., *Lipopolysaccharide impairs fracture healing - An experimental study in rats.* Acta Orthopaedica, 2005. **76**(6): p. 749-753.

297. Reilkeras, O., et al., *Staphylococcus aureus peptidoglycan impairs fracture healing: An experimental study in rats.* Journal of Orthopaedic Research, 2007. **25**(2): p. 262-266.

298. Grundnes, O. and O. Reikeraas, *Effects of macrophage activation on bone healing.* Journal of Orthopaedic Science, 2000. **5**(3): p. 243-247.

299. Claes, L., et al., *The effect of both a thoracic trauma and a soft-tissue trauma on fracture healing in a rat model.* Acta Orthopaedica, 2011. **82**(2): p. 223-227.

300. Recknagel, S., et al., *Experimental Blunt Chest Trauma Impairs Fracture Healing in Rats.* Journal of Orthopaedic Research, 2011. **29**(5): p. 734-739.

301. Wu, A.C., et al., *Unraveling macrophage contributions to bone repair.* BoneKEy reports, 2013. **2**: p. 373-373.

302. Minutti, C.M., et al., *Tissue-specific contribution of macrophages to wound healing.* Seminars in Cell & Developmental Biology, 2017. **61**: p. 3-11.

303. Kato, T., et al., *Diminished corneal angiogenesis in gelatinase A-deficient mice.* Febs Letters, 2001. **508**(2): p. 187-190.

304. Heissig, B., et al., *Low-dose irradiation promotes tissue revascularization through VEGF release from mast cells and MMP-9-mediated progenitor cell mobilization.* Journal of Experimental Medicine, 2005. **202**(6): p. 739-750.

305. Chantrain, C.F., et al., *Stromal matrix metalloproteinase-9 regulates the vascular architecture in neuroblastoma by promoting pericyte recruitment.* Cancer Research, 2004. **64**(5): p. 1675-1686.

306. Nielsen, B.S., et al., *Expression of matrix metalloprotease 9 in vascular pericytes in human breast cancer.* Laboratory Investigation, 1997. **77**(4): p. 345-355.

307. LeBert, D.C., et al., *Matrix metalloproteinase 9 modulates collagen matrices and wound repair.* Development, 2015. **142**(12): p. 2136-+.

308. Jetten, N., et al., *Anti-inflammatory M2, but not pro-inflammatory M1 macrophages promote angiogenesis in vivo.* Angiogenesis, 2014. **17**(1): p. 109-118.

309. Greenlee, K.J., et al., *Proteomic identification of in vivo substrates for matrix metalloproteinases 2 and 9 reveals a mechanism for resolution of inflammation.* Journal of Immunology, 2006. **177**(10): p. 7312-7321.

310. Senft, A.P., et al., *Surfactant protein-D regulates soluble CD14 through matrix metalloproteinase-12.* Journal of Immunology, 2005. **174**(8): p. 4953-4959.

311. Skokos, E.A., et al., *Lack of TNF-alpha-Induced MMP-9 Production and Abnormal E-Cadherin Redistribution Associated with Compromised Fusion in MCP-1-Null Macrophages.* American Journal of Pathology, 2011. **178**(5): p. 2311-2321.

312. Wood, S., et al., *Pro-Inflammatory Chemokine CCL2 (MCP-1) Promotes Healing in Diabetic Wounds by Restoring the Macrophage Response.* Plos One, 2014. **9**(3).

313. Kawahara, Y., et al., *Role of Macrophage Colony-Stimulating Factor (M-Csf)-Dependent Macrophages in Gastric Ulcer Healing in Mice.* Journal of Physiology and Pharmacology, 2011. **62**(4): p. 441-448.

314. Svensson, J., et al., *Macrophages at the Fetal-Maternal Interface Express Markers of Alternative Activation and Are Induced by M-CSF and IL-10.* Journal of Immunology, 2011. **187**(7): p. 3671-3682.

315. Rider, P., et al., *IL-1 alpha and IL-1 beta Recruit Different Myeloid Cells and Promote Different Stages of Sterile Inflammation.* Journal of Immunology, 2011. **187**(9): p. 4835-4843.

316. England, H., et al., *Release of Interleukin-1 alpha or Interleukin-1 beta Depends on Mechanism of Cell Death.* Journal of Biological Chemistry, 2014. **289**(23): p. 15942-15950.

317. MacLeod, A.S. and J.N. Mansbridge, *The Innate Immune System in Acute and Chronic Wounds.* Advances in Wound Care, 2016. **5**(2): p. 65-78.

318. Blad, C.C., C. Tang, and S. Offermanns, *G protein-coupled receptors for energy metabolites as new therapeutic targets.* Nat Rev Drug Discov, 2012. **11**(8): p. 603-619.

319. Husted, A.S., et al., *GPCR-Mediated Signaling of Metabolites.* Cell Metabolism. **25**(4): p. 777-796.

320. Lampropoulou, V., et al., *Itaconate Links Inhibition of Succinate Dehydrogenase with Macrophage Metabolic Remodeling and Regulation of Inflammation.* Cell Metab, 2016. **24**(1): p. 158-66.

321. Zhang, Z.H., et al., *Identification of lysine succinylation as a new post-translational modification.* Nature Chemical Biology, 2011. **7**(1): p. 58-63.

322. Yang, L., et al., *Triggering the succinate receptor GPR91 enhances pressure overload-induced right ventricular hypertrophy.* International Journal of Clinical and Experimental Pathology, 2014. **7**(9): p. 5415-5428.

323. Littlewood-Evans, A., et al., *GPR91 senses extracellular succinate released from inflammatory macrophages and exacerbates rheumatoid arthritis.* Journal of Experimental Medicine, 2016. **213**(9): p. 1655-1662.

324. Chouchani, E.T., et al., *Ischaemic accumulation of succinate controls reperfusion injury through mitochondrial ROS.* Nature, 2014. **515**(7527): p. 431-+.

325. Lu, Y.T., et al., *Succinate induces aberrant mitochondrial fission in cardiomyocytes through GPR91 signaling.* Cell Death & Disease, 2018. **9**.

326. Nowicki, S. and E. Gottlieb, *Oncometabolites: tailoring our genes.* Febs Journal, 2015. **282**(15): p. 2796-2805.

327. Jackson, L., et al., *Adult mesenchymal stem cells: Differentiation potential and therapeutic applications.* Journal of Postgraduate Medicine, 2007. **53**(2): p. 121-127.

328. Ko, S.H., et al., *Succinate promotes stem cell migration through the GPR91-dependent regulation of DRP1-mediated mitochondrial fission.* Scientific Reports, 2017. **7**.

329. Mumme, M., et al., *Interleukin-1beta modulates endochondral ossification by human adult bone marrow stromal cells.* Eur Cell Mater, 2012. **24**: p. 224-36.

330. Li, Y.H., et al., *Succinate causes alpha-SMA production through GPR91 activation in hepatic stellate cells.* Biochemical and Biophysical Research Communications, 2015. **463**(4): p. 853-858.

331. Liu, T.F., et al., *Fueling the flame: bioenergy couples metabolism and inflammation.* Journal of Leukocyte Biology, 2012. **92**(3): p. 499-507.

332. Bhuniya, D., et al., *Discovery of a potent and selective small molecule hGPR91 antagonist.* Bioorg Med Chem Lett, 2011. **21**(12): p. 3596-602.

333. Trauelsen, M., et al., *Receptor structure-based discovery of non-metabolite agonists for the succinate receptor GPR91.* Molecular Metabolism, 2017. **6**(12): p. 1585-1596.

7. Publications related to this work

7.1. Published

Loeffler, J., Duda, G., N., Sass, F., A. and Dienelt, A., The Metabolic Microenvironment Steers Bone Tissue Regeneration. Trends in Endocrinology and Metabolism, 2018. 29(2): p. 99-110.

7.2. In preparation

Loeffler, J., Sass, F., A., Filter, S., Ellinghaus, A., Duda, G., N. and Dienelt, A. Compromised bone healing is associated with impaired macrophage function in rats.

Loeffler, J., Dienelt, A., Kempa, S. and Duda, G., N., Metabolites of the central carbon metabolism shape the fracture healing microenvironment and fuel bone regeneration.

I. Supplement

a. Project-related data

Table 9. Expression data of rat fracture tissue relative to Tbp ± standard deviation.

	Young			Aged		
Gene	**Day 3**	**Day 7**	**Day 14**	**Day 3**	**Day 7**	**Day 14**
CCR7	1.00±0.00	0.81±0.09	0.93±0.02	16.37±3.09	0.42±0.13	0.38±0.12
CD14	1.00±0.00	1.07±0.05	0.53±0.17	0.37±0.15	0.20±0.06	0.81±0.10
CD68	1.00±0.00	6.44±1.24	5.05±1.99	0.51±0.18	0.58±0.24	10.10±1.33
CD80	1.00±0.00	0.76±0.14	1.26±0.10	1.49±0.37	0.91±0.04	1.87±0.40
CD163	1.00±0.00	0.10±0.02	0.56±0.11	0.31±0.16	0.10±0.12	0.71±0.14
Col1a2	1.00±0.00	1.59±0.36	1.24±0.16	0.14±0.05	0.49±0.12	1.28±0.15
Dectin-1	1.00±0.00	3.66±1.33	9.82±1.01	1.77±0.67	3.26±0.88	8.63±1.27
HIF-1α	1.00±0.00	1.30±0.20	1.44±0.29	0.35±0.18	0.47±0.17	2.24±0.61
IL-1ra	1.00±0.00	2.77±0.71	1.42±0.16	0.65±0.26	0.69±0.17	1.41±0.23
IL-1β	1.00±0.00	0.70±0.18	26.16±1.78	1.82±0.37	0.82±0.10	12.25±1.62
MMP-2	1.00±0.00	5.23±1.38	2.44±0.98	0.26±0.09	0.96±0.04	3.90±0.95
MMP-9	1.00±0.00	50.26±2.87	186.06±7.41	0.83±0.10	12.32±2.62	120.73±3.62
MMP-13	1.00±0.00	3.71±1.35	230.60±11.35	0.08±0.02	0.47±0.22	237.25±5.67
PDGFα	1.00±0.00	1.54±0.33	3.43±0.59	0.28±0.11	0.35±0.09	3.94±0.83
PDGFβ	1.00±0.00	1.72±0.42	2.22±0.53	0.62±0.15	0.54±0.17	4.54±1.16
Spp1	1.00±0.00	2.58±0.81	2.65±1.14	0.86±0.23	1.11±0.10	1.81±0.43
Sucnr1	1.00±0.00	1.07±0.05	0.32±0.06	18.49±1.92	0.68±0.15	0.23±0.05
TNF-α	1.00±0.00	1.43±0.25	0.14±0.02	30.40±2.55	0.85±0.09	0.35±0.09
Wnt5a	1.00±0.00	1.22±0.21	1.28±0.29	0.29±0.10	0.28±0.11	1.62±0.42

Table 10. Expression data of THP-1 cells relative to *RLP13A* ± standard deviation.

Gene	Day 0	Day 7 M0	Day 7 M1	Day 7 M2
CD40	1.00±0.00	20.95±3.64	124.70±2.64	46.05±14.10
CD68	1.00±0.00	19.83±2.71	21.43±26.78	23.28±4.81
CD163	1.00±0.00	164.30±48.56	34.22±33.01	194.90±74.47
MRC1	1.00±0.00	24.59±13.21	-	103.80±36.77
IL-1β	1.00±0.00	305.80±41.35	30.19±25.76	32.63±24.39
TNF-α	1.00±0.00	0.91±0.66	3.28±3.42	0.32±0.20
TGF-β	1.00±0.00	135.20±27.42	11.76±14.71	76.63±35.38
Sucnr1	1.00±0.00	16.31±0.00	3.16±4.11	36.04±32.85

Table 11. Expression data of THP-1 cells under succinate treatment relative to *RPL13A* ± standard deviation.

		50 µM Succinate		
Gene	**D0**	**M0**	**M1**	**M2**
CD40	1.00±0.00	0.64±0.53	11.97±4.50	2.26±1.80
CD68	1.00±0.00	1.82±0.19	0.89±0.21	1.08±0.61
CD163	1.00±0.00	1018.00±711.90	338.40±18.59	971.00±244.40
MRC1	1.00±0.00	37.30±12.69	0.90±0.02	33.77±9.95
IL-1β	1.00±0.00	1.84±1.96	340.60±121.10	4.74±5.98
TNF-α	1.00±0.00	0.02±0.01	0.13±0.18	0.13±0.18
TGF-β	1.00±0.00	2.76±2.68	0.21±0.23	3.93±3.56
Sucnr1	1.00±0.00	2.06±1.58	1.40±1.03	21.34±23.16

Table 11 continued. Expression data of THP-1 cells under succinate treatment relative to *RPL13A* ± standard deviation.

	500 µM Succinate		
Gene	**M0**	**M1**	**M2**
CD40	1.42±0.04	35.88±37.79	12.18±5.60
CD68	2.43±0.09	1.73±1.83	2.82±0.33
CD163	584.50±62.98	655.40±563.70	789.70±88.59
MRC1	57.53±3.96	0.88±0.04	116.00±7.39
IL-1β	0.94±0.10	65.49±91.03	5.03±3.45
TNF-α	0.04±0.04	0.10±0.07	0.12±0.01
TGF-β	1.89±0.45	0.26±0.03	1.87±0.74
Suncr1	1.68±0.81	1.50±0.00	19.61±5.55

Table 12. Gene ontology enrichment results for successful fracture healing at day 3 after osteotomy in rats.

KEGG ID	KEGG pathway	Gene symbol	Category
04874	Protein digestion and adsorption	Col6a2, Col1a2, Col6a1, Col14a1, Col1a1, Col3a1	Protein break down
00561	Glycerolipid metabolism	Akr1a1, Aldh7a1, Akr1b1, Aldh9a1	Glycerolipid metabolism
00400	Phenylalanine, tyrosine and tryptophan biosynthesis	Got1, Got2	Amino acid metabolism
00520	Amino sugar and nucleotide sugar metabolism	Hexa, Pgm3, Galk1, Pmm2, Gmppb, Uap1l1, Galk2	Sugar and nucleotide metabolism
00360	Phenylalanine metabolism	Got1, Got2, Prdx6	Amino acid metabolism
04510	Focal adhesion	Col6a2, Tnc, Crkl, Flnb, Actn2, Thbs4, Tln2, Ppp1cb, Col1a2, Ilk, Col6a1, Col1a1, Col3a1, Vcl, Crk	Focal adhesion
00270	Cysteine and methionine metabolism	Mpst, Got1, Ldha, Got2, Ahcy	Amino acid metabolism

04512	ECM-receptor interaction	Col6a2, Tnc, Col1a2, Col6a1, Col1a1, Thbs4, Col3a1	ECM receptor interaction
00330	Arginine and proline metabolism	Got1, Aldh7a1, Got2, Lap3, Ckb, Aldh9a1	Amino acid metabolism
04530	Tight junction	Myh11, Zak, Actn2, Cttn, Myh3, Myh10, Myh2	Tight junction
04610	Complement and coagulation cascades	C6, Fgb, Plg, Serpina1, Cpb2, C4bpa, F12, Cfi, C8a, Serpinf2, Serping1, C1qb, F2, Fgg, Kng1, F13a1, C8g, Fga, C9, Serpinc1, C8b, C1qc, Klkb1, C3	Complement/ immune processes
05322	Systemic lupus erythematosus	C6, Hist1h4b, C9, C8a, C8b, C1qc, C3, C8g, C1qb	Complement/ immune processes
05020	Prion diseases	C6, C9, C8a, C8b, C1qc, C8g, C1qb	Complement/ immune processes
05150	Staphylococcus aureus infection	Cfi, Fgg, C1qc, Plg, C3, C1qb	Complement/ immune processes
05146	Amoebiasis	Serpinb1a, Arg1, Serpinb10, C9, C8a, C8b, C8g	Complement/ immune processes
04080	Neuroactive ligand-receptor interaction	F2, Plg	Complement/ immune processes
04977	Vitamin digestion and adsorption	Apoa4, Apoa1	Vitamin/fat digestion
04975	Fat digestion and adsorption	Apoa4, Apoa1	Vitamin/fat digestion
05144	Malaria	Thbs1, LOC287167	Complement/ immune processes

Table 13. Gene ontology enrichments for successful fracture healing at day 7 after osteotomy.

KEGG ID	KEGG pathway	Gene symbol	Category
00190	Oxidative metabolism	Uqcrb, Uqcrc1, Atp5b, Uqcrc2, Ndufv3, LOC683884, Uqcrq, Atp5o, Ndufa11, Atp5c1, Ndufs2	Oxidative metabolism
00010	Glycolysis/Gluconeogenesis	Dld, Aldoa, Gpi, Gapdh, Pfkm, Bpgm	Glycolysis/ TCA
00640	Propanoate metabolism	Pcca, Sucla2, Aldh6a1, Suclg1	Glycolysis/ TCA
04060	Cytokine-cytokine receptor interaction	Lifr, Pf4	Cytokine receptor interaction
04146	Peroxisome	Ech1, Crat, Cat, Acsl1	Peroxisome
04260	Cardiac muscle contraction	Uqcrb, Uqcrc2, Cacna2d1, Uqcrq, Uqcrc1	Oxidative metabolism
04141	Protein processing in endoplasmic reticulum	Vcp, Erp29, P4hb, Rrbp1, Calr, Pdia3, Pdia6, Prkcsh, Sec13, Pdia4, Sec61b, Lman2, Sec31a, Hsp90b1, Sec23a, Eif2s1, Txndc5, Hspa5, Ganab, Hyou1, Capn2	Protein processing (ER)
04722	Neutrophin signaling pathway	Crkl, Ywhaz, Ywhab, Ywhah, Ywhaq, Grb2, Ywhag, Crk, Akt1, Camk2d	Signaling/ Cell cycle
03050	Proteasome	Psma6, Psmd3, Psmc4, Psmc1, Psmd11, Psma5, Psmb1, Psmd13, Psma2, Psmd7, Psmc2	Proteasome/ antigen presenting
04012	ErbB signaling pathway	Grb2, Crkl, Crk, Akt1, Camk2d	Signaling/ Cell cycle
04510	Focal adhesion	Zyx, Tnc, Crkl, Actn4, Grb2, Lamc1, Col1a1, Col3a1, Vcl, Col5a2, Crk, Akt1, Capn2	Focal adhesion
03060	Protein export	Srp68, Hspa5, Sec61b	Protein processing (ER)
04110	Cell cycle	Ywhaq, Ywhaz, Ywhag, Ywhab, Ywhah	Signaling/ Cell cycle
04612	Antigen processing and presentation	Hspa4, Hspa5, Calr, B2m, Pdia3	Proteasome/ antigen presenting

Table 14. Gene ontology enrichment results for successful fracture healing at day 14 after osteotomy in rats.

KEGG ID	KEGG pathway	Gene symbol	Category
04610	Complement and coagulation cascades	Fgb, Plg, Serpina1, C4bpa, F12, Cfi, C8a, Serpinf2, Serping1, F2, Cfd, Fgg, C8g, Fga, C9, Serpinc1, C8b, C3	Complement/ immune processes
05150	Staphylococcus aureus infection	Itgam, Itgb2, Cfi, Cfd, Fgg, Plg, C3	Complement/ immune processes
05146	Amoebiasis	Serpinb1a, Itgam, C8g, Itgb2, Fn1, C9, C8a, C8b, Lama2	Complement/ immune processes
04612	Antigen processing and presentation	Ctsb, Hspa5, Hsp90ab1, Calr, Lgmn	Antigen presenting
04977	Vitamin digestion and adsorption	Apoa4, Apoa1	Vitamin/Fat digestion
04810	Regulation of actin cytoskeleton	Itgam, Cfl1, Arpc1b, F2, Arpc3, Itgb2, Fn1, Msn	Regulation of actin cytoskeleton
04975	Fat digestion and adsorption	Apoa4, Apoa1	Vitamin/Fat digestion
00620	Pyruvate metabolism	Glo1, Ldha, Mdh2, Dlat, Aldh1a1, Akr1b1, Aldh9a1	Glycolysis/ TCA
05010	Alzheimer's disease	Capn1, Hsd17b10, Uqcrc2, Uqcrq, Ndufc2, Gapdh, Ndufa4, Ndufa11, Atp2a3, Atp5f1, Uqcrfs1	Oxidative metabolism
00640	Propanoate metabolism	Ldha, Pcca, Aldh1a1, Sucla2, Aldh9a1	Glycolysis/ TCA
00020	Citrate cycle (TCA cycle)	Idh3a, Mdh2, Idh3g, Dlat, Sucla2, Cs	Glycolysis/ TCA
00010	Glycolysis/Gluconeogenesis	Ldha, Pgm1, Dlat, Aldh1a1, Gapdh, Pgam2, Aldh9a1	Glycolysis/ TCA
00500	Starch and sucrose metabolism	Pgm1, Pygmm, Agl, Gys1	Glycogen metabolism
00190	Oxidative phosphorylation	Atp5i, Atp5l, Uqcrc2, Uqcrq, Ndufc2, Ndufa4, Ndufa11, Atp5f1, Uqcrfs1	

Table 15. Gene ontology enrichment results for impaired fracture healing at day 3 after osteotomy in rats.

KEGG ID	KEGG pathway	Gene symbol	Category
04974	Protein digestion and adsorption	Col6a2, Col1a2, Col6a1, Col1a1, Col3a1	Protein processing (ER)
04512	ECM-receptor interaction	Col6a2, Col1a2, Col6a1, Col1a1, Lamc1, Thbs4, Col3a1	ECM-receptor interaction
00561	Glycerolipid metabolism	Akr1a1, Aldh7a1, Akr1b1	Glycerolipid metabolism
05412	Arrhythmogenic right ventricular cardiomyopathy (ARVC)	Lmna, Actn3, Cacna2d1, Actn4, Des	Calcium/muscle signaling
04510	Focal adhesion	Col6a2, Flnb, Actn3, Thbs4, Actn4, Col1a2, Col6a1, Lamc1, Col1a1, Col3a1, Crk, Capn2	Focal adhesion
04141	Protein processing in endoplasmatic reticulum	Erp29, P4hb, Rrbp1, Sec31a, Ckap4, Ddost, Plaa, Txndc5, Sec13, Ssr4, Capn2	Protein processing (ER)
00330	Arginine and proline metabolism	P4ha1, Aldh7a1, Glud1, Got2, Lap3, Ckb	Amino acid metabolism
04740	Olfactory transduction	Camk2g, Camk2d	Calcium/muscle signaling
049622	Vasopressin-regulated water reabsorption	Dync1h1, Dctn1, Dctn2, Arhgdia	Focal adhesion
05146	Amoebiasis	Col1a2, Actn3, Col1a1, Lamc1, Serpinb6, Actn4, Col3a1	ECM-receptor interaction
04670	Leukocyte transendothelial migration	Itgam, Gnai2, Itgb2, Ezr, Rac2, Mmp9, Ncf2	Immune cell activation/migration
00860	Porphyrin and chlorophyll metabolism	Blvrb, Fth1, Hmox1, Alad	Heme metabolism
00860	Regulation of actin cytoskeleton	Itgam, Pak2, Rac2, Arpc3, Itgb3, Itgb2, Myh9, Itga2b, Ezr	Regulation of actin cytoskeleton
05140	Leishmaniasis	Itgam, Itgb2, Ncf2, Ptpn6	Immune cell activation/migration

04110	Cell cycle	Mcm4, Smc1a, Mcm6, Pcna, Hdac1	Cell cycle
00670	One carbon pool by folate	Mthfd1, Dhfr, Shmt2	Folate metabolism
03030	DNA replication	Mcm4, Mcm6, Pcna	Cell cycle
00790	Folate biosynthesis	Dhfr, Spr	Folate metabolism
00910	Nitrogen metabolism	Asns, Ca2	Folate metabolism

Table 16. Gene ontology enrichment results for impaired fracture healing at day 7 after osteotomy in rats.

KEGG ID	KEGG pathway	Gene symbol	Category
04670	Leukocyte transendothelial migration	Vasp, Cdc42, Mmp9, Ncf2, Rac1	Immune cell activation/ migration
04510	Focal adhesion	Itga2b, Vasp, Cdc42, Tln2, Rac1	Focal adhesion
00980	Metabolism of xenobiotics by cytochrome P450	Gstp1, Gsto1	Glutathione metabolism
05100	Bacterial invasion of epithelial cells	Hcls1, Cdc42, Rac1	Immune cell activation/ migration
04666	Fc gamma R-mediated phagocytosis	Vasp, Cdc42, Rac1	Immune cell activation/ migration
03010	Ribosome	Rps2, Rplp2, Rplp0, Rpl17, Rpl3, Rps19	Ribosome
03050	Proteasome	Psma6, Psmc4, Psmc2, Psmd11	Proteasome
04512	ECM-receptor interaction	Tnc, Lamc1	ECM receptor interaction
03013	RNA transport	Eif2b2, Eif2s2	Ribosome
01415	Phagosome	Dync1i2, Tubb6	ECM receptor interaction

Table 17. Gene ontology enrichment results for impaired fracture healing at day 14 after osteotomy in rats.

KEGG ID	KEGG pathway	Gene symbol	Category
03010	Ribosome	Rpl23, Rpl10, Rpl19, Rps11, Rps3, Rpl34, Rpl17, Rpl3, Rpl18a, Rps9, Rps5, Rpl6, Rps12, Rps17, Rps27, Rpl26, Rpl30, Rplp0, Rps18, Rps6, Rpl13	Ribosome
04110	Cell cycle	Mcm4, Smc1a, Mcm6, Pcna, Ywhab, Hdac1, Ywhah	Cell cycle
05322	Systemic lupus erythematosus	Hist1h4b, Ctsg, C9, Hist2h2ac, H2afz, C3, C8g	Immune cell activation/ complement
00460	Cyanoamino acid metabolism	Shmt1, Shmt2	Amino acid metabolism
04914	Progesterone-mediated oocyte maturation	Gnai2, Hsp90ab1, Hsp90aa1, Mapk1	Signal transduction
04610	Complement and coagulation cascades	Fgb, Fgg, C8g, Fga, C9, Serping1, Vwf, C3	Immune cell activation/ complement
05140	Leishmaniasis	Itgam, C3, Ptpn6, Mapk1	Signal transduction
03030	DNA replication	Mcm4, Mcm6, Pcna	Cell cycle
05020	Prion diseases	C9, Sod1, C8g, Mapk1	Immune cell activation/ complement
00020	Citrate cycle (TCA cycle)	Aco2, Ogdh, Pck2, Fh, Pdha1, Cs	TCA cycle
00280	Valine, leucine and isoleucine degradation	Hadha, Ivd, Aldh6a1, Hadhb, Aldh9a1, Oxct1	Amino acid degradation
00620	Pyruvate metabolism	Glo1, Me2, Pck2, Pdha1, Aldh9a1	TCA cycle
04530	Tight junction	Cdc42, Actn4, Ppp2r1a, Cttn, Myh10	Tight junction

00310	Lysine degradation	Hadha, Ogdh, Aldh9a1	Amino acid degradation

Table 18. Gene ontology enrichment analysis for proteins and protein cluster underrepresented in impaired healing fractures compared to successful fracture healing for the time points, day 3, day 7 and day 14 after osteotomy.

KEGG ID	KEGG pathway	Gene symbol	Category	Time point
05410	Hypertrophic cardiomyopathy (HCM)	Cacna1s, Cacna2d1Tnnc1, Ttn, Des, Lama2, Tpm2	Muscle cell contraction; Ca^{2+}	Day 3
00500	Starch and sucrose metabolsim	Pygm, Agl, Gys1, Ugp2, Hk2	Sugar metabolsim	
05414	Dilated cardiomyopathy	Cacna1s, Cacna2d1, Tnnc1, Ttn, Des, Lama2, Tpm2	Muscle cell contraction; Ca^{2+}	
05412	Arrhythmogenic right ventricular cardiomyopathy (ARVC)	Cacna1s, Actn3, Cacna2d1, Des, Lama2	Muscle cell contraction; Ca^{2+}	
05146	Amoebiasis	Hspb1, Actn3, Lamc1, Serpinb6, Col3a1, C8b, Lama2	Migration and cytoskeleton	
04260	Cardiac muscle contraction	Cacna1s, Cacna2d1, Tnnc1, Uqcrh, Tpm2, LOC685322	Muscle cell contraction; Ca^{2+}	
04020	Calcium signalling pathway	Cacna1s, Tnnc1, Camk2a, Atp2a3, Tnnc2	Muscle cell contraction; Ca^{2}	
00250	Alanine, aspartate and glutamate metabolism	Adssl1, Nit2, Aldh5a1	Amino acid metabolism	
04530	Tight junction	Actn3, Mylpf, Cttn, Myh1, Myh3	Migration and cytoskeleton	

00051	Fructose and mannose metabolism	Pmm2, Pfkp, Gmppb, Hk2	Sugar metabolism	Day 7
00310	Lysine degradation	Aldh7a1, Plod1, Plod3	Protein break down	
05160	Hepatitis C	Stat2, Stat3, Ppp2r2a	ECM adhesion	
04530	Tight junction	Myh8, Cttn, Myh1, Myh3, Myh10, Ppp2r2a	ECM adhesion	
00330	Arginine and proline metabolism	P4ha1, Aldh7a1, P4ha2, Ckb	Amino acid metabolism	
04142	Lysosome	Igf2r, Ppt1, Arsb, Clta, Atp6v1h, Hexa, Acp5, Ap1g1, Ctsk	Protein break down	
04510	Focal adhesion	Tnc, Flnb, Pak2, Vasp, Tln2, Spp1, Ilk, Col5a1, Col11a1	ECM, adhesion	
00531	Glycosaminoglycan degradation	Hexa, Arsb	Protein break down	
00190	Oxidative phosphorylation	Ndufb8, Atp5i, Uqcrc1, LOC685322, Ndufa7, Ndufa9, Ndufa11, Ndufs2, Atp5a1, Ndufb10, Ndufa8, Ndufb5, Atp5l, Atp5h, Ndufs7, Cox5b, Ndufs3, Ndufa10, Atp5b, Ndufv1, Ndufa6, Uqcrb, Ndufs1, Cox4i1, Atp5j, Atp5o, Cyc1, Cox7a2, Uqcrfs1, Ndufb9, Cox5a, Ndufb7, Ndufv3, Uqcrq, LOC683884, Uqcrh, Ndufv2, Ndufa4	Oxidative metabolism	Day 14
04260	Cardiac muscle contraction	Uqcrb, Atp2a2, Uqcrc1, Myl3, Tpm2, LOC685322, Atp1a2, Cox4i1, Tnnc1, Cyc1, Uqcrfs1, Cox7a2, Cox5a, Cox5b, Myl2, Uqcrq, Uqcrh	Muscle cell contraction, Ca^{2+}	
00650	Butanoate metabolism	Bdh1, Acads, Acat1, Hadha, Echs1, Hadh, Pdhb, Oxct1	Fatty acid metabolism	
00071	Fatty acid metabolism	Acadm, Acads, Acaa2, Acat1, Hadha, Echs1, Acsl1, Cpt1b, Acadvl, Hadh	Fatty acid metabolsim	
01100	Metabolic pathways	Ndufb8, Atp5i, Asns, Ldhb, Ugp2, Acads, Tkt, Ndufa7, Spr, Ndufa11, Ndufs2, Atp5a1, Ndufb10, Ndufa8, Dhfr, Sucla2, Atp5h,	Oxidative metabolism	

		Acaa2, Ndufs7, Gclm, Idh3B, Hadha, Atp5b, Rpe, Fh, Dbt, Ndufa6, Acsl1, Pdhx, Idh3g, Cmbl, Ndufs1, Cox4i1, Plcg2, Atp5o, Nnt, Uqcrfs1, Acadm, Urod, Ndufb9, Cox5a, Uqcrh, LOC683884, Uqcrq, Ndufv3, Ndufv2, Ndufa4, Ivd, Bdh1, Uqcrc1, Pgp, Cpox, Acat1, LOC685322, Rpia, Ctps, Echs1, Ampd1, Hmbs, Agl, Pfkm, Pgam2, Ckmt2, Ndufa9, Eno3, Ndufb5, Mthfd1, Atp5l, Fbp2, Alad, Cox5b, Ndufs3, Ndufa10, Ndufv1, Got2, Man2a1, Hadh, Rrm1, Coq6, Uqcrb, Gpt, Fech, Mat2b, Atp5j, Cyc1, Ldha, Hibadh, Pfas, Aco2, Ndufb7, Bckdhb, Phgdh, Acadvl, Hk2, Pdhb		
04020	Calcium signalling pathway	Atp2a2, Atp2a1, Tnnc2, Phka1, Vdac3, Camk2g, Slc25a4, Tnnc1, Plcg2, Camk2a, Phkg1, Atp2a3	Muscle cell contraction, Ca^{2+}	

Table 19. Gene ontology enrichment analysis for proteins and protein cluster underrepresented in impaired healing fractures compared to successful fracture healing for the time points, day 3, day 7 and day 14 after osteotomy.

KEGG ID	KEGG pathway	Gene symbol	Category	Time point
03030	DNA replication	Mcm4, Mcm5, Mcm6, Mcm7, Mcm3, Mcm2	Cell cycle	Day 3
04640	Hematopoietic cell lineage	Itgb3, Anpep, Itga2b, Tfrc, Gp1ba, Cd9	Immune cell process	
00860	Porphyrin and chlorophyll metabolism	Urod, Blvrb, Fth1, Fech, Alad, Cpox	Heme& folate metabolism	
04110	Cell cycle	Mcm4, Mcm5, Mcm6, Mcm7, Mcm3, Mcm2	Cell cycle	
04380	Osteoclast differentation	Itgb3, Ppp3ca, Syk, Ncf1, Sirpa, Cybb	Immune cell process	
05310	Asthma	Prg2, Epx	Immune cell process	
00790	Folate biosynthesis	Dhfr, Spr	Heme& folate metabolism	
04142	Lysosome	Napsa, Ctsg, Cltb, Ap3b1, Ap1g1, Ctsz, Arsb	Lysosomal activity	
04662	B cell receptor signalling pathway	Ppp3ca, Rac2, Syk	Immune cell process	
04610	Complement and coagulation cascades	C6, Fga, C4bpa, F12, C1qc, C8g, Serping1, Vwf	Immune& complement processes	Day 7
05322	Systemic lupus erythematosus	C6, Ctsg, Elane, C1qc, C8g	Immune& complement processes	
03030	DNA replication	Mcm6, Mcm7, Mcm2	Cell cycle	
05416	Viral myocarditis	Sgcg, RT1-EC2, Myh4, Rac2	ECM and ECM receptor interaction	
00860	Porphyrin and chlorophyll	Blvrb, Fth1, Hmox1	Heme& folate metabolism	

04512	ECM-receptor interaction	Itga2b, Lamb2, Vwf, Comp	ECM and ECM receptor interaction	
05020	Prion diseases	C6, C1qc, C8g	Immune& complement processes	
05222	Small cell lung cancer	Itga2b, Lamb2	ECM and ECM receptor interaction	
04142	Lysosome	M6pr, Ctsa, Ctsd, Ppt1, Lamp2, Gm2a, Ctss, Lgmn, Igf2r, Hexa, Acp5, Ctsk, Arsb, Lipa, Asah1	Lysosomal activity	Day 14
05146	Amoebiasis	Col5a2, Col1a2, Itgam, Lama2, Lama4, C8g, Lamc1, C8b, Itgb2, C8a, Fn1, Col1a1	ECM, adhesion	
04512	ECM-receptor interaction	Col5a2, Col1a2, Lama2, Lama4, Comp, Lamc1, Itgav, Fn1, Col1a1, Hspg2, Thbs2	ECM, adhesion	
05222	Small cell lung cancer	Lama2, Itgav, Akt1, Lama4, Fn1, Lamc1	ECM, adhesion	
04610	Complement and coagulation cascades	Cfd, F2, C8g, C8b, F12, C8a, Serping1, Cfi, C6, Plg	Immune cell process	
04145	Phagosome	M6pr, Itgam, Lamp2, Mrc1, Ctss, Atp6v1c1, Comp, Itgb2, Itgav, Atp6v1a, Mrc2, Thbs2	Immune cell process	
05323	Rheumatoid arthritis	Itgb2, Atp6v1a, Atp6v1c1, Acp5, Ctsk	Immune cell process	
04514	Cell adhesion molecules (CAM)	Itgb2, Itgam, Glg1, Itgav	ECM, adhesion	
05150	Staphylococcus aureus infection	Itgb2, Itgam, Cfi, Cfd, Plg	Immune cell process	

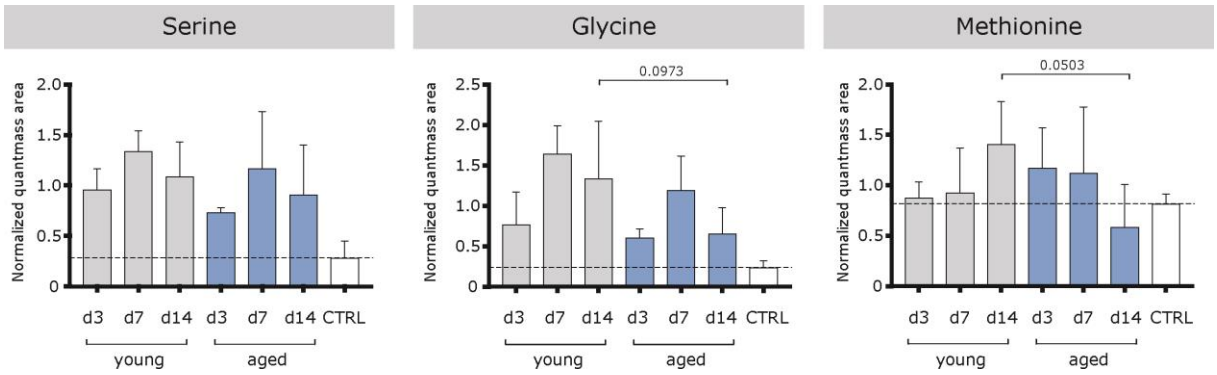

Supplement figure 1. Relative amino acid levels involved in one-carbon cycle in fracture tissue of young and aged animals.

Amino acids that feed into the one-carbon cycle coming from 3PG show a higher trend in fractures of day 14 young animals. Data points indicating trends and close to significant difference were marked with the respective p-value. n=3-5, for experimental groups, n= 2 for control. Welch's t-test.

b. Materials

Table 20. Consumables.

Consumable	Manufacturer
Autosampler, MPS2Xl-Twister	Gerstel, Mühlheim a.d.Ruhr, Germany
BD Vacutainer, serum and citrate	Becton Dickinson, Franklin lakes, New York, United States
Biosphere® Filter Tips	Sarstedt AG, Nümbrecht, Germany
Bone Forceps	Medicon, Tuttlingen, Germany
Cell culture safety hood - Herasafe™	Thermo Fisher Scientific, Waltham, Massachusetts, United States
CasyTT cell counter	Schärfe Systems, Reutlingen, Germany
Cell culture flasks – tissue culture	Becton Dickinson, Franklin lakes, New York, United States
Cell culture plates – tissue culture 6-well, 48- well, 96-well, Falcon	Corning Inc., Corning, New York, United States
Cell culture plates – non tissue culture; 6-well flat bottom , Falcon	Becton Dickinson, Franklin lakes, New York, United States
Cell culture inserts	Becton Dickinson, Franklin lakes, New York, United States
Cell scraper	TPP AG, Trasadingen, Switzerland
Cell strainer, Falcon	Becton Dickinson, Franklin lakes, New York, United States
Centrifuge Mikro 22R	Hettich AG, Bäch, Switzerland
Combitips advanced	Eppendorf, Hamburg, Germany
CoolCell® LX	Corning Inc., Corning, New York, Germany
Cooling plate	EG 1130, Fa. Leica, Bensheim, Germany
Countess® Automated Cell Counter	Life Technologies, Carlsbad, CA, United States
Cryo-film C9	Kawamotos Sectioing Lab , Hiroshima, Japan

Cryo tubes	Thermo Fisher Scientific, Waltham, Massachusetts, United States
Disposable sterile filter	Sigma-Aldrich, St. Louis, MI, United States
Drainage vaccum	Medap, Atmos MedizinTecnick, Rastatt, Germany
Drill bit	Proxoon, Niersbach/Eifel/Germany
Durapore™ wide adhesive tape	3M, St. Paul, Minnesota, USA
Electrical drilling device 16.000 U/min	Implantmeds, W&H Oral Surgery, Büromoos, Austria
ep.T.I.P.S® pipette tips	Eppendorf, Hamburg, Germany
Falcon tubes 15 ml + 50 ml	Becton Dickinson, Franklin lakes, New York, United States
Feather disposable scalpel no.21	FEATHER® Safety Razor Co.Ltd., Osaka, Japan
Feather microtome blades stainless steel N35HR	FEATHER® Safety Razor Co.Ltd., Osaka, Japan
Fixateur external	Custom made
Fluorescent digital imaging system	VWR, Radnor, PA, United States
Freezer	Liebherr, Bulle, Germany
Fridge	Liebherr, Bulle, Germany
Gas liner, CI34	Gerstel, Mühlheim a.d.Ruhr, Germany
Gas chromatograph, Agilent 6890N	Leco, St. Joseph, United States
GentleMACS Dissociater	Milteny Biotec GmbH, Bergisch Gladbach, Germany
Humid chamber	Custom made
Incubator	Heraeus, Hanau, Germany/ Binder, Tuttlingen, Germany
Vacusafe	Integra Biosciences AG, Zizers, Switzerland
Inverted microscope	Leica Microsystems, Wetzlar, Germany
Light Cycler 480 PCR Cycler	Roche, LifeScience, Basel, Switzerland

LightCycler® 480 Multiwell Plate 384, white	Roche, LifeScience, Basel, Switzerland
Kirschner Wires and clamps, titanium	Fa. M. Jagel, Bad Blankenburg/ Germany
Leica RM 2125®, rotary microtome	Leica Microsystems Nussloch GmbH, Bensheim/Germany
MACS Quant	Milteny Biotec GmbH, Bergisch Gladbach, Germany
MACS® MS columns	Milteny Biotec GmbH, Bergisch Gladbach, Germany
Metric threads	Fa. M. Jagel, Bad Blankenburg/ Germany
Microscope (cell culture)	Leica Microsystems Nussloch GmbH, Bensheim/Germany
Microscope (histology)	Zeiss, Oberkochen, Germany
Microscopy slides	Marienfeld GmbH & Co KG, Lauda- Königshofen, Germany
Minicentrifuge for qPCR tubes	Roth, Karlsruhe, Germany
Minilys ® PreCellys	Bertin Technologies, Montigny le Bretonneux, France
MS-TOF, Pegasus IV	Leco, St. Joseph, United States
Multipette® M4	Eppendorf, Hamburg, Germany
Nunc™ EasYFlask™ 75 cm cell culture flask-non-tissue treated	Thermo Fisher Scientific, Waltham, Massachusetts, United States
Parafilm® "M"	Bemis, Neenah, United Stated
Perfect Spin Mini, minicentrifuge	Peqlab, VWR, Radnor, PA, United States
Pipettes	Eppendorf, Hamburg, Germany
Plate reader infinite M200 pro	Tecan Group, Männedorf, Switzerland
PreCellys zirconium oxide beads	Bertin Technologies, Montigny le Bretonneux, France
Precision balance	Sartorius, Göttingen, Germany
qPCR tubes	Eppendorf, Hamburg, Germany

Reaction tubes 0,5ml, 1ml, 2ml	Eppendorf, Hamburg, Germany
Red light lamp 230 V A.C., type S-29-04	Kerbl, Buchbach, Germany
Rotational-Vacuum-Concentrator, 2-33CD plus	Christ, Osterode, Germany
Safety gloves Vasco® Nitril long	Braun, Melsungen, Germany
SCEM-Medium	Leica Microsystems, Wetzlar, Germany
Serological pipettes 5ml, 10ml, 25ml, 50ml, Flacon	Corning Inc., Corning, United States
S-8R saw blades	Implantmeds, W&H Oral Surgery, Büromoos, Austria
Sonicator, Sonorex Digitech	Bandelin electronic, Berlin, Germany
Suture material, non-absorbable	Ethicon, Johnson and Johnson, New Brunswick, New Jersey
Syringes	Braun, Melsungen, Germany
Tecan Reader, Multimode microplate reader m200 pro	Tecan Group AG, Maennedorf, Switzerland
Thermal cycler PTC-200	MJ Research, Bio-rad Laboratories, Hercules, United Stated
Thermomixer comfort	Eppendorf, Hamburg, Germany
Thin-wall 8-cap strips	Thermo Fisher Scientific, Waltham, Massachusetts, United States
Tissue-Tek® O.C.T.™ Compound	Sakura Finetek, Alphen aan den Rijn, The Netherlands
Tweezers and scissors	Medicon, Tuttlingen, Germany
Ultracut S microtome	Leica Microsystems, Wetzlar, Germany
Vicryl suture material, absorbable	Ethicon, Johnson and Johnson, New Brunswick, New Jersey
Vortexer Reax Top	Heidolph Instruments, Schwabach, Germany
Waterbath	Memmert GmbH, Schwabach, Germany

Table 21. Chemicals.

Chemical	Manufacturer
2-mercaptoethanol	Sigma-Aldrich, St. Louis, MI, United States
4′,6-diamidino-2-phenylindole (DAPI)	Sigma-Aldrich, St. Louis, MI, United States
4-Nitrophenylphosphate (*p*NPP)	Sigma-Aldrich, St. Louis, MI, United States
β-glycerolphosphate	Sigma-Aldrich, St. Louis, MI, United States
Acetic acid	Merck, Darmstadt, Germany
Alcian blue 8GS	Chroma Waldeck, Münster, Germany
Alizarin Red S	Merck, Darmstadt, Germany
Ammonia	Merck, Darmstadt, Germany
Antisedan	Pfizer, Karlsruhe, Germany
Aquatex®	Merck, Darmstadt, Germany
Ascorbic acid 2-phosphate sesquimagnesium salt hydrate	Sigma-Aldrich, St. Louis, MI, United States
Bepanthen® eye ointment	Bayer Vital GmbH, Germany
Bovine serum albumin (BSA)	Sigma-Aldrich, St. Louis, MI, United States
Braunoderm®	B. Braun Melsungen AG, Germany
Brilliant Crocein R	Chroma Waldeck, Münster, Germany
$CaCl_2$	Merck, Darmstadt, Germany
Cetylpyridinium chloride	Sigma-Aldrich, St. Louis, MI, United States
Chloroform	Merck, Darmstadt, Germany
Cinnamic acid	Sigma-Aldrich, St. Louis, MI, United States
Clindamycin	Ratiopharm, Ulm, Germany
Dexamethasone	Sigma-Aldrich, St. Louis, MI, United States
Diethanolamine (DEA)	Sigma-Aldrich, St. Louis, MI, United States
Dithiothreitol (DTT)	Sigma-Aldrich, St. Louis, MI, United States
Dulbecco's Modified Eagle Medium – low glucose D6646-500ml	Gibco, Grand Island, NY, United States

Dulbecco's Modified Eagle Medium – high glucose	Gibco, Grand Island, NY, United States
Dulbecco's Phosphate buffered saline	Gibco, Grand Island, NY, United States
Ethanol for cell culture buffer	Merck, Darmstadt, Germany
Ethanol for histology	Herbeta, Berlin, Germany
Ethylenediamine tetraacetic acid (EDTA)	Herbeta Arzneimittel, Germany/ Sigma-Aldrich, St. Louis, MI, United States
Fetal calve serum Superior	Biochrom AG, Berlin, Germany
Fuchsine acid	Merck, Darmstadt, Germany
Glacial acetic acid	Merck, Darmstadt, Germany
Glutamax	Gibco, Grand Island, NY, United States
Glycogen	Invitrogen by Thermo Fisher Scientific, Waltham, Massachusetts, United States
Hematoxylin	Chroma Waldeck, Münster, Germany
Hoechst (bisBenzimide)	Sigma-Aldrich, St. Louis, MI, United States
Hydrogen Chloride	Merck, Darmstadt, Germany
Indomethacin	Sigma-Aldrich, St. Louis, MI, United States
Insulin-transferrin-sodium selenite media supplement (ITS)	Sigma-Aldrich, St. Louis, MI, United States
iScript™ cDNA synthesis kit	Bio-Rad Laboratories, Hercules, United States
Isopropyl alcohol (2-propanol)	Sigma-Aldrich, St. Louis, MI, United States
Ketamin	Actavis, Dublin, Ireland
Linoleic acid	Sigma-Aldrich, St. Louis, MI, United States
Lipopolysaccharide	Sigma-Aldrich, St. Louis, MI, United States
Magnesiumchloride ($MgCl_2$)	Roth, Karlsruhe, Germany
Mayer Hämalaun solution	Merck, Darmstadt, Germany
Methanol (MeOH)	Merck, Darmstadt, Germany
Methoxyamine hydrochloride (MeOx)	Sigma-Aldrich, St. Louis, MI, United States

N-Methyl-N-(trimethylsilyl) trifluoroacetamide (MSTFA)	VWR, Radnor United States
N_2, liquid	Linde, Munich, Germany
NanoDrop spectrophotometer	Thermo Fisher Scientific, Waltham, Massachusetts, United States
Neufuchsin	Dako CemMate, Dako A/S, Denmark
N-N-Dimethylformamid	Sigma-Aldrich, St. Louis, MI, United States
Normal serum horse	Vector laboratories Inc, Burlingame, CA, United States
Nuclease-free water	Thermo Fisher Scientific, Waltham, Massachusetts, United States
Paraformaldehyde 20% Solution, EM Grade 15713	Electron Microscopy Sciences, Hatfield, United States
Penicillin/Streptomycin	Biochrom AG, Berlin, Germany
Phospho wolframic acid	Chroma Waldeck, Münster, Germany
Phorbol 12-myristate 13-acetate	Sigma-Aldrich, St. Louis, MI, United States
Potassium chloride	Fresenius Kabi, Bad Homburg, Germany
PrestoBlue™ Cell Viability Reagent	Invitrogen, Thermo Fisher Scientific, Waltham, Massachusetts, United States
Pyridine	Sigma-Aldrich, St. Louis, MI, United States
Recombinant human IL-4	Miltenyi Biotec, Bergisch Gladbach, Germany
Recombinant human IL-13	Miltenyi Biotec, Bergisch Gladbach, Germany
Recombinant human INF-g	BioLegend, San Diego, United States
RNAse Zap™	Sigma-Aldrich, St. Louis, MI, United Stated
RPMI-1640 Medium R8758-500ml	Sigma-Aldrich, St. Louis, MI, United States
Saffron du Gatinas	Chroma Waldeck, Münster, Germany
Sodium actetate	Merck, Darmstadt, Germany
Sodium azide, NaN_3	Roth, Karlsruhe, Germany
Sodium chloride	Merck, Darmstadt, Germany

Sodium citrate	From BD Vacutainer, Becton Dickinson, Franklin lakes, New York, United States
Sodium hydroxide	Merck, Darmstadt, Germany
Sodium tartrate	Merck, Darmstadt, Germany
Sodiumchloride (NaCl)	Merck, Darmstadt, Germany
Sodiumhydroxyde solution (NaOH) 1M	Sigma-Aldrich, St. Louis, MI, United States
Sodium pyruvate	AppliChem, Darmstadt, Germany
Succinic acid S9512-100g	Sigma-Aldrich, St. Louis, MI, United States
SYBR®Green I Master LightCyler®480	Roche, Basel, Switzerland
Tramal®	Grünenthal GmbH, Aachen, Germany
Tris(Hydroxymethyl)-aminomethan (Tris)	Merck, Darmstadt, Germany
TrisBase	Sigma-Aldrich, St. Louis, MI, United States
Triton X	Sigma-Aldrich, St. Louis, MI, United States
Trizol	Ambion, Life Technologies, Carlsbad, CA, United States
Trypan blue	Life Technologies, Carlsbad, CA, United States
Urea	Roth, Karlsruhe, Germany
Vanadyl Ribosnucleosid Complex	New England Biolabs, Ipswich, United States
Vektor®	Laboratories, Burlingame, USA
Vitro-Clud®	R. Langenbrinck, Emmendingen, Germany
Weigerts's Iron hematoxylin	Chroma, Bellows Falls, Vermont, United States
Xylol	J.T. Baker, Avantor Performance Materials, Center Valley, PA, United States

Table 22. Antibodies.

Antigen	Host species	Flurochrome	Manufaturer	Clone
α-SMA primary antibody	Anti rat	-	Dako, Hamburg, Germany	1A4
AP – AP2000	Anti-mouse		Vector laboratories Inc, Burlingame, CA, United States	
secondary antibody	Anti mouse, rat adsorbed	Bio-tinylated	Vector laboratories Inc, Burlingame, CA, United States	

Table 23. Buffer and media formulation.

Buffer	Formulation
70% Ethanol	15 ml ddH2O 35 ml 100% EtOH
AP Buffer	0.5844 g NaCl with 1.2114 g Tris and 0.0095 g MgCL2 in 100 ml dH2O Adjust to pH 9.0 with HCL and NaOH
AP substrate	Dissolve 1 mg/ml pNPP in 100 ml 1 M diethanolamin (DEA) (10.514 g/l)
Brilliant crocein-acid magenta solution	4 parts 0.1 g Brilliant Crocein R/ 0.5 ml glacial acetic acid 1 part fuchsine acid/ 0.5 ml glacial acetic acid
Chromogen Buffer	3,96 g HCLT 0,54 g Tris Base 2,63 g NaCl Adjust to pH 8,2 with HCL and NaOH

	Fill up to 300 ml with aqua dest
Dissolving buffer	40 mg MeOx 1ml Pyridine
DMEM Expansion Medium	DMEM low glucose 10% FCS 1 % penicillin/ streptomycin 1% Glutamax
FC Buffer	1% bovine serum albuminum 0,1 % NaN_3
MCW	50 ml MeOH 20ml Chloroform 2 µg/ml cinnamic acid 10 ml bi-dest H_2O
MeOH (50%)	50 ml MeOH 2 µg/ml cinnamic acid adjust buffer to 200 ml with bi-dest H_2O
MSTFA	1 ml MSTFA 10 µg/ml alkane standart
Osteogenic Differentiation Medium	DMEM 10%FCS 1% Glutamax 1%Penicillin/Streptomycin 0.2µM dexamethasone 20mM ß-Glycerolphosphate disodium salt hydrate 100µM L-Ascorbic acid 2—phosphate sesquimagnesium salt hydrate
RPMI Expansion Medium	RPMI

	10 % FCS 1 % penicillin/ streptomycin 0.05mM β-mercaptoethanol
Urea buffer	2.4 g Urea 3.2 ml 100 mM Tris

Table 24. Primer sequences human and rat. Synthesized by Invitrogen.

Gene	Forward primer human	Reverse primer human
CD40	GGTCTCACCTCGCTATGGTT	CAGTGGGTGGTTCTGGATG
CD68	GTCCACCTCGACCTGCTCT	CACTGGGGCAGGAGAAACT
CD80	CCGAGTACAAGAACCGGACC	GGTGTAGGGAAGTCAGCTTTGA
CD163	TCAGCTGATTTCAGTGCTGCT	AGGCTGAACTCACTGGGTTATAAAT
CD206/MRC1	GGGCCAAGCTTCTCTGGAAT	TTTATCCACAGCCACGTCCC
IL-1β	GCGTGCTAATGGTGGAAACC	GCTTCTCGGAGCTCTGATGT
TNF-α	TCCCCAGGGACCTCTCTCTA	GAGGGTTTGCTACAACATGGG
TGF-β	GCGTGCTAATGGTGGAAAACC	GCTTCTCGGAGCTCTGATGT
RLP13A	CCTGGAGGAGAAGAGGAAAGAGA	TTGAGGACCTCTGTGTATTTGTCAA
Gene	**Forward primer rat**	**Reverse primer rat**
CCR7	TACATCGGCGAGAACACCAC	CAGGACTTGGCTTCGCTGTA
CD14	CTGAAGCCTTTCTCGGAGCC	AGCATAAGCTTCATGGTCGG
CD68	GCCACTCTTCTGCCATCCTT	TGTGGTGGGAGAAACTGTGG
CD80	GCTGCTGGTTGGTCTTTTCC	TTCTTGTACTCGGGCCACAC
CD163	CTGGAGCATGAACGAGGTGT	TTCCTGAGCATCGGTTGTCC
Col1a2	GGAGAGAGTGCCAACTCCAG	CCACCCCAGGGATAAAAACT
Dectin-1	CGTCTTTTCTGGACCTTGCC	ACGGCCCTTCACTCTGATTG
HIF-1α	AATCTGAGGACACGAGCTGC	TGGGACTGTTAGGCTCAGGT
IL-1ra	AAGCTGTGCCTGTCTTGTGT	TCTCGGAGCGGATGAAGGTA

IL-1β	CAGCTTTCGACAGTGAGGAGA	TGTCGAGATGCTGCTGTGAG
MMP-2	TGGAATGCCATCCCTGATAA	GTGCAGTGAAGATTGTACGG
MMP-9	GTCTGGATAAGTTGGGGCTA	GCCTTGTCTTGGTAGTGAAA
MMP-13	CAGTCTCTCTATGGTCCAGG	TGGTCAAAAACAGTTCAGGC
PDGFα	TTGAACATGACCCGAGCACA	ACACCTCTGTACGCGTCTTG
PDGFβ	TTGAACATGACCCGAGCACA	ACACCTCTGTACGCGTCTTG
Spp1	GAGGAGAAGGCGCATTACAG	ATGGCTTTCATTGGAGTTGC
Sucnr1	CAGCAGGCAACTGTGCTATC	CCAGCTATCCAAGCGTGAGG
Tbp	GGACCAGAAGGATGGCAA	CCGTAAGGCATCATTGGACT
TNF-α	CGTCGTAGCAAACCACCAAG	GAGGCTGACTTTCTCCTGGT
Wnt5a	TACCGCTTCGCCAACCAATT	ACTCCATGGCACTTACAGGC

Table 25. Kits.

Kit	Manufacturer
BCA assay kit, protein determination	Thermo Fisher Scientific, Waltham, Massachusetts, United States
Bio-Plex® Rro™Rat cytokine 23-plex	Bio-rad, Hercules, California, United States
cDNA synthesis iScript	Bio-rad, Hercules, California, United States
CyQuant™ Cell Proliferation Assay	Life Technologies, Carlsbad, CA, United states
PathScan® Th1/Th2/Th17 Cytokine Antibody Array Kit	Cell Signaling Technology, Cambridge, United Kingdom
PureLink™ RNA Mini Kit	Invitrogen by Thermo Fisher Scientific, Waltham, Massachusetts, United States
Quantikine® ELISA human IL-10	R & D Systems, Minneapolis, MN, United States
Quantikine® ELISA human IL-1β/IL-1F2	R & D Systems, Minneapolis, MN, United States
Quantikine® ELISA human TNF-α	R & D Systems, Minneapolis, MN, United States
RapidOut DNA Removal Kit	Thermo Fisher Scientific, Waltham, Massachusetts, United States
RNeasy® Plus Mini Kit	Qiagen, Venlo, The Netherlands
Vectastain ABC Kit (alpha-SMA stain)	Vector® Labs, Burlingame, CA, US

Table 26. Software.

Software	Source and Version	Manufacturer
AxioVision 4.4		Carl Zeiss, Göttingen, Germany
ChromaTOF		Leco, St. Joseph, United States
GraphPad Prism	Version 8 https://www.graphpad.com/company/	GraphPad Software, LaJolla, United States
ImageJ	1.44p; http://rsbweb.nih.gov/ij/	NIH, United states
IOCT. Sass.Dienelt.1.03	ImageJ Macro	Custom made – Julius-Wolff Institut, Berlin, Germany
MAUI	SILVIA	Kuich, MDC Berlin
PCR ΔΔCt method, Data Analysis Center	http://www.qiagen.com/us/products/genes%20and%20pathways/data-analysis-center-overview-page/	Qiagen, Venlo/ Limburg, Netherlands
Primer3	http://primer3.ut.ee/	Whitehead Institute for Biomedical Research, Cambridge, MA, United States
REST software	https://www.gene-quantification.de/rest.html	Pfaffl, Technical University Munich, Qiagen
Reverse ePCR	http://www.ncbi.nlm.nih.gov/tools/epcr/	NCBI, Rockville Pike, MD, United States
Scanco Software	http://mrcb-s010.charite.de/~stimulation/	Scanco Medical AG, Brüttisellen, Switzerland
UVP fluorescence imaging software		VWR, Radnor, PA, United States

Table 27. Animals and cells.

Cell line/ Animal strain	Distributor	Origin
MSCs	Charité, Berlin, Germany	Primary isolation from iliac crest
THP-1 cell line Aco.No 88081201	ECACC	Human monocytic cell line
Spraque Dawley rat	Charles River WIGA, Sulzfeld, Germany	Female, age 3 - 12 months

Table 28. Ethical approvals.

	Number
Animal experiment approvals	Institutional Animal Care and Use Committees, G 0172/15, G0181/14 and G0120/14
MSC isolation	IRB approval EA1/072/08

Table 29. Animal IDs and the applied techniques.

Animal-ID	Age group	Day	Application
501-504	Aged	7	Histology
505-508	Aged	3	Histology
631-635	Aged	7	RNA/OMICs
636-639	Young	7	Histology
641-643	Aged	3	RNA/OMICs
644-647	Aged	3	Histology
661-664	Young	7	RNA/OMICs
665-668	Young	7	Bioplex
671-674	Young	3	RNA/OMICs
705-708	Aged	7	Bioplex
745-748	Young	3	Bioplex
751-754	Aged	14	OMICs

755-758	Aged	14	Histology
761-766	Aged	14	Histology
771-774	Young	14	Bioplex
775-778	Young	14	OMICs
781-786	Young	14	Histology
794-798	Young	14	RNA
801-806	Aged	14	RNA

Table 30. Compounds of the quantification standard in pmol.

Compound	Minimum quantity in pmol (1:200)	Maximum quantity in pmol (1:1)
Adenine	37	7400
Adenosine	94	18709
Alanine	673	134695
Alanine, beta	56	11225
Arginine	57	11481
Asparagine	114	22707
Aspartic acid	75	15025
Butyric acid, 3-hydroxy	144	28818
Butyric acid, 4-amino	48	9697
Citric acid	260	52051
Creatinine	221	44201
Cysteine	41	8254
Cytosine	45	9001
Dihydroxyacetone phosphate	441	88183
Erythritol, meso	409	81887
Fructose	416	83259
Fructose-1,6-bisphosphate	271	54288

Fructose-6-phosphate	66	13154
Fumaric acid	172	34462
Gluconic-acid-6-phosphate	73	14616
Glucosamine	23	4638
Glucose	1943	388544
Glucose-1-phosphate	59	11894
Glucose-6-phosphate	164	32884
Glutamic acid	680	135934
Glutamine	684	136855
Glutaric acid	151	30278
Glutaric acid, 2-hydroxy	286	57268
Glutaric acid, 2-oxo	171	34223
Glyceraldehyde-3-phosphate	323	64668
Glyceric acid	80	15987
Glyceric acid-3-phosphate	323	64668
Glycerol	326	65154
Glycerol-3-phosphate	135	26996
Glycine	333	66605
GMP	101	20113
Hypotaurine	92	18323
Inosine	56	11184
Inositol, myo	278	55506
Isoleucine	191	38116
Lactic acid	2231	446190
Leucine	457	91484
Lysine	103	20531
Malic acid	224	44746

Methionine	34	6702
Pantothenic acid	84	16788
Phenylalanine	242	48429
Phosphoenolpyruvic acid	75	15036
Proline	304	60801
Putrescine	31	6208
Pyroglutamic acid	465	92937
Pyruvate	1454	290803
Ribose	100	19983
Ribose, 2-deoxy	37	7455
Ribose-5-phosphate	456	91208
Serine	571	114188
Succinic acid	212	42341
Threonine	839	167898
Tyrosine	55	11038
Uracil	134	26764
Uridine-5-monophosphate	407	81489
Valine	213	42680